Reiwa 5th academic year

Nagaoka University of Technology,

Graduate School of Engineering

Academic Dissertation for Doctor of Engineering

Proposal and verification of modified optimality criteria method in topology optimization analysis

February, 2024

Major : Science of Technology Innovation

Student ID Number : 17302991

Name : Masayuki Kishida

Supervisor : Professor Takahiko Kurahashi

Table of Contents

List of Figures

Chapter 1

Introduction

1.1 Optimum design and topology optimization

Most of the products have been developed through trial and error and repeated development to bring them closer to convenient products that can be used safely by the all users. However, there is not perfect product. There is a problem somewhere in them, and they will fail at anytime. Maybe it will lead to a recall or a major life-threatening accident. As a countermeasure, researches and developments on optimum design by numerical analysis is being performed daily in the numerical computation to create better products[1]. Optimum design is a technique of determining the most appropriate design variables and parameters to maximize or minimize a performance function (objective function) by satisfying constraints such as safety and cost. Structural optimization, which is the optimum design for a structure, can be classified into three types: size optimization[2, 3], shape optimization[4, 5, 6, 7], and topology optimization[8, 9, 10, 11]. Each optimization is explained below. Size optimization is the easiest method in structural optimization, as shown in Figure 1.1. It uses dimensions such as length and diameter within a design domain as design variables, and uses mathematical optimization methods to perform. Shape optimization is an optimization method that changes the shape of boundary containing the external shape within a design domain, as shown in Figure 1.2. Thus, it is expected to obtained a structure with high performance because it has the higher degree of freedom than that of size optimization. However, shape optimization cannot generate new boundaries, such as changing the number

of voids in a design domain because it only changes the boundaries. On the other hand, topology optimization is represented by material distribution within a design domain, as shown in Figure 1.3. Thus, the number of voids can be changed. Compared to the other structural optimization, topology optimization has the highest degree of freedom of design variables and is expected to significantly improve performance. In recent years, the demand for topology optimization in product design has been increasing. It has been incorporated in Solidworks[12], which is a mechanical design software, ANSYS[13], which is an analysis software, and Fusion 360[14], which is a mechanical design software that will be partially free of charge in 2023. It is growing a familiar method in the field of engineering.

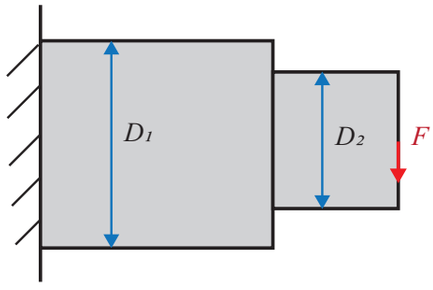

Figure 1.1: Size optimization.

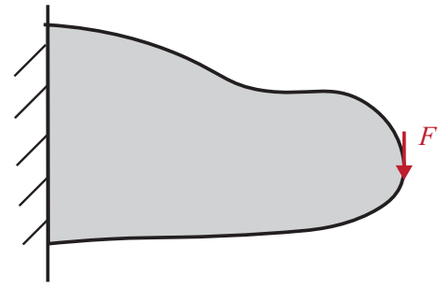

Figure 1.2: Shape optimization.

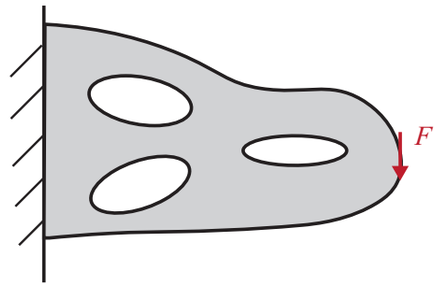

Figure 1.3: Topology optimization.

As mentioned above, topology optimization represents a optimum structure by material distribution and is employed for conceptual design and weighting reduction to reduce material costs. Structural optimization, including topology optimization, requires obtaining state variables, which are output results in a general analysis. To obtain state variables, a given mathematical model (differential equations) must be discretized based on a discretization method to obtain approximate solutions. The discretization method includes the difference method, the finite element method (FEM), the finite volume method (FVM), and the boundary element method (BEM)[15]. These methods will be explained. The difference method is a method of numerically solving unknowns at grid points by approximating derivatives in difference equations by differences and creating difference equations. This method is characterized by its simple discretization and versatility. For this reason, it is still the major methods used in the field of computational fluid dynamics. The FEM[16, 17, 18, 19] was developed for aircraft structural analysis in mid 1950s. The method divides a domain into a finite number of subdomains and approximates unknowns by superposition of simple functions. Because a subdomains are arbitrarily shapes, it can be on either structured and unstructured meshes. This domain part is called an element and the grid point is called node. In two dimensional problems, there are triangles and quadrilateral elements. Additionally, a technique was developed to automatically divide the element[20]. Because an element geometry is arbitrary, element dividing is relatively easy, even for complex structures and boundaries, compared to the difference method. The FVM was developed in 1960s for fluid analysis based on unstructured mesh. As in the FEM, a domain is divided into a finite number of arbitrarily shapes subdomain called cell. The governing equation is discretized into integral equation obtained in a control volume controlled at a cell. Thus, it is also called control volume method. In the discretization, a difference approximation is commonly used to approximate a derivative, and a midpoint formula is commonly used to approximate an integral. Thus, the theory of discretization is simple for unstructured meshes and is often used in commercial fluid analysis codes. The BEM became a popular method in 1970s. It is based on the old integral equation method and the boundary integral equation method. A

differential equation representing a phenomenon is expressed in terms of a boundary integral equation to obtain a numerically approximate solution. It is possible to reduce the number of dimensions to be analyzed. Thus, this method reduces the domain segmentation. For example, it is suitable for problems with infinite domains, such as wave propagation in a ground, and problems with singularity in a solution, such as stress concentration. In this study, since both structured and unstructured meshes are targeted, the state variables are obtained based on FEM, and topology optimization is performed. Next, a classification of topology optimization is explained. There are three methods to represent material distribution in topology optimization. The homogenization method[21, 22] creates a microstructure with a certain shape of vacancy in an element and determines the presence or absence of material by a size of vacancy, as shown in Figure 1.4. The shapes of vacancies vary, including layered microstructure[23, 24, 25], rectangular microstructure[26], and hexagonal microstructure[27]. The method can be used to obtain mathematically rigorous function for presence or absence of material. However, it is well known that numerical calculations are difficult. Moreover, as long as a function that shows even a qualitative trend is used, it does not require to be that rigorous in an optimization. Thus, the density method[28, 29] was proposed as a simple method for engineering. The method represents a material by using density, which is a non-dimensional quantity, as the design variable, as shown in Figure 1.5. The range is from 0 to 1. The image of density is similar to a 3D printer's fill factor, with a density value closer to 0 indicating no material(void) and a density value closer to 1 indicating material. There are two methods in the density method, which will be introduced in the next chapter. However, the method is inconvenient for products because it represents grayscale, which is an intermediate material. Several countermeasures were proposed. One of the measures is the level set method[30, 31, 32]. The method expresses a material distribution by the sign of a function called the level set function, as shown in Figure 1.6. The advantage is that there is no grayscale and the boundaries between object and cavity domains are clear. In contrast, the disadvantage is that it is difficult to derive topological derivative for complex problems such as elastoplastic materials[33]. Thus, this limits to apply. On the other hand, the den-

sity method can be applied to complex problem such as the elastoplastic materials described above, and many methods have been studied to suppress grayscale. In addition, compared to the density method, the level set method is required a large number of iterations, even for linear problems. It also has the disadvantage of being strongly dependent on the inital design and conditions[34]. In light of the above, there is no universal method within topology optimization, as all three methods have their own characteristics. Therefore, it is important to consider the characteristics of optimum design problem and select an appropriate topology optimization methodology. In recent years, besides performance improvement, topology optimization has also been studied with aesthetic preferences in mind.

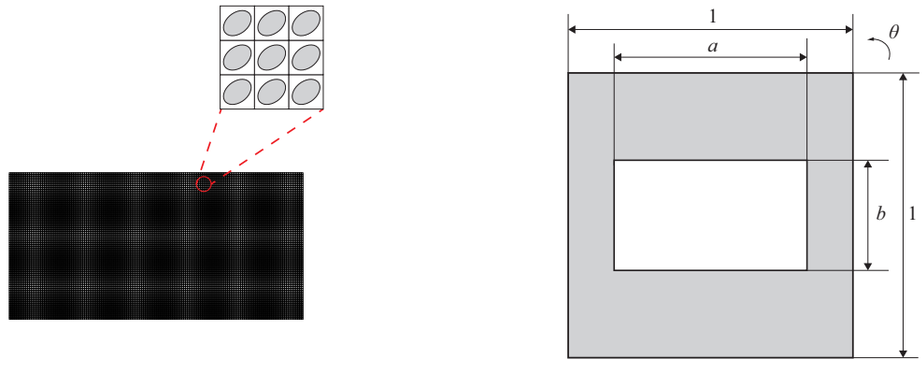

(a) Microstructure. (b) Unit cell.

Figure 1.4: Homogenization method.

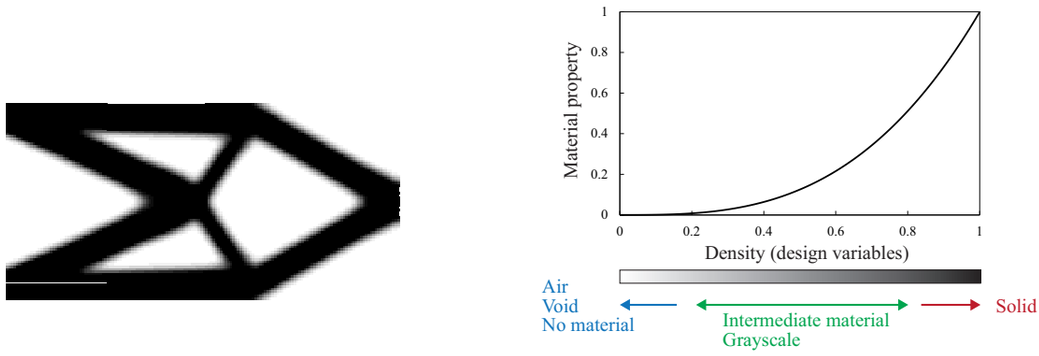

(a) Material distribution. (b) Graph of density method.

Figure 1.5: Density method.

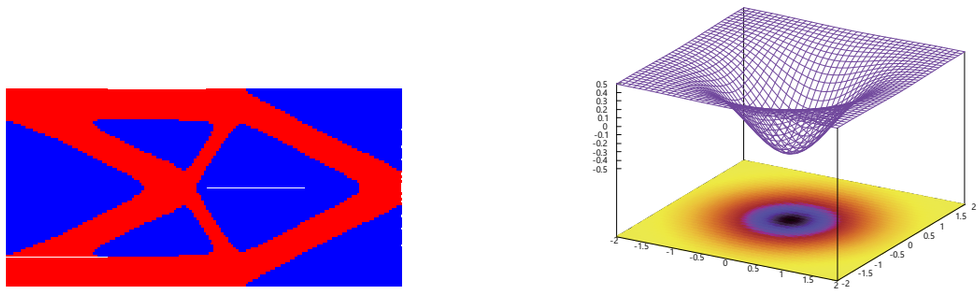

(a) Material distribution. (b) Image of level set function.

Figure 1.6: Level set method.

1.2 Research trend in topology optimization and modern manufacturing

Manufacturing and production technologies are growing and changing rapidly. In recent years, further development has continued based on the guidelines such as the Sustainable Development Goals (SDGs)[36] and Society 5.0[37]. The SDGs are international goals for a sustainable and better world by 2030, decided at the United Nations Summit in September

2015 It was planned after the Millennium Development Goals (MDGs)[38] in 2001. The MDGs have 8 goals. However, the SDGs have 17 goals and 169 targets. Among the added goals, guidelines related to manufacturing such as “No.9: Industry, innovation and infrastructure” and “No.12: Responsible consumption and production” have been added. It can be said that the importance of these goals is increasing year by year in the world. In particular, the targets in No.9 are not just about developing industry. There are targets such as making resourses use less wastefully and making infrastructure and industry sustainable for the environment. In other words, it is globally important to establish technologies for efficient use of resources. Next, the Society 5.0, which is was performed from 2016 to 2020, will be explained. The Society 5.0 is a concept for the future society proposed by Japan in 5th science and technology basic plan The aims is to achieve both economic developments, including industry and solutions of social issues through advanced technologies. Social issues include a review of industry to reduce greenhouse gas emissions, increase production, and reduce losses. In light of the above, the manufacturing is being considered again in Japan as well as the SDGs. This trend is also described in a statutory white paper based on Japan’s basic law for the promotion of basic manufacturing technology. The 2020 white peper[39] states that deign capability will be enhanced by strengthening the first half of the engineering chain, lead times from design to production will be shortened, and corporate transformation capabilities will be enhanced through front-loading, as shown in Figures 1.7 and 1.8. This strategy has led to the use of computer aided engineering (CAE) in the product design, and has emphasized the importance of design before manufacturing. The 2023 white paper states that in Japan’s manufacturing industry, about 90% of large enterprise and 50% of small and Medium-sized enterprise have begun decarbonization efforts. This includes not only the front-loading mentioned above, but also a review due to weight reduction. Here, hybrid vehicles, in which Japanese firms have a 56.3% share of the global market, are cited as an example. Japan Automobile Manufactures Associate (JAMA) introduced major fuel efficiency important technologies as part of its efforts to improve automobile fuel economy to reduce CO_2 emissions by 2022. Specifically, JAMA stated that the weight reduction of

vehicle is a factor that contributes to improved fuel economy, and suggested improvements in body structure and increased use of lightweight materials. Researchers at the Toyota Central R&D Labs., Inc. also noted the importance of weighting reduction They described that its weighting reduction is more important than ever in longer driving ranges for electric vehicles and other vehicles. The above shows the importance and difficulty of weight reduction in the industry. Figure 1.9 shows the number of papers by year when "Topology optimization" is used as a search term in Science direct and Scopus, which are the paper search services. The number of papers has been increasing since around 2015, and research is active.

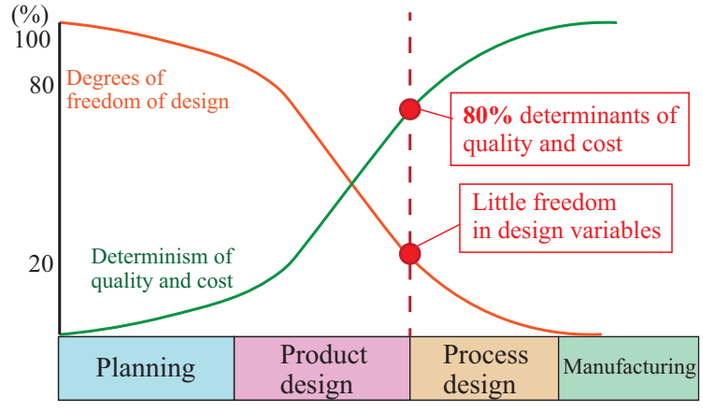

Figure 1.7: Relationship between degrees of freedom of design and quality/cost.

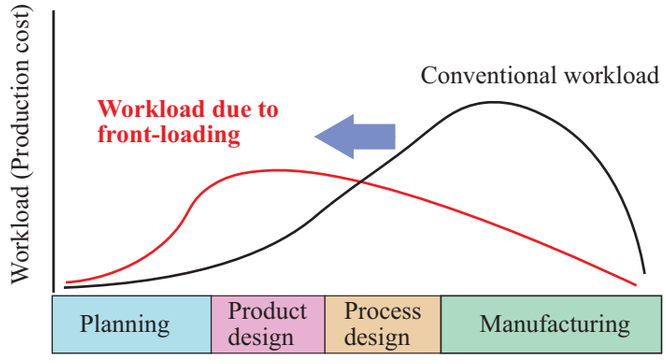

Figure 1.8: Reduced workload through front-loading.

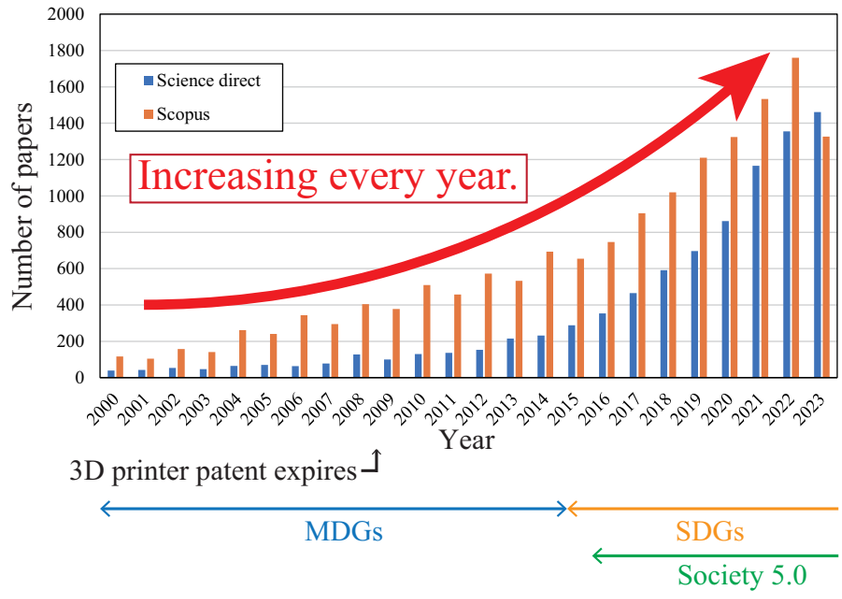

Figure 1.9: Relationship between number of papers and published year on "Topology optimization" by paper services Science direct and Scopus(date of search: September 28th, 2023).

1.3 Aims in the research

The aim of this research is to propose a new updating method for the optimality criteria (OC) method[43], which is an update equation for design variables used in density-based topology optimization, by incorporating Newton's method, which is a fast algorithm for nonlinear equation. Density-based topology optimization is topology optimization based on the density method, a theory that is also implemented in the commercial software mentioned above. The derivation of the performance function is needed to solve optimum design problems involving topology optimization. When the performance function is a function of the state variables, the derivative of the performance function with respect to variations in the design variables must be obtained under equality constraints of state decision problems. The direct derivative method using the chain rue of differentiation and the adjoint variable method using the Lagrange multiplier method are available. The direct derivative method is suitable for multi-constraint problems with few design variables. In contrast, the adjoint variable method is suitable for problems with fewer constraints and more design variables. From above, the adjoint variable method is employed in this topology optimization to find optimum design variables for the number of elements.

Next, the update equation is explained. Since the proposed method is based on the OC method and Newton's method, each method is described below. Before explaining the OC method, the explanation of the fully stressed design, which is considered to be closely related to the OC method, is described. The fully stressed design is the method before size optimization was proposed, and refers to the design in which each member reaches its allowable stress assuming a static truss structure. The feature is that the design aims to ensure that each structural member reaches a critical value, rather than including a minimizing or maximizing performance function and constraint conditions in problem formulations as in optimum design problems. Thus, it is not a mathematical concept that existed from the beginning, but a basic design concept that was developed from the intuition and experience of engineers. Moreover, the algorithm is quite intuitive, since the design aims to ensure all

stress in each structural member satisfy the allowable value. The theory is not necessarily accurate as a mathematical theory. However, it has had a significant impact on optimum design theories and methods, and is still considered the useful design methods from an engineering perspective. The iterative method for the fully stressed method uses the ratio of the current stress value to the critical value to defines the updating of design variables as

$$d_{\langle i \rangle}^{(k+1)} = d_{\langle i \rangle}^{(k)} \left(\frac{\sigma_{\langle i \rangle}^{(k)}}{\bar{\sigma}_{\langle i \rangle}^{(k)}} \right)^{\alpha} \tag{1.1}$$

where $d_{\langle i \rangle}$ is the i-th design variable, $\sigma_{\langle i \rangle}$ is the stress in i-th structural member, $\bar{\sigma}_{\langle i \rangle}^{(k)}$ is critical value of the member, and α is the relaxation factor. The relaxation factor α is generally set to 1. Equation (1.1) is an equation similar to the update equation for the OC method described later. The OC method used to update design variables is closely related to the fully stressed design, which is as mentioned above. The method employs heuristics to find an optimum solution that satisfies the Karush-Kuhn-Tucker (KKT) condition. A new updating method is derived that incorporates the concept of Newton's method for nonlinear equations into the OC method, which is to find solutions that are close to correct solution to some extent. The Newton's method is characterized by faster convergence than other iterative methods. Newton's method was developed by the physicist and mathematician Sir Isaac Newton (1642–1727). The detailed description is described in **chapter 2**. In the optimum design problems, the approximate analysis time is determined by three factors: state analysis, sensitivity analysis, and the number of iterations of the entire computational flow, as shown in Figure 1.11. High performance computer systems such as supercomputers, Fugaku, have been developed to perform high speed calculations. Recently, giga-voxel computational morphogenesis for structural design using the density-based topology optimization was reported in Nature, one of the world's top three journals, with an element count of about 1.1 billion[46]. This allows for, preference-based topology optimization for vehicle concept design with concurrent static and crash load cases[47], and topology optimization of frequency responses of fluid–structure interaction systems[48], all on high performance computer systems. As shown in the research examples above, topology optimization is being performed on

a large scale and in a wide range of fields. However, when performing these optimizations, it is impractical to perform iterative analyses for appropriate parameter settings. In addition, overconfidence in the performance of supercomputer systems is to be avoided. Thus, various studies have been conducted on the three factors mentioned above to improve calculation speed and accuracy by revising the theory. Recent researches for sensitivity analysis have reported studies on accuracy of sensitivity analysis[49, 50] and on the suppression of sensitivity oscillations in the iteration direction[51]. Several other recent researches on the update equation have been reported, including studies on gradient method considering higher-order gradients[52, 53] and on accelerated gradient methods[54, 55]. However, few researches have improved the OC method. Although the OC method is faster than gradient methods such as the steepest descent method, it is not a perfect method. There are several parameters that the engineer must set, which will be shown in the next chapter, and the results obtained will vary depending on how they are set[56]. In addition, it has the disadvantage that it can not be employed under conditions such as when the sensitivity is positive. The OC method required the setting of weighting factor and move-limit as described below. Some methods have been developed that do not set the move-limit, but no method has been developed that does not require arbitrary parameters such move-limit and weighting factor. When the move-limit is set small, an optimal solution is obtained steadily, but the update speed becomes slow. On the other hand, when it is set large, the update speed becomes rapid. The relationship between the update speed is not only related to the move-limit. The weighting factor is also related. Figure 1.10 shows the differences in density distribution depending on the move-limit setting value. When the move-limit is set appropriately, the density is gradually updated to obtaine an optimal density distribution, as shown in the uppar side of Figure 1.10. The density values never suddenly approach zero, and a structure is always updated so that there is always a connection between the elements. On the other hand, when the move-limit is set large, the density is updated rapidly and the update becomes unstable, as shown in the lower side of Figure 1.10. This may lead to a structure with a high performance function. The weighting factor and the move-limit are empirical parameters,

and their appropriate values differ for each analysis. This leads me to contemplate that it is important to provide appropriate weighting factor for an optimization problem. It is important to provide appropriate weighting factor for an optimization problem. If the weighting factor is given as a function of the design variables, the move-limit is not required to be set. The aim of this research is to propose a new update equation based on the OC method to reduce the number of iterations for obtaining optimum results and to reduce the burden on engineers using topology optimization.

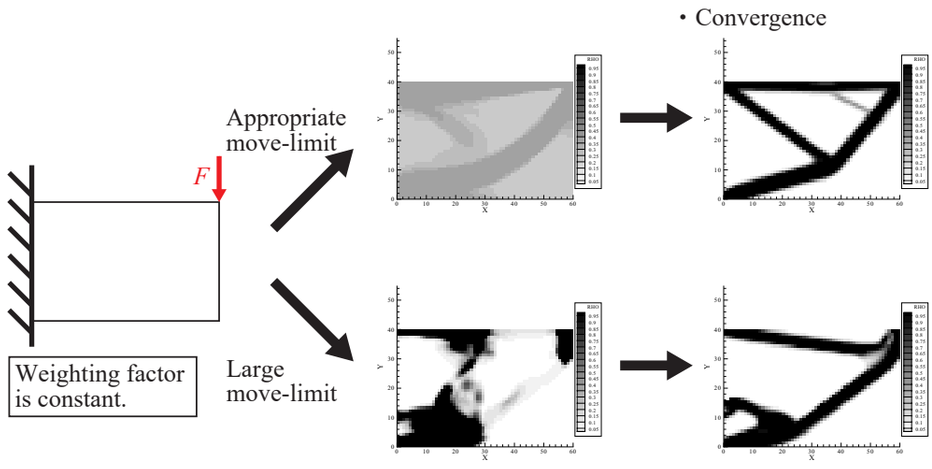

Figure 1.10: Differences in density distributions depending on the move-limit setting value.

In the next and subsequent chapters, density-based topology optimization for strain energy minimization and introduce the proposed modified OC method. The strain energy minimization problem is a problem of self-adjoint relationship that does not require solving an adjoint equation. After that, density-based topology optimization is performed for von Mises stress minimization, which is a problem of non-self-adjoint relationship that require solving an adjoint equation. While strain energy minimization problems are fundamental consideration in structural optimization, they are not often employed in actual design. When designing machines and structures, the materials must be able to wishstand the actual load adequately. In addition, consideration must be given to ensure that they will not break

down during their service life. This is important when designing, because if the machines a structure do not function safely, it will lead to a serious accident. It is the engineer's responsibility to prevent this. Therefore, in mechanical design, the engineer must calculate the stresses in each part of them and take care that they do not exceed the allowable limits of the material used. The factor for safety required for strength calculations is determined by the allowable stress and reference strength. Thus, the topology optimization for von Mises stress minimization problems is performed The von Mises stress is a scalar value that aggregates the stresses used as a design safety index in actual design. The verification of the results obtained by these optimization problems will be demonstrated by actual experiments. From the results, their industrial applicability and usefulness will be discussed. Finally, a multi-objective topology optimization combining the performances of the strain energy minimization problem and the von Mises stress minimization problem is performed. From all results, the usefulness of the proposed method is described.

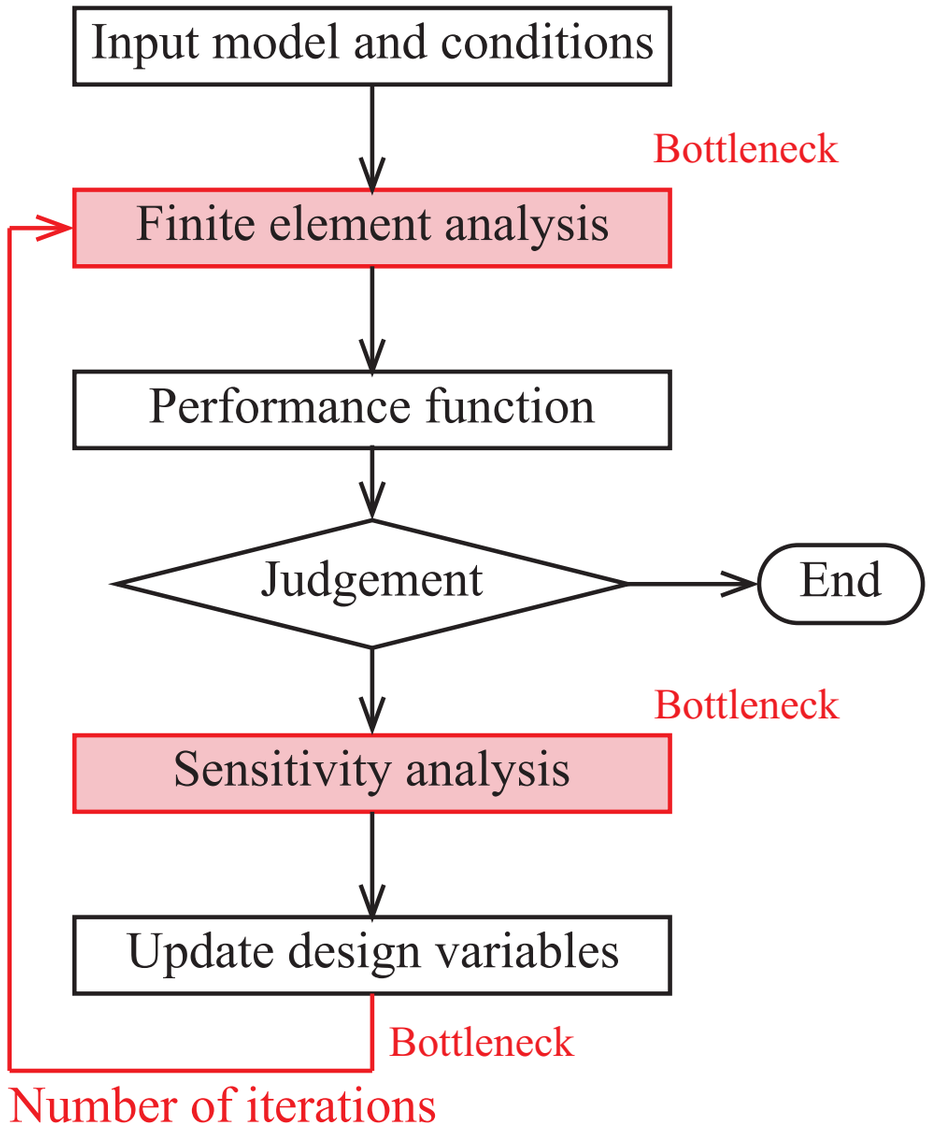

Figure 1.11: Flowchart of structural optimization.

1.4 Thesis structure

The subsequent chapters of this thesis are organized as follows.

- **Chapter 2** Topology optimization in the problems of self-adjoint relation and derivation of the modified OC method
- **Chapter 3** Topology optimization in the problems of non-self-adjoint relation
- **Chapter 4** Demonstration of numerical results by uniaxial tensile testing
- **Chapter 5** Multi-objective topology optimization
- **Chapter 6** Conclusion

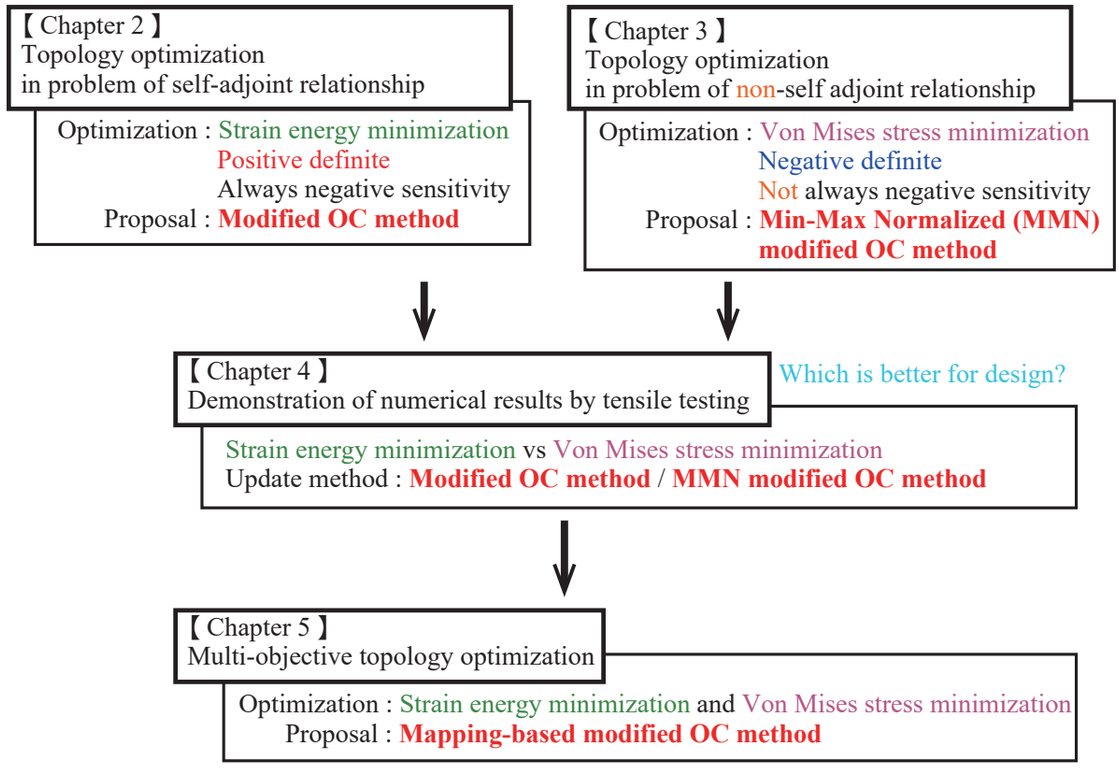

Figure 1.12: Relationship between chapters.

Chapter 2

Topology optimization in the problem of self-adjoint relationship and derivation of a modified optimality criteria method

2.1 Formulation of topology optimization for strain energy minimization in steady problems

The optimization problem consists of a performance function and constraint conditions. It is found the maximum or minimum performance function while satisfying the constrains. Thus, the optimization problem performed in this chapter aims to find a material distribution that minimizes a strain energy in steady state and satisfies the target volume in the design domain Ω. It is a basic study for the topology optimization. Equation (2.1) shows the strain energy in steady state, which is the performance function, Equation (2.2) shows the discretized governing equation for isotropic linear elastic body in steady state, Equation (2.3) shows the volume constraint for a target volume, and Equation (2.4) shows the density constraint for the value of density $\rho_{\langle e \rangle}$ in an element e to be 0 to 1, respectively. Optimization problems including constraint such as the volume constraint are called inequality-constrained

optimization problem.

$$\text{minimize} \quad J = \sum_{e\in\Omega} \frac{1}{2} \left\{f_{\langle e\rangle}\right\}^T \left\{u_{\langle e\rangle}\right\} = \sum_{e\in\Omega} \frac{1}{2} \left\{u_{\langle e\rangle}\right\}^T \left[K_{\langle e\rangle}\right] \left\{u_{\langle e\rangle}\right\} \tag{2.1}$$

$$\text{subject to} \quad [K]\{u\} = \{f\} \tag{2.2}$$

$$V = \sum_{e\in\Omega} \frac{V_{\langle e\rangle}\rho_{\langle e\rangle}}{V_{\text{total}}} - \bar{\rho_0} \leq 0 \tag{2.3}$$

$$0 \leq \rho_{\langle e\rangle} \leq 1 \tag{2.4}$$

Here, $\left[K_{\langle e\rangle}\right]$, $\left\{u_{\langle e\rangle}\right\}$, and $\left\{f_{\langle e\rangle}\right\}$ are the stiffness matrix in an element, displacement vector, and load vector, respectively. In addition, $V_{\langle e\rangle}$, $\rho_{\langle e\rangle}$, V_{total}, and $\bar{\rho_0}$ are the volume or area in an element, density (design variable), total volume or area in the design domain Ω, and initial density average, respectively. Here, $\{\,\}$ represents the vector and $[\,]$ represents the matrix. The superscript T denotes the transposed matrix and the subscript $\langle e\rangle$ denotes the element e. The displacement vector $\left\{u_{\langle e\rangle}\right\}$ is related to all density functions $\rho_{\langle e\rangle}(e \in \Omega)$, however the displacement of element e is dominated by the value of the density in element e. Thus, the stiffness matrix $\left[K_{\langle e\rangle}\right]$ and displacement vector $\left\{u_{\langle e\rangle}\right\}$ are assumed to be function of the density $\rho_{\langle e\rangle}$. The effect of density values of neighboring elements is taken into account using the sensitivity filter described below. To solve the optimization problem shown above, the Lagrange multiplier method is employed. The method is a mathematical technique for optimization subject to constraints. Here, the optimization is performed to satisfy the governing equation shown in Equation (2.2) and to minimize the performance function shown in Equation (2.1). The Lagrange function J^* is defined as

$$\begin{aligned} J^* &= \sum_{e\in\Omega} J^*_{\langle e\rangle} \\ &= \sum_{e\in\Omega} J_{\langle e\rangle} + \left\{\lambda_{\langle e\rangle}\right\}^T \left(\left[K_{\langle e\rangle}\right]\left\{u_{\langle e\rangle}\right\} - \left\{f_{\langle e\rangle}\right\}\right) \end{aligned} \tag{2.5}$$

where $\left\{\lambda_{\langle e\rangle}\right\}$ is the Lagrange multiplier vector. In the subsequent expansions, the performance function $J_{\langle e\rangle}$ in the element e is calculated because the calculation is performed independently for each element. The optimum solution in an optimization problem is the extreme value in mathematics. Maximization problems search for maximum value, and minimization problems search for minimum value. Note that the maximum or minimum in

mathematics is the global optimum solution. In this study, the objective is to find a local optimum solution, which is an extreme value. Moreover, not all optimization problems can be solved. It is difficult to solve the optimization problem unless the KKT condition is satisfied, as in

$$\begin{aligned}
&\frac{\partial L}{\partial x_i} = \frac{\partial f(\boldsymbol{x})}{\partial x_i} + \lambda \frac{\partial g(\boldsymbol{x})}{\partial x_i} = 0 \\
&\lambda g(\boldsymbol{x}) = 0 \\
&\lambda \geq 0 \\
&g(\boldsymbol{x}) \leq 0 \\
&(i = 1, 2, ..., n)
\end{aligned} \tag{2.6}$$

Extreme value is the value of a function when the gradient of a function is zero. That is, each term should be zero as shown in Equation (2.7), and the first variate of the Lagrange function $\delta J^*_{\langle e \rangle}$ should be zero.

$$\delta J^*_{\langle e \rangle} = \left\{ \frac{\partial J^*_{\langle e \rangle}}{\partial \lambda_{\langle e \rangle}} \right\}^T \left\{ \delta \lambda_{\langle e \rangle} \right\} + \left\{ \frac{\partial J^*_{\langle e \rangle}}{\partial u_{\langle e \rangle}} \right\}^T \left\{ \delta u_{\langle e \rangle} \right\} + \frac{\partial J^*_{\langle e \rangle}}{\partial \rho_{\langle e \rangle}} \delta \rho_{\langle e \rangle} = 0 \tag{2.7}$$

The constant terms may also be written, but need not be expanded since the variates are zero. Each of the gradients and variables shown in Equation (2.7) can be expressed as

$$\left\{ \frac{\partial J^*_{\langle e \rangle}}{\partial \lambda_{\langle e \rangle}} \right\} = \{0\}, \quad \left\{ \delta \lambda_{\langle e \rangle} \right\} \neq \{0\} \tag{2.8}$$

$$\left\{ \frac{\partial J^*_{\langle e \rangle}}{\partial u_{\langle e \rangle}} \right\} = \{0\}, \quad \left\{ \delta u_{\langle e \rangle} \right\} \neq \{0\} \tag{2.9}$$

$$\frac{\partial J^*_{\langle e \rangle}}{\partial \rho_{\langle e \rangle}} = 0, \quad \delta \rho_{\langle e \rangle} \neq 0 \tag{2.10}$$

As shown in Equations (2.8) to (2.10), the variates are not zero. Thus, the gradients with respect to the density $\rho_{\langle e \rangle}$ are obtained zero, as shown in Equations (2.8) to (2.10). Next, each gradient is expanded. The gradient of the Lagrange function J with respect to the Lagrange multiplier vector $\left\{ \lambda_{\langle e \rangle} \right\}$ shown in Equation (2.8) is expanded as

$$\left\{ \frac{\partial J^*_{\langle e \rangle}}{\partial \lambda_{\langle e \rangle}} \right\} = \left[K_{\langle e \rangle} \right] \left\{ u_{\langle e \rangle} \right\} - \left\{ f_{\langle e \rangle} \right\} = \{0\} \tag{2.11}$$

Equation (2.11) does not need to be solve because it is the same equation as the governing equation shown in Equation (2.2). Next, the gradient of the Lagrange function J with respect to the displacement vector $\left\{u_{\langle e\rangle}\right\}$ shown in Equation (2.9) is obtained. The gradient of the Lagrange function J with respect to the displacement vector $\left\{u_{\langle e\rangle}\right\}$ is expanded as

$$\begin{aligned}
\left\{\frac{\partial J^*_{\langle e\rangle}}{\partial u_{\langle e\rangle}}\right\} &= \left\{\frac{\partial J_{\langle e\rangle}}{\partial u_{\langle e\rangle}}\right\} + \left\{\lambda_{\langle e\rangle}\right\}^T \left(\left[K_{\langle e\rangle}\right]\left\{\frac{\partial}{\partial u_{\langle e\rangle}}\right\}\left(\left\{u_{\langle e\rangle}\right\}\right)\right) \\
&= \frac{1}{2}\left\{\frac{\partial}{\partial u_{\langle e\rangle}}\right\}\left(\left\{u_{\langle e\rangle}\right\}^T\right)\left[K_{\langle e\rangle}\right]\left\{u_{\langle e\rangle}\right\} \\
&\quad + \frac{1}{2}\left\{u_{\langle e\rangle}\right\}^T\left[K_{\langle e\rangle}\right]\left\{\frac{\partial}{\partial u_{\langle e\rangle}}\right\}\left(\left\{u_{\langle e\rangle}\right\}\right) + \left\{\lambda_{\langle e\rangle}\right\}^T\left[K_{\langle e\rangle}\right] \\
&= \left[K_{\langle e\rangle}\right]\left\{u_{\langle e\rangle}\right\} + \left[K_{\langle e\rangle}\right]\left\{\lambda_{\langle e\rangle}\right\} \\
&= \{0\} \qquad (2.12)
\end{aligned}$$

where the stiffness matrix $\left[K_{\langle e\rangle}\right]$ is assumed to be a symmetric matrix. From Equation (2.12), the relationship can be obtained as

$$\left\{\lambda_{\langle e\rangle}\right\} = -\left\{u_{\langle e\rangle}\right\} \qquad (2.13)$$

This relationship is called the self-adjoint relationship. It is not necessary to solve the adjoint equation to find the adjoint variables, which are the Lagrange multipliers. Finally, the gradient of the Lagrange function J with respect to the density $\rho_{\langle e\rangle}$ is expanded as

$$\begin{aligned}
\frac{\partial J^*_{\langle e\rangle}}{\partial \rho_{\langle e\rangle}} &= \frac{\partial J_{\langle e\rangle}}{\partial \rho_{\langle e\rangle}} + \left\{\lambda_{\langle e\rangle}\right\}^T\left(\frac{\partial\left[K_{\langle e\rangle}\right]}{\partial \rho_{\langle e\rangle}}\left\{u_{\langle e\rangle}\right\} + \left[K_{\langle e\rangle}\right]\left\{\frac{\partial u_{\langle e\rangle}}{\partial \rho_{\langle e\rangle}}\right\}\right) \\
&= \frac{1}{2}\left\{\frac{\partial u_{\langle e\rangle}}{\partial \rho_{\langle e\rangle}}\right\}^T\left[K_{\langle e\rangle}\right]\left\{u_{\langle e\rangle}\right\} + \frac{1}{2}\left\{u_{\langle e\rangle}\right\}^T\frac{\partial\left[K_{\langle e\rangle}\right]}{\partial \rho_{\langle e\rangle}}\left\{u_{\langle e\rangle}\right\} + \frac{1}{2}\left\{u_{\langle e\rangle}\right\}^T\left[K_{\langle e\rangle}\right]\left\{\frac{\partial u_{\langle e\rangle}}{\partial \rho_{\langle e\rangle}}\right\} \\
&\quad + \left\{\lambda_{\langle e\rangle}\right\}^T\frac{\partial\left[K_{\langle e\rangle}\right]}{\partial \rho_{\langle e\rangle}}\left\{u_{\langle e\rangle}\right\} + \left\{\lambda_{\langle e\rangle}\right\}^T\left[K_{\langle e\rangle}\right]\left\{\frac{\partial u_{\langle e\rangle}}{\partial \rho_{\langle e\rangle}}\right\} \\
&= \left(\left\{u_{\langle e\rangle}\right\}^T\left[K_{\langle e\rangle}\right] + \left\{\lambda_{\langle e\rangle}\right\}^T\left[K_{\langle e\rangle}\right]\right)\left\{\frac{\partial u_{\langle e\rangle}}{\partial \rho_{\langle e\rangle}}\right\} + \frac{1}{2}\left\{u_{\langle e\rangle}\right\}^T\frac{\partial\left[K_{\langle e\rangle}\right]}{\partial \rho_{\langle e\rangle}}\left\{u_{\langle e\rangle}\right\} \\
&\quad + \left\{\lambda_{\langle e\rangle}\right\}^T\frac{\partial\left[K_{\langle e\rangle}\right]}{\partial \rho_{\langle e\rangle}}\left\{u_{\langle e\rangle}\right\} \qquad (2.14)
\end{aligned}$$

Using the self-adjoint relationship shown in Equation (2.13), the gradient of the Lagrange function J with respect to the density $\rho_{\langle e \rangle}$ is rewritten as

$$\frac{\partial J^*_{\langle e \rangle}}{\partial \rho_{\langle e \rangle}} = -\frac{1}{2} \left\{ u_{\langle e \rangle} \right\}^T \frac{\partial \left[K_{\langle e \rangle} \right]}{\partial \rho_{\langle e \rangle}} \left\{ u_{\langle e \rangle} \right\} \tag{2.15}$$

This gradient is called sensitivity. Up to here, only the governing equation have been considered as constraint. From next, the Lagrange function L is defined to satisfy the volume constraint shown in Equation (2.3). The gradient of the Lagrange function L with respect to the density $\rho_{\langle e \rangle}$ is calculated as

$$\frac{\partial L_{\langle e \rangle}}{\partial \rho_{\langle e \rangle}} = \frac{\partial J^*_{\langle e \rangle}}{\partial \rho_{\langle e \rangle}} + \Lambda \frac{\partial V}{\partial \rho_{\langle e \rangle}} = 0 \tag{2.16}$$

where Λ is the Lagrange multiplier. Equation (2.16) can be transformed as

$$\frac{\frac{\partial J^*_{\langle e \rangle}}{\partial \rho_{\langle e \rangle}}}{-\Lambda \frac{\partial V}{\partial \rho_{\langle e \rangle}}} = 1 \tag{2.17}$$

where the sensitivity in the numerator of Equation (2.17) is always negative and the gradient of the Lagrange function L with respect to the density $\rho_{\langle e \rangle}$ and the Lagrange multiplier Λ in the denominator of Equation (2.17) are always positives. Thus, there exists a solution that satisfies the KKT condition. From the above, the OC method, which is an update equation, is derived as

$$\begin{aligned} \rho^{(k+1)}_{\langle e \rangle} &= \rho^{(k)}_{\langle e \rangle} \left(\frac{\frac{\partial J^*_{\langle e \rangle}}{\partial \rho_{\langle e \rangle}}^{(k)}}{-\Lambda^{(k)} \frac{\partial V}{\partial \rho_{\langle e \rangle}}^{(k)}} \right)^{\eta} \\ &= \rho^{(k)}_{\langle e \rangle} \left(A^{(k)}_{\langle e \rangle} \right)^{\eta} \end{aligned} \tag{2.18}$$

where η is the weighting factor and is a constant. Moreover, the superscript (k) is the number of iterations. The OC method will always update $A^{(k)}_{\langle e \rangle}$ to be 1 through this iterative calculation, thus satisfying Equation (2.17). The OC method is characterized by a faster update speed that the steepest descent method. The steepest descent is popular method for update equation in structural optimization problems. On the other hand, it may be too fast and therefore exceed the upper and lower limits of the design variables initially set during

the design variables update phase. As a countermeasure, the following updating constraints are applied to the Equation (2.18).

$$\rho_{\langle e\rangle}^{(k+1)} = \begin{cases} {\rho_{\langle e\rangle}^{L}}^{(k)} & \left(\text{if } \ \rho_{\langle e\rangle}^{(k)} \left(A_{\langle e\rangle}^{(k)}\right)^{\eta} \leq {\rho_{\langle e\rangle}^{L}}^{(k)}\right), \\ \rho_{\langle e\rangle}^{(k)} \left(A_{\langle e\rangle}^{(k)}\right)^{\eta} & \left(\text{if } \ {\rho_{\langle e\rangle}^{L}}^{(k)} \leq \rho_{\langle e\rangle}^{(k)} \left(A_{\langle e\rangle}^{(k)}\right)^{\eta} \leq {\rho_{\langle e\rangle}^{U}}^{(k)}\right), \\ {\rho_{\langle e\rangle}^{U}}^{(k)} & \left(\text{if } \ \rho_{\langle e\rangle}^{(k)} \left(A_{\langle e\rangle}^{(k)}\right)^{\eta} \geq {\rho_{\langle e\rangle}^{U}}^{(k)}\right) \end{cases} \tag{2.19}$$

Here, ${\rho_{\langle e\rangle}^{L}}^{(k)}$ and ${\rho_{\langle e\rangle}^{U}}^{(k)}$ are set as the upper and lower limits as in

$$\begin{aligned} {\rho_{\langle e\rangle}^{L}}^{(k)} &= \max\left(\rho_{\langle e\rangle}^{(k)} - \rho_{\text{move}}, \ \ 0\right) \\ {\rho_{\langle e\rangle}^{U}}^{(k)} &= \min\left(\rho_{\langle e\rangle}^{(k)} + \rho_{\text{move}}, \ \ 1\right) \end{aligned} \tag{2.20}$$

2.2 Topology optimization for strain energy minimization in dynamic oscillation problems

2.2.1 Formulation and sensitivity of topology optimization in dynamic oscillation problems

This subsection describes the formulation of topology optimization for strain energy minimization in dynamic oscillation problems. Figure 2.1 shows the history of strain energy versus time for an element. When strain energy is used as the performance function, as in steady problems, dynamic oscillation problems can be classified into positive work and negative work in an element, as shown in Figure 2.1. Thus, simply using the sum of strain energy as the performance function may cancel each other out.

In this study, strain energy is classified into two works: positive work and negative work, and optimization problems are solved as maximization and minimization problems, respectively. The maximization problem can be replaced by a minimization problem by adding a negative sign to the performance function. Equation (2.21) shows the performance function

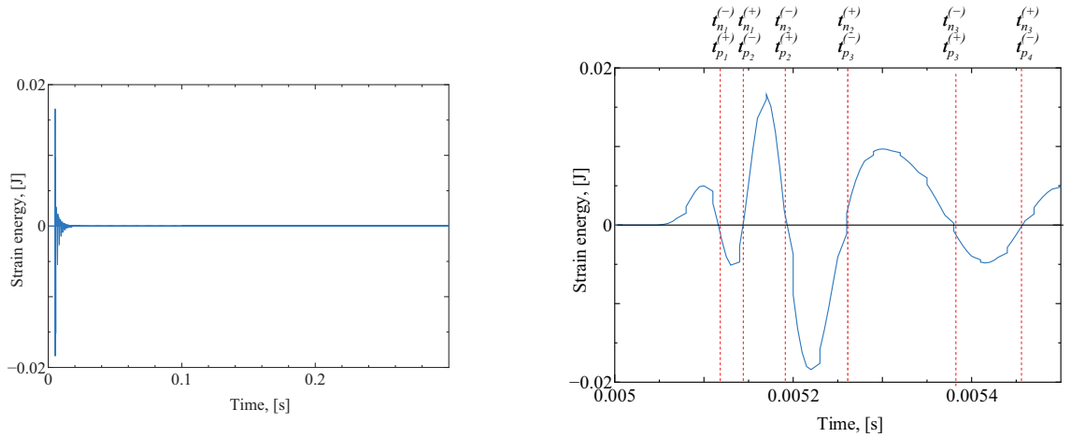

(a) Overall view.

(b) Detailed view.

Figure 2.1: Strain energy waveform in an element.

in dynamic oscillation problem, Equation (2.22) shows the equation of work expressed in absolute value for this optimization problem, Equation (2.23) shows the discretized governing equation in dynamic oscillation problem, Equation (2.24) shows the volume constraint, and Equation (2.25) shows the density constraint, respectively. The volume constraint shown in Equation (2.24) and the density constraint shown in Equation (2.25) are the same as the constrains used in the topology optimization for steady problem described in the previous section. In this thesis, the constraints do not change in subsequent optimization problems as well because the same constraint conditions are employed in topology optimization.

$$\text{minimize} \qquad J = \int_0^{t_f} \sum_{e \in \Omega} J_{\langle e \rangle} dt \tag{2.21}$$

$$J_{\langle e \rangle} = \frac{1}{2} \left| \left\{ f_{\langle e \rangle} \right\}^T \left\{ u_{\langle e \rangle} \right\} \right| \tag{2.22}$$

$$\text{subject to} \qquad [M] \{\ddot{u}\} + [C] \{\dot{u}\} + [K] \{u\} = \{f\} \tag{2.23}$$

$$V = \sum_{e \in \Omega} \frac{V_{\langle e \rangle} \rho_{\langle e \rangle}}{V_{\text{total}}} - \bar{\rho}_0 \leq 0 \tag{2.24}$$

$$0 \leq \rho_{\langle e \rangle} \leq 1 \tag{2.25}$$

Here, the mass matrix $[M]$ is defined as Equation (2.26), and the damping matrix $[C]$ is defined as Equation (2.27) from the Rayleigh damping.

$$\left[M_{\langle e\rangle}\right] = \int_{\Omega_{\langle e\rangle}} d_{\langle e\rangle} \left[N_{\langle e\rangle}\right]^T \left[N_{\langle e\rangle}\right] d\Omega \tag{2.26}$$

$$\left[C_{\langle e\rangle}\right] = \zeta_{\langle e\rangle} \left(\alpha_1 \left[M_{0\langle e\rangle}\right] + \alpha_2 \left[K_{0\langle e\rangle}\right]\right) \tag{2.27}$$

Here, $\left[M_{0\langle e\rangle}\right]$ and $\left[K_{0\langle e\rangle}\right]$ is the mass and stiffness matrices for certain material. Moreover, α_1 and α_2 are the parameters for the Rayleigh damping. First, the Lagrange function J^* is defined to consider only the governing equation, as in topology optimization for strain energy minimization in steady problems.

$$\begin{aligned} J^* &= \sum_{e\in\Omega} \int_0^{t_f} J_{\langle e\rangle} + \frac{1}{2} \left\{\lambda_{\langle e\rangle}\right\}^T \left(\left[M_{\langle e\rangle}\right] \left\{\ddot{u}_{\langle e\rangle}\right\} + \left[C_{\langle e\rangle}\right] \left\{\dot{u}_{\langle e\rangle}\right\} + \left[K_{\langle e\rangle}\right] \left\{u_{\langle e\rangle}\right\} - \left\{f_{\langle e\rangle}\right\}\right) dt \\ &= \sum_{e\in\Omega} J^*_{\langle e\rangle} \end{aligned} \tag{2.28}$$

The first variable of the Lagrange function $J^*_{\langle e\rangle}$ in the element e shown in Equation (2.28) is taken. As in the previous section, before solving for the gradient of the Lagrange function $J^*_{\langle e\rangle}$ for each variable, the time segments required for the case assignment of the performance function shown in Equation (2.22) are defined. The time segments are classified into four categories: starting time of an integral domain for positive work $t^{(-)}_{p_i}$, end time of an integral domain for positive work $t^{(+)}_{p_i}$, starting time of an integral domain for negative work $t^{(-)}_{n_i}$, and end time of an integral domain for negative work $t^{(+)}_{n_i}$. First, the gradient of the Lagrange function J with respect to the Lagrange multiplier vector $\left\{\lambda_{\langle e\rangle}\right\}$ is calculated as

$$\begin{aligned} \left\{\frac{\partial J^*_{\langle e\rangle}}{\partial \lambda_{\langle e\rangle}}\right\} &= \int_0^{t_f} \frac{1}{2} \left\{\frac{\partial}{\partial \lambda_{\langle e\rangle}}\right\} \left(\left\{\lambda_{\langle e\rangle}\right\}^T\right) \\ &\quad \left(\left[M_{\langle e\rangle}\right] \left\{\ddot{u}_{\langle e\rangle}\right\} + \left[C_{\langle e\rangle}\right] \left\{\dot{u}_{\langle e\rangle}\right\} + \left[K_{\langle e\rangle}\right] \left\{u_{\langle e\rangle}\right\} - \left\{f_{\langle e\rangle}\right\}\right) dt \\ &= \{0\} \end{aligned} \tag{2.29}$$

Equation (2.29) is zero from the governing equation shown in Equation (2.23). Next, the gradient of the Lagrange function J with respect to the displacement vector $\left\{u_{\langle e\rangle}\right\}$ is calculated

as

$$\left\{\frac{\partial J^*_{\langle e\rangle}}{\partial u_{\langle e\rangle}}\right\} = \int_0^{t_f}\left\{\frac{\partial J_{\langle e\rangle}}{\partial u_{\langle e\rangle}}\right\} + \frac{1}{2}\left\{\lambda_{\langle e\rangle}\right\}^T\left(\left[M_{\langle e\rangle}\right]\left\{\frac{\partial}{\partial u_{\langle e\rangle}}\right\}\left(\left\{\ddot{u}_{\langle e\rangle}\right\}\right) + \left[C_{\langle e\rangle}\right]\left\{\frac{\partial}{\partial u_{\langle e\rangle}}\right\}\left(\left\{\dot{u}_{\langle e\rangle}\right\}\right) + \left[K_{\langle e\rangle}\right]\left\{\frac{\partial}{\partial u_{\langle e\rangle}}\right\}\left(\left\{u_{\langle e\rangle}\right\}\right)\right) dt \tag{2.30}$$

Assuming that the summed gradient is smaller when the respective gradients are minimized, the positive work and negative work are separated, as shown in

$$\left\{\frac{\partial J^*_{\langle e\rangle}}{\partial u_{\langle e\rangle}}\right\} = \sum_{i=1}^{m_+}\left\{\frac{\partial J^*_{\langle e\rangle_{p_i}}}{\partial u_{\langle e\rangle}}\right\} + \sum_{i=1}^{m_-}\left\{\frac{\partial J^*_{\langle e\rangle_{n_i}}}{\partial u_{\langle e\rangle}}\right\} \tag{2.31}$$

where m_+ and m_- are the number of positive work and negative work integral domains. It is calculated from positive work case shown in the first term of Equation (2.31).

$$\left\{\frac{\partial J^*_{\langle e\rangle_{p_i}}}{\partial u_{\langle e\rangle}}\right\} = \int_{t_{p_i}^{(-)}}^{t_{p_i}^{(+)}}\frac{1}{2}\left\{f_{\langle e\rangle}\right\}^T\left\{\frac{\partial}{\partial u_{\langle e\rangle}}\right\}\left(\left\{u_{\langle e\rangle}\right\}\right) + \frac{1}{2}\left\{\lambda_{\langle e\rangle}\right\}^T\left(\left[M_{\langle e\rangle}\right]\left\{\frac{\partial}{\partial u_{\langle e\rangle}}\right\}\left(\left\{\ddot{u}_{\langle e\rangle}\right\}\right) + \left[C_{\langle e\rangle}\right]\left\{\frac{\partial}{\partial u_{\langle e\rangle}}\right\}\left(\left\{\dot{u}_{\langle e\rangle}\right\}\right) + \left[K_{\langle e\rangle}\right]\left\{\frac{\partial}{\partial u_{\langle e\rangle}}\right\}\left(\left\{u_{\langle e\rangle}\right\}\right)\right) dt \tag{2.32}$$

Using integration by parts, the acceleration vector $\left\{\ddot{u}_{\langle e\rangle}\right\}$ and velocity vector $\left\{\dot{u}_{\langle e\rangle}\right\}$ are transformed into the displacement vector $\left\{u_{\langle e\rangle}\right\}$. Assuming that the acceleration vector $\left\{\ddot{u}_{\langle e\rangle}\right\}$, velocity vector $\left\{\dot{u}_{\langle e\rangle}\right\}$, and displacement vector $\left\{u_{\langle e\rangle}\right\}$ are zero at the starting time of an integral domain for positive work $t_{p_i}^{(-)}$, end time of an integral domain for positive work $t_{p_i}^{(+)}$, Equations (2.33) and (2.34) are obtained.

$$\begin{aligned}
&\int_{t_{p_i}^{(-)}}^{t_{p_i}^{(+)}}\left\{\lambda_{\langle e\rangle}\right\}^T\left[M_{\langle e\rangle}\right]\left\{\frac{\partial}{\partial u_{\langle e\rangle}}\right\}\left(\left\{\ddot{u}_{\langle e\rangle}\right\}\right) dt \\
&= \left[\left\{\lambda_{\langle e\rangle}\right\}^T\left[M_{\langle e\rangle}\right]\left\{\frac{\partial}{\partial u_{\langle e\rangle}}\right\}\left(\left\{\dot{u}_{\langle e\rangle}\right\}\right)\right]_{t_{p_i}^{(-)}}^{t_{p_i}^{(+)}} - \left[\left\{\dot{\lambda}_{\langle e\rangle}\right\}^T\left[M_{\langle e\rangle}\right]\left\{\frac{\partial}{\partial u_{\langle e\rangle}}\right\}\left(\left\{u_{\langle e\rangle}\right\}\right)\right]_{t_{p_i}^{(-)}}^{t_{p_i}^{(+)}} \\
&\quad + \int_{t_{p_i}^{(-)}}^{t_{p_i}^{(+)}}\left\{\ddot{\lambda}_{\langle e\rangle}\right\}^T\left[M_{\langle e\rangle}\right]\left\{\frac{\partial}{\partial u_{\langle e\rangle}}\right\}\left(\left\{u_{\langle e\rangle}\right\}\right) dt \\
&= \int_{t_{p_i}^{(-)}}^{t_{p_i}^{(+)}}\left\{\ddot{\lambda}_{\langle e\rangle}\right\}^T\left[M_{\langle e\rangle}\right]\left\{\frac{\partial}{\partial u_{\langle e\rangle}}\right\}\left(\left\{u_{\langle e\rangle}\right\}\right) dt
\end{aligned} \tag{2.33}$$

$$
\begin{aligned}
&\int_{t_{p_i}^{(-)}}^{t_{p_i}^{(+)}} \left\{\lambda_{\langle e\rangle}\right\}^T \left[C_{\langle e\rangle}\right] \left\{\frac{\partial}{\partial u_{\langle e\rangle}}\right\} \left(\left\{\dot{u}_{\langle e\rangle}\right\}\right) dt \\
= &\left[\left\{\lambda_{\langle e\rangle}\right\}^T \left[M_{\langle e\rangle}\right] \left\{\frac{\partial}{\partial u_{\langle e\rangle}}\right\} \left(\left\{u_{\langle e\rangle}\right\}\right)\right]_{t_{p_i}^{(-)}}^{t_{p_i}^{(+)}} - \int_{t_{p_i}^{(-)}}^{t_{p_i}^{(+)}} \left\{\dot{\lambda}_{\langle e\rangle}\right\}^T \left[M_{\langle e\rangle}\right] \left\{\frac{\partial}{\partial u_{\langle e\rangle}}\right\} \left(\left\{u_{\langle e\rangle}\right\}\right) dt \\
= &-\int_{t_{p_i}^{(-)}}^{t_{p_i}^{(+)}} \left\{\dot{\lambda}_{\langle e\rangle}\right\}^T \left[M_{\langle e\rangle}\right] \left\{\frac{\partial}{\partial u_{\langle e\rangle}}\right\} \left(\left\{u_{\langle e\rangle}\right\}\right) dt \qquad (2.34)
\end{aligned}
$$

Substituting Equations (2.33) and (2.34) into Equation (2.32), it is written as

$$
\begin{aligned}
\left\{\frac{\partial J^*_{\langle e\rangle_{p_i}}}{\partial u_{\langle e\rangle}}\right\} = &\frac{1}{2}\int_{t_{p_i}^{(-)}}^{t_{p_i}^{(+)}} \left(\left\{f_{\langle e\rangle}\right\}^T + \left\{\ddot{\lambda}_{\langle e\rangle}\right\}^T \left[M_{\langle e\rangle}\right] - \left\{\dot{\lambda}_{\langle e\rangle}\right\}^T \left[C_{\langle e\rangle}\right] + \left\{\lambda_{\langle e\rangle}\right\}^T \left[K_{\langle e\rangle}\right]\right) \\
&\left\{\frac{\partial}{\partial u_{\langle e\rangle}}\right\} \left(\left\{u_{\langle e\rangle}\right\}\right) dt \qquad (2.35)
\end{aligned}
$$

The gradient of the Lagrange function with respect to the displacement vector is zero in the positive work domain if the parenthesis in Equation (2.35) is zero. Using the fact that the mass matrix $\left[M_{\langle e\rangle}\right]$, damping matrix $\left[C_{\langle e\rangle}\right]$, and stiffness matrix $\left[K_{\langle e\rangle}\right]$ are symmetric matrices, the parenthesis is rewritten as

$$
\left[M_{\langle e\rangle}\right] \left\{\ddot{\lambda}_{\langle e\rangle}\right\}^T - \left[C_{\langle e\rangle}\right] \left\{\dot{\lambda}_{\langle e\rangle}\right\}^T + \left[K_{\langle e\rangle}\right] \left\{\lambda_{\langle e\rangle}\right\}^T = -\left\{f_{\langle e\rangle}\right\}^T \qquad (2.36)
$$

From Equations (2.24) and (2.36), the following self-adjoint relationships hold for positive work.

$$
\left\{\ddot{\lambda}_{\langle e\rangle}\right\} = -\left\{\ddot{u}_{\langle e\rangle}\right\}, \quad \left\{\dot{\lambda}_{\langle e\rangle}\right\} = \left\{\dot{u}_{\langle e\rangle}\right\}, \quad \left\{\lambda_{\langle e\rangle}\right\} = -\left\{u_{\langle e\rangle}\right\} \qquad (2.37)
$$

It is calculated from negative work case shown in the second term of Equation (2.31).

$$
\begin{aligned}
\left\{\frac{\partial J^*_{\langle e\rangle_{n_i}}}{\partial u_{\langle e\rangle}}\right\} = &\int_{t_{n_i}^{(-)}}^{t_{n_i}^{(+)}} -\frac{1}{2}\left\{f_{\langle e\rangle}\right\}^T \left\{\frac{\partial}{\partial u_{\langle e\rangle}}\right\} \left(\left\{u_{\langle e\rangle}\right\}\right) + \frac{1}{2}\left\{\lambda_{\langle e\rangle}\right\}^T \left(\left[M_{\langle e\rangle}\right] \left\{\frac{\partial}{\partial u_{\langle e\rangle}}\right\} \left(\left\{\ddot{u}_{\langle e\rangle}\right\}\right) + \right. \\
&\left. \left[C_{\langle e\rangle}\right] \left\{\frac{\partial}{\partial u_{\langle e\rangle}}\right\} \left(\left\{\dot{u}_{\langle e\rangle}\right\}\right) + \left[K_{\langle e\rangle}\right] \left\{\frac{\partial}{\partial u_{\langle e\rangle}}\right\} \left(\left\{u_{\langle e\rangle}\right\}\right)\right) dt \qquad (2.38)
\end{aligned}
$$

The same procedure is used for negative work as for positive work. Using integration by parts, the acceleration vector $\left\{\ddot{u}_{\langle e\rangle}\right\}$ and velocity vector $\left\{\dot{u}_{\langle e\rangle}\right\}$ are transformed into the displacement vector $\left\{u_{\langle e\rangle}\right\}$. Assuming that the acceleration vector $\left\{\ddot{u}_{\langle e\rangle}\right\}$, velocity vector

$\left\{\dot{u}_{\langle e\rangle}\right\}$, and displacement vector $\left\{u_{\langle e\rangle}\right\}$ are zero at the starting time of an integral domain for negative work $t_{n_i}^{(-)}$, end time of an integral domain for negative work $t_{n_i}^{(+)}$, Equation (2.39) and Equation (2.40) are obtained.

$$\begin{aligned}
&\int_{t_{n_i}^{(-)}}^{t_{n_i}^{(+)}} \left\{\lambda_{\langle e\rangle}\right\}^T \left[M_{\langle e\rangle}\right] \left\{\frac{\partial}{\partial u_{\langle e\rangle}}\right\} \left(\left\{\ddot{u}_{\langle e\rangle}\right\}\right) dt \\
= &\left[\left\{\lambda_{\langle e\rangle}\right\}^T \left[M_{\langle e\rangle}\right] \left\{\frac{\partial}{\partial u_{\langle e\rangle}}\right\} \left(\left\{\dot{u}_{\langle e\rangle}\right\}\right)\right]_{t_{n_i}^{(-)}}^{t_{n_i}^{(+)}} - \left[\left\{\dot{\lambda}_{\langle e\rangle}\right\}^T \left[M_{\langle e\rangle}\right] \left\{\frac{\partial}{\partial u_{\langle e\rangle}}\right\} \left(\left\{u_{\langle e\rangle}\right\}\right)\right]_{t_{n_i}^{(-)}}^{t_{n_i}^{(+)}} \\
&+ \int_{t_{n_i}^{(-)}}^{t_{n_i}^{(+)}} \left\{\ddot{\lambda}_{\langle e\rangle}\right\}^T \left[M_{\langle e\rangle}\right] \left\{\frac{\partial}{\partial u_{\langle e\rangle}}\right\} \left(\left\{u_{\langle e\rangle}\right\}\right) dt \\
= &\int_{t_{n_i}^{(-)}}^{t_{n_i}^{(+)}} \left\{\ddot{\lambda}_{\langle e\rangle}\right\}^T \left[M_{\langle e\rangle}\right] \left\{\frac{\partial}{\partial u_{\langle e\rangle}}\right\} \left(\left\{u_{\langle e\rangle}\right\}\right) dt
\end{aligned} \tag{2.39}$$

$$\begin{aligned}
&\int_{t_{n_i}^{(-)}}^{t_{n_i}^{(+)}} \left\{\lambda_{\langle e\rangle}\right\}^T \left[C_{\langle e\rangle}\right] \left\{\frac{\partial}{\partial u_{\langle e\rangle}}\right\} \left(\left\{\dot{u}_{\langle e\rangle}\right\}\right) dt \\
= &\left[\left\{\lambda_{\langle e\rangle}\right\}^T \left[M_{\langle e\rangle}\right] \left\{\frac{\partial}{\partial u_{\langle e\rangle}}\right\} \left(\left\{u_{\langle e\rangle}\right\}\right)\right]_{t_{n_i}^{(-)}}^{t_{n_i}^{(+)}} - \int_{t_{n_i}^{(-)}}^{t_{n_i}^{(+)}} \left\{\dot{\lambda}_{\langle e\rangle}\right\}^T \left[M_{\langle e\rangle}\right] \left\{\frac{\partial}{\partial u_{\langle e\rangle}}\right\} \left(\left\{u_{\langle e\rangle}\right\}\right) dt \\
= &-\int_{t_{n_i}^{(-)}}^{t_{n_i}^{(+)}} \left\{\dot{\lambda}_{\langle e\rangle}\right\}^T \left[M_{\langle e\rangle}\right] \left\{\frac{\partial}{\partial u_{\langle e\rangle}}\right\} \left(\left\{u_{\langle e\rangle}\right\}\right) dt
\end{aligned} \tag{2.40}$$

Substituting Equations (2.39) and (2.40) into Equation (2.38), it is written as

$$\begin{aligned}
\left\{\frac{\partial J^*_{\langle e\rangle n_i}}{\partial u_{\langle e\rangle}}\right\} = &\frac{1}{2}\int_{t_{n_i}^{(-)}}^{t_{n_i}^{(+)}} \left(-\left\{f_{\langle e\rangle}\right\}^T + \left\{\ddot{\lambda}_{\langle e\rangle}\right\}^T \left[M_{\langle e\rangle}\right] - \left\{\dot{\lambda}_{\langle e\rangle}\right\}^T \left[C_{\langle e\rangle}\right] + \left\{\lambda_{\langle e\rangle}\right\}^T \left[K_{\langle e\rangle}\right]\right) \\
&\left\{\frac{\partial}{\partial u_{\langle e\rangle}}\right\} \left(\left\{u_{\langle e\rangle}\right\}\right) dt
\end{aligned} \tag{2.41}$$

The gradient of the Lagrange function with respect to the displacement vector is zero for the negative work domain if the parenthesis in Equation (2.41) is zero. Using the fact that the mass matrix $\left[M_{\langle e\rangle}\right]$, damping matrix $\left[C_{\langle e\rangle}\right]$, and stiffness matrix $\left[K_{\langle e\rangle}\right]$ are symmetric matrices, the parenthesis is rewritten as

$$\left[M_{\langle e\rangle}\right] \left\{\ddot{\lambda}_{\langle e\rangle}\right\}^T - \left[C_{\langle e\rangle}\right] \left\{\dot{\lambda}_{\langle e\rangle}\right\}^T + \left[K_{\langle e\rangle}\right] \left\{\lambda_{\langle e\rangle}\right\}^T = \left\{f_{\langle e\rangle}\right\}^T \tag{2.42}$$

From Equations (2.24) and (2.42), the following self-adjoint relationships hold for negative work.

$$\left\{\ddot{\lambda}_{\langle e\rangle}\right\} = \left\{\ddot{u}_{\langle e\rangle}\right\}, \quad \left\{\dot{\lambda}_{\langle e\rangle}\right\} = -\left\{\dot{u}_{\langle e\rangle}\right\}, \quad \left\{\lambda_{\langle e\rangle}\right\} = \left\{u_{\langle e\rangle}\right\} \tag{2.43}$$

Finally, the gradient of the Lagrange function $J_{\langle e\rangle}$ with respect to the density $\rho_{\langle e\rangle}$, which is the sensitivity, is extended as

$$\begin{aligned}\frac{\partial J^*_{\langle e\rangle}}{\partial \rho_{\langle e\rangle}} &= \int_0^{t_f} \frac{\partial J_{\langle e\rangle}}{\partial \rho_{\langle e\rangle}} + \frac{1}{2}\left\{\lambda_{\langle e\rangle}\right\}\left(\frac{\partial\left[M_{\langle e\rangle}\right]}{\partial \rho_{\langle e\rangle}}\left\{\ddot{u}_{\langle e\rangle}\right\} + \left[M_{\langle e\rangle}\right]\left\{\frac{\partial \ddot{u}_{\langle e\rangle}}{\partial \rho_{\langle e\rangle}}\right\} + \frac{\partial\left[C_{\langle e\rangle}\right]}{\partial \rho_{\langle e\rangle}}\left\{\dot{u}_{\langle e\rangle}\right\}\right. \\ &\quad \left. + \left[C_{\langle e\rangle}\right]\left\{\frac{\partial \dot{u}_{\langle e\rangle}}{\partial \rho_{\langle e\rangle}}\right\} + \frac{\partial\left[K_{\langle e\rangle}\right]}{\partial \rho_{\langle e\rangle}}\left\{u_{\langle e\rangle}\right\} + \left[K_{\langle e\rangle}\right]\left\{\frac{\partial u_{\langle e\rangle}}{\partial \rho_{\langle e\rangle}}\right\}\right) dt \end{aligned} \tag{2.44}$$

Similar to the gradients of the Lagrange function with respect to the displacement vector shown in Equation (2.31), it is assumed that the summed gradients are smaller when the respective gradients are minimized, and the positive and negative work cases are separated, as shown in

$$\frac{\partial J^*_{\langle e\rangle}}{\partial \rho_{\langle e\rangle}} = \sum_{i=1}^{m_+} \frac{\partial J^*_{\langle e\rangle_{p_i}}}{\partial \rho_{\langle e\rangle}} + \sum_{i=1}^{m_-} \frac{\partial J^*_{\langle e\rangle_{n_i}}}{\partial \rho_{\langle e\rangle}} \tag{2.45}$$

The first term in Equation (2.45), which is the positive work case, is expanded as

$$\begin{aligned}\frac{\partial J^*_{\langle e\rangle_{p_i}}}{\partial \rho_{\langle e\rangle}} &= \int_{t_{p_i}^{(-)}}^{t_{p_i}^{(+)}} \frac{1}{2}\left\{f_{\langle e\rangle}\right\}^T\left\{\frac{\partial u_{\langle e\rangle}}{\partial \rho_{\langle e\rangle}}\right\} + \frac{1}{2}\left\{\lambda_{\langle e\rangle}\right\}^T\left(\frac{\partial\left[M_{\langle e\rangle}\right]}{\partial \rho_{\langle e\rangle}}\left\{\ddot{u}_{\langle e\rangle}\right\} + \left[M_{\langle e\rangle}\right]\left\{\frac{\partial \ddot{u}_{\langle e\rangle}}{\partial \rho_{\langle e\rangle}}\right\}\right. \\ &\quad + \frac{\partial\left[C_{\langle e\rangle}\right]}{\partial \rho_{\langle e\rangle}}\left\{\dot{u}_{\langle e\rangle}\right\} + \left[C_{\langle e\rangle}\right]\left\{\frac{\partial \dot{u}_{\langle e\rangle}}{\partial \rho_{\langle e\rangle}}\right\} + \\ &\quad \left.\frac{\partial\left[K_{\langle e\rangle}\right]}{\partial \rho_{\langle e\rangle}}\left\{u_{\langle e\rangle}\right\} + \left[K_{\langle e\rangle}\right]\left\{\frac{\partial u_{\langle e\rangle}}{\partial \rho_{\langle e\rangle}}\right\}\right) dt \end{aligned} \tag{2.46}$$

Similar to the gradient of the Lagrange function with respect to the displacement vector, an integration by parts is performed on each term, as shown in

$$\begin{aligned}
&\int_{t_{p_i}^{(-)}}^{t_{p_i}^{(+)}} \left\{\lambda_{\langle e\rangle}\right\}^T \left[M_{\langle e\rangle}\right] \left\{\frac{\partial \ddot{u}_{\langle e\rangle}}{\partial \rho_{\langle e\rangle}}\right\} dt \\
= &\left[\left\{\lambda_{\langle e\rangle}\right\}^T \left[M_{\langle e\rangle}\right] \left\{\frac{\partial \dot{u}_{\langle e\rangle}}{\partial \rho_{\langle e\rangle}}\right\}\right]_{t_{p_i}^{(-)}}^{t_{p_i}^{(+)}} - \left[\left\{\dot{\lambda}_{\langle e\rangle}\right\}^T \left[M_{\langle e\rangle}\right] \left\{\frac{\partial u_{\langle e\rangle}}{\partial \rho_{\langle e\rangle}}\right\}\right]_{t_{p_i}^{(-)}}^{t_{p_i}^{(+)}} \\
&+ \int_{t_{p_i}^{(-)}}^{t_{p_i}^{(+)}} \left\{\ddot{\lambda}_{\langle e\rangle}\right\}^T \left[M_{\langle e\rangle}\right] \left\{\frac{\partial u_{\langle e\rangle}}{\partial \rho_{\langle e\rangle}}\right\} dt \\
= &\int_{t_{p_i}^{(-)}}^{t_{p_i}^{(+)}} \left\{\ddot{\lambda}_{\langle e\rangle}\right\}^T \left[M_{\langle e\rangle}\right] \left\{\frac{\partial u_{\langle e\rangle}}{\partial \rho_{\langle e\rangle}}\right\} dt
\end{aligned} \tag{2.47}$$

$$\begin{aligned}
&\int_{t_{p_i}^{(-)}}^{t_{p_i}^{(+)}} \left\{\lambda_{\langle e\rangle}\right\}^T \left[C_{\langle e\rangle}\right] \left\{\frac{\partial \dot{u}_{\langle e\rangle}}{\partial \rho_{\langle e\rangle}}\right\} dt \\
= &\left[\left\{\lambda_{\langle e\rangle}\right\}^T \left[C_{\langle e\rangle}\right] \left\{\frac{\partial u_{\langle e\rangle}}{\partial \rho_{\langle e\rangle}}\right\}\right]_{t_{p_i}^{(-)}}^{t_{p_i}^{(+)}} - \int_{t_{p_i}^{(-)}}^{t_{p_i}^{(+)}} \left\{\dot{\lambda}_{\langle e\rangle}\right\}^T \left[C_{\langle e\rangle}\right] \left\{\frac{\partial u_{\langle e\rangle}}{\partial \rho_{\langle e\rangle}}\right\} dt \\
= &-\int_{t_{p_i}^{(-)}}^{t_{p_i}^{(+)}} \left\{\dot{\lambda}_{\langle e\rangle}\right\}^T \left[C_{\langle e\rangle}\right] \left\{\frac{\partial u_{\langle e\rangle}}{\partial \rho_{\langle e\rangle}}\right\} dt
\end{aligned} \tag{2.48}$$

Using Equations (2.47) and (2.48), Equation (2.46) is rewritten as

$$\begin{aligned}
\frac{\partial J^*_{\langle e\rangle_{p_i}}}{\partial \rho_{\langle e\rangle}} = &\frac{1}{2}\int_{t_{p_i}^{(-)}}^{t_{p_i}^{(+)}} \left(\left\{f_{\langle e\rangle}\right\}^T + \left\{\ddot{\lambda}_{\langle e\rangle}\right\}^T \left[M_{\langle e\rangle}\right] - \left\{\dot{\lambda}_{\langle e\rangle}\right\}^T \left[C_{\langle e\rangle}\right] + \left\{\lambda_{\langle e\rangle}\right\}^T \left[K_{\langle e\rangle}\right]\right) \left\{\frac{\partial u_{\langle e\rangle}}{\partial \rho_{\langle e\rangle}}\right\} \\
&+ \left\{\lambda_{\langle e\rangle}\right\}^T \left(\frac{\partial \left[M_{\langle e\rangle}\right]}{\partial \rho_{\langle e\rangle}} \left\{\ddot{u}_{\langle e\rangle}\right\} + \frac{\partial \left[C_{\langle e\rangle}\right]}{\partial \rho_{\langle e\rangle}} \left\{\dot{u}_{\langle e\rangle}\right\} + \frac{\partial \left[K_{\langle e\rangle}\right]}{\partial \rho_{\langle e\rangle}} \left\{u_{\langle e\rangle}\right\}\right) dt
\end{aligned} \tag{2.49}$$

From Equation (2.36), the first term in the integration of Equation (2.49) is zero. Moreover, using the self-adjoint relationship for positive work, Equation (2.49) is shown in

$$\frac{\partial J^*_{\langle e\rangle_{p_i}}}{\partial \rho_{\langle e\rangle}} = -\frac{1}{2}\int_{t_{p_i}^{(-)}}^{t_{p_i}^{(+)}} \left\{u_{\langle e\rangle}\right\}^T \left(\frac{\partial \left[M_{\langle e\rangle}\right]}{\partial \rho_{\langle e\rangle}} \left\{\ddot{u}_{\langle e\rangle}\right\} + \frac{\partial \left[C_{\langle e\rangle}\right]}{\partial \rho_{\langle e\rangle}} \left\{\dot{u}_{\langle e\rangle}\right\} + \frac{\partial \left[K_{\langle e\rangle}\right]}{\partial \rho_{\langle e\rangle}} \left\{u_{\langle e\rangle}\right\}\right) dt \tag{2.50}$$

Next, the second term in Equation (2.45), which is the negative work case, is expanded as

$$\begin{aligned}\frac{\partial J^*_{\langle e\rangle_{ni}}}{\partial \rho_{\langle e\rangle}} &= \int_{t_{pi}^{(-)}}^{t_{pi}^{(+)}} -\frac{1}{2}\left\{f_{\langle e\rangle}\right\}^T\left\{\frac{\partial u_{\langle e\rangle}}{\partial \rho_{\langle e\rangle}}\right\}+\frac{1}{2}\left\{\lambda_{\langle e\rangle}\right\}^T\left(\frac{\partial\left[M_{\langle e\rangle}\right]}{\partial \rho_{\langle e\rangle}}\left\{\ddot{u}_{\langle e\rangle}\right\}+\left[M_{\langle e\rangle}\right]\left\{\frac{\partial \ddot{u}_{\langle e\rangle}}{\partial \rho_{\langle e\rangle}}\right\}\right.\\ &\quad+\frac{\partial\left[C_{\langle e\rangle}\right]}{\partial \rho_{\langle e\rangle}}\left\{\dot{u}_{\langle e\rangle}\right\}+\left[C_{\langle e\rangle}\right]\left\{\frac{\partial \dot{u}_{\langle e\rangle}}{\partial \rho_{\langle e\rangle}}\right\}+\\ &\quad\left.\frac{\partial\left[K_{\langle e\rangle}\right]}{\partial \rho_{\langle e\rangle}}\left\{u_{\langle e\rangle}\right\}+\left[K_{\langle e\rangle}\right]\left\{\frac{\partial u_{\langle e\rangle}}{\partial \rho_{\langle e\rangle}}\right\}\right)dt \qquad (2.51)\end{aligned}$$

Similar to the gradient of the Lagrange function with respect to the displacement vector, an integration by parts is performed on each term, as shown in

$$\begin{aligned}&\int_{t_{n_i}^{(-)}}^{t_{n_i}^{(+)}}\left\{\lambda_{\langle e\rangle}\right\}^T\left[M_{\langle e\rangle}\right]\left\{\frac{\partial \ddot{u}_{\langle e\rangle}}{\partial \rho_{\langle e\rangle}}\right\}dt\\ &= \left[\left\{\lambda_{\langle e\rangle}\right\}^T\left[M_{\langle e\rangle}\right]\left\{\frac{\partial \dot{u}_{\langle e\rangle}}{\partial \rho_{\langle e\rangle}}\right\}\right]_{t_{n_i}^{(-)}}^{t_{n_i}^{(+)}}-\left[\left\{\dot{\lambda}_{\langle e\rangle}\right\}^T\left[M_{\langle e\rangle}\right]\left\{\frac{\partial u_{\langle e\rangle}}{\partial \rho_{\langle e\rangle}}\right\}\right]_{t_{n_i}^{(-)}}^{t_{n_i}^{(+)}}\\ &\quad+\int_{t_{n_i}^{(-)}}^{t_{n_i}^{(+)}}\left\{\ddot{\lambda}_{\langle e\rangle}\right\}^T\left[M_{\langle e\rangle}\right]\left\{\frac{\partial u_{\langle e\rangle}}{\partial \rho_{\langle e\rangle}}\right\}dt\\ &= \int_{t_{n_i}^{(-)}}^{t_{n_i}^{(+)}}\left\{\ddot{\lambda}_{\langle e\rangle}\right\}^T\left[M_{\langle e\rangle}\right]\left\{\frac{\partial u_{\langle e\rangle}}{\partial \rho_{\langle e\rangle}}\right\}dt \qquad (2.52)\end{aligned}$$

$$\begin{aligned}&\int_{t_{n_i}^{(-)}}^{t_{n_i}^{(+)}}\left\{\lambda_{\langle e\rangle}\right\}^T\left[C_{\langle e\rangle}\right]\left\{\frac{\partial \dot{u}_{\langle e\rangle}}{\partial \rho_{\langle e\rangle}}\right\}dt\\ &= \left[\left\{\lambda_{\langle e\rangle}\right\}^T\left[C_{\langle e\rangle}\right]\left\{\frac{\partial u_{\langle e\rangle}}{\partial \rho_{\langle e\rangle}}\right\}\right]_{t_{n_i}^{(-)}}^{t_{n_i}^{(+)}}-\int_{t_{n_i}^{(-)}}^{t_{n_i}^{(+)}}\left\{\dot{\lambda}_{\langle e\rangle}\right\}^T\left[C_{\langle e\rangle}\right]\left\{\frac{\partial u_{\langle e\rangle}}{\partial \rho_{\langle e\rangle}}\right\}dt\\ &= -\int_{t_{n_i}^{(-)}}^{t_{n_i}^{(+)}}\left\{\dot{\lambda}_{\langle e\rangle}\right\}^T\left[C_{\langle e\rangle}\right]\left\{\frac{\partial u_{\langle e\rangle}}{\partial \rho_{\langle e\rangle}}\right\}dt \qquad (2.53)\end{aligned}$$

Using Equations (2.52) and (2.53), Equation (2.51) is rewritten as

$$\begin{aligned}\frac{\partial J^*_{\langle e\rangle_{ni}}}{\partial \rho_{\langle e\rangle}} &= \frac{1}{2}\int_{t_{n_i}^{(-)}}^{t_{n_i}^{(+)}}\left(-\left\{f_{\langle e\rangle}\right\}^T+\left\{\ddot{\lambda}_{\langle e\rangle}\right\}^T\left[M_{\langle e\rangle}\right]-\left\{\dot{\lambda}_{\langle e\rangle}\right\}^T\left[C_{\langle e\rangle}\right]+\left\{\lambda_{\langle e\rangle}\right\}^T\left[K_{\langle e\rangle}\right]\right)\left\{\frac{\partial u_{\langle e\rangle}}{\partial \rho_{\langle e\rangle}}\right\}\\ &\quad+\left\{\lambda_{\langle e\rangle}\right\}^T\left(\frac{\partial\left[M_{\langle e\rangle}\right]}{\partial \rho_{\langle e\rangle}}\left\{\ddot{u}_{\langle e\rangle}\right\}+\frac{\partial\left[C_{\langle e\rangle}\right]}{\partial \rho_{\langle e\rangle}}\left\{\dot{u}_{\langle e\rangle}\right\}+\frac{\partial\left[K_{\langle e\rangle}\right]}{\partial \rho_{\langle e\rangle}}\left\{u_{\langle e\rangle}\right\}\right)dt \qquad (2.54)\end{aligned}$$

From Equation (2.42), the first term in the integration of Equation (2.54) is zero. Moreover, using the self-adjoint relationship for negative work, Equation (2.54) is shown in

$$\frac{\partial J^*_{\langle e\rangle_{n_i}}}{\partial \rho_{\langle e\rangle}} = \frac{1}{2}\int_{t_{n_i}^{(-)}}^{t_{n_i}^{(+)}} \left\{u_{\langle e\rangle}\right\}^T \left(\frac{\partial\left[M_{\langle e\rangle}\right]}{\partial \rho_{\langle e\rangle}}\left\{\ddot{u}_{\langle e\rangle}\right\} + \frac{\partial\left[C_{\langle e\rangle}\right]}{\partial \rho_{\langle e\rangle}}\left\{\dot{u}_{\langle e\rangle}\right\} + \frac{\partial\left[K_{\langle e\rangle}\right]}{\partial \rho_{\langle e\rangle}}\left\{u_{\langle e\rangle}\right\}\right) dt \tag{2.55}$$

From Equations (2.45), (2.50), and (2.55), the gradient of the Lagrange function with respect to the density, which is the sensitivity, is shown in

$$\begin{aligned}\frac{\partial J^*_{\langle e\rangle}}{\partial \rho_{\langle e\rangle}} &= \sum_{i=1}^{m_+}\frac{1}{2}\int_{t_{n_i}^{(-)}}^{t_{n_i}^{(+)}} -\left\{u_{\langle e\rangle}\right\}^T \left(\frac{\partial\left[M_{\langle e\rangle}\right]}{\partial \rho_{\langle e\rangle}}\left\{\ddot{u}_{\langle e\rangle}\right\} + \frac{\partial\left[C_{\langle e\rangle}\right]}{\partial \rho_{\langle e\rangle}}\left\{\dot{u}_{\langle e\rangle}\right\} + \frac{\partial\left[K_{\langle e\rangle}\right]}{\partial \rho_{\langle e\rangle}}\left\{u_{\langle e\rangle}\right\}\right) dt \\ &\quad + \sum_{i=1}^{m_-}\frac{1}{2}\int_{t_{n_i}^{(-)}}^{t_{n_i}^{(+)}} \left\{u_{\langle e\rangle}\right\}^T \left(\frac{\partial\left[M_{\langle e\rangle}\right]}{\partial \rho_{\langle e\rangle}}\left\{\ddot{u}_{\langle e\rangle}\right\} + \frac{\partial\left[C_{\langle e\rangle}\right]}{\partial \rho_{\langle e\rangle}}\left\{\dot{u}_{\langle e\rangle}\right\} + \frac{\partial\left[K_{\langle e\rangle}\right]}{\partial \rho_{\langle e\rangle}}\left\{u_{\langle e\rangle}\right\}\right) dt \\ &= \frac{1}{2}\int_0^{t_f} S_e \left\{u_{\langle e\rangle}\right\}^T \left(\frac{\partial\left[M_{\langle e\rangle}\right]}{\partial \rho_{\langle e\rangle}}\left\{\ddot{u}_{\langle e\rangle}\right\} + \frac{\partial\left[C_{\langle e\rangle}\right]}{\partial \rho_{\langle e\rangle}}\left\{\dot{u}_{\langle e\rangle}\right\} + \frac{\partial\left[K_{\langle e\rangle}\right]}{\partial \rho_{\langle e\rangle}}\left\{u_{\langle e\rangle}\right\}\right) dt\end{aligned} \tag{2.56}$$

where S_e is the sign function as shown in

$$S_e = \begin{cases} -1 & \left(\text{if} \quad \left\{f_{\langle e\rangle}\right\}^T \left\{u_{\langle e\rangle}\right\} \geq 0\right), \\ 1 & \left(\text{if} \quad \left\{f_{\langle e\rangle}\right\}^T \left\{u_{\langle e\rangle}\right\} < 0\right) \end{cases} \tag{2.57}$$

2.2.2 Discretization method for time

Time derivative terms for unknown variables are included in the governing equation in dynamic oscillation problem shown in Equation (2.24). Thus, when performing a discretization analysis, in addition to discretization in the spatial direction, discretization in the time direction is also required. In the FEM, the difference method is employed for discretization in the time direction. In the discretization in the time direction by the difference method, the time derivative terms in an ordinary differential equation is solved by a difference approximation. In this research, the Newmark-β method is employed in the direct integration method used for nonlinear problems. Besides the Newmark-β method, there are the linear acceleration method and Wilson θ-method. The Newmark-β method is an extension of the

linear acceleration method, and is assumed that the relationship between displacement and velocity shown in

$$\left\{u_{\langle e\rangle}\right\}^{(t+1)} = \left\{u_{\langle e\rangle}\right\}^{(t)} + \Delta t \left\{\dot{u}_{\langle e\rangle}\right\}^{(t)} + \Delta t^2 \left(\frac{1}{2} - \beta\right) \left\{\ddot{u}_{\langle e\rangle}\right\}^{(t)} + \Delta t^2 \beta \left\{\ddot{u}_{\langle e\rangle}\right\}^{(t+1)} \tag{2.58}$$

$$\left\{\dot{u}_{\langle e\rangle}\right\}^{(t+1)} = \left\{\dot{u}_{\langle e\rangle}\right\}^{(t)} + \Delta t \left(1 - \beta_\gamma\right) \left\{\ddot{u}_{\langle e\rangle}\right\}^{(t)} + \Delta t \beta_\gamma \left\{\ddot{u}_{\langle e\rangle}\right\}^{(t+1)} \tag{2.59}$$

where β and β_γ are the parameter for the Newmark-β method, and the superscript (t) is the time t. Generally, $\beta_\gamma = 1/2$, and Equation (2.59) becomes as

$$\left\{\dot{u}_{\langle e\rangle}\right\}^{(t+1)} = \left\{\dot{u}_{\langle e\rangle}\right\}^{(t)} + \frac{\Delta t}{2} \left(\left\{\ddot{u}_{\langle e\rangle}\right\}^{(t)} + \left\{\ddot{u}_{\langle e\rangle}\right\}^{(t+1)}\right) \tag{2.60}$$

Equation (2.60) is a trapezoidal equation in numerical integration. The another parameter β has the constraint shown in

$$0 \leq \beta \leq \frac{1}{2} \tag{2.61}$$

Generally, the setting values of β are 0, 1/4 and 1/6. In this study, $\beta = 1/4$ is used because it is an unconditionally stable integration method. Substituting $\beta = 1/4$, Equation (2.58) is written as

$$\left\{u_{\langle e\rangle}\right\}^{(t+1)} = \left\{u_{\langle e\rangle}\right\}^{(t)} + \Delta t \left\{\dot{u}_{\langle e\rangle}\right\}^{(t)} + \frac{\Delta t^2}{2} \left(\frac{\left\{\ddot{u}_{\langle e\rangle}\right\}^{(t)} + \left\{\ddot{u}_{\langle e\rangle}\right\}^{(t+1)}}{2}\right) \tag{2.62}$$

The method used in Equation (2.62) is called the mean acceleration method, the acceleration is assumed to be constant during the time increment Δt. Applying the difference equation in the Newmark-β method shown in Equations (2.58) and (2.59) to the governing equation shown in Equation (2.24), it is obtained as

$$\begin{aligned}
&\left(\left[M_{\langle e\rangle}\right] + \frac{\Delta t}{2}\left[C_{\langle e\rangle}\right] + \beta \Delta t^2 \left[K_{\langle e\rangle}\right]\right) \left\{\ddot{u}_{\langle e\rangle}\right\}^{(t+1)} \\
&= \left\{f_{\langle e\rangle}\right\}^{(t+1)} - \left[C_{\langle e\rangle}\right] \left(\left\{\dot{u}_{\langle e\rangle}\right\}^{(t)} + \frac{\Delta t}{2} \left\{\ddot{u}_{\langle e\rangle}\right\}^{(t)}\right) \\
&- \left[K_{\langle e\rangle}\right] \left(\left\{u_{\langle e\rangle}\right\}^{(t)} + \Delta t \left\{\dot{u}_{\langle e\rangle}\right\}^{(t)} + \left(\frac{1}{2} - \beta\right) \Delta t^2 \left\{\ddot{u}_{\langle e\rangle}\right\}^{(t)}\right)
\end{aligned} \tag{2.63}$$

After solving this algebraic equation and finding the acceleration at time $t+1$, the displacement and velocity shown in Equations (2.58) and (2.59) are calculated.

2.3 Density method and filter

First, the density method is explained. As described in the previous chapter, the density method represents material distribution by giving a non-dimensional density as a parameter for each element. The generalized density method is shown in

$$E_{\langle e\rangle} = E_0 f\left(\rho_{\langle e\rangle}\right) \tag{2.64}$$

where E_0 is the Young's modulus for a certain material. The function f is used to express the Young's modulus $E_{\langle e\rangle}$ in the element e ,as shown in Equation (2.64). When the function is close to zero, the Young's modulus $E_{\langle e\rangle}$ is also close to zero. In addition, when the function is close to one, the Young's modulus $E_{\langle e\rangle}$ is also close to one. The method of expressing this function as follows is called the solid Isotropic material with penalization (SIMP) method[61].

$$E_{\langle e\rangle} = E_0 {\rho_{\langle e\rangle}}^{p_s} \tag{2.65}$$

Here, p_s is penalization parameter for the SIMP method, the value of the function f varies depending on how the penalization parameter p_s is set. The Hashin–Shtrikman bound condition, which provides a boundary for the Young's modulus when two materials are mixed, is an indicator of the penalization parameter p_s. From the Hashin–Shtrikman bound condition, the setting range of the penalization parameter p_s is shown in

$$p_s \geq \max\left(\frac{2}{1-\nu},\ \ \frac{4}{1+\nu}\right) \quad \text{(in 2D)} \tag{2.66}$$

$$p_s \geq \max\left(15\frac{1-\nu}{7-5\nu},\ \ \frac{3}{2}\frac{1-\nu}{1-2\nu}\right) \quad \text{(in 3D)} \tag{2.67}$$

where ν is poisson ratio. As shown in Equations (2.66) and (2.67), the setting range of the penalization parameter p_s depends on the number of dimensions. However, since the condition is an indicator, it is difficult to evaluate them strictly according to actual materials. When the penalization parameter p_s is set small, the gradient of the function with respect to the density $\rho_{\langle e\rangle}$ also becomes small. Thereby, there exists the grayscale, which represent the intermediate material, in a density distribution. Thus, the setting value of the penalization

parameter p_s should satisfy the condition shown in Equations (2.66) and (2.67). In addition to the SIMP method, there is the rational approximation of material properties (RAMP) method[62], shown in

$$E_{\langle e\rangle} = E_0 \frac{\rho_{\langle e\rangle}}{1 + c\left(1 - \rho_{\langle e\rangle}\right)} \tag{2.68}$$

where c is the appropriate constant. The RAMP method produces a less grayscale in a density distribution. However, in this study, the SIMP method is employed to represent density because the method is also used in many researches. In addition, in Equation (2.65), numerical instability remains when the density value is zero. Thus, the improved SIMP method, which avoids numerical instability, is shown in

$$f\left(\rho_{\langle e\rangle}\right) = \left(1 - \rho_{\min}\right) {\rho_{\langle e\rangle}}^{p_s} + \rho_{\min} \tag{2.69}$$

where $\rho_{\min}$ is the parameter to avoid numerical instability and should be as close to 0 as possible. In the dynamic oscillation problem, besides the stiffness matrix $\left[K_{\langle e\rangle}\right]$, there exists the mass matrix $\left[M_{\langle e\rangle}\right]$ and damping matrix $\left[C_{\langle e\rangle}\right]$. Similar to the expression of Young's modulus shown in Equation (2.69), the mass $d_{\langle e\rangle}$ is defied in the mass matrix $\left[M_{\langle e\rangle}\right]$, and the damping $\zeta_{\langle e\rangle}$ is defied in the damping matrix $\left[C_{\langle e\rangle}\right]$.

$$d_{\langle e\rangle} = \left(d_0 - d_{\min}\right) {\rho_{\langle e\rangle}}^{p_s} + d_{\min} \tag{2.70}$$

$$\zeta_{\langle e\rangle} = \left(1 - \zeta_{\min}\right) {\rho_{\langle e\rangle}}^{p_s} + \zeta_{\min} \tag{2.71}$$

Here, $d_{\min}$ and $\zeta_{\min}$ is also the parameter to avoid numerical instability and should be as close to 0 as possible. d_0 is the mass density for a certain material.

Next, the filter is explained. Density-based topology optimization, which gives design variables to elements, is computed independently for each element. When shear forces dominate the structure, a checkerboard is seen within a density distribution, as shown in Figure 2.3. From a manufacturing perspective, this checkerboard is point-connected rather than line-connected and surface-connected. Thereby, it is difficult to actually manufacture. Thus, the

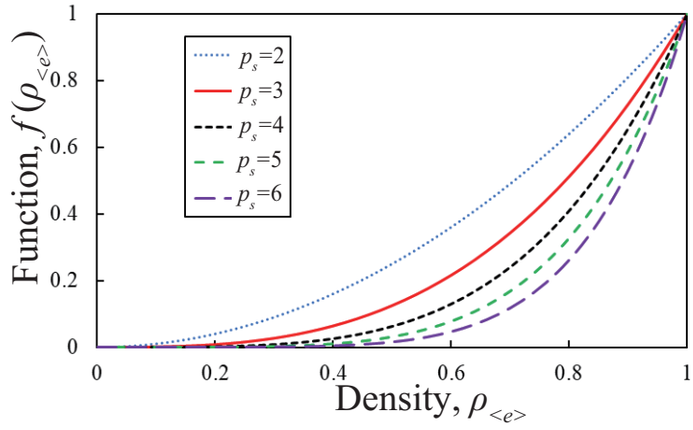

Figure 2.2: Graph of SIMP method.

filter is employed for density-based topology optimization to avoid a checkerboard. However, if the filter radius R is set too large, numerous grayscales is seen within a density distribution, as shown in Figure 2.4. Filtering methods can be categorized as filtering on sensitivity, filtering on density, and filtering based on image processing techniques. In this thesis, filtering on sensitivity is employed. Hereafter, it is called sensitivity filter. There are several types of filtering methods. Only the most representative methods are introduced here with generalized equations. First, the sensitivity filter[63], which is employed in this study, is explained. The sensitivity filter shown in Equation (2.72) transforms the sensitivity into a smooth sensitivity distribution in the design domain Ω by averaging the sensitivities of elements with their neighbors.

$$\frac{\partial \bar{f}_{\langle e\rangle}}{\partial \rho_{\langle e\rangle}} = \frac{\sum_{j\in\Omega_{\text{filter}}} w_{\text{filter}\langle j\rangle} \frac{\partial f}{\partial \rho_{\langle j\rangle}} \frac{1}{V_{\langle j\rangle}}}{\frac{1}{V_{\langle e\rangle}} \sum_{j\in\Omega_{\text{filter}}} w_{\text{filter}\langle j\rangle} \rho_{\langle j\rangle}} \tag{2.72}$$

Here, w_{filter} is the weight function for filter, and there are several suggestions. In this study, a weight function is employed in which the weights are determined by a norm that represents the length of a geometric vector in space. The weight function w_{filter} is shown in

$$w_{\text{filter}} = R - \|\boldsymbol{x}_j - \boldsymbol{x}_e\| \tag{2.73}$$

where R is the filtering radius which determines the filtering domain Ω_{filter}, as shown in Figure 2.5. Additionally, $\boldsymbol{x}_e$ is the coordinates of the element e in the natural coordinate system. In the following, it is assumed that a sensitivity filter is employed and corrected for sensitivity before updating the density. Next, the filtering on density[65] is introduced. Hereafter, it is called density filter. The density filter shown in Equation (2.74) is expressed similar to the sensitivity filter.

$$\rho_{\text{filter}\langle e\rangle} = \frac{\sum_{j\in\Omega_{\text{filter}}} w_{\text{filter}\langle j\rangle} V_{\langle j\rangle} \rho_{\langle j\rangle}}{\sum_{j\in\Omega_{\text{filter}}} w_{\text{filter}\langle j\rangle} V_{\langle j\rangle}} \tag{2.74}$$

Finally, the filtering based on image processing techniques[66] is briefly introduced. The filter considers the elements as pixels in an image, and uses processes such as open and close to obtain a clear distribution. However, depending on the problem setup, the number of iterations for repeated calculations a may increase compared to sensitivity or density filters.

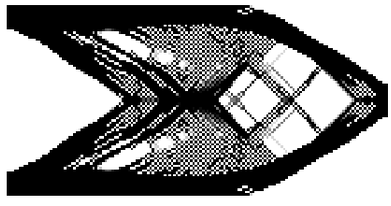

Figure 2.3: Density distribution when the filter is not employed.

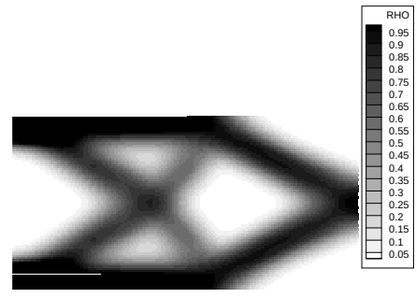

Figure 2.4: Density distribution when the filter radius is too large.

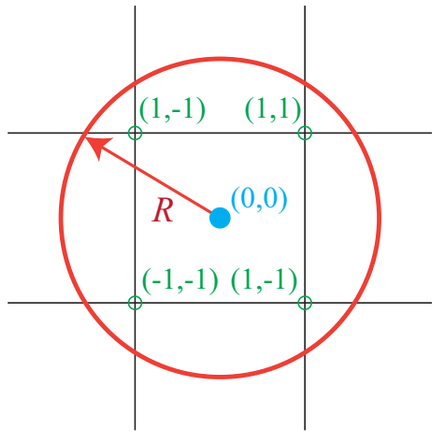

Figure 2.5: Filtering area.

2.4 New optimality criteria method incorporating the concept of Newton's method

2.4.1 Formulation of modified optimality criteria method

First of all, update equations used in general gradient-based optimization problems will be introduced. The steepest descent method and Newton's method are often employed as update equations for structural optimization. Equation (2.75) shows the generalized steepest descent method, Equations (2.76) and (2.77) show the generalized Newton's method for linear and multivariate variables.

$$x^{(k+1)} = x^{(k)} - \alpha_s \frac{df\,(x)}{dx}^{(k)} \tag{2.75}$$

$$x^{(k+1)} = x^{(k)} - \left(\frac{d^2 f\,(x)}{dx^2}^{(k)} \right)^{-1} \frac{df\,(x)}{dx}^{(k)} \tag{2.76}$$

$$\begin{Bmatrix} x_1^{(k+1)} \\ x_2^{(k+1)} \\ \vdots \\ x_N^{(k+1)} \end{Bmatrix} = \begin{Bmatrix} x_1^{(k)} \\ x_2^{(k)} \\ \vdots \\ x_N^{(k)} \end{Bmatrix} - \begin{bmatrix} \frac{d^2 f}{dx_1^2}^{(k)} & \frac{d^2 f}{dx_1 dx_2}^{(k)} & \cdots & \frac{d^2 f}{dx_1 dx_N}^{(k)} \\ \frac{d^2 f}{dx_2 dx_1}^{(k)} & \frac{d^2 f}{dx_2^2}^{(k)} & \cdots & \frac{d^2 f}{dx_2 dx_N}^{(k)} \\ \vdots & \vdots & \ddots & \vdots \\ \frac{d^2 f}{dx_N dx_1}^{(k)} & \frac{d^2 f}{dx_N dx_2}^{(k)} & \cdots & \frac{d^2 f}{dx_N^2}^{(k)} \end{bmatrix}^{-1} \begin{Bmatrix} \frac{df}{dx_1}^{(k)} \\ \frac{df}{dx_2}^{(k)} \\ \vdots \\ \frac{df}{dx_N}^{(k)} \end{Bmatrix} \tag{2.77}$$

Here, α_s is step length. The steepest descent method shown in Equation (2.75) is a reliable search method, but the number of iterations required to find an optimum solution may be high. On the other hand, Newton's method for multivariate variables shown in Equation (2.77) requires to solve the Hessian. Newton's method is characterized by rapid updates and a small number of iterations. However, the inverse of Hessian in Newton's method is not always solved in a short analysis time due to its high computational cost. In particular, topology optimization has numerous design variables that make it somewhat difficult to employ.

This sub section presents the formulation of the modified OC method which is the proposed

method. As mentioned in **chapter 1**, the modified OC method is update method that incorporates the concept of Newton's method for nonlinear equations into the OC method. The Newton's method is mathematically proven the quadratic convergence, which is superior to the speed of convergence among iterative methods. The OC method shown in Equation (2.18) is multiplicative and differs from gradient methods such as the steepest descent method and Newton's method. Thus, the OC method is also modified in the form of additive equation. First of all, taking the natural logarithm for both sides of Equation (2.18), it is transformed as

$$\ln \rho_{\langle e \rangle}^{(k+1)} = \ln \rho_{\langle e \rangle}^{(k)} + \eta \ln A_{\langle e \rangle}^{(k)} \tag{2.78}$$

Thereafter, the calculation is performed in the same procedure as when deriving Newton's method for nonlinear equations. When the second term in Equation (2.78) is zero, the density update has been finalized. Thus, since the weighting factor η is a constant, $\ln A_{\langle e \rangle}^{(k)}$ should be zero. For $\ln A_{\langle e \rangle}^{(k)}$ to be 0, $A_{\langle e \rangle}^{(k)}$ must be 1, which is consistent with Equation (2.17). Using Taylor expansion, $\ln A_{\langle e \rangle}^{(k)}$ is expanded as

$$\ln A_{\langle e \rangle}^{(k+1)} = \ln A_{\langle e \rangle}^{(k)} + \Delta\rho_{\langle e \rangle} \frac{\partial}{\partial \rho_{\langle e \rangle}} \left(\ln A_{\langle e \rangle}^{(k)} \right) + o\left({\Delta\rho_{\langle e \rangle}}^2 \right) \tag{2.79}$$

where o is terms of higher order than the second order terms. Next, when $\ln A_{\langle e \rangle}^{(k+1)}$ shown in the left side of Equation (2.79) is close to zero, the following equation holds.

$$\Delta\rho_{\langle e \rangle} = \left(-\frac{\partial}{\partial \rho_{\langle e \rangle}} \left(\ln A_{\langle e \rangle}^{(k)} \right) \right)^{-1} \ln A_{\langle e \rangle}^{(k)} \tag{2.80}$$

From Equation (2.80), the difference in density update $\Delta\rho_{\langle e \rangle}$ is obtained. From the concept of the gradient method, it is expanded as

$$\begin{aligned} \ln \rho_{\langle e \rangle}^{(k+1)} &= \ln \rho_{\langle e \rangle}^{(k)} + \Delta\rho_{\langle e \rangle} \\ &= \ln \rho_{\langle e \rangle}^{(k)} + \left(-\frac{\partial}{\partial \rho_{\langle e \rangle}} \left(\ln A_{\langle e \rangle}^{(k)} \right) \right)^{-1} \ln A_{\langle e \rangle}^{(k)} \end{aligned} \tag{2.81}$$

Finally, to convert the additive equation shown in Equation (2.81) to the same multiplication equation as the OC method, Equation (2.81) takes the antilogarithm as in

$$\rho_{\langle e \rangle}^{(k+1)} = \rho_{\langle e \rangle}^{(k)} \left(A_{\langle e \rangle}^{(k)} \right)^{\left(-\frac{\partial}{\partial \rho_{\langle e \rangle}} \left(\ln A_{\langle e \rangle}^{(k)} \right) \right)^{-1}} \tag{2.82}$$

Equation (2.82) is the modified OC method, which is the proposed method. One difference from the OC method shown in Equation (2.18) has the weighting factor η, whereas the modified OC method replaces it with a function of density, which has different values for each element. The function $A_{\langle e \rangle}$ is derived for each optimization problem because it depends on the optimization problem.

2.4.2 Modified optimality criteria method for strain energy minimization problems in steady problems

This subsection describes the modified OC method for topology optimization to minimize strain energy in steady problem shown in Equations (2.1) and (2.3). As mentioned in the previous subsection, the exponent corresponding to the weighting factor η is replaced by a function, it is expended as

$$\begin{aligned} -\frac{\partial}{\partial \rho_{\langle e \rangle}} \left(\ln A_{\langle e \rangle}^{(k)} \right) &= \frac{-\frac{\partial^2 J^*_{\langle e \rangle}}{\partial \rho_{\langle e \rangle}}^{(k)} \Lambda^{(k)} \frac{\partial V}{\partial \rho_{\langle e \rangle}}^{(k)} + \frac{\partial J^*_{\langle e \rangle}}{\partial \rho_{\langle e \rangle}}^{(k)} \frac{\partial}{\partial \rho_{\langle e \rangle}} \left(\Lambda^{(k)} \frac{\partial V}{\partial \rho_{\langle e \rangle}}^{(k)} \right)}{\left(-\Lambda^{(k)} \frac{\partial V}{\partial \rho_{\langle e \rangle}}^{(k)} \right)^2} \left(\frac{\frac{\partial J^*_{\langle e \rangle}}{\partial \rho_{\langle e \rangle}}^{(k)}}{-\Lambda^{(k)} \frac{\partial V}{\partial \rho_{\langle e \rangle}}^{(k)}} \right)^{-1} \\ &= -\frac{\partial^2 J^*_{\langle e \rangle}}{\partial \rho_{\langle e \rangle}^2}^{(k)} \left(\frac{\partial J^*_{\langle e \rangle}}{\partial \rho_{\langle e \rangle}}^{(k)} \right)^{-1} \end{aligned} \tag{2.83}$$

Using the SIMP method shown in Equation (2.65), the second-order derivative of the Lagrange function $J^*_{\langle e \rangle}$ with respect to the density $\rho_{\langle e \rangle}$ shown in Equation (2.83), which is the

gradient of the sensitivity with respect to the density $\rho_{\langle e\rangle}$, is calculated as

$$\begin{aligned}
\frac{\partial^2 {J^*_{\langle e\rangle}}^{(k)}}{\partial {\rho_{\langle e\rangle}}^2} &= \frac{\partial}{\partial \rho_{\langle e\rangle}}\left(-\frac{1}{2}\left\{u_{\langle e\rangle}\right\}^T \frac{\partial\left[K_{\langle e\rangle}\right]}{\partial \rho_{\langle e\rangle}}\left\{u_{\langle e\rangle}\right\}\right) \\
&= -\frac{\partial\left\{u_{\langle e\rangle}\right\}^T}{\partial \rho_{\langle e\rangle}}\frac{\partial\left[K_{\langle e\rangle}\right]}{\partial \rho_{\langle e\rangle}}\left\{u_{\langle e\rangle}\right\} - \frac{1}{2}\left\{u_{\langle e\rangle}\right\}^T \frac{\partial^2\left[K_{\langle e\rangle}\right]}{\partial {\rho_{\langle e\rangle}}^2}\left\{u_{\langle e\rangle}\right\} \\
&= -\frac{\partial}{\partial \rho_{\langle e\rangle}}\left(\left\{f_{\langle e\rangle}\right\}^T\left[K_{\langle e\rangle}\right]^{-1}\right)\frac{\partial\left[K_{\langle e\rangle}\right]}{\partial \rho_{\langle e\rangle}}\left\{u_{\langle e\rangle}\right\} - \frac{1}{2}\left\{u_{\langle e\rangle}\right\}^T \frac{\partial^2\left[K_{\langle e\rangle}\right]}{\partial {\rho_{\langle e\rangle}}^2}\left\{u_{\langle e\rangle}\right\} \\
&= -\left\{f_{\langle e\rangle}\right\}^T \frac{\partial\left[K_{\langle e\rangle}\right]^{-1}}{\partial \rho_{\langle e\rangle}}\frac{\partial\left[K_{\langle e\rangle}\right]}{\partial \rho_{\langle e\rangle}}\left\{u_{\langle e\rangle}\right\} - \frac{1}{2}\left\{u_{\langle e\rangle}\right\}^T \frac{\partial^2\left[K_{\langle e\rangle}\right]}{\partial {\rho_{\langle e\rangle}}^2}\left\{u_{\langle e\rangle}\right\} \\
&= -\frac{\partial {E_{\langle e\rangle}}^{-1}}{\partial \rho_{\langle e\rangle}}\frac{\partial E_{\langle e\rangle}}{\partial \rho_{\langle e\rangle}}\left\{f_{\langle e\rangle}\right\}^T\left[K_{s\langle e\rangle}\right]^{-1}\left[K_{s\langle e\rangle}\right]\left\{u_{\langle e\rangle}\right\} - \frac{1}{2}\frac{\partial^2 E_{\langle e\rangle}}{\partial {\rho_{\langle e\rangle}}^2}\left\{u_{\langle e\rangle}\right\}^T\left[K_{\langle e\rangle}\right]\left\{u_{\langle e\rangle}\right\} \\
&= {p_s}^2 {\rho_{\langle e\rangle}}^{-2}\left\{f_{\langle e\rangle}\right\}^T\left\{u_{\langle e\rangle}\right\} - \frac{1}{2}p_s\left(p_s-1\right){\rho_{\langle e\rangle}}^{-2}\left\{u_{\langle e\rangle}\right\}^T\left[K_{\langle e\rangle}\right]\left\{u_{\langle e\rangle}\right\} \\
&= 2{p_s}^2 {\rho_{\langle e\rangle}}^{-2} J_{\langle e\rangle} - p_s\left(p_s-1\right){\rho_{\langle e\rangle}}^{-2} J_{\langle e\rangle} \\
&= \left(p_s+1\right)p_s {\rho_{\langle e\rangle}}^{-2} J_{\langle e\rangle}
\end{aligned} \tag{2.84}$$

Here, $\left[K_{s\langle e\rangle}\right]$ is the stiffness matrix without the Young's modulus $E_{\langle e\rangle}$. Using the sensitivity and the gradient of the sensitivity with respect to the density shown in Equations (2.15) and (2.84), the function located in the weighting factor η is calculated as

$$\begin{aligned}
\left(-\frac{\partial}{\partial \rho_{\langle e\rangle}}\left(\ln A^{(k)}_{\langle e\rangle}\right)\right)^{-1} &= \left(-\frac{{\partial^2 J^*_{\langle e\rangle}}^{(k)}}{\partial \rho_{\langle e\rangle}}\left(\frac{\partial {J^*_{\langle e\rangle}}^{(k)}}{\partial \rho_{\langle e\rangle}}\right)^{-1}\right)^{-1} \\
&= \frac{-p_s {\rho^{(k)}_{\langle e\rangle}}^{-1} J^{(k)}_{\langle e\rangle}}{\left(p_s+1\right)p_s {\rho^{(k)}_{\langle e\rangle}}^{-2} J^{(k)}_{\langle e\rangle}} \\
&= \frac{\rho^{(k)}_{\langle e\rangle}}{p_s+1}
\end{aligned} \tag{2.85}$$

Finally, by substituting Equation (2.85) into the modified OC method shown in Equation (2.82), the modified OC method for strain energy minimization in steady problem when using the SIMP method can be expressed simply as

$$\rho^{(k+1)}_{\langle e\rangle} = \rho^{(k)}_{\langle e\rangle}\left(A^{(k)}_{\langle e\rangle}\right)^{\frac{\rho^{(k)}_{\langle e\rangle}}{p_s+1}} \tag{2.86}$$

2.4.3 Modified optimality criteria method for strain energy minimization problems in dynamic oscillation problems

This subsection describes the modified OC method for topology optimization to minimize strain energy in dynamic oscillation problem shown in Equations (2.21) and (2.24). Since the constraint conditions are the same as in the previous subsection, the function of the exponent corresponding to the weighting factor η is the same as in Equation (2.83). Thus, the gradient of the sensitivity with respect to the density $\rho_{\langle e\rangle}$ is obtained as

$$\begin{aligned}
&\frac{\partial^2 J^*_{\langle e\rangle}}{\partial {\rho_{\langle e\rangle}}^2} \\
&= \frac{\partial}{\partial \rho_{\langle e\rangle}}\left(\frac{1}{2}\int_0^{t_f} S_e \left\{u_{\langle e\rangle}\right\}^T \left(\frac{\partial\left[M_{\langle e\rangle}\right]}{\partial \rho_{\langle e\rangle}}\left\{\ddot{u}_{\langle e\rangle}\right\} + \frac{\partial\left[C_{\langle e\rangle}\right]}{\partial \rho_{\langle e\rangle}}\left\{\dot{u}_{\langle e\rangle}\right\} + \frac{\partial\left[K_{\langle e\rangle}\right]}{\partial \rho_{\langle e\rangle}}\left\{u_{\langle e\rangle}\right\}\right) dt\right) \\
&= \frac{1}{2}\int_0^{t_f} S_e \left\{\frac{\partial u_{\langle e\rangle}}{\partial \rho_{\langle e\rangle}}\right\}^T \left(\frac{\partial\left[M_{\langle e\rangle}\right]}{\partial \rho_{\langle e\rangle}}\left\{\ddot{u}_{\langle e\rangle}\right\} + \frac{\partial\left[C_{\langle e\rangle}\right]}{\partial \rho_{\langle e\rangle}}\left\{\dot{u}_{\langle e\rangle}\right\} + \frac{\partial\left[K_{\langle e\rangle}\right]}{\partial \rho_{\langle e\rangle}}\left\{u_{\langle e\rangle}\right\}\right) \\
&\quad + S_e \left\{u_{\langle e\rangle}\right\}^T \left(\frac{\partial^2\left[M_{\langle e\rangle}\right]}{\partial {\rho_{\langle e\rangle}}^2}\left\{\ddot{u}_{\langle e\rangle}\right\} + \frac{\partial^2\left[C_{\langle e\rangle}\right]}{\partial {\rho_{\langle e\rangle}}^2}\left\{\dot{u}_{\langle e\rangle}\right\} + \frac{\partial^2\left[K_{\langle e\rangle}\right]}{\partial {\rho_{\langle e\rangle}}^2}\left\{u_{\langle e\rangle}\right\}\right) \\
&\quad + S_e \left\{u_{\langle e\rangle}\right\}^T \left(\frac{\partial\left[M_{\langle e\rangle}\right]}{\partial \rho_{\langle e\rangle}}\left\{\frac{\partial \ddot{u}_{\langle e\rangle}}{\partial \rho_{\langle e\rangle}}\right\} + \frac{\partial\left[C_{\langle e\rangle}\right]}{\partial \rho_{\langle e\rangle}}\left\{\frac{\partial \dot{u}_{\langle e\rangle}}{\partial \rho_{\langle e\rangle}}\right\} + \frac{\partial\left[K_{\langle e\rangle}\right]}{\partial \rho_{\langle e\rangle}}\left\{\frac{\partial u_{\langle e\rangle}}{\partial \rho_{\langle e\rangle}}\right\}\right) dt
\end{aligned} \tag{2.87}$$

The gradient of the displacement vector $\left\{u_{\langle e\rangle}\right\}$ with respect to the density $\rho_{\langle e\rangle}$ shown in the first term of Equation (2.87) is difficult to obtain directly. Thus, differentiating the displacement vector, velocity vector, and acceleration vector, which are shown in Equations (2.58), (2.59) and (2.63), by the density $\rho_{\langle e\rangle}$ yields

$$\begin{aligned}
\left\{\frac{\partial u_{\langle e\rangle}}{\partial \rho_{\langle e\rangle}}\right\}^{(t+1)} &= \left\{\frac{\partial u_{\langle e\rangle}}{\partial \rho_{\langle e\rangle}}\right\}^{(t)} + \Delta t\left\{\frac{\partial \dot{u}_{\langle e\rangle}}{\partial \rho_{\langle e\rangle}}\right\}^{(t)} + \Delta t^2\left(\frac{1}{2}-\beta\right)\left\{\frac{\partial \ddot{u}_{\langle e\rangle}}{\partial \rho_{\langle e\rangle}}\right\}^{(t)} \\
&\quad + \Delta t^2\beta\left\{\frac{\partial \ddot{u}_{\langle e\rangle}}{\partial \rho_{\langle e\rangle}}\right\}^{(t+1)}
\end{aligned} \tag{2.88}$$

$$\left\{\frac{\partial \dot{u}_{\langle e\rangle}}{\partial \rho_{\langle e\rangle}}\right\}^{(t+1)} = \left\{\frac{\partial \dot{u}_{\langle e\rangle}}{\partial \rho_{\langle e\rangle}}\right\}^{(t)} + \Delta t\left(1-\beta_\gamma\right)\left\{\frac{\partial \ddot{u}_{\langle e\rangle}}{\partial \rho_{\langle e\rangle}}\right\}^{(t)} + \Delta t\beta_\gamma\left\{\frac{\partial \ddot{u}_{\langle e\rangle}}{\partial \rho_{\langle e\rangle}}\right\}^{(t+1)} \tag{2.89}$$

$$
\begin{aligned}
&\left(\left[M_{\langle e\rangle}\right]+\frac{\Delta t}{2}\left[C_{\langle e\rangle}\right]+\beta\Delta t^2\left[K_{\langle e\rangle}\right]\right)\left\{\frac{\partial\ddot{u}_{\langle e\rangle}}{\partial\rho_{\langle e\rangle}}\right\}^{(t+1)}\\
=\ &-\left(\frac{\partial\left[M_{\langle e\rangle}\right]}{\partial\rho_{\langle e\rangle}}+\frac{\Delta t}{2}\frac{\partial\left[C_{\langle e\rangle}\right]}{\partial\rho_{\langle e\rangle}}+\beta\Delta t^2\frac{\partial\left[K_{\langle e\rangle}\right]}{\partial\rho_{\langle e\rangle}}\right)\left\{\ddot{u}_{\langle e\rangle}\right\}^{(t+1)}\\
&-\frac{\partial\left[C_{\langle e\rangle}\right]}{\partial\rho_{\langle e\rangle}}\left(\left\{\dot{u}_{\langle e\rangle}\right\}^{(t)}+\frac{\Delta t}{2}\left\{\ddot{u}_{\langle e\rangle}\right\}^{(t)}\right)-\left[C_{\langle e\rangle}\right]\left(\left\{\frac{\partial\dot{u}_{\langle e\rangle}}{\partial\rho_{\langle e\rangle}}\right\}^{(t)}+\frac{\Delta t}{2}\left\{\frac{\partial\ddot{u}_{\langle e\rangle}}{\partial\rho_{\langle e\rangle}}\right\}^{(t)}\right)\\
&-\frac{\partial\left[K_{\langle e\rangle}\right]}{\partial\rho_{\langle e\rangle}}\left(\left\{u_{\langle e\rangle}\right\}^{(t)}+\Delta t\left\{\dot{u}_{\langle e\rangle}\right\}^{(t)}+\left(\frac{1}{2}-\beta\right)\Delta t^2\left\{\ddot{u}_{\langle e\rangle}\right\}^{(t)}\right)\\
&-\left[K_{\langle e\rangle}\right]\left(\left\{\frac{\partial u_{\langle e\rangle}}{\partial\rho_{\langle e\rangle}}\right\}^{(t)}+\Delta t\left\{\frac{\partial\dot{u}_{\langle e\rangle}}{\partial\rho_{\langle e\rangle}}\right\}^{(t)}+\left(\frac{1}{2}-\beta\right)\Delta t^2\left\{\frac{\partial\ddot{u}_{\langle e\rangle}}{\partial\rho_{\langle e\rangle}}\right\}^{(t)}\right) \qquad (2.90)
\end{aligned}
$$

Using the SIMP method, Equation (2.90) is expended as

$$
\begin{aligned}
&\rho_{\langle e\rangle}{p_s}^{-1}\left(\left[M_{\langle e\rangle}\right]+\frac{\Delta t}{2}\left[C_{\langle e\rangle}\right]+\beta\Delta t^2\left[K_{\langle e\rangle}\right]\right)\left\{\frac{\partial\ddot{u}_{\langle e\rangle}}{\partial\rho_{\langle e\rangle}}\right\}^{(t+1)}\\
=\ &-\left\{f_{\langle e\rangle}\right\}^{(t+1)}-\rho_{\langle e\rangle}{p_s}^{-1}\left(\frac{\partial\left[C_{\langle e\rangle}\right]}{\partial\rho_{\langle e\rangle}}\left(\left\{\dot{u}_{\langle e\rangle}\right\}^{(t)}+\frac{\Delta t}{2}\left\{\ddot{u}_{\langle e\rangle}\right\}^{(t)}\right)\right.\\
&\left.+\left[K_{\langle e\rangle}\right]\left(\left\{\frac{\partial u_{\langle e\rangle}}{\partial\rho_{\langle e\rangle}}\right\}^{(t)}+\Delta t\left\{\frac{\partial\dot{u}_{\langle e\rangle}}{\partial\rho_{\langle e\rangle}}\right\}^{(t)}+\left(\frac{1}{2}-\beta\right)\Delta t^2\left\{\frac{\partial\ddot{u}_{\langle e\rangle}}{\partial\rho_{\langle e\rangle}}\right\}^{(t)}\right)\right) \qquad (2.91)
\end{aligned}
$$

From Equations (2.88), (2.89) and (2.91), the gradient of the displacement vector with respect to the density is obtained. Next, using the concept of the SIMP method, the second term of Equation (2.87) is calculated as

$$
\begin{aligned}
&S_e\left\{u_{\langle e\rangle}\right\}^T\left(\frac{\partial^2\left[M_{\langle e\rangle}\right]}{\partial{\rho_{\langle e\rangle}}^2}\left\{\ddot{u}_{\langle e\rangle}\right\}+\frac{\partial^2\left[C_{\langle e\rangle}\right]}{\partial{\rho_{\langle e\rangle}}^2}\left\{\dot{u}_{\langle e\rangle}\right\}+\frac{\partial^2\left[K_{\langle e\rangle}\right]}{\partial{\rho_{\langle e\rangle}}^2}\left\{u_{\langle e\rangle}\right\}\right)\\
=\ &S_e p_s\left(p_s-1\right){\rho_{\langle e\rangle}}^{-2}\left\{u_{\langle e\rangle}\right\}^T\left(\left[M_{\langle e\rangle}\right]\left\{\ddot{u}_{\langle e\rangle}\right\}+\left[C_{\langle e\rangle}\right]\left\{\dot{u}_{\langle e\rangle}\right\}+\left[K_{\langle e\rangle}\right]\left\{u_{\langle e\rangle}\right\}\right)\\
=\ &2S_e p_s\left(p_s-1\right){\rho_{\langle e\rangle}}^{-2}J_e \qquad (2.92)
\end{aligned}
$$

Finally, the third term of Equation (2.87) is calculated. Before that, the governing equation shown in Equation (2.23) are differentiated with density to replace the gradient of the acceleration vector with respect to the density and the gradient of the velocity vector with

respect to the density.

$$\begin{aligned} & \left[M_{\langle e\rangle}\right]\left\{\frac{\partial \ddot{u}_{\langle e\rangle}}{\partial \rho_{\langle e\rangle}}\right\}+\left[C_{\langle e\rangle}\right]\left\{\frac{\partial \dot{u}_{\langle e\rangle}}{\partial \rho_{\langle e\rangle}}\right\}+\left[K_{\langle e\rangle}\right]\left\{\frac{\partial u_{\langle e\rangle}}{\partial \rho_{\langle e\rangle}}\right\} \\ = & -\frac{\partial\left[M_{\langle e\rangle}\right]}{\partial \rho_{\langle e\rangle}}\left\{\ddot{u}_{\langle e\rangle}\right\}-\frac{\partial\left[C_{\langle e\rangle}\right]}{\partial \rho_{\langle e\rangle}}\left\{\dot{u}_{\langle e\rangle}\right\}-\frac{\partial\left[K_{\langle e\rangle}\right]}{\partial \rho_{\langle e\rangle}}\left\{u_{\langle e\rangle}\right\} \end{aligned} \tag{2.93}$$

Using Equation (2.93), the third term of Equation (2.87) is calculated as

$$\begin{aligned} & S_e\left\{u_{\langle e\rangle}\right\}^T\left(\frac{\partial\left[M_{\langle e\rangle}\right]}{\partial \rho_{\langle e\rangle}}\left\{\frac{\partial \ddot{u}_{\langle e\rangle}}{\partial \rho_{\langle e\rangle}}\right\}+\frac{\partial\left[C_{\langle e\rangle}\right]}{\partial \rho_{\langle e\rangle}}\left\{\frac{\partial \dot{u}_{\langle e\rangle}}{\partial \rho_{\langle e\rangle}}\right\}+\frac{\partial\left[K_{\langle e\rangle}\right]}{\partial \rho_{\langle e\rangle}}\left\{\frac{\partial u_{\langle e\rangle}}{\partial \rho_{\langle e\rangle}}\right\}\right) \\ = & S_e p_s {\rho_{\langle e\rangle}}^{-1}\left\{u_{\langle e\rangle}\right\}^T\left(\left[M_{\langle e\rangle}\right]\left\{\frac{\partial \ddot{u}_{\langle e\rangle}}{\partial \rho_{\langle e\rangle}}\right\}+\left[C_{\langle e\rangle}\right]\left\{\frac{\partial \dot{u}_{\langle e\rangle}}{\partial \rho_{\langle e\rangle}}\right\}+\left[K_{\langle e\rangle}\right]\left\{\frac{\partial u_{\langle e\rangle}}{\partial \rho_{\langle e\rangle}}\right\}\right) \\ = & S_e {p_s}^2 {\rho_{\langle e\rangle}}^{-2}\left\{u_{\langle e\rangle}\right\}^T\left(\left[M_{\langle e\rangle}\right]\left\{\ddot{u}_{\langle e\rangle}\right\}+\left[C_{\langle e\rangle}\right]\left\{\dot{u}_{\langle e\rangle}\right\}+\left[K_{\langle e\rangle}\right]\left\{u_{\langle e\rangle}\right\}\right) \\ = & S_e {p_s}^2 {\rho_{\langle e\rangle}}^{-2} J_{\langle e\rangle} \end{aligned} \tag{2.94}$$

Using Equations (2.87), (2.92) and (2.94), Equation (2.83) is expended as

$$\begin{aligned} & -\frac{\partial}{\partial \rho_{\langle e\rangle}}\left(\ln A_{\langle e\rangle}^{(k)}\right) \\ = & -\frac{1}{2}\int_{t_0}^{t_f}\left(S_e\left\{\frac{\partial u_{\langle e\rangle}}{\partial \rho_{\langle e\rangle}}\right\}^T\left(\frac{\partial\left[M_{\langle e\rangle}\right]}{\partial \rho_{\langle e\rangle}}\left\{\ddot{u}_{\langle e\rangle}\right\}+\frac{\partial\left[C_{\langle e\rangle}\right]}{\partial \rho_{\langle e\rangle}}\left\{\dot{u}_{\langle e\rangle}\right\}+\frac{\partial\left[K_{\langle e\rangle}\right]}{\partial \rho_{\langle e\rangle}}\left\{u_{\langle e\rangle}\right\}\right)\right. \\ & \left.+2S_e p_s\left(p_s-1\right){\rho_{\langle e\rangle}}^{-2} J_e^{(k)}+S_e {p_s}^2 {\rho_{\langle e\rangle}}^{-2} J_{\langle e\rangle}^{(k)}\right) dt \times\left(\frac{\partial {J_{\langle e\rangle}^*}^{(k)}}{\partial \rho_{\langle e\rangle}}\right)^{-1} \\ = & -\int_{t_0}^{t_f}\left(\frac{1}{2}S_e\left\{\frac{\partial u_{\langle e\rangle}}{\partial \rho_{\langle e\rangle}}\right\}^T\left(\frac{\partial\left[M_{\langle e\rangle}\right]}{\partial \rho_{\langle e\rangle}}\left\{\ddot{u}_{\langle e\rangle}\right\}+\frac{\partial\left[C_{\langle e\rangle}\right]}{\partial \rho_{\langle e\rangle}}\left\{\dot{u}_{\langle e\rangle}\right\}+\frac{\partial\left[K_{\langle e\rangle}\right]}{\partial \rho_{\langle e\rangle}}\left\{u_{\langle e\rangle}\right\}\right)\right. \\ & \left.-S_e p_s {\rho_{\langle e\rangle}}^{-2} J_e^{(k)}\right) dt \times\left(\frac{\partial {J_{\langle e\rangle}^*}^{(k)}}{\partial \rho_{\langle e\rangle}}\right)^{-1} \\ = & -\int_{t_0}^{t_f}\left(\frac{1}{2}S_e\left\{\frac{\partial u_{\langle e\rangle}}{\partial \rho_{\langle e\rangle}}\right\}^T\left(\frac{\partial\left[M_{\langle e\rangle}\right]}{\partial \rho_{\langle e\rangle}}\left\{\ddot{u}_{\langle e\rangle}\right\}+\frac{\partial\left[C_{\langle e\rangle}\right]}{\partial \rho_{\langle e\rangle}}\left\{\dot{u}_{\langle e\rangle}\right\}+\frac{\partial\left[K_{\langle e\rangle}\right]}{\partial \rho_{\langle e\rangle}}\left\{u_{\langle e\rangle}\right\}\right)\right. \\ & \left.+p_s J_e^{(k)}\right) dt \times\left({\rho_{\langle e\rangle}}^2 \frac{\partial {J_{\langle e\rangle}^*}^{(k)}}{\partial \rho_{\langle e\rangle}}\right)^{-1} \end{aligned} \tag{2.95}$$

2.5 Flow of density-based topology optimization for strain energy minimization

This section described the flow of the density-based topology optimization for strain energy minimization in steady and dynamic oscillation problems. The optimizations are performed using procedure shown in Figure 2.6 and below.

1. Input of the computation model and calculation conditions shown in next section.

2. The finite element analysis for linear elastic body is performed. For steady problems, the governing equation shown in Equation (2.2) is used, and for dynamic oscillation problems, the governing equation shown in Equation (2.23) is used to obtain the displacement vector $\{u\}$.

3. The strain energy, which is the performance function is calculated. Using the displacement vector $\{u\}$ obtained in the previous step, the performance function shown in Equation (2.1) is calculated for steady problems, and the performance function shown in Equation (2.21) is calculated for dynamic oscillation problems.

4. If the judgement of convergence $\frac{|J^{(k)}-J^{(k-1)}|}{J^{(0)}} < \varepsilon_{\mathrm{conv}}$ is satisfied, the computation is finalized. Otherwise, go to the next step.

5. Using self-adjoint relationship, the sensitivity, which is the gradient of the Lagrange function $J^{*}_{\langle e \rangle}$ with respect to the density $\rho_{\langle e \rangle}$, is calculated. For steady problems, the sensitivity shown in Equation (2.15) is calculated using the self-adjoint relationship shown in Equation (2.13). For dynamic oscillation problems, the sensitivity shown in Equation (2.56) is calculated using the self-adjoint relationships shown in Equations (2.37) and (2.43).

6. The sensitivity filter shown in Equation (2.72) is applied.

7. The density $\rho_{\langle e \rangle}$, which is the design variable, is updated. When using the OC method, Equation (2.18) is employed, when using the modified OC method, Equation (2.82)

is employed, and when using the gradient method with first-order and second-order derivatives, Equation (2.76) is employed. Note that when using the modified OC method, the expansion of equation after Equation (2.82) varies depending on the optimization problem. After updating, the number of iterations is updated to the $k+1$-th step and the process returns to step 2.

However, depending on the setting of the optimization problem, the judgement of convergence described above may not be satisfied. Then, if the number of iterations k exceeds the maximum number of iterations $k_{\max}$, the optimization calculation is finalized because no solution can be obtained by continuing the calculation any further. The gradient method with first-order and second-order derivatives assumes to be updated independently on an element-by-element basis, as is the OC method. The gradient method is a general term for methods that use information about the gradient of a function in the search for a solution to an optimization problem. Thus, it differs from Newton's method that uses the Hessian and is referred to as the gradient method with first-order and second-order derivatives in this study.

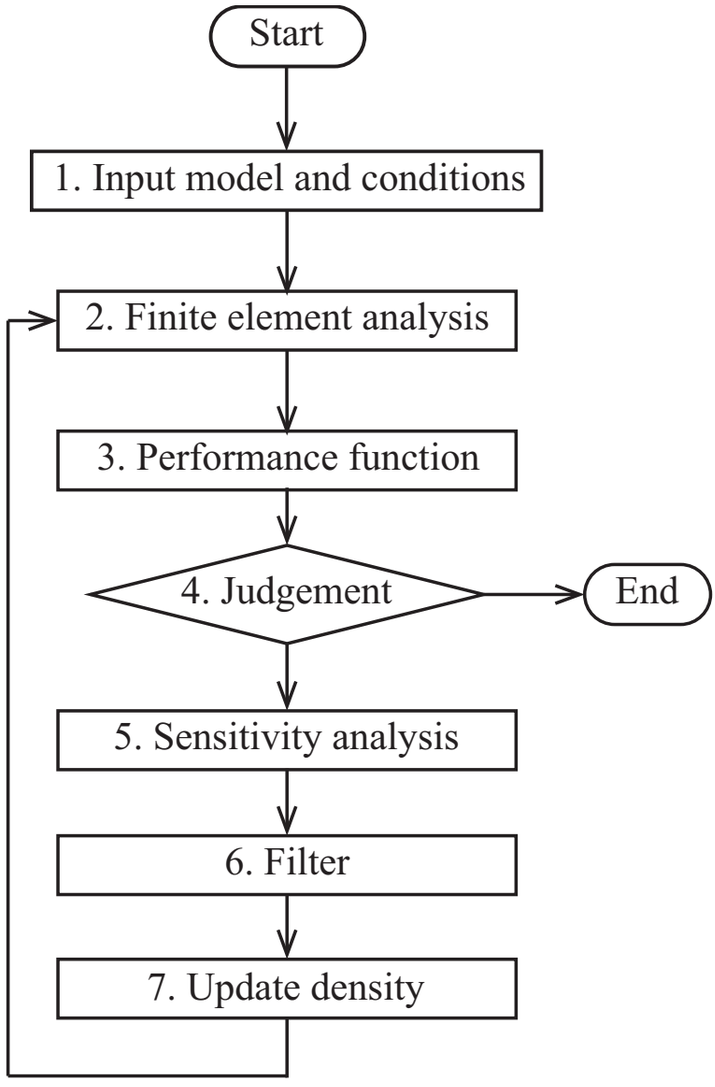

Figure 2.6: Flowchart of density-based topology optimization for the strain energy minimization problems.

2.6 Calculation conditions in density-based topology optimization for strain energy minimization

This section explains about the calculation model and conditions. In this chapter, topology optimization for steady and dynamic oscillation problems is performed. First, the topology optimization is performed for two dimensional models of cantilever beam and Messerschmitt-Bölkow-Blohm (MBB), shown in Figure 2.7, to minimize strain energy in steady problem. The cantilever beam model is a general analytical model and MBB beam model is a model commonly used in the field of topology optimization. The results are to verify the usefulness of the modified OC method. As a verification method, it is checked whether the results of topology optimization when using the OC method, the Gradient method with first-order and second-order derivatives, and the modified OC method change when the value of the move-limit ρ_{move} is changed. Next, based on the results of topology optimization in two dimensional steady problems, topology optimization is performed for the three dimensional models of cantilever beam and MBB beam shown in Figure 2.8, with the thickness direction added to Figure 2.7. Here, the influence of the updating equations and parameters on three dimensional optimum results is investigated. Finally, the usefulness of the modified OC method for topology optimization in dynamic oscillation problems is demonstrated using the three dimensional models of cantilever beam and MBB beam shown in Figure 2.8.

First of all, the calculation conditions and models used in topology optimization for two dimensional steady problems will be explained in detail. The two dimensional model shown in Figure 2.7 uses a 4-node quadrilateral element and has a structural grid divided by squares of 1 [mm] per side. The cantilever beam model shown in Figure 2.7(a) is added a uniformly distribution load of total load 90 [N] from coordinates (60,16) to (60,24). The MBB beam model shown in Figure 2.7(b) is added 10 [N]. However, the value of load does not significantly affect the topology optimization, because the model is a liner elastic body. Other calculation conditions are shown in Table 2.1. Next, the calculation conditions and models used in topology optimization for three dimensional steady problems will be explained in detail.

The three dimensional model shown in Figure 2.8 uses a 8-node hexahedral element and has a structural grid divided by cube of 1 [mm] per side. The cantilever beam model shown in Figure 2.8(a) is added a uniformly distribution load of total load 100 [N]. The MBB beam model shown in Figure 2.8(b) is also added 100 [N]. The other calculation conditions are shown in Table 2.2 as for two dimensional steady problem. Finally, the calculation conditions and models used in topology optimization for three dimensional dynamic oscillation problems will be explained in detail. Similar to the topology optimization for three dimensional steady problems, the models shown in Figure 2.8 is used. The models shown in Figures 2.8(a) and 2.8(b) are added a load such as impulse response, as shown in Figure 2.9. The reason for this load setting is that for the optimization problem in this chapter, the displacement vector $\{u\}$ and the Lagrange multiplier vector $\{\lambda\}$ must be zero at the starting time and end time. Thus, the time after applying the load must be sufficient. The other calculation conditions are shown in Table 2.3 as for two dimensional steady problem. The initial density in the design domain Ω is given uniformly by $\bar{\rho_0}$. Here, the Rayleigh damping coefficients α_1 and α_2 are set for numerical verification, unlike the physical properties of real materials.

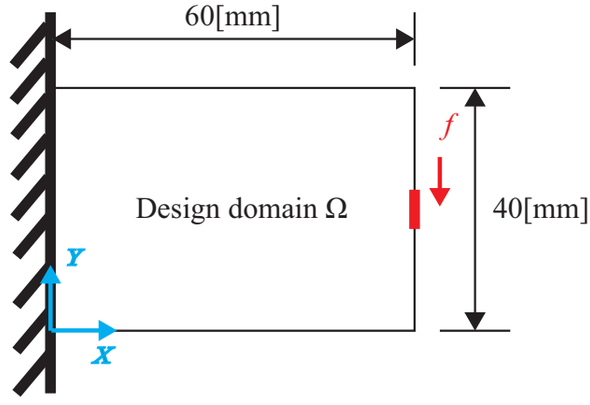

(a) Cantilever beam model.

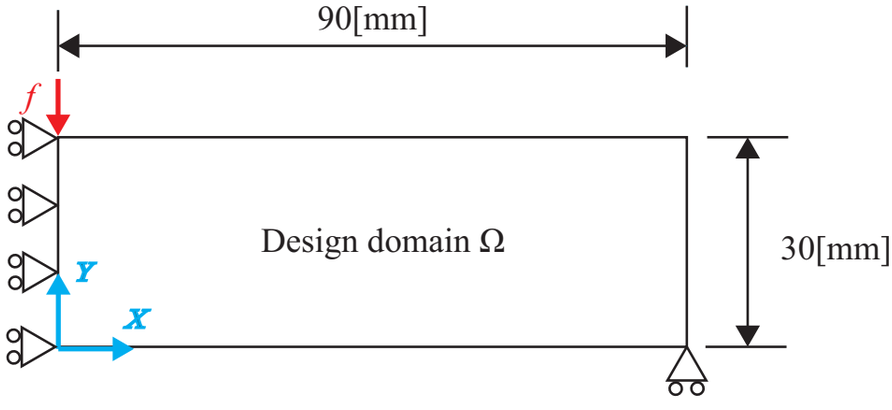

(b) MBB beam model.

Figure 2.7: Computation models on two dimension in strain energy minimization problems.

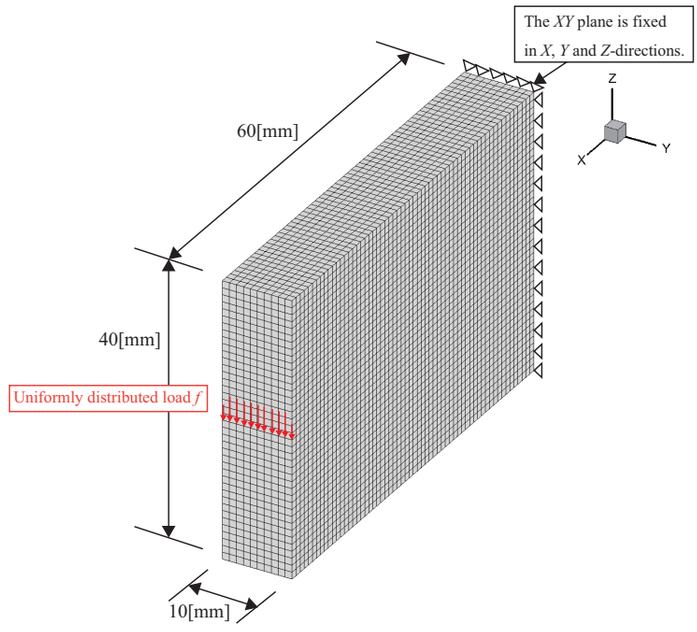

(a) Cantilever beam model.

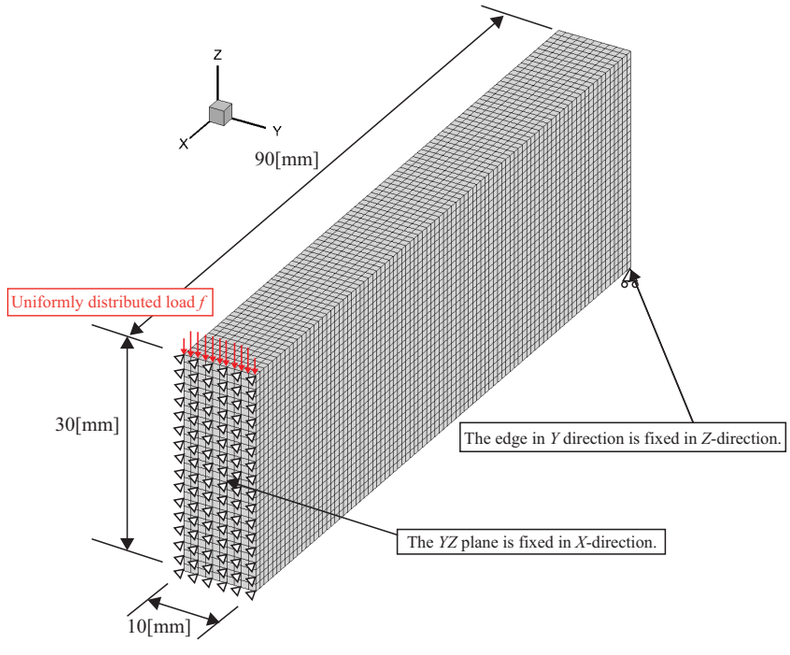

(b) MBB beam model.

Figure 2.8: Computation models on three dimension in strain energy minimization problems.

Table 2.1: Calculation conditions of topology optimization for strain energy minimization in two dimensional static problems.

Model	Cantilever beam	MBB beam
Number of elements	2400	2700
Number of nodes	2501	2821
Initial density average, $\bar{\rho_0}$	0.5	0.3
Penalization parameter for the SIMP method, p_s	4.5	4.5
Weighting factor, η	0.75	0.75
Filter radius, R	1.5	1.5
Convergence criterion, $\varepsilon_{\mathrm{conv}}$	5.0×10^{-4}	5.0×10^{-4}
Maximum number of iterations, $k_{\max}$	150	150
Young's modulus, E_0 [Pa]	1.0×10^6	1.0×10^6
Poisson ratio, ν	0.3	0.3

Table 2.2: Calculation conditions of topology optimization for strain energy minimization in three dimensional static problems.

Model	Cantilever beam	MBB beam
Number of elements	24000	27000
Number of nodes	27511	31031
Initial density average, $\bar{\rho_0}$	0.5	0.3
Penalization parameter for the SIMP method, p_s	4.5	4.5
Weighting factor, η	0.75	0.75
Filter radius, R	1.5	1.5
Convergence criterion, $\varepsilon_{\mathrm{conv}}$	1.0×10^{-3}	1.0×10^{-4}
Maximum number of iterations, $k_{\max}$	150	150
Young's modulus, E_0 [Pa]	1.0×10^6	1.0×10^6
Poisson ratio, ν	0.3	0.3

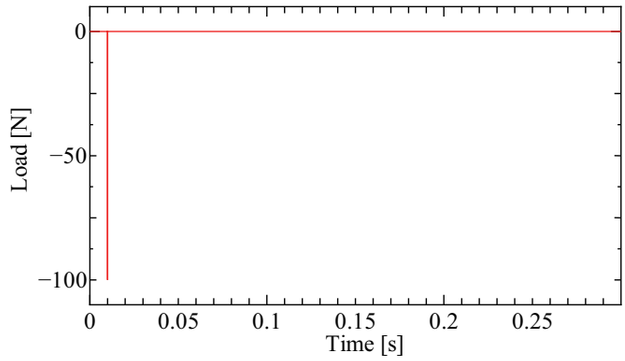

Figure 2.9: Load waveform for dynamic oscillation problem.

Table 2.3: Calculation conditions of topology optimization for strain energy minimization in three dimensional dynamic oscillation problems.

Model	Cantilever beam	MBB beam
Number of elements	24000	27000
Number of nodes	27511	31031
Total time, [s]	0.3	0.3
Time increments, Δt [s]	1.0×10^{-5}	1.0×10^{-5}
Parameter for Newmark-β method, β	0.25	0.25
Initial density average, $\bar{\rho}_0$	0.5	0.3
Penalization parameter for the SIMP method, p_s	4.5	4.5
Weighting factor, η	0.75	0.75
Filter radius, R	1.5	1.5
Convergence criterion, $\varepsilon_{\mathrm{conv}}$	1.0×10^{-4}	1.0×10^{-4}
Maximum number of iterations, $k_{\max}$	100	100
Mass density, d_0 [kg/m^3]	7860	7860
Rayleigh damping, α_1, α_2	90, 1.0×10^{-5}	90, 1.0×10^{-5}
Young's modulus, E_0 [Pa]	208×10^9	208×10^9
Poisson ratio, ν	0.3	0.3

2.7 Results and considerations of density-based topology optimization for strain energy minimization

2.7.1 Results of topology optimization in two dimensional steady problems

This subsection describes the results of density-based topology optimization for strain energy minimization in two dimensional steady problems. Figures 2.10 to 2.12 show the density distributions at convergence in the cantilever beam model, with the OC method, the Gradient method with first-order and second-order derivatives, and the modified OC method and the update method changed, respectively. Sub caption (a) in Figures 2.10 to 2.12 show the results when the move-limit $\rho_{\text{move}} = 0.01$, and (b) shows the results when the move-limit $\rho_{\text{move}} = 0.40$ or $\rho_{\text{move}} = 1.00$. Sub caption (a) is set as a small value, and (b) is set as a large value. Since the move-limit is the constraint for the update width of density update, topology optimization when the move-limit $\rho_{\text{move}} = 0.01$ is assumed to steadily find an optimum results. In contrast, topology optimization when the move-limit $\rho_{\text{move}} = 1.00$ is synonymous with not setting a move-limit constraint for density update. In other words, only density constraint shown in Equation (2.4) is set. If the move-limit is set to large value, the speed of updating the design variables increases. However, this does not guarantee that a steady optimum result will be obtained. The results will be reviewed in turn.

First of all, the results of topology optimization when using the OC method for the cantilever beam model, shown in Figure 2.7(a), is described. The result of topology optimization when the move-limit ρ_{move} is set to 0.01, shown in Figure 2.10(a), show that the optimum density distribution is obtained at convergence. The history of performance function shown in Figure 2.13 also confirms that the performance function converges to a certain value. On the other hand, the result of topology optimization when the move-limit ρ_{move} is set to 0.40, shown in Figure 2.10(b), yield a different result than in Figure 2.10(a). Moreover, the results is hardly an optimum density distribution. The history of performance function

shown in Figure 2.13 also confirms that the performance function does not converge to a certain value. The performance function vibrates up to the maximum number of iterations $k_{\max}$. In other words, when using the OC method, it is necessary to set an appropriate move-limit ρ_{move} to some extent. Next, the results of topology optimization when using the gradient method with first-order and second-order derivatives is described. The result of topology optimization when the move-limit ρ_{move} is set to 0.01, shown in Figure 2.11(a), also show that the optimum density distribution is obtained at convergence. Similarly, the history of performance function shown in Figure 2.13 confirms that the performance function converges to a certain value. However, the result of topology optimization when the move-limit ρ_{move} is set to 1.00 show a partially dispersed density distribution. The history of performance function shown in Figure 2.13 indicates that the computation speed was too fast, and another result was found. In addition, its converged value is larger than the performance function of topology optimization when the move-limit ρ_{move} is set to 1.00. Thus, it is clear that simply using the second-order derivative is problematic. Finally, the results of topology optimization when using the modified OC method is described. Similar to the results obtained when using the other methods, the result of topology optimization when the move-limit ρ_{move} is set to 0.01, shown in Figure 2.12(a), also show that the optimum density distribution is obtained at convergence. The same trend is obtained for the performance function, which converges to a certain value. When the move limit ρ_{move} is set to 1.00, the topology optimization when using the OC method and Newton's method did not obtained an optimum density distribution. However, the topology optimization when using the modified OC method produce an optimum density distribution similar to that of Figure 2.12(a), as shown in Figure 2.12(b). Compared to the results obtained for other optimum solutions, the history of performance function confirms that the performance function drops rapidly in the initial iteration and that the number of iterations is small. From Table 2.4, under conditions where similar forms were obtained, the value of the normalized performance function at convergence did not change significantly.

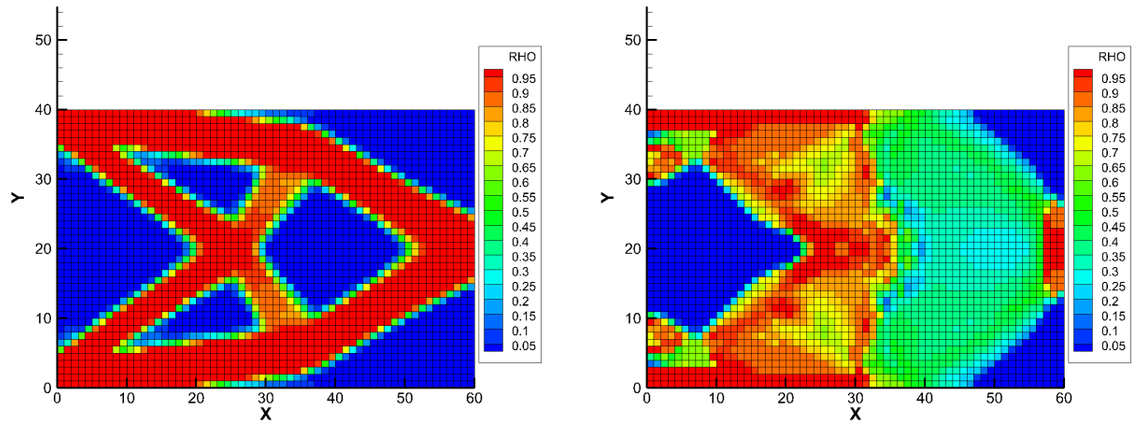

(a) OC method when $\rho_{\text{move}} = 0.01$. (b) OC method when $\rho_{\text{move}} = 0.40$.

Figure 2.10: Density distributions at convergence of topology optimization for strain energy minimization when using the OC method in the cantilever beam model for the two dimensional static problem.

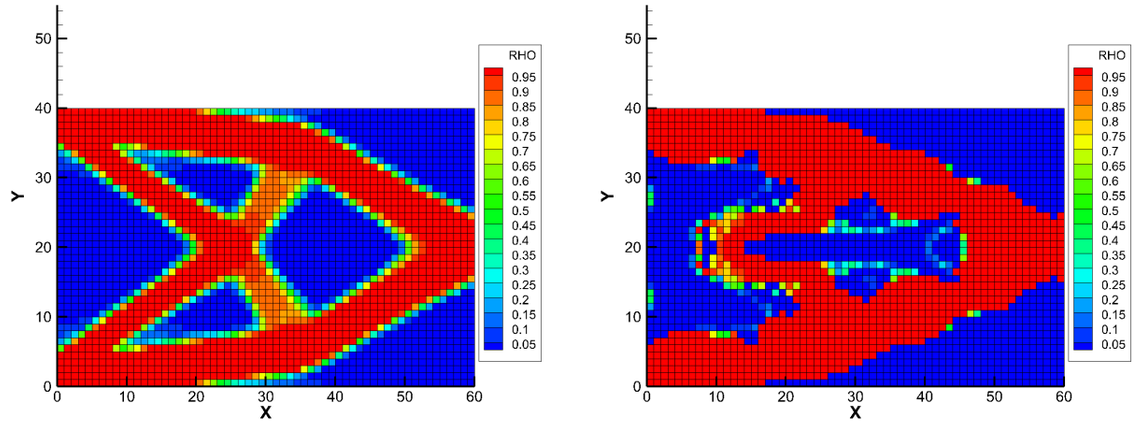

(a) Newton's method when $\rho_{\text{move}} = 0.01$. (b) OC method when $\rho_{\text{move}} = 1.00$.

Figure 2.11: Density distributions at convergence of topology optimization for strain energy minimization when using Newton's method in the cantilever beam model for the two dimensional static problem.

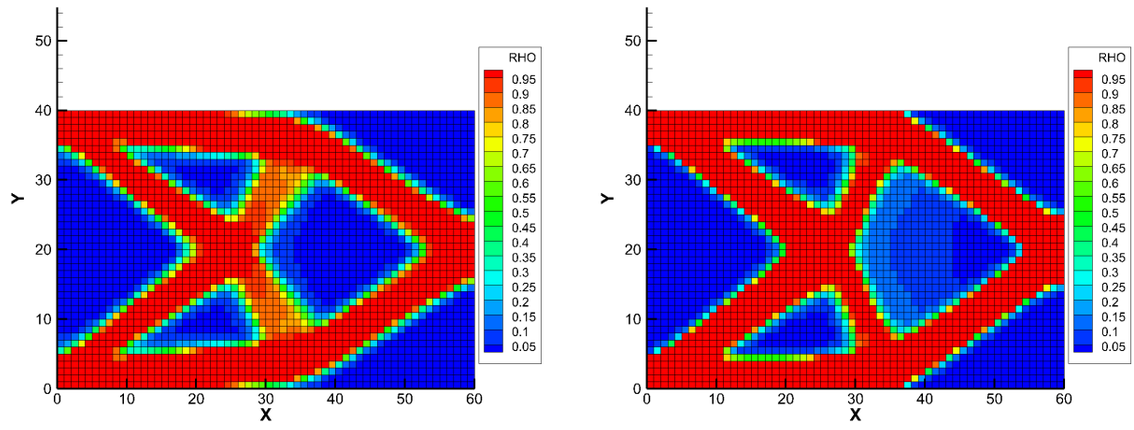

(a) Modified OC method when $\rho_{\text{move}} = 0.01$. (b) Modified OC method when $\rho_{\text{move}} = 1.00$.

Figure 2.12: Density distributions at convergence of topology optimization for strain energy minimization when using the modified OC method in the cantilever beam model for the two dimensional static problem.

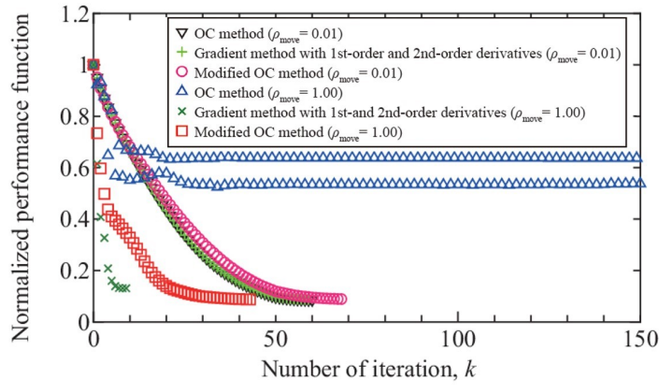

Figure 2.13: The history of normalized performance function in the topology optimization for strain energy minimization in the cantilever beam model for the two dimensional static problem.

Table 2.4: Normalized performacne function at final iteration in topology optimization for strain energy minimization in the cantilever beam model for the two dimensional static problem.

Update method	Move-limit ρ_{move}	Normalized performance function
OC	0.01	0.085
Gradient	0.01	0.086
Modified OC	0.01	0.089
OC	0.40	0.640
Gradient	1.00	0.131
Modified OC	1.00	0.087

*Gradient: Gradient method with first-order and second-order derivatives.

Next, the results of topology optimization when using the OC method for the MBB beam model, shown in Figure 2.7(b), is described. As shown in Figure 2.14, the topology optimization when the move-limit ρ_{move} is set to 0.01 obtains an optimum density distribution such as a structure. However, the topology optimization when the move-limit ρ_{move} is set to 0.40 does not obtain an optimum density distribution. The results follow the same trend as the results of topology optimization when using the OC method in cantilever beam model shown in Figure 2.10. Next, the results of topology optimization when using the gradient method with first-order and second-order derivatives is described. As shown in Figure 2.15, the topology optimization when the move-limit ρ_{move} is set to 0.01 obtains an optimum density distribution such as a structure. However, the topology optimization when the move-limit ρ_{move} is set to 1.00 does not obtain an optimum density distribution. The results follow the same trend as the results of topology optimization when using the OC method in cantilever beam model shown in Figure 2.11. Finally, the results of topology optimization when using the modified OC method is described. As shown in Figure 2.16, the topology optimization when the move-limit ρ_{move} is set to 0.01 and 1.00 obtains an optimum density distribution such as a structure. Similar to the history of performance function in cantilever beam model shown in Figure 2.13, it can be seen from the history of the performance function shown in Figure 2.17. In addition, from Table 2.5, under conditions where similar forms were obtained, the value of the normalized performance function at convergence did not change significantly. From the above, it can be said that the modified OC method, which is the proposed method, does not require the setting of the move-limit ρ_{move} by the results of numerical analysis. Additionally, in the modified OC method, the weighting factor η becomes a function of density $\rho_{\langle e \rangle}$.

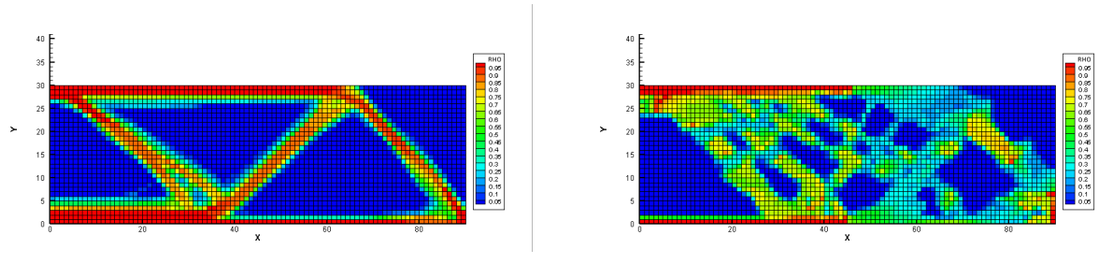

(a) OC method when $\rho_{\text{move}} = 0.01$. (b) OC method when $\rho_{\text{move}} = 0.40$.

Figure 2.14: Density distributions at convergence of topology optimization for strain energy minimization when using the OC method in the MBB beam model for the two dimensional static problem.

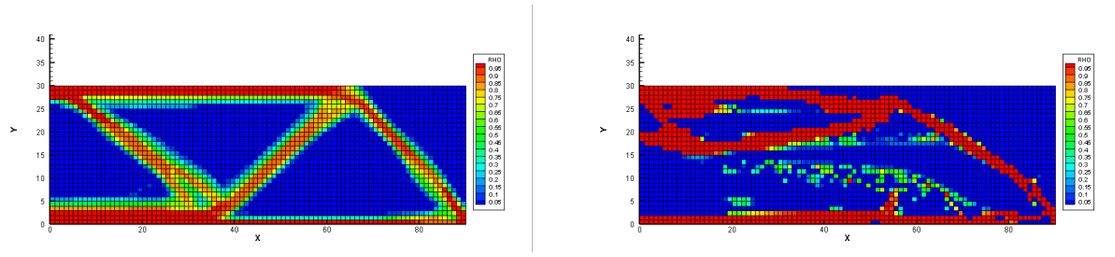

(a) Newton's method when $\rho_{\text{move}} = 0.01$. (b) OC method when $\rho_{\text{move}} = 1.00$.

Figure 2.15: Density distributions at convergence of topology optimization for strain energy minimization when using Newton's method in the MBB beam model for the two dimensional static problem.

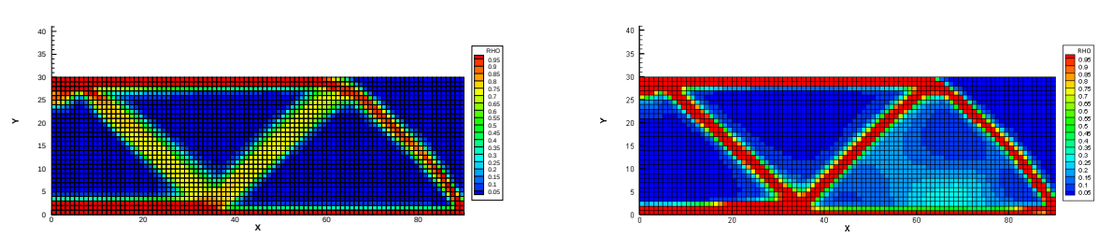

(a) Modified OC method when $\rho_{\text{move}} = 0.01$. (b) Modified OC method when $\rho_{\text{move}} = 1.00$.

Figure 2.16: Density distributions at convergence of topology optimization for strain energy minimization when using the modified OC method in the MBB beam model for the two dimensional static problem.

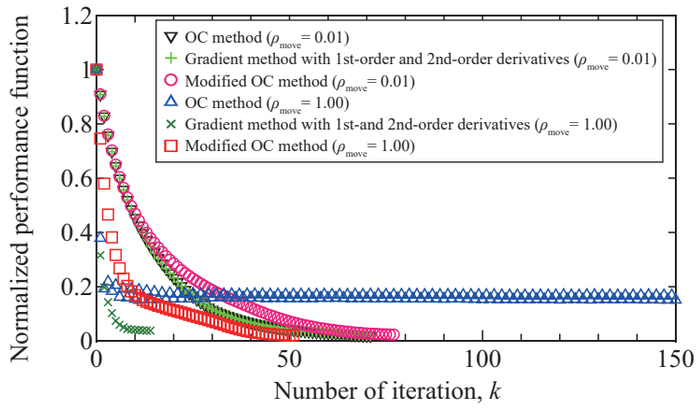

Figure 2.17: The history of normalized performance function in the topology optimization for strain energy minimization in the MBB beam model for the two dimensional static problem.

Table 2.5: Normalized performacne function at final iteration in topology optimization for strain energy minimization in the MBB beam model for the two dimensional static problem.

Update method	Move-limit ρ_{move}	Normalized performance function
OC	0.01	0.019
Gradient	0.01	0.019
Modified OC	0.01	0.024
OC	0.40	0.168
Gradient	1.00	0.038
Modified OC	1.00	0.021

*Gradient: Gradient method with first-order and second-order derivatives.

2.7.2 Parametric study for move-limit when using the modified optimality criteria method

This sub section describes the results when the modified OC method is employed and the value of the move-limit ρ_{move} is set more finely than in the previous sub section. The move-limit ρ_{move} is set to 0.01, which is the value shown in the previous sub section, plus increasing values in increments of 0.1. Other calculation conditions are same as in the previous sub section. Figures 2.18 and 2.19 show the density distributions obtained by topology optimization for the cantilever beam model and the MBB beam model, respectively. From Figure 2.18, which is the result for cantilever beam model, shows that a similar structure is obtained for all value of the move-limit ρ_{move} setting. Similarly, Figure 2.19, which is the result for MBB beam model, shows that a similar structure is obtained for all value of the move-limit ρ_{move} setting. Next, the history of performance function is confirmed. Figures 2.20 and 2.21 show the histories of normalized performance function obtained by topology optimization for each model. Figures 2.20 and 2.21, it can be confirmed that the history of normalized performance fucntion when the move-limit ρ_{move} is set between 0.10 and 1.00 are generally consistent. In other words, even when the upper and lower limits of update, the move-limit ρ_{move}, are changed, the process of updating the dentisy distribution is also the same because all iteration performance functions are identical. The OC method, which the modified OC method is based, often finds local solutions.[67] Thus, it is assumed that the modified OC method tends to find local solutions as well. In the OC method, the update speed depends on the adjusment of the weighting factor η and the move-limit ρ_{move}. However, in the proposed modified OC method, the weighting factor is defined as a function, as shown in Equation (2.85). Therefore, it is thought that appropriate updates were made rather than cumbersome searches. From Equation (2.85), in the strain energy minimization problem with volume constraint, the value of the exponent, which is the weighting factor, is given as the value the exponent increases as the value of the density approaches 1, so that the density is updated significantly. In contrast, as the value of the density approaches zero, the value

of the exponent decreases and the density is updated slowly. Thus, the grayscale elements do not rapidly decrease in density value and become no-material, indicating that the update is gradual. This ensures that structural connections between elements are maintained and updated. In addition, from the SIMP method, a larger value of the penalization parameter p_s results in a larger value of sensitivity and a smaller value of exponent. Conversely, a smaller value of the penalization pramter p_s results in a smaller value of sensitivity and larger value of exponent. Thus, even if the penalization parameter p_s is set to a difficult value, the update is automatically changed as well. THe industrial advantage of obtaining similar density distributions is that it reduces the analysis time required for parametric studies, allowing an optimum design to be efficiently applied to actual products. It also eliminates the need to examine different structures when an equivalent performance is obtained.

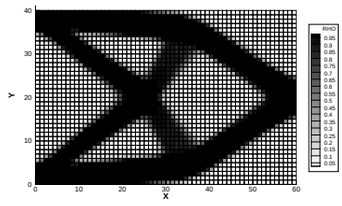

(a) When $\rho_{\mathrm{move}} = 0.01$.

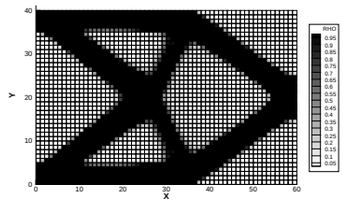

(b) When $\rho_{\mathrm{move}} = 0.10$.

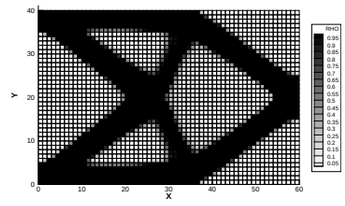

(c) When $\rho_{\mathrm{move}} = 0.20$.

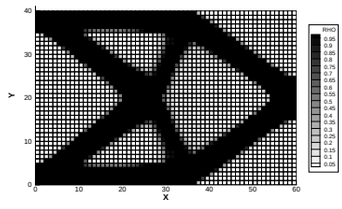

(d) When $\rho_{\mathrm{move}} = 0.30$.

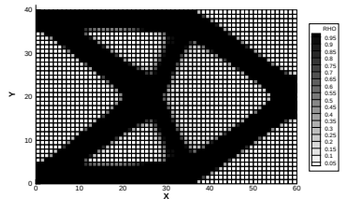

(e) When $\rho_{\mathrm{move}} = 0.40$.

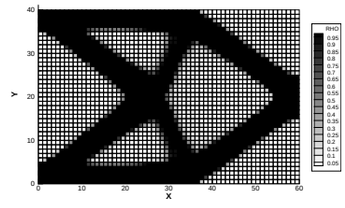

(f) When $\rho_{\mathrm{move}} = 0.50$.

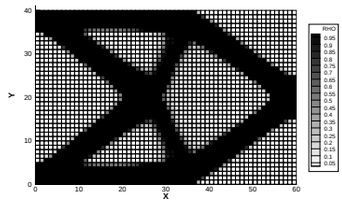

(g) When $\rho_{\mathrm{move}} = 0.60$.

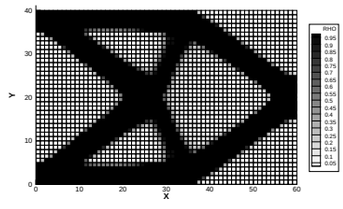

(h) When $\rho_{\mathrm{move}} = 0.70$.

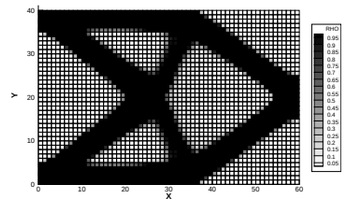

(i) When $\rho_{\mathrm{move}} = 0.80$.

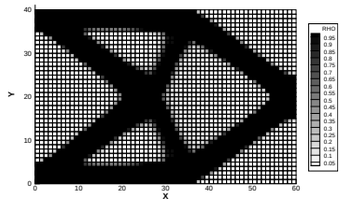

(j) When $\rho_{\mathrm{move}} = 0.90$.

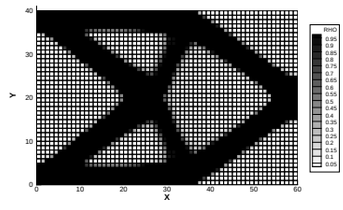

(k) When $\rho_{\mathrm{move}} = 1.00$.

Figure 2.18: Density distributions at convergence of topology optimization for strain energy minimization when changing the move-limit ρ_{move} and using the modified OC method in the cantilever beam model.

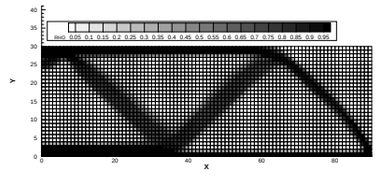

(a) When $\rho_{\text{move}} = 0.01$.

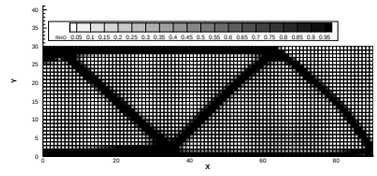

(b) When $\rho_{\text{move}} = 0.10$.

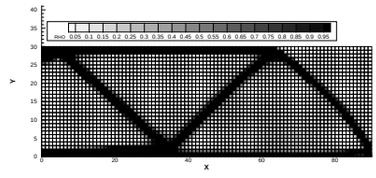

(c) When $\rho_{\text{move}} = 0.20$.

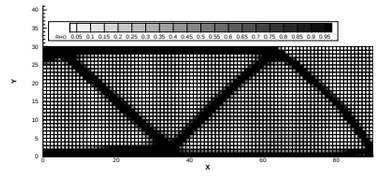

(d) When $\rho_{\text{move}} = 0.30$.

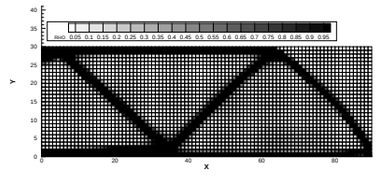

(e) When $\rho_{\text{move}} = 0.40$.

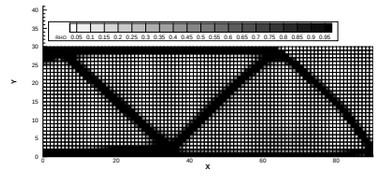

(f) When $\rho_{\text{move}} = 0.50$.

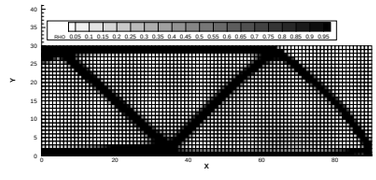

(g) When $\rho_{\text{move}} = 0.60$.

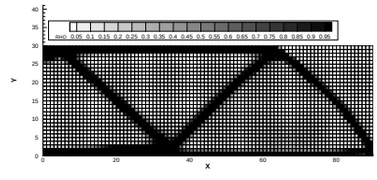

(h) When $\rho_{\text{move}} = 0.70$.

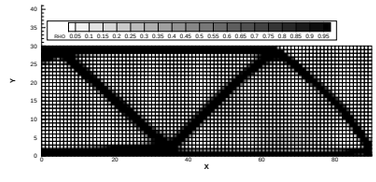

(i) When $\rho_{\text{move}} = 0.80$.

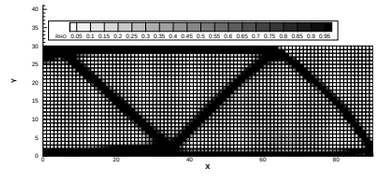

(j) When $\rho_{\text{move}} = 0.90$.

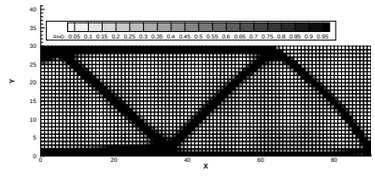

(k) When $\rho_{\text{move}} = 1.00$.

Figure 2.19: Density distributions at convergence of topology optimization for strain energy minimization when changing the move-limit ρ_{move} and using the modified OC method in the MBB beam model.

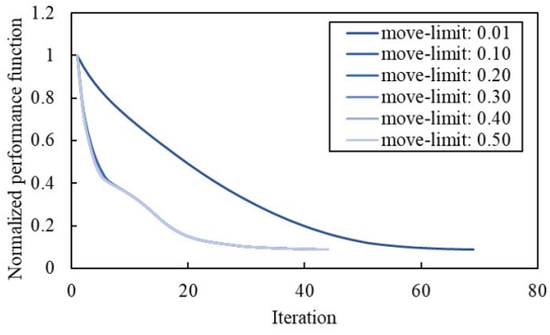

(a) When $\rho_{\text{move}} = 0.01, 0.10, 0.20,$ $0.30, 0.40$ and 0.50.

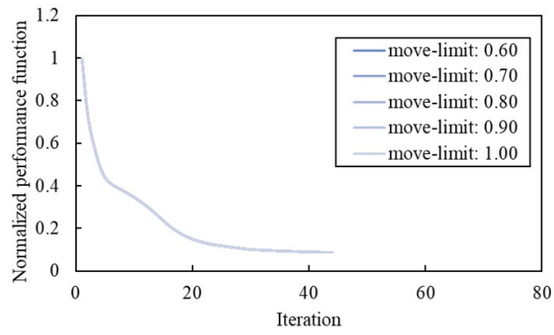

(b) When $\rho_{\text{move}} = 0.60, 0.70, 0.80,$ 0.90 and 1.00.

Figure 2.20: The history of normalized performance function when changing the move-limit ρ_{move} and using the modified OC method in the cantilever beam model.

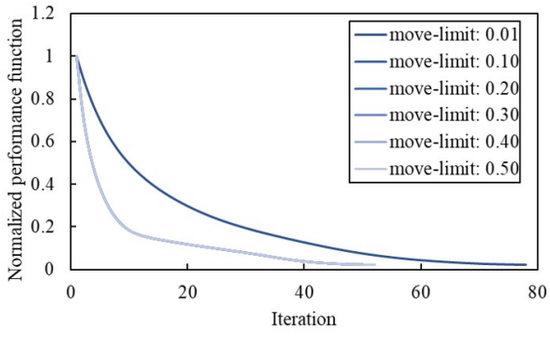

(a) When $\rho_{\text{move}} = 0.01, 0.10, 0.20,$ $0.30, 0.40$ and 0.50.

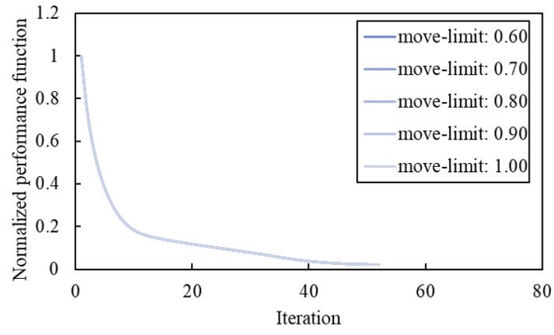

(b) When $\rho_{\text{move}} = 0.60, 0.70, 0.80,$ 0.90 and 1.00.

Figure 2.21: The history of normalized performance function when changing the move-limit ρ_{move} and using the modified OC method in the MBB beam model.

2.7.3 Results of topology optimization in three dimensional steady problems

This subsection is described the results of topology optimization for strain energy minimization in three dimensional steady problems. Based on the results of topology optimization for strain energy minimization in two dimensional steady problems described in the previous subsection, topology optimization was performed when using the conventional OC method and the proposed modified OC method. The move limit ρ_{move} is set to 0.01 when using the OC method and 1.00 when using the modified OC method. The calculation models are the cantilever beam model and MBB beam model shown in 2.8. First, the results of topology optimization when using the OC method in the cantilever beam model is described. Figures 2.22(a) and 2.22(b) show an isometric and side view of the density distribution at convergence obtained by topology optimization when using the OC method. In addition, Figures 2.22(c) and 2.22(d) show the density distributions with the elements with density values less than 0.5 in the density distribution, shown in Figures 2.22(a) and 2.22(b), eliminated. Compared to the density distribution of topology optimization in two dimensional steady problems shown in Figure 2.10(a), there appear to be more domain of material, even though the initial density average mean density $\bar{\rho}_0$ has the same value. This can be predicated that the material is distributed on the outside such as a hollow. The reason is that the value of density became smaller from the boundary between material and no material (cavity and air), which is the point where stiffness is less affected. Moreover, the small update rang of density also means that the update is gradual. Next, the results of topology optimization when using the modified OC method is described. Figure 2.23 is the density distribution at convergence obtained by topology optimization when using the modified OC method, as well as Figure 2.22. In contrast, the cavities can be seen as well as the density distribution of topology optimization when using the modified OC method in two dimensional steady problem shown in Figure 2.12. In other words, it is not a hollow material, but a solid material. It is consider to be the effect of setting $\rho = 1.00$. $\rho = 1.00$ is synonymous with

not using the move-limit. This facilitated the density distribution such as a truss, and a structure such as solid material was obtained. From a manufacturing standpoint, hollow materials, as shown in Figure 2.22, are difficult to machine when cutting, while solid materials, as shown in Figure 2.23, are easy to machine. In this respect, the modified OC method, which does not require the setting of the move-limit ρ_{move}, is a useful method. Next, the history of performance function shown in Figure 2.24 is described. Similar to the history of performance function obtained by topology optimization in two dimensional steady problems, the topology optimization when using the modified OC method confirms a significant drop in the initial iterations and fewer iterations. However, it can be seen that the performance function increases from the 4th iteration to the 12th iteration. Table 2.6 shows that the value of normalized performance fucntion at convergence when using the modified OC method was slightly larger than the value when using the OC method. The cause can be seen in the density distribution and the distribution of normalized performance function for the topology optimization in progress, shown in Figures 2.25 and 2.26. The normalized performance function here is the function of dividing the performance function $J_{\langle e \rangle}^{(k)}$ in the element e by the value of the total performance function in an iteration. From the distribution of normalized performance function shown in Figure 2.26, the performance function is higher for the element located at the tip in 4th iteration. It can also be confirmed that the normalized performance function becomes smaller as the iterations progress. When confirmed with Figure 2.25, the normalized performance function tends to be higher when the value of density in the element is small. This is probably due to the fact that it was more easily deformed when the value of density was small. The history of performance function for topology optimization when using the OC method, shown in Figure 2.24, also confirms this trend, shown in a temporary change in the decrease in the performance around the 4th iteration. Thus, the temporary increase of the performance function is considered to depend on the calculation model.

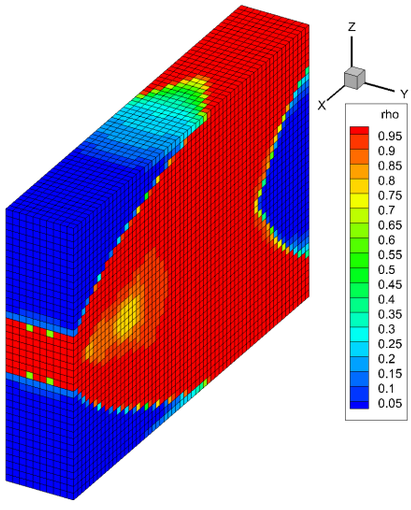

(a) Isometric view.

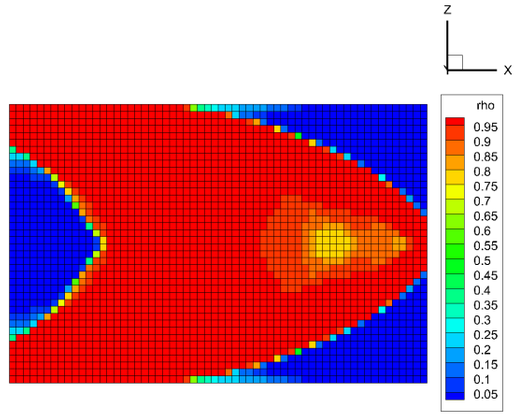

(b) Side view.

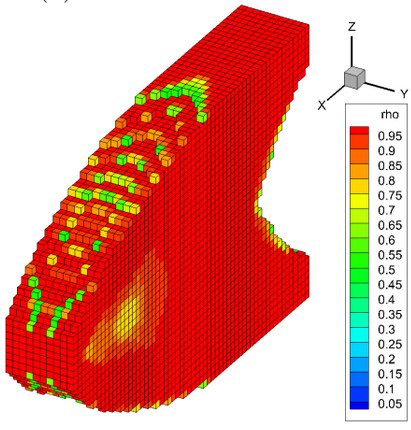

(c) Isometric view without any elements of density less than 0.5.

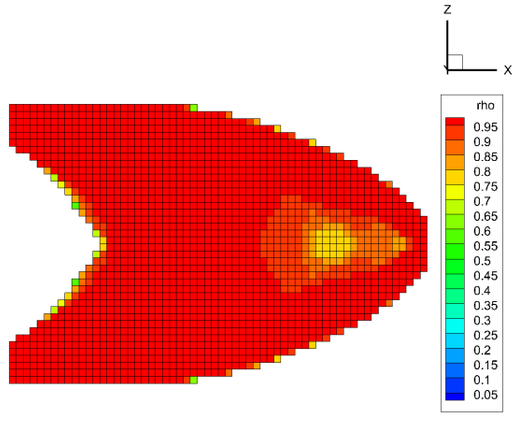

(d) Side view without any elements of density less than 0.5.

Figure 2.22: Density distributions at convergence of topology optimization for strain energy minimization when using the OC method ($\rho_{\text{move}} = 0.01$) in the cantilever beam model for the three dimensional static problem.

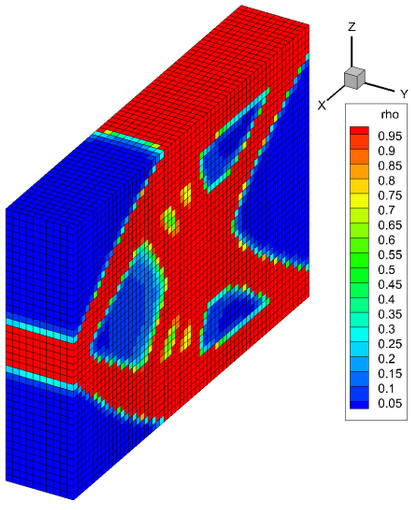

(a) Isometric view.

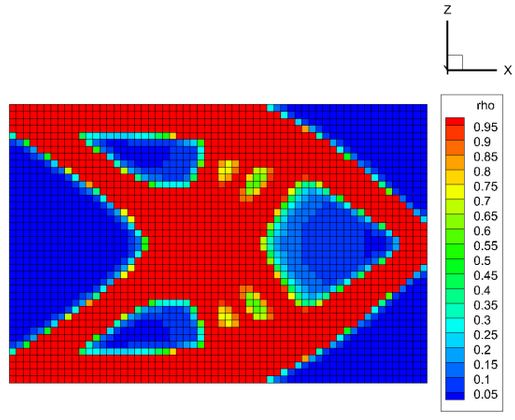

(b) Side view.

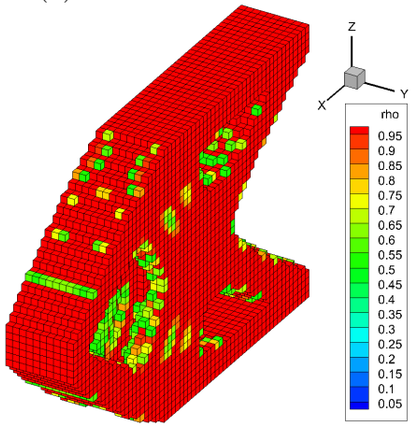

(c) Isometric view without any elements of density less than 0.5.

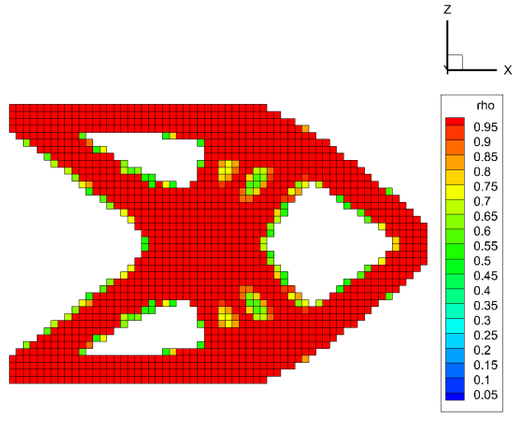

(d) Side view without any elements of density less than 0.5.

Figure 2.23: Density distributions at convergence of topology optimization for strain energy minimization when using the modified OC method ($\rho_{\text{move}} = 1.00$) in the cantilever beam model for the three dimensional static problem.

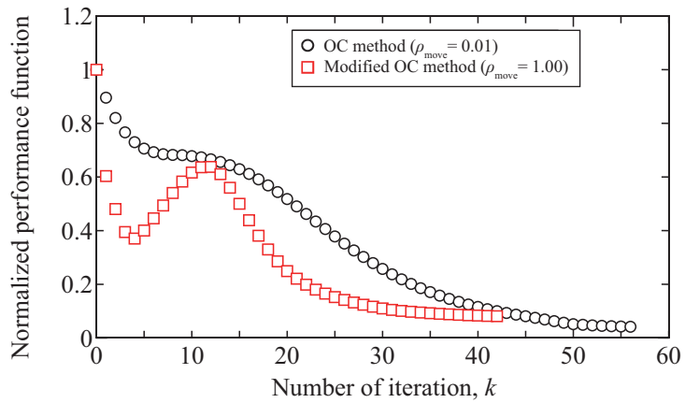

Figure 2.24: The history of normalized performance function in the topology optimization for strain energy minimization in the cantilever beam model for the three dimensional static problem.

Table 2.6: Normalized performacne function at final iteration in topology optimization for strain energy minimization in the cantilever beam model for the three dimensional static problem.

Update method	Move-limit ρ_{move}	Normalized performance function
OC	0.01	0.042
Modified OC	1.00	0.081

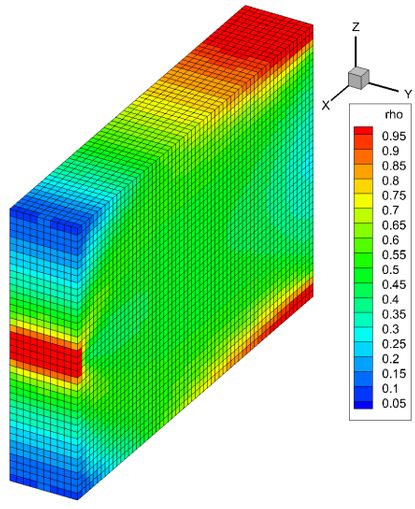

(a) Isometric view at the 4th iteration.

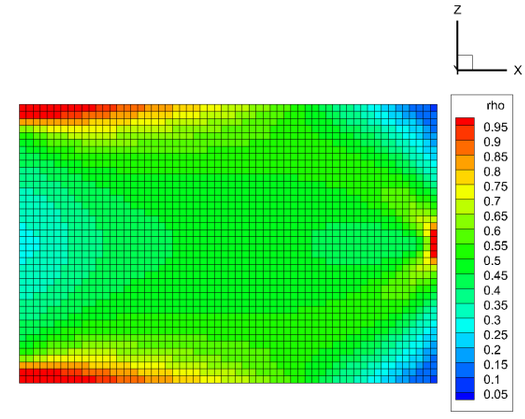

(b) Side view at the 4th iteration.

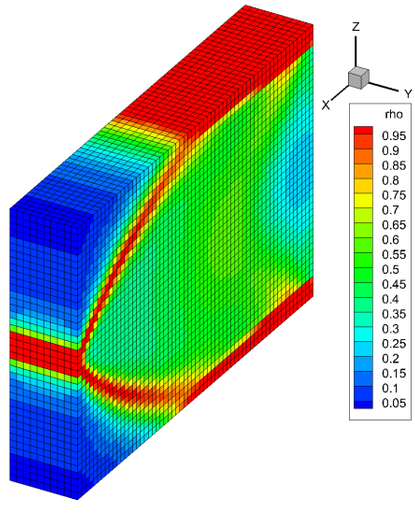

(c) Isometric view at the 12th iteration.

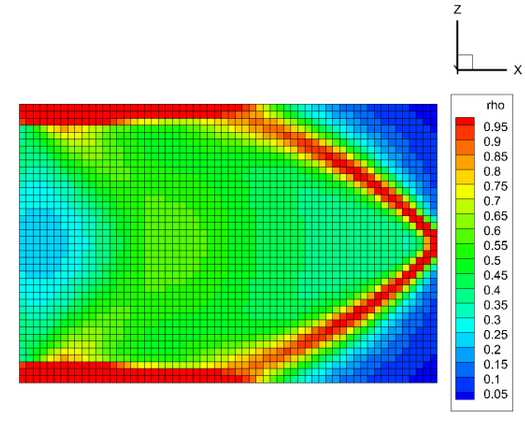

(d) Side view at the 12th iteration.

Figure 2.25: Density distributions at the 4th and 12th iterations of topology optimization when using the modified OC method ($\rho_{\text{move}} = 1.00$) in the cantilever beam model for the three dimensional static problem.

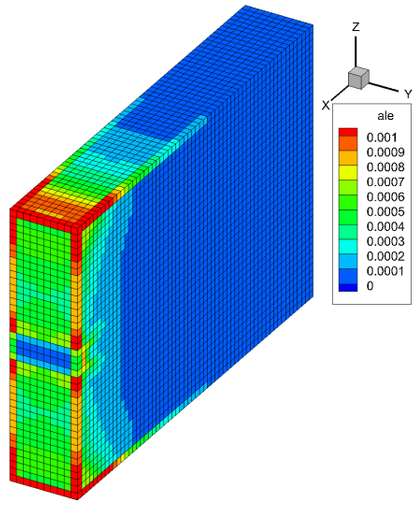

(a) At the 4th iteration.

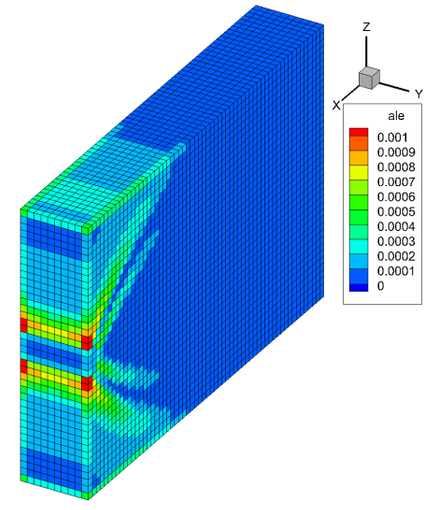

(b) At the 12th iteration.

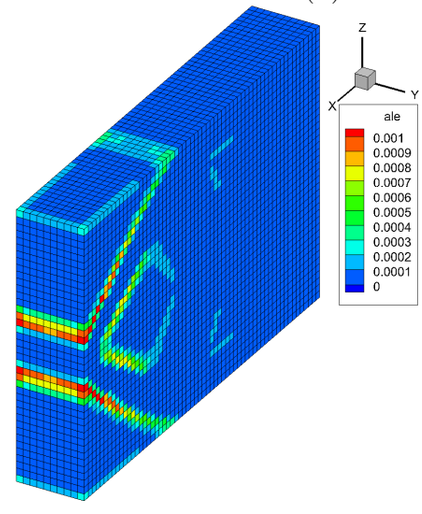

(c) At convergence.

Figure 2.26: Isometric views of the distribution of the normalized strain energy when using the modified OC method.

Next, the results of topology optimization when using the OC method in the MBB beam model shown in Figure 2.8(b) is described. Similar to the density distribution in the cantilever beam model described above, Figures 2.27 and 2.28 show isometric and side views of the density distribution at convergence obtained by topology optimization when using the OC method and the modified OC method. In addition, the sub captions (c) and (d) of Figures 2.27 and 2.28 show the density distributions with the elements with density values less than 0.5 in the density distribution, shown in the sub captions (a) and (b) of Figures 2.27 and 2.28, eliminated. Similar to the density distribution shown in Figures 2.22 and 2.23, it can be confirmed that the results differ depending on the update method. The density distribution of topology optimization when using the OC method, shown in Figure 2.27, is obtained a density distribution with trusses with thin members. On the other hand, the density distribution of topology optimization when using the OC method, shown in Figure 2.28, is obtained a density distribution with trusses with thicker members. From a manufacturing standpoint, the structure with thin members, as shown in Figure 2.27, is difficult to machine when cutting, while the structure with thicker members, as shown in Figure 2.28, is relatively easy to machine. The history of performance function for topology optimization when using the modified OC method, shown in Figure 2.29, converges earlier than one when using the OC method, with a larger drop in the initial iteration. Table 2.7 shows that the value of normalized performance fucntion at convergence when using the modified OC method was as same as the value when using the OC method.

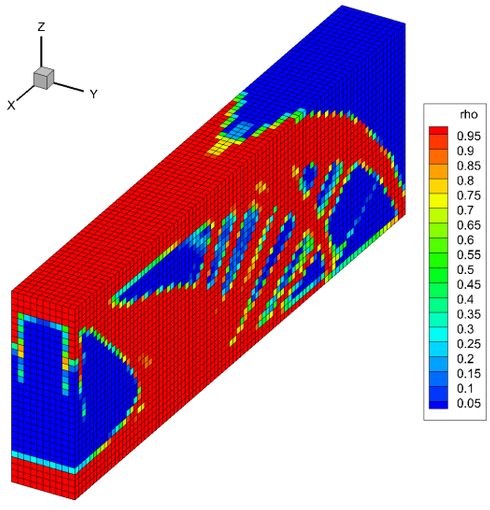

(a) Isometric view.

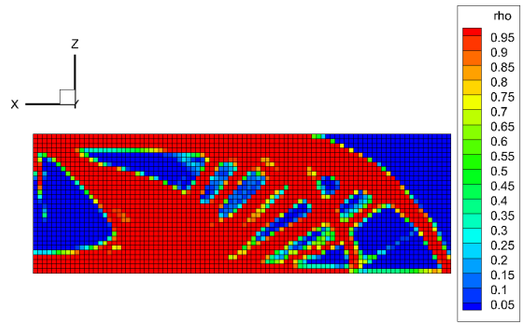

(b) Side view.

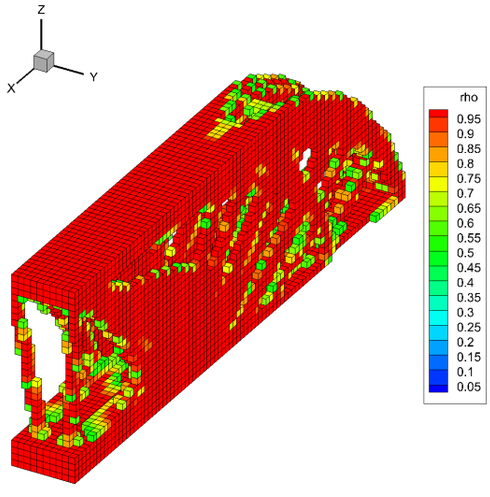

(c) Isometric view without any elements of density less than 0.5.

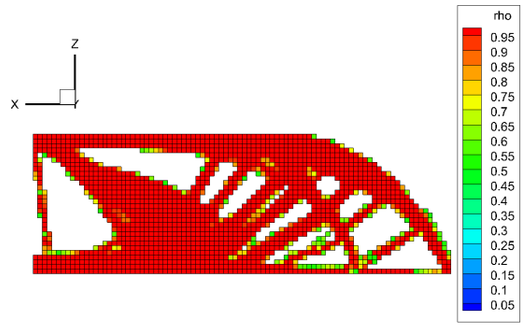

(d) Side view without any elements of density less than 0.5.

Figure 2.27: Density distributions at convergence of topology optimization for strain energy minimization when using the OC method ($\rho_{\text{move}} = 0.01$) in the MBB beam model for the three dimensional static problem.

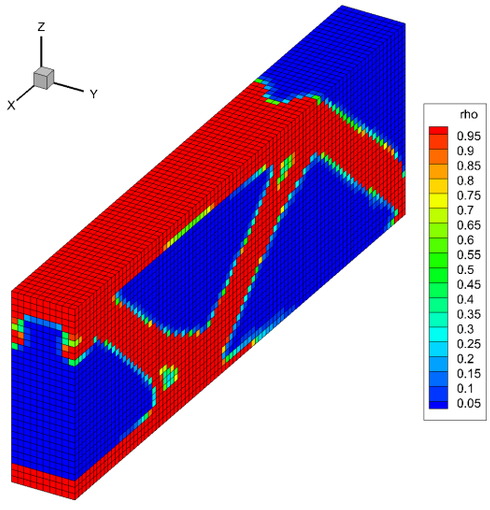

(a) Isometric view.

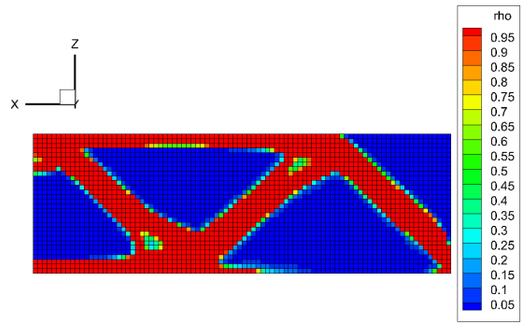

(b) Side view.

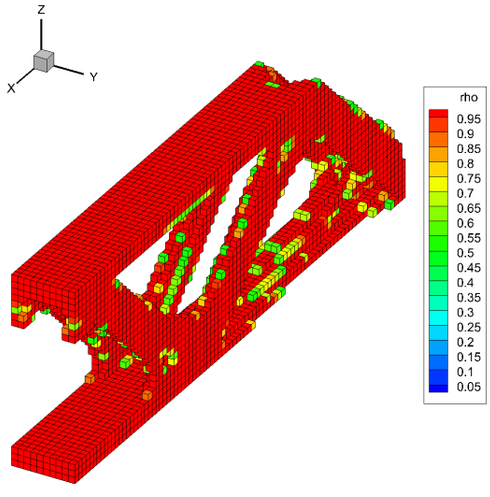

(c) Isometric view without any elements of density less than 0.5.

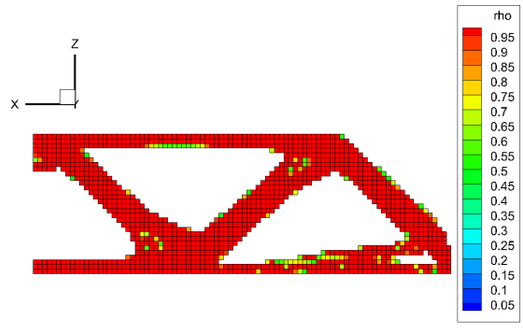

(d) Side view without any elements of density less than 0.5.

Figure 2.28: Density distributions at convergence of topology optimization for strain energy minimization when using the modified OC method ($\rho_{\text{move}} = 1.00$) in the MBB beam model for the three dimensional static problem.

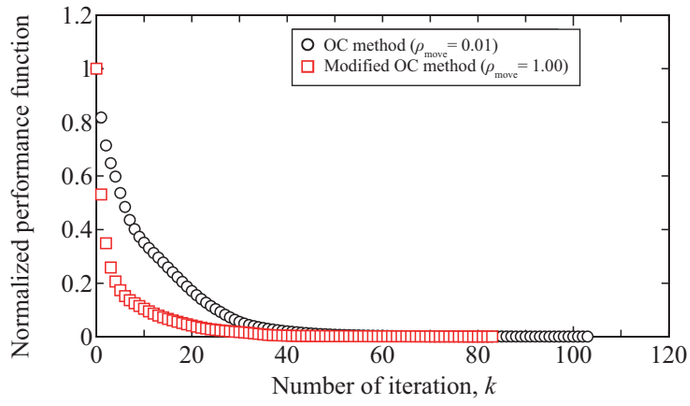

Figure 2.29: The history of normalized performance function in the topology optimization for strain energy minimization in the MBB beam model for the three dimensional static problem.

Table 2.7: Normalized performacne function at final iteration in topology optimization for strain energy minimization in the MBB beam model for the three dimensional static problem.

Update method	Move-limit ρ_{move}	Normalized performance function
OC	0.01	0.013
Modified OC	1.00	0.013

2.7.4 Results of topology optimization in three dimensional dynamic oscillation problems

This subsection is described the results of topology optimization for strain energy minimization in three dimensional dynamic oscillation problems. As in the previous subsection, the move-limit ρ_{move} is set to 0.01 when using the OC method, and it is set to 1.00 when using the modified OC method. The calculation models are the cantilever beam model and

MBB beam model shown in Figure 2.8, and is added impact loads as shown in Figure 2.9. First, the density distribution of topology optimization when using the OC method in the cantilever beam model is described. Similar to the density distribution of topology optimization in three dimensional steady problems, Figure 2.30 shows isometric and side views of the density distribution. Compared to the density distribution of topology optimization for three dimensional steady problem shown in Figure 2.22, while both of these results obtain a structure such as a hollow material, the density distribution of topology optimization for three dimensional dynamic oscillation problem shown in Figure 2.30 is characterized by a density distribution concentrated at the tip. Next, the density distribution of topology optimization when using the modified OC method is described. Also, compared to the density distribution of topology optimization for three dimensional steady problem shown in Figure 2.23, while both of these results obtain a structure such as a solid material, the density distribution of topology optimization for three dimensional dynamic oscillation problem shown in Figure 2.31 is characterized by a density distribution concentrated at the tip. This was confirmed by both update methods, suggesting that the inertia term, which is only present in dynamic oscillation problem, is influential. It is not possible to determine which is better based solely on the density distributions. However, from a manufacturing standpoint, as with the steady problem, the density distribution when using the modified OC method is considered easier to process. Next, as a verification of problem setup for topology optimization, the displacement waveforms at the loading point are described. Figure 2.32 shows the displacement waveforms in Z-direction at first iteration before optimization and at the optimum solution obtained by topology optimization when using the OC method. From Figure 2.32, the significant reduction of displacement waveforms indicates that the topology optimization has been properly implemented. Next, the differences in the optimum results depending on the update method are discussed. Figure 2.33 shows the displacement waveforms in Z-direction at optimum solutions obtained by topology optimization when using the OC method and the modified OC method. From the detailed view of displacement waveform shown in Figure 2.33(b), the displacement waveform obtained by topology optimization when using the

modified OC method is confirmed the shorter period than one when using the OC method. However, no significant difference in amplitude can be observed. Finally, from the history of performance function shown in Figure 2.34, the history of performance function for topology optimization when using the modified OC method shows that the performance function drops significantly in the initial iteration and converges in fewer iterations than one when using the OC method. Table 2.8 shows that the value of normalized performance fucntion at convergence when using the modified OC method was as same as the value when using the OC method. In topology optimization for density oscillation problems, reduction of the number of iterations is directly related to reduction of the number of finite element analysis, which are sequential analysis. However, the history of performance function for topology optimization when using the modified OC method confirms that it is constant from a certain number of iterations.

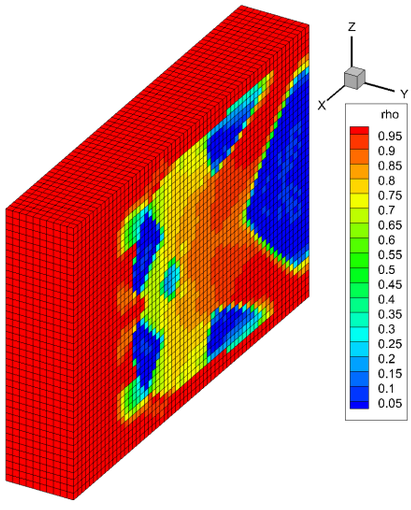

(a) Isometric view.

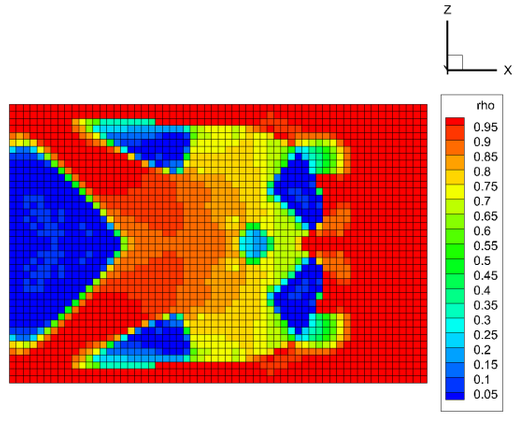

(b) Side view.

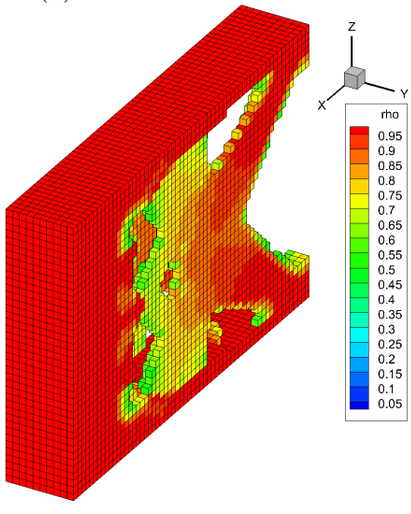

(c) Isometric view without any elements of density less than 0.5.

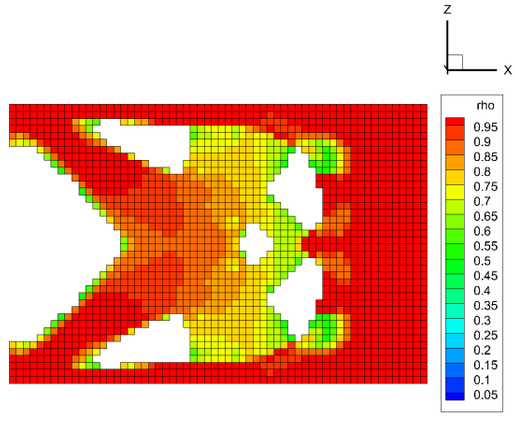

(d) Side view without any elements of density less than 0.5.

Figure 2.30: Density distributions at convergence of topology optimization for strain energy minimization when using the OC method ($\rho_{\mathrm{move}} = 0.01$) in the cantilever beam model for the three dimensional dynamic oscillation problem.

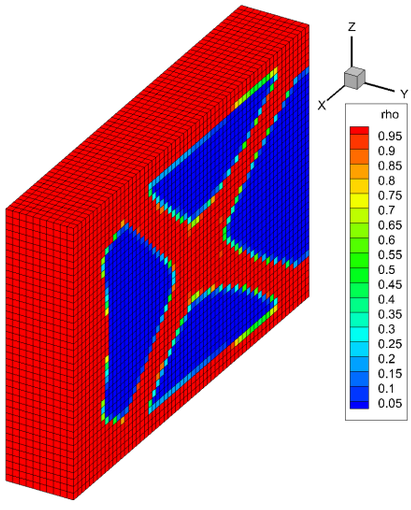

(a) Isometric view.

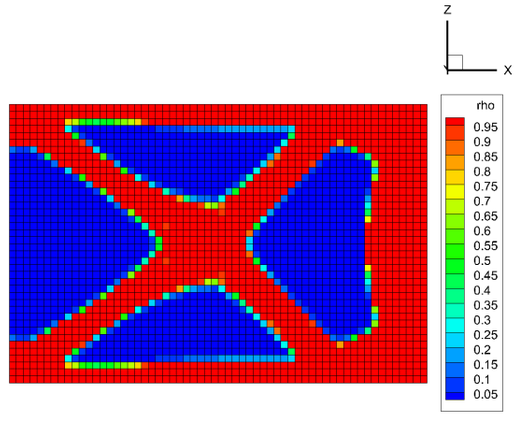

(b) Side view.

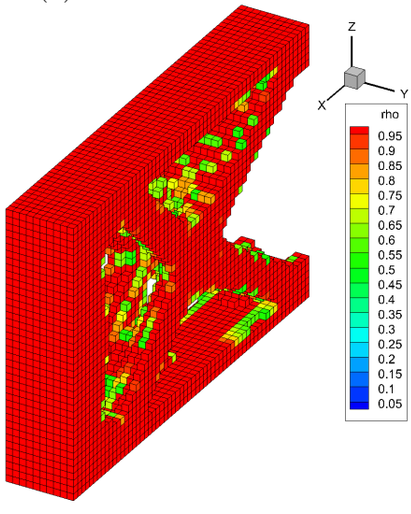

(c) Isometric view without any elements of density less than 0.5.

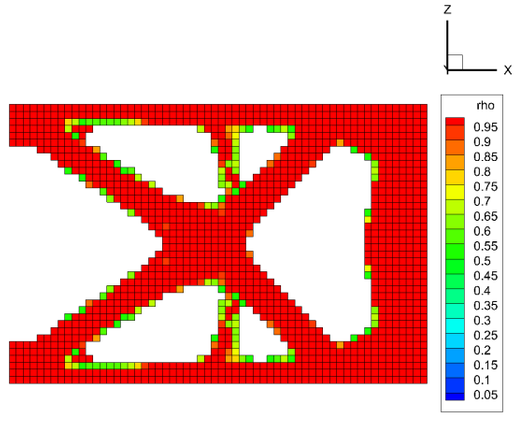

(d) Side view without any elements of density less than 0.5.

Figure 2.31: Density distributions at convergence of topology optimization for strain energy minimization when using the modified OC method ($\rho_{\text{move}} = 1.00$) in the cantilever beam model for the three dimensional dynamic oscillation problem.

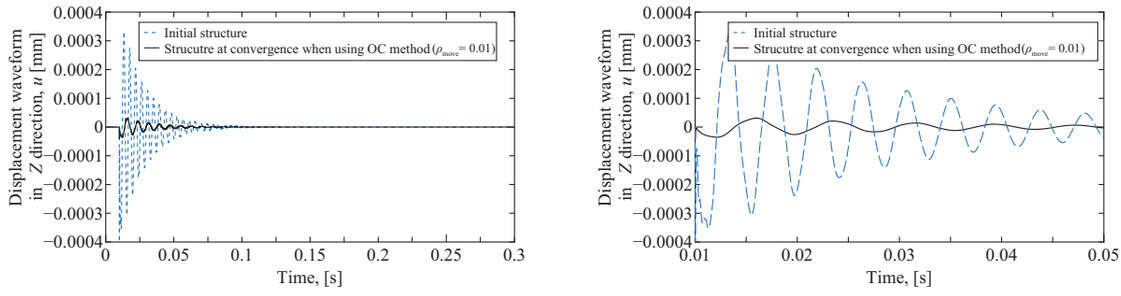

(a) Overall view. (b) Detailed view.

Figure 2.32: Displacement waveform of the initial cantilever beam model in the Z–direction at the load point, and displacement waveform of the initial cantilever beam model in the Z direction at the load point when topology optimization is performed using the OC method.

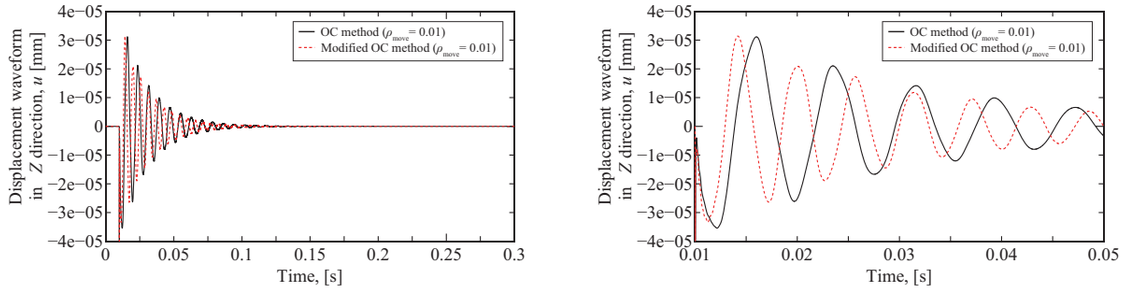

(a) Overall view. (b) Detailed view.

Figure 2.33: Displacement waveform in the Z–direction at the load point on the cantilever beam model at convergence when topology optimization is performed using the OC method or modified OC method.

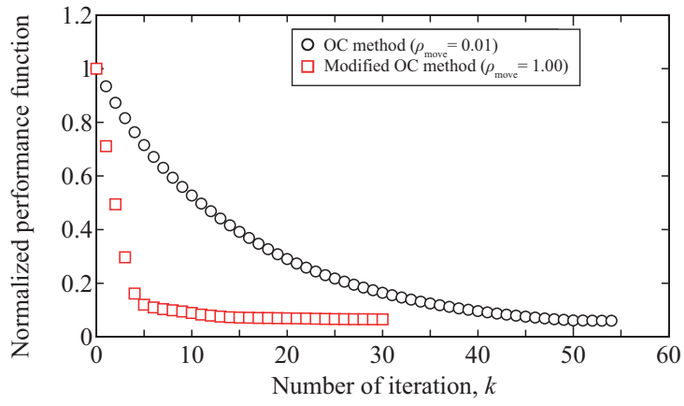

Figure 2.34: The history of normalized performance function in the topology optimization for strain energy minimization in the cantilever beam model for the three dimensional dynamic oscillation problem.

Table 2.8: Normalized performacne function at final iteration in topology optimization for strain energy minimization in the cantilever beam model for the three dimensional dynamic problem.

Update method	Move-limit ρ_{move}	Normalized performance function
OC	0.01	0.060
Modified OC	1.00	0.065

Next, the results of topology optimization when using the OC method and the modified OC method in the MBB beam model, shown in Figure 2.8(b), is described. Similar to the results in the cantilever beam model described above, it can be confirmed that the density distributions are obtained for both update methods, as shown in Figures 2.35 and 2.36. However, it can be seen that numerous grayscale remains within the density distribution than in any of the aforementioned results. On the other hand, from the displacement waveforms shown in Figures 2.37 and 2.38, the topology optimization reliably reduces the oscillation.

Similar to the results for cantilever beam model described above, the displacement waveform of topology optimization when using the modified OC method has a shorter period. The reason why numerous grayscales remain is thought to be due to the difficulty of determining convergence. From the history of the performance function shown in Figure 2.39, similar to the results of the other analyses, the history of performance function for topology optimization when using the modified OC method shows a significant drop in the initial iteration. Table 2.9 shows that the value of normalized performance fucntion at convergence when using the modified OC method was slightly smaller than the value when using the OC method. However, it was found that even if the performance function is a certain value, the density distribution could still contain grayscale. Thus, the convergence equation in the next and subsequent chapters is set to finalize the calculation at the maximum number of iterations.

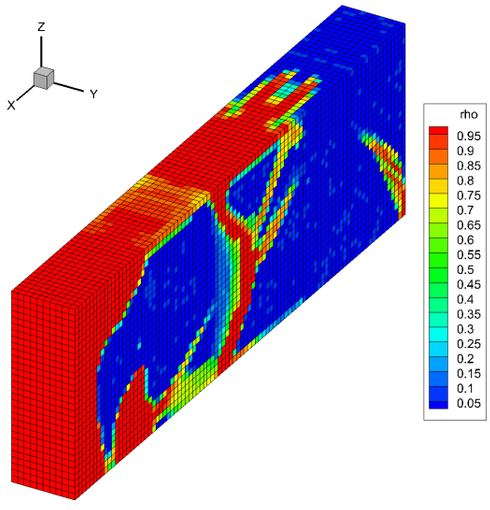

(a) Isometric view.

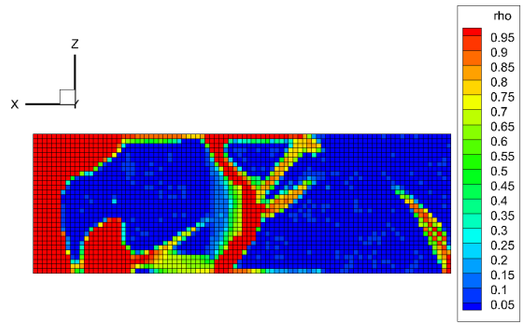

(b) Side view.

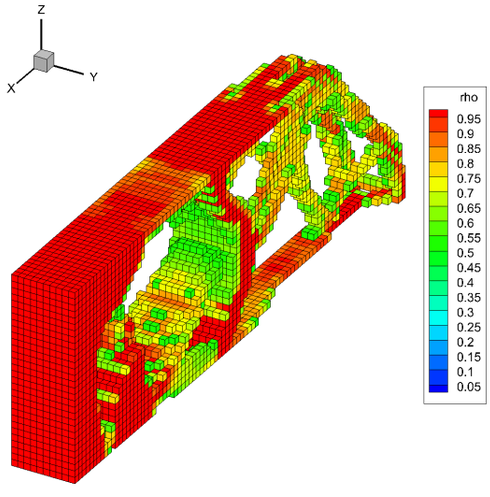

(c) Isometric view without any elements of density less than 0.5.

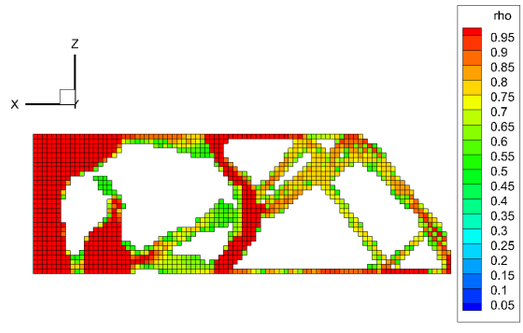

(d) Side view without any elements of density less than 0.5.

Figure 2.35: Density distributions at convergence of topology optimization for strain energy minimization when using the OC method ($\rho_{\text{move}} = 0.01$) in the MBB beam model for the three dimensional dynamic oscillation problem.

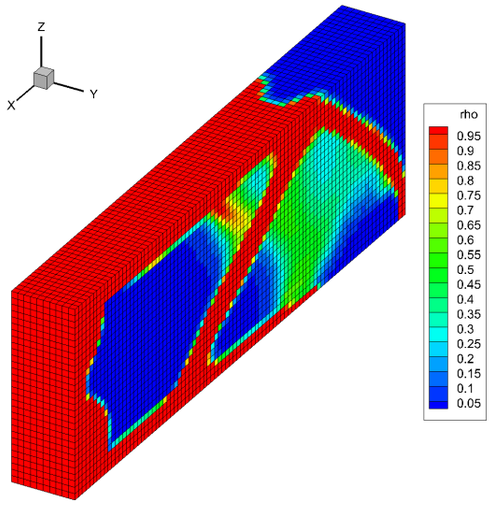

(a) Isometric view.

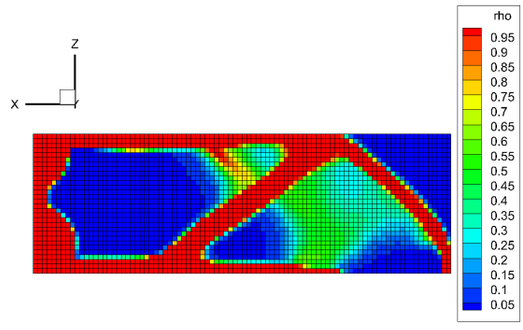

(b) Side view.

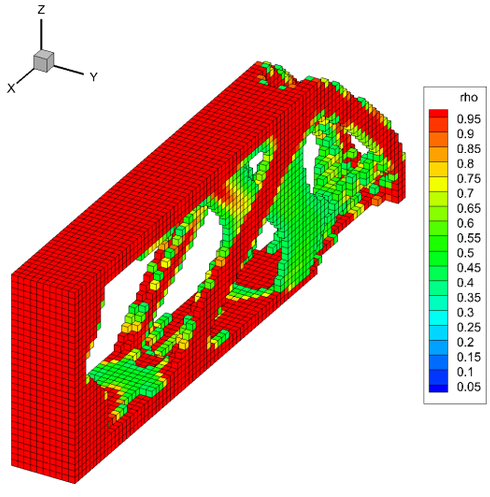

(c) Isometric view without any elements of density less than 0.5.

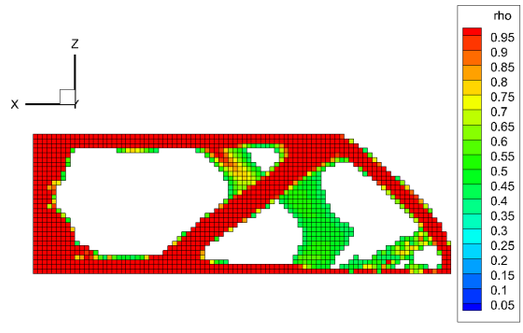

(d) Side view without any elements of density less than 0.5.

Figure 2.36: Density distributions at convergence of topology optimization for strain energy minimization when using the modified OC method ($\rho_{\text{move}} = 1.00$) in the MBB beam model for the three dimensional dynamic oscillation problem.

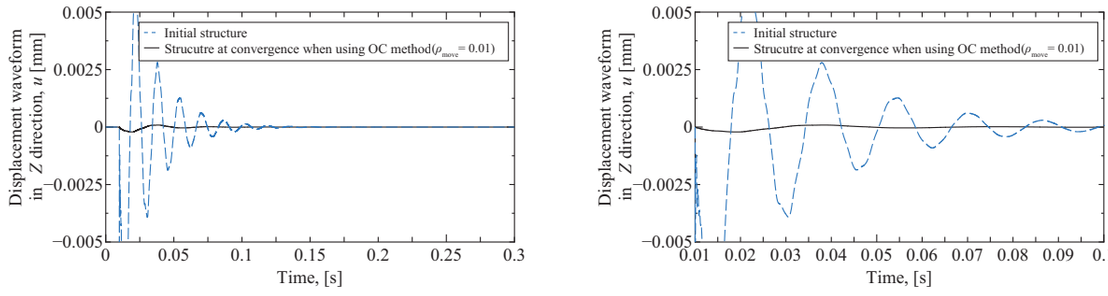

(a) Overall view. (b) Detailed view.

Figure 2.37: Displacement waveform of the initial cantilever beam model in the Z–direction at the load point, and displacement waveform of the initial cantilever beam model in the Z direction at the load point when topology optimization is performed using the OC method.

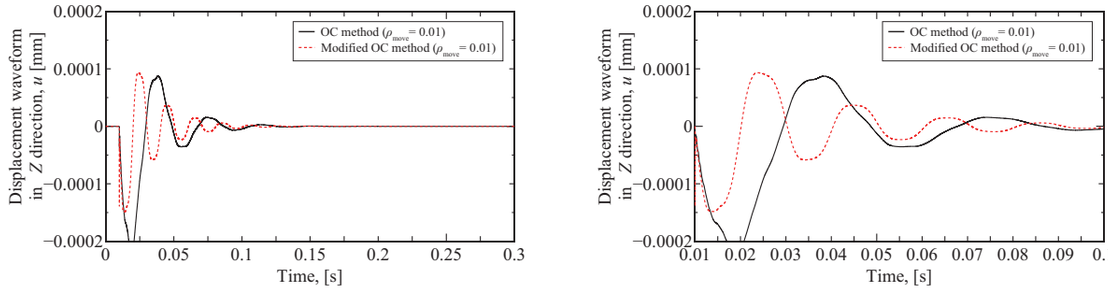

(a) Overall view. (b) Detailed view.

Figure 2.38: Displacement waveform in the Z–direction at the load point on the MBB model at convergence when topology optimization is performed using the OC method and the modified OC method.

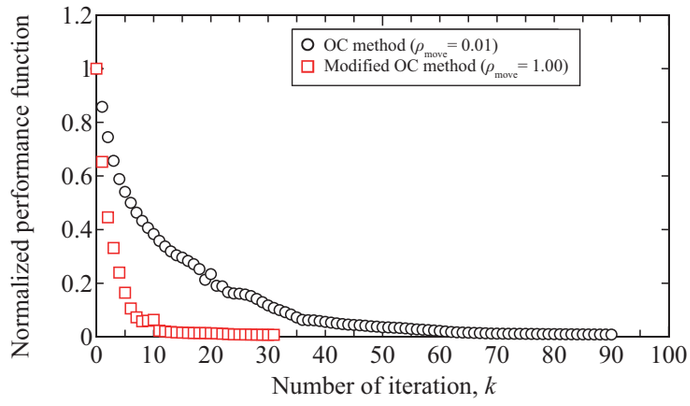

Figure 2.39: The history of normalized performance function in the topology optimization for strain energy minimization in the cantilever beam model for the three dimensional dynamic oscillation problem.

Table 2.9: Normalized performacne function at final iteration in topology optimization for strain energy minimization in the MBB beam model for the three dimensional dynamic problem.

Update method	Move-limit ρ_{move}	Normalized performance function
OC	0.01	0.0087
Modified OC	1.00	0.0078

2.7.5 Consideration of the influence of the setting value of the move-limit on an optimum result

This subsection discusses the reasons why the optimum solutions can not be obtained or differs depending on the setting value of the move-limit ρ_{move}, as described above. The difference between the OC method and the modified OC method is whether the weighting

factor η is given as a constant or as a function. From the expression for the natural logarithm of both sides of the OC method shown in Equation (2.78), it is inferred that the OC method updates the linear search in the same way as the steepest descent method. In contrast, since the modified OC method is based on Newton's method, it can be inferred that updates are made in Newtonian direction. The search speed of Newton's method is faster than that of other methods, but it is also dependent on the analysis model and initial values. The characteristics may have had a positive effect. Figure 2.40 illustrates the image of the search to the optimum solution. Figure 2.40(a) shows the image of the search when the move-limit ρ_{move} is set to too small value ($\rho_{\text{move}} = 0.01$). In this case, the number of iterations increases due to the small update range, but the optimum solution is steadily obtained. However, topology optimization using the OC method when the move-limit ρ_{move} is set to large value, as shown in Figure 2.40(b), requires a large update range, making the search for the optimum solution complicated. Thus, the analysis will either settle on a different solution or continue searching around the optimum solution. This is confirmed by the reusults of topology optimization in two dimensional steady problems. On the other hand, topology optimization using the modified OC method when the move-limit ρ_{move} is set to large value, as shown in Figure 2.40(c), is not subject to the update constraint by the move-limit ρ_{move}. And, it is assumed that the optimum solution was steadily obtained by finding a mathematically appropriate update length. In addition, because the initial model and initial conditions are the same, it is assumed that the topology optimization in two dimensional problem produced similar density distributions even when the move-limit ρ_{move} was changed. However, in three dimensional steady problems, more design degrees of freedom is obtained because of the greater effect of the update constraints due to the move-limit ρ_{move}. Also, similar density distributions can not be obtained. In the next chapter, the density distribution will be compared in more detail.

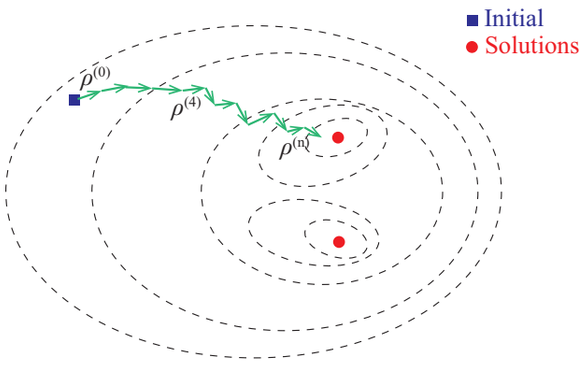

(a) Move-limit ρ_{move} is set to a smaller value.

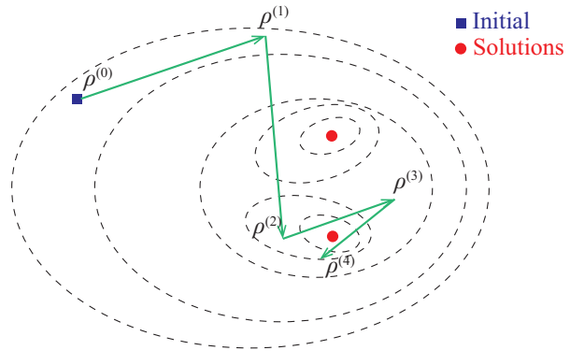

(b) Move-limit ρ_{move} is set to a larger value in the OC method.

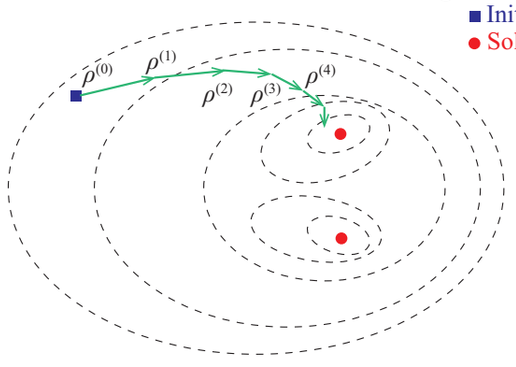

(c) Move-limit ρ_{move} is set to a larger value in the modified OC method.

Figure 2.40: Image of solution update by each update method.

Chapter 3

Topology optimization in the problem of non-self-adjoint relationship

3.1 Formulation of topology optimization for von Mises stress minimization

The previous chapter discusses the topology optimization for strain energy minimization. The strain energy minimization problem is a fundamental optimization problem in structural optimization because the self-adjoint relationship holds. The self-adjoint relationship is characterized by the fact that the adjoint equation does not required to be solved and the Lagrange multiplier (adjoint variable) is replaced as the state variable, as shown in Equation (2.13). Thus, the time required for a single iteration is reduced. In contrast, strain energy is not widely employed in industry. Therefore, an optimization problem is performed here to minimize the von Mises stress used in the strength design. The von Mises stress is a scale amount of stress calculated from the vertical and shear stresses, also called equivalent stress. However, topology optimization for stress remains a challenging problem. First of all, stress-constrained topology optimization focused on the optimization problem for truss structures[68]. The optimization for truss structures was solved by the ε–relaxation method[69] and smooth envelope function[70]. After that, it is applied to stress-constrained design of continuum structures. Recently, normalized global or local stress schemes have

been developed based on the p-norm of von Mises stress[72, 73]. In this study, the p-norm of von Mises stress is employed as performance function to make the same constraints as in the previous chapter. The optimization problem in this chapter consists of performance function shown in Equation (3.1) and the same conditions as shown in Equations (2.2) to (2.4).

$$\text{minimize} \quad J = \left(\sum_{e \in \Omega} \left({\rho_{\langle e \rangle}}^{\frac{1}{2}} \sigma_{VM\langle e \rangle} \right)^p V_{\langle e \rangle} \right)^{\frac{1}{p}} \tag{3.1}$$

$$\text{subject to} \quad [K]\{u\} = \{f\} \tag{3.2}$$

$$V = \sum_{e \in \Omega} \frac{V_{\langle e \rangle} \rho_{\langle e \rangle}}{V_{\text{total}}} - \bar{\rho_0} \leq 0 \tag{3.3}$$

$$0 \leq \rho_{\langle e \rangle} \leq 1 \tag{3.4}$$

Here, $\left[K_{\langle e \rangle}\right]$, $\left\{u_{\langle e \rangle}\right\}$, and $\left\{f_{\langle e \rangle}\right\}$ are the stiffness matrix in an element, displacement vector in an element, and load vector in an element, respectively. In addition, p, $V_{\langle e \rangle}$, $\rho_{\langle e \rangle}$, V_{total}, and $\bar{\rho_0}$ are the penalization parameter for p-norm, the volume or area in an element, density, and total volume or area in the design domain Ω, respectively. If p is set to a large value, it is approximately equal to the maximum value in the domain. If you want to focus on elements with higher stresses, p should be set to a large value. However, if p is set to a large value, an empirical setup is essential because of the strong nonlinearities and discontinuities. The von Mises stress $\sigma_{VM\langle e \rangle}$ in two dimensional problem, which is a plane stress state, and three dimensional problem are shown in

$$\sigma_{VM\langle e \rangle} = \sqrt{{\sigma_{xx\langle e \rangle}}^2 + {\sigma_{yy\langle e \rangle}}^2 - \sigma_{xx\langle e \rangle}\sigma_{yy\langle e \rangle} + 3{\sigma_{xy\langle e \rangle}}^2} \quad \text{(in 2D)} \tag{3.5}$$

$$\begin{aligned} {\sigma_{VM\langle e \rangle}}^2 &= \frac{1}{2}\Big(\left(\sigma_{xx\langle e \rangle} - \sigma_{yy\langle e \rangle} \right)^2 + \left(\sigma_{yy\langle e \rangle} - \sigma_{zz\langle e \rangle} \right)^2 + \left(\sigma_{zz\langle e \rangle} - \sigma_{xx\langle e \rangle} \right)^2 \\ &\quad +6\left({\sigma_{xy\langle e \rangle}}^2 + {\sigma_{yz\langle e \rangle}}^2 + {\sigma_{xz\langle e \rangle}}^2 \right) \Big) \quad \text{(in 3D)} \end{aligned} \tag{3.6}$$

The stress is a function of density, and is defined as

$$\begin{aligned} \left\{\sigma_{\langle e \rangle}\right\} &= [D_e]\left\{\varepsilon_{\langle e \rangle}\right\} \\ &= [D_e][B_e]\left\{u_{\langle e \rangle}\right\} \end{aligned} \tag{3.7}$$

Here, $\left\{\sigma_{\langle e\rangle}\right\}$ is the stress vector aggregating the components of stress, and $\left\{\varepsilon_{\langle e\rangle}\right\}$ is the strain vector aggregating the components of strain. In Equation (3.7), the D matrix $[D_e]$, which represents the material properties in element e, and the B matrix $[B_e]$, which represents the shape, are not a function of density. Only the displacement vector $\left\{u_{\langle e\rangle}\right\}$ is a function of density. The sensitivity is obtained using a procedure similar to the topology optimization for strain energy minimization shown in the previous chapter. Thus, the duplicated contents are omitted. The optimization is performed to satisfy the governing equation shown in Equation (3.2) and to minimize the performance function shown in Equation (3.1). The Lagrange function J^* is defined as

$$\begin{aligned} J^* &= \sum_{e\in\Omega} J^*_{\langle e\rangle} \\ &= \sum_{e\in\Omega} J_{\langle e\rangle} + \left\{\lambda_{\langle e\rangle}\right\}^T \left(\left[K_{\langle e\rangle}\right]\left\{u_{\langle e\rangle}\right\} - \left\{f_{\langle e\rangle}\right\}\right) \end{aligned} \tag{3.8}$$

where $\left\{\lambda_{\langle e\rangle}\right\}$ is the Lagrange multiplier vector. It is sufficient if the variate of the Lagrange function $\delta J^*_{\langle e\rangle}$ is zero, as shown in

$$\delta J^*_{\langle e\rangle} = \left\{\frac{\partial J^*_{\langle e\rangle}}{\partial \lambda_{\langle e\rangle}}\right\}^T \left\{\delta\lambda_{\langle e\rangle}\right\} + \left\{\frac{\partial J^*_{\langle e\rangle}}{\partial u_{\langle e\rangle}}\right\}^T \left\{\delta u_{\langle e\rangle}\right\} + \frac{\partial J^*_{\langle e\rangle}}{\partial \rho_{\langle e\rangle}}\delta\rho_{\langle e\rangle} = 0 \tag{3.9}$$

As in the previous chapter, each term is calculated to be zero. First, the gradient of the Lagrange function with respect to the Lagrange multiplier vector shown in the first term is the same as the governing equation shown in Equation (3.2). Thus, it is therefore not explained. Next, the gradient of the Lagrange function with respect to the displacement vector shown in the second term is calculated as

$$\left\{\frac{\partial J^*_{\langle e\rangle}}{\partial u_{\langle e\rangle}}\right\}^T = G^{\frac{1}{p}-1}{\rho_{\langle e\rangle}}^{\frac{p}{2}}{\sigma_{VM\langle e\rangle}}^{p-1}V_{\langle e\rangle}\left\{\frac{\partial \sigma_{VM\langle e\rangle}}{\partial u_{\langle e\rangle}}\right\}^T + \left\{\lambda_{\langle e\rangle}\right\}^T\left[K_{\langle e\rangle}\right] = \{0\}^T \tag{3.10}$$

where G is as

$$G = \sum_{e\in\Omega}\left({\rho_{\langle e\rangle}}^{\frac{1}{2}}\sigma_{VM\langle e\rangle}\right)^p V_{\langle e\rangle} \tag{3.11}$$

From Equation (3.10), the Lagrange multiplier vector is calculated as

$$\left\{\lambda_{\langle e\rangle}\right\}^T\left[K_{\langle e\rangle}\right] = -G^{\frac{1}{p}-1}{\rho_{\langle e\rangle}}^{\frac{p}{2}}{\sigma_{VM\langle e\rangle}}^{p-1}V_{\langle e\rangle}\left\{\frac{\partial \sigma_{VM\langle e\rangle}}{\partial u_{\langle e\rangle}}\right\}^T \tag{3.12}$$

The gradient of the von Mises stress with respect to the displacement vector in Equation (3.12) is calculated as follows. The gradients of the von Mises stress with respect to the displacement vector in the X, Y, and Z-directions for three dimensional problem are shown in

$$\begin{aligned}\frac{\partial \sigma_{VM\langle e\rangle}}{\partial u} &= \frac{1}{2\sigma_{VM\langle e\rangle}}\left(\left(2\sigma_{xx\langle e\rangle}-\sigma_{yy\langle e\rangle}-\sigma_{zz\langle e\rangle}\right)D_{11}\frac{\partial \varepsilon_{xx\langle e\rangle}}{\partial u}\right.\\ &+\left(2\sigma_{yy\langle e\rangle}-\sigma_{xx\langle e\rangle}-\sigma_{zz\langle e\rangle}\right)D_{21}\frac{\partial \varepsilon_{xx\langle e\rangle}}{\partial u}\\ &+\left(2\sigma_{zz\langle e\rangle}-\sigma_{xx\langle e\rangle}-\sigma_{yy\langle e\rangle}\right)D_{31}\frac{\partial \varepsilon_{xx\langle e\rangle}}{\partial u}\\ &\left.+6\tau_{xy\langle e\rangle}D_{44}\frac{\partial \gamma_{xy\langle e\rangle}}{\partial u}+6\tau_{zx\langle e\rangle}D_{66}\frac{\partial \gamma_{zx\langle e\rangle}}{\partial u}\right) \qquad (3.13)\end{aligned}$$

$$\begin{aligned}\frac{\partial \sigma_{VM\langle e\rangle}}{\partial v} &= \frac{1}{2\sigma_{VM\langle e\rangle}}\left(\left(2\sigma_{xx\langle e\rangle}-\sigma_{yy\langle e\rangle}-\sigma_{zz\langle e\rangle}\right)D_{12}\frac{\partial \varepsilon_{yy\langle e\rangle}}{\partial v}\right.\\ &+\left(2\sigma_{yy\langle e\rangle}-\sigma_{xx\langle e\rangle}-\sigma_{zz\langle e\rangle}\right)D_{22}\frac{\partial \varepsilon_{yy\langle e\rangle}}{\partial v}\\ &+\left(2\sigma_{zz\langle e\rangle}-\sigma_{xx\langle e\rangle}-\sigma_{yy\langle e\rangle}\right)D_{32}\frac{\partial \varepsilon_{yy\langle e\rangle}}{\partial v}\\ &\left.+6\tau_{xy\langle e\rangle}D_{44}\frac{\partial \gamma_{xy\langle e\rangle}}{\partial v}+6\tau_{yz\langle e\rangle}D_{55}\frac{\partial \gamma_{yz\langle e\rangle}}{\partial v}\right) \qquad (3.14)\end{aligned}$$

$$\begin{aligned}\frac{\partial \sigma_{VM\langle e\rangle}}{\partial w} &= \frac{1}{2\sigma_{VM\langle e\rangle}}\left(\left(2\sigma_{xx\langle e\rangle}-\sigma_{yy\langle e\rangle}-\sigma_{zz\langle e\rangle}\right)D_{13}\frac{\partial \varepsilon_{zz\langle e\rangle}}{\partial w}\right.\\ &+\left(2\sigma_{yy\langle e\rangle}-\sigma_{xx\langle e\rangle}-\sigma_{zz\langle e\rangle}\right)D_{23}\frac{\partial \varepsilon_{zz\langle e\rangle}}{\partial w}\\ &+\left(2\sigma_{zz\langle e\rangle}-\sigma_{xx\langle e\rangle}-\sigma_{yy\langle e\rangle}\right)D_{33}\frac{\partial \varepsilon_{zz\langle e\rangle}}{\partial w}\\ &\left.+6\tau_{yz\langle e\rangle}D_{55}\frac{\partial \gamma_{yz\langle e\rangle}}{\partial w}+6\tau_{zx\langle e\rangle}D_{66}\frac{\partial \gamma_{zx\langle e\rangle}}{\partial w}\right) \qquad (3.15)\end{aligned}$$

The gradients of the von Mises stress with respect to the displacement vector in the X and Y-directions for two dimensional problem are shown in

$$\begin{aligned}\frac{\partial \sigma_{VM\langle e\rangle}}{\partial u} &= \frac{1}{2\sigma_{VM\langle e\rangle}}\left(\left(2\sigma_{xx\langle e\rangle}-\sigma_{yy\langle e\rangle}\right)D_{11}\frac{\partial \varepsilon_{xx\langle e\rangle}}{\partial u}+\left(2\sigma_{yy\langle e\rangle}-\sigma_{xx\langle e\rangle}\right)D_{21}\frac{\partial \varepsilon_{xx\langle e\rangle}}{\partial u}\right.\\ &\left.+6\tau_{xy\langle e\rangle}D_{33}\frac{\partial \gamma_{xy\langle e\rangle}}{\partial u}\right) \qquad (3.16)\end{aligned}$$

$$\begin{aligned}\frac{\partial \sigma_{VM\langle e\rangle}}{\partial v} &= \frac{1}{2\sigma_{VM\langle e\rangle}}\left(\left(2\sigma_{xx\langle e\rangle}-\sigma_{yy\langle e\rangle}\right)D_{12}\frac{\partial \varepsilon_{yy\langle e\rangle}}{\partial v}+\left(2\sigma_{yy\langle e\rangle}-\sigma_{xx\langle e\rangle}\right)D_{22}\frac{\partial \varepsilon_{yy\langle e\rangle}}{\partial v}\right.\\ &\quad \left.+6\tau_{xy\langle e\rangle}D_{33}\frac{\partial \gamma_{xy\langle e\rangle}}{\partial v}\right) \qquad (3.17)\end{aligned}$$

Finally, the gradient of the Lagrange function with respect to the density, shown in the third term of Equation (3.9), is obtained. From Equation (3.10), the gradient of the Lagrange function with respect to the density is calculated as

$$\begin{aligned}\frac{\partial J^*_{\langle e\rangle}}{\partial \rho_{\langle e\rangle}} &= \frac{1}{2}G^{\frac{1}{p}-1}{\rho_{\langle e\rangle}}^{\frac{p}{2}-1}{\sigma_{VM\langle e\rangle}}^{p}V_{\langle e\rangle}+\left\{\lambda_{\langle e\rangle}\right\}^T\frac{\partial\left[K_{\langle e\rangle}\right]}{\partial \rho_{\langle e\rangle}}\left\{u_{\langle e\rangle}\right\}\\ &\quad +\left(G^{\frac{1}{p}-1}{\rho_{\langle e\rangle}}^{\frac{p}{2}-1}{\sigma_{VM\langle e\rangle}}^{p-1}V_{\langle e\rangle}\left\{\frac{\partial \sigma_{VM\langle e\rangle}}{\partial u_{\langle e\rangle}}\right\}^T+\left\{\lambda_{\langle e\rangle}\right\}^T\left[K_{\langle e\rangle}\right]\right)\left\{\frac{\partial u_{\langle e\rangle}}{\partial \rho_{\langle e\rangle}}\right\}\\ &= \frac{1}{2}G^{\frac{1}{p}-1}{\rho_{\langle e\rangle}}^{\frac{p}{2}-1}{\sigma_{VM\langle e\rangle}}^{p}V_{\langle e\rangle}+\left\{\lambda_{\langle e\rangle}\right\}^T\frac{\partial\left[K_{\langle e\rangle}\right]}{\partial \rho_{\langle e\rangle}}\left\{u_{\langle e\rangle}\right\} \qquad (3.18)\end{aligned}$$

Next, the extended Lagrange function L is defined by considering the volume constraint shown in Equation (3.3). As in the previous chapter, the gradient of the Lagrange function with respect to the density, which is the sensitivity, is calculated as

$$\frac{\partial L_{\langle e\rangle}}{\partial \rho_{\langle e\rangle}}=\frac{\partial J^*_{\langle e\rangle}}{\partial \rho_{\langle e\rangle}}+\Lambda\frac{V_{\langle e\rangle}}{V_{\text{total}}}=0 \qquad (3.19)$$

However, unlike the previous section, this optimization problem does not guarantee that the sensitivity is always negative, as shown in Figure 3.1. That is, there is no guarantee that the extended Lagrange multiplier Λ also always be positive.

Thus, as it is, it is impossible to employ the OC method and the modified OC method. In other words, when the sensitivity is always negative, the extended Lagrange multiplier Λ is always positive, and the OC method and the modified OC method can be employed. Therefore, to ensure that the sensitivity term is always negative, the Equation (3.19) is offset as

$$\frac{\partial J^*_{\langle e\rangle}}{\partial \rho_{\langle e\rangle}}+\Lambda\frac{V_{\langle e\rangle}}{V_{\text{total}}}+g_{\max}-g_{\max}=0 \qquad (3.20)$$

where $g_{\max}$ is an offset function, can be given in various ways. In this chapter, based on the concept that the modified sensitivity should be less than or equal to zero, the offset function

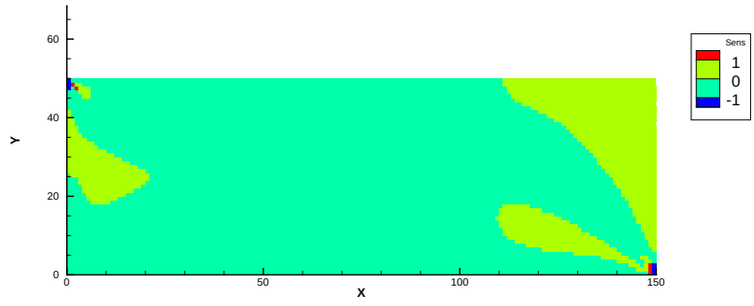

Figure 3.1: Sensitivity distribution at 1st iteration obtained in a numerical example.

$g_{\max}$ is defined as

$$g_{\max} = \max_{e \in \Omega} \left(0, \ \frac{\partial J^*_{\langle e \rangle}}{\partial \rho_{\langle e \rangle}} \right) \tag{3.21}$$

Equation (3.20) is rewritten as

$$\begin{aligned} A_{\langle e \rangle} &= \frac{\frac{\partial J^*_{\langle e \rangle}}{\partial \rho_{\langle e \rangle}} - g_{\max}}{-\left(\Lambda \frac{V_{\langle e \rangle}}{V_{\text{total}}} + g_{\max} \right)} \\ &= \frac{\frac{\partial J^*_{\langle e \rangle}}{\partial \rho_{\langle e \rangle}} - g_{\max}}{-\Lambda_{\text{mod}}} \end{aligned} \tag{3.22}$$

where Λ_{mod} is the modified extended Lagrange multiplier, which is obtained by the bisection method. The offset ensures that the numerator and denominator shown in Equation (3.22) are always negative and the function $A_{\langle e \rangle}$ is positive. Thus, the OC and the modified OC methods can be employed.

3.2 Modified optimality criteria method corresponding to negative values

This section derives a modified OC method that takes into account when the exponent located in the weighting factor are negative. Search direction is an important factor in

optimization problems. Sometimes the search direction is different, and what should be a minimization problem becomes maximization one. Thus, in the steepest descent method, the step length α_s is given such that its set value exceeds 0. In addition, the modified Newton's method [74] is often employed to correct negative definite values to positive definite value. Negative definite means when the sign is negative, and positive definite when the sign is positive. Moreover, when the sign is greater than or equal to 0, it is called semi-positive definite, and when the sign is less than or equal to 0, it is called semi-negative definite. The modified OC method modifies the diagonal components by adding a matrix to the negative definite Hessian $[H]$, as shown in

$$[Q] = [H] + \mu\,[I] \tag{3.23}$$

where $[Q]$ and $[I]$ are the modified Hessian and identity matrix. μ is a parameter that is adjusted to be a positive definite. The modified OC method is employed in the strain energy minimization problem because the function located at the weighting factor η was always guaranteed to be positive. However, in the von Mises stress minimization problem in this chapter, there is no guarantee that this function will always be positive, as shown in Figure 3.2. In the modified OC method, a sign reversal causes a reversal of the numerator-denominator, which makes it impossible to search for an optimum solution. Thus, a new proposal is needed to employ the modified OC method.

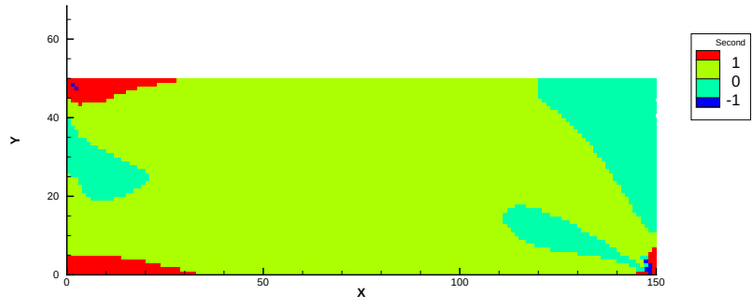

Figure 3.2: Second order derivative distribution at 1st iteration obtained in a numerical example.

Based on the above, this chapter derives a new modified OC method that incorporates the concept of the modified Newton's method to modify the negative value. First, the function located at the weighting factor η is obtained. By assuming that $g_{\max}$ is zero when differentiated by density, the function located at the weighting factor η become as

$$\left(-\frac{\partial}{\partial \rho_{\langle e\rangle}}\left(\ln A_{\langle e\rangle}^{(k)}\right)\right)^{-1} = -\left(\frac{\frac{\partial^2 J^*_{\langle e\rangle}{}^{(k)}}{\partial \rho_{\langle e\rangle}{}^2}}{\frac{\partial J^*_{\langle e\rangle}{}^{(k)}}{\partial \rho_{\langle e\rangle}}} - g_{\max}\right)^{-1} \tag{3.24}$$

The denominator in Equation (3.24) can be calculated by Equations (3.18) and (3.21). The calculation method of the numerator in Equation (3.24) will be explained. The gradient of the sensitivity shown in the numerator of Equation (3.24) is obtained as

$$\begin{aligned}
\frac{\partial^2 J^*_{\langle e\rangle}}{\partial \rho_{\langle e\rangle}{}^2} &= \frac{\partial}{\partial \rho_{\langle e\rangle}}\left(\frac{1}{2}G^{\frac{1}{p}-1}\rho_{\langle e\rangle}{}^{\frac{p}{2}-1}\sigma_{VM\langle e\rangle}{}^{p}V_{\langle e\rangle} + \left\{\lambda_{\langle e\rangle}\right\}^T\frac{\partial\left[K_{\langle e\rangle}\right]}{\partial \rho_{\langle e\rangle}}\left\{u_{\langle e\rangle}\right\}\right) \\
&= \frac{1}{2}\left(\frac{1}{p}-1\right)G^{\frac{1}{p}-2}\frac{\partial G}{\partial \rho_{\langle e\rangle}}\rho_{\langle e\rangle}{}^{\frac{p}{2}-1}\sigma_{VM\langle e\rangle}{}^{p}V_{\langle e\rangle} + \frac{1}{2}\left(\frac{p}{2}-1\right)G^{\frac{1}{p}-1}\rho_{\langle e\rangle}{}^{\frac{p}{2}-2}\sigma_{VM\langle e\rangle}{}^{p}V_{\langle e\rangle} \\
&\quad + \frac{1}{2}pG^{\frac{1}{p}-1}\rho_{\langle e\rangle}{}^{\frac{p}{2}-1}\sigma_{VM\langle e\rangle}{}^{p-1}V_{\langle e\rangle}\frac{\partial \sigma_{VM\langle e\rangle}}{\partial \rho_{\langle e\rangle}} + \left\{\frac{\partial \lambda_{\langle e\rangle}}{\partial \rho_{\langle e\rangle}}\right\}^T\frac{\partial\left[K_{\langle e\rangle}\right]}{\partial \rho_{\langle e\rangle}}\left\{u_{\langle e\rangle}\right\} \\
&\quad + \left\{\lambda_{\langle e\rangle}\right\}^T\frac{\partial^2\left[K_{\langle e\rangle}\right]}{\partial \rho_{\langle e\rangle}{}^2}\left\{u_{\langle e\rangle}\right\} + \left\{\lambda_{\langle e\rangle}\right\}^T\frac{\partial\left[K_{\langle e\rangle}\right]}{\partial \rho_{\langle e\rangle}}\left\{\frac{\partial u_{\langle e\rangle}}{\partial \rho_{\langle e\rangle}}\right\}
\end{aligned} \tag{3.25}$$

Differentiating the governing equation, shown in Equation (3.2) by the density, it is obtained

as

$$\frac{\partial \left[K_{\langle e\rangle}\right]}{\partial \rho_{\langle e\rangle}} \left\{u_{\langle e\rangle}\right\} + \left[K_{\langle e\rangle}\right] \left\{\frac{\partial u_{\langle e\rangle}}{\partial \rho_{\langle e\rangle}}\right\} = \{0\} \tag{3.26}$$

The gradient of the Lagrange multiplier vector with respect to the density in Equation (3.25) is unknown variable. Thus, differentiating the adjoint equation shown in Equation (3.12), the gradient of the Lagrange multiplier vector with respect to the density is obtained as

$$\begin{aligned}
\left\{\frac{\partial \lambda_{\langle e\rangle}}{\partial \rho_{\langle e\rangle}}\right\}^T \left[K_{\langle e\rangle}\right] &= -\left\{\lambda_{\langle e\rangle}\right\}^T \frac{\partial \left[K_{\langle e\rangle}\right]}{\partial \rho_{\langle e\rangle}} \\
&\quad - \left(\frac{1}{p} - 1\right) G^{\frac{1}{p}-2} \frac{\partial G}{\partial \rho_{\langle e\rangle}} {\rho_{\langle e\rangle}}^{\frac{p}{2}} {\sigma_{VM\langle e\rangle}}^{p-1} V_{\langle e\rangle} \left\{\frac{\partial \sigma_{VM\langle e\rangle}}{\partial u_{\langle e\rangle}}\right\}^T \\
&\quad - \frac{p}{2} G^{\frac{1}{p}-1} {\rho_{\langle e\rangle}}^{\frac{p}{2}-1} {\sigma_{VM\langle e\rangle}}^{p-1} V_{\langle e\rangle} \left\{\frac{\partial \sigma_{VM\langle e\rangle}}{\partial u_{\langle e\rangle}}\right\}^T \\
&\quad - (p-1) G^{\frac{1}{p}-1} {\rho_{\langle e\rangle}}^{\frac{p}{2}} {\sigma_{VM\langle e\rangle}}^{p-2} \frac{\partial \sigma_{VM\langle e\rangle}}{\partial \rho_{\langle e\rangle}} V_{\langle e\rangle} \left\{\frac{\partial \sigma_{VM\langle e\rangle}}{\partial u_{\langle e\rangle}}\right\}^T \\
&\quad - G^{\frac{1}{p}-1} {\rho_{\langle e\rangle}}^{\frac{p}{2}} {\sigma_{VM\langle e\rangle}}^{p-1} V_{\langle e\rangle} \frac{\partial}{\partial \rho_{\langle e\rangle}} \left(\left\{\frac{\partial \sigma_{VM\langle e\rangle}}{\partial u_{\langle e\rangle}}\right\}^T\right)
\end{aligned} \tag{3.27}$$

From Equations (3.26) and (3.27), Equation (3.25) is written as

$$
\begin{aligned}
\frac{\partial^2 J^*_{\langle e\rangle}}{\partial {\rho_{\langle e\rangle}}^2} &= \frac{1}{2}\left(\frac{1}{p}-1\right) G^{\frac{1}{p}-2}\frac{\partial G}{\partial \rho_{\langle e\rangle}}{\rho_{\langle e\rangle}}^{\frac{p}{2}-1}{\sigma_{VM\langle e\rangle}}^{p} V_{\langle e\rangle} + \frac{1}{2}\left(\frac{p}{2}-1\right) G^{\frac{1}{p}-1}{\rho_{\langle e\rangle}}^{\frac{p}{2}-2}{\sigma_{VM\langle e\rangle}}^{p} V_{\langle e\rangle} \\
&\quad + \frac{1}{2} p G^{\frac{1}{p}-1}{\rho_{\langle e\rangle}}^{\frac{p}{2}-1}{\sigma_{VM\langle e\rangle}}^{p-1} V_{\langle e\rangle}\frac{\partial \sigma_{VM\langle e\rangle}}{\partial \rho_{\langle e\rangle}} + \left\{\frac{\partial \lambda_{\langle e\rangle}}{\partial \rho_{\langle e\rangle}}\right\}^T \frac{\partial\left[K_{\langle e\rangle}\right]}{\partial \rho_{\langle e\rangle}}\left\{u_{\langle e\rangle}\right\} \\
&\quad + \left\{\lambda_{\langle e\rangle}\right\}^T \frac{\partial^2\left[K_{\langle e\rangle}\right]}{\partial {\rho_{\langle e\rangle}}^2}\left\{u_{\langle e\rangle}\right\} + \left\{\lambda_{\langle e\rangle}\right\}^T \frac{\partial\left[K_{\langle e\rangle}\right]}{\partial \rho_{\langle e\rangle}}\left\{\frac{\partial u_{\langle e\rangle}}{\partial \rho_{\langle e\rangle}}\right\} \\
&= \frac{1}{2}\left(\frac{1}{p}-1\right) G^{\frac{1}{p}-2}\frac{\partial G}{\partial \rho_{\langle e\rangle}}{\rho_{\langle e\rangle}}^{\frac{p}{2}-1}{\sigma_{VM\langle e\rangle}}^{p} V_{\langle e\rangle} + \frac{1}{2}\left(\frac{p}{2}-1\right) G^{\frac{1}{p}-1}{\rho_{\langle e\rangle}}^{\frac{p}{2}-2}{\sigma_{VM\langle e\rangle}}^{p} V_{\langle e\rangle} \\
&\quad + \frac{1}{2} p G^{\frac{1}{p}-1}{\rho_{\langle e\rangle}}^{\frac{p}{2}-1}{\sigma_{VM\langle e\rangle}}^{p-1} V_{\langle e\rangle}\frac{\partial \sigma_{VM\langle e\rangle}}{\partial \rho_{\langle e\rangle}} - \left\{\frac{\partial \lambda_{\langle e\rangle}}{\partial \rho_{\langle e\rangle}}\right\}^T \left[K_{\langle e\rangle}\right]\left\{\frac{\partial u_{\langle e\rangle}}{\partial \rho_{\langle e\rangle}}\right\} \\
&\quad + \left\{\lambda_{\langle e\rangle}\right\}^T \frac{\partial^2\left[K_{\langle e\rangle}\right]}{\partial {\rho_{\langle e\rangle}}^2}\left\{u_{\langle e\rangle}\right\} + \left\{\lambda_{\langle e\rangle}\right\}^T \frac{\partial\left[K_{\langle e\rangle}\right]}{\partial \rho_{\langle e\rangle}}\left\{\frac{\partial u_{\langle e\rangle}}{\partial \rho_{\langle e\rangle}}\right\} \\
&= \frac{1}{2}\left(\frac{1}{p}-1\right) G^{\frac{1}{p}-2}\frac{\partial G}{\partial \rho_{\langle e\rangle}}{\rho_{\langle e\rangle}}^{\frac{p}{2}-1}{\sigma_{VM\langle e\rangle}}^{p} V_{\langle e\rangle} + \frac{1}{2}\left(\frac{p}{2}-1\right) G^{\frac{1}{p}-1}{\rho_{\langle e\rangle}}^{\frac{p}{2}-2}{\sigma_{VM\langle e\rangle}}^{p} V_{\langle e\rangle} \\
&\quad + \frac{1}{2} p G^{\frac{1}{p}-1}{\rho_{\langle e\rangle}}^{\frac{p}{2}-1}{\sigma_{VM\langle e\rangle}}^{p-1} V_{\langle e\rangle}\frac{\partial \sigma_{VM\langle e\rangle}}{\partial \rho_{\langle e\rangle}} + \left\{\lambda_{\langle e\rangle}\right\}^T \frac{\partial^2\left[K_{\langle e\rangle}\right]}{\partial {\rho_{\langle e\rangle}}^2}\left\{u_{\langle e\rangle}\right\} \\
&\quad + 2\left\{\lambda_{\langle e\rangle}\right\}^T \frac{\partial\left[K_{\langle e\rangle}\right]}{\partial \rho_{\langle e\rangle}}\left\{\frac{\partial u_{\langle e\rangle}}{\partial \rho_{\langle e\rangle}}\right\} + \left(\frac{1}{p}-1\right) G^{\frac{1}{p}-2}\frac{\partial G}{\partial \rho_{\langle e\rangle}}{\rho_{\langle e\rangle}}^{\frac{p}{2}}{\sigma_{VM\langle e\rangle}}^{p-1} V_{\langle e\rangle}\frac{\partial \sigma_{VM\langle e\rangle}}{\partial \rho_{\langle e\rangle}} \\
&\quad + \frac{p}{2} G^{\frac{1}{p}-1}{\rho_{\langle e\rangle}}^{\frac{p}{2}-1}{\sigma_{VM\langle e\rangle}}^{p-1} V_{\langle e\rangle}\frac{\partial \sigma_{VM\langle e\rangle}}{\partial \rho_{\langle e\rangle}} \\
&\quad + (p-1)\, G^{\frac{1}{p}-1}{\rho_{\langle e\rangle}}^{\frac{p}{2}}{\sigma_{VM\langle e\rangle}}^{p-2}\frac{\partial \sigma_{VM\langle e\rangle}}{\partial \rho_{\langle e\rangle}} V_{\langle e\rangle}\frac{\partial \sigma_{VM\langle e\rangle}}{\partial \rho_{\langle e\rangle}} \\
&\quad + G^{\frac{1}{p}-1}{\rho_{\langle e\rangle}}^{\frac{p}{2}}{\sigma_{VM\langle e\rangle}}^{p-1} V_{\langle e\rangle}\frac{\partial}{\partial \rho_{\langle e\rangle}}\left(\left\{\frac{\partial \sigma_{VM\langle e\rangle}}{\partial u_{\langle e\rangle}}\right\}^T\right)\left\{\frac{\partial u_{\langle e\rangle}}{\partial \rho_{\langle e\rangle}}\right\}^T
\end{aligned}
\tag{3.28}
$$

In three dimensions, differentiating the gradient of the von Mises stress with respect to the

displacement vector by density, they are obtained as

$$\begin{aligned}
\frac{\partial}{\partial \rho_{\langle e\rangle}}\left(\frac{\partial \sigma_{VM\langle e\rangle}}{\partial u}\right) &= \frac{1}{2{\sigma_{VM\langle e\rangle}}^2}\left(\left(2\frac{\partial \sigma_{xx\langle e\rangle}}{\partial \rho_{\langle e\rangle}}-\frac{\partial \sigma_{yy\langle e\rangle}}{\partial \rho_{\langle e\rangle}}-\frac{\partial \sigma_{zz\langle e\rangle}}{\partial \rho_{\langle e\rangle}}\right)D_{11}\frac{\partial \varepsilon_{xx\langle e\rangle}}{\partial u}\sigma_{VM\langle e\rangle}\right.\\
&-\left(2\sigma_{xx\langle e\rangle}-\sigma_{yy\langle e\rangle}-\sigma_{zz\langle e\rangle}\right)D_{11}\frac{\partial \varepsilon_{xx\langle e\rangle}}{\partial u}\frac{\partial \sigma_{VM\langle e\rangle}}{\partial \rho_{\langle e\rangle}}\\
&+\left(2\frac{\partial \sigma_{yy\langle e\rangle}}{\partial \rho_{\langle e\rangle}}-\frac{\partial \sigma_{xx\langle e\rangle}}{\partial \rho_{\langle e\rangle}}-\frac{\partial \sigma_{zz\langle e\rangle}}{\partial \rho_{\langle e\rangle}}\right)D_{21}\frac{\partial \varepsilon_{xx\langle e\rangle}}{\partial u}\sigma_{VM\langle e\rangle}\\
&-\left(2\sigma_{yy\langle e\rangle}-\sigma_{xx\langle e\rangle}-\sigma_{zz\langle e\rangle}\right)D_{21}\frac{\partial \varepsilon_{xx\langle e\rangle}}{\partial u}\frac{\partial \sigma_{VM\langle e\rangle}}{\partial \rho_{\langle e\rangle}}\\
&+\left(2\frac{\partial \sigma_{zz\langle e\rangle}}{\partial \rho_{\langle e\rangle}}-\frac{\partial \sigma_{xx\langle e\rangle}}{\partial \rho_{\langle e\rangle}}-\frac{\partial \sigma_{yy\langle e\rangle}}{\partial \rho_{\langle e\rangle}}\right)D_{31}\frac{\partial \varepsilon_{xx\langle e\rangle}}{\partial u}\sigma_{VM\langle e\rangle}\\
&-\left(2\sigma_{zz\langle e\rangle}-\sigma_{xx\langle e\rangle}-\sigma_{yy\langle e\rangle}\right)D_{31}\frac{\partial \varepsilon_{xx\langle e\rangle}}{\partial u}\frac{\partial \sigma_{VM\langle e\rangle}}{\partial \rho_{\langle e\rangle}}\\
&+6\frac{\partial \tau_{xy\langle e\rangle}}{\partial \rho_{\langle e\rangle}}D_{44}\frac{\partial \gamma_{xy\langle e\rangle}}{\partial u}\sigma_{VM\langle e\rangle}-6\tau_{xy\langle e\rangle}D_{44}\frac{\partial \gamma_{xy\langle e\rangle}}{\partial u}\frac{\partial \sigma_{VM\langle e\rangle}}{\partial \rho_{\langle e\rangle}}\\
&\left.+6\frac{\partial \tau_{zx\langle e\rangle}}{\partial \rho_{\langle e\rangle}}D_{66}\frac{\partial \gamma_{zx\langle e\rangle}}{\partial u}\sigma_{VM\langle e\rangle}-6\tau_{zx\langle e\rangle}D_{66}\frac{\partial \gamma_{zx\langle e\rangle}}{\partial u}\frac{\partial \sigma_{VM\langle e\rangle}}{\partial \rho_{\langle e\rangle}}\right) \quad (3.29)
\end{aligned}$$

$$\begin{aligned}
\frac{\partial}{\partial \rho_{\langle e\rangle}}\left(\frac{\partial \sigma_{VM\langle e\rangle}}{\partial v}\right) &= \frac{1}{2{\sigma_{VM\langle e\rangle}}^2}\left(\left(2\frac{\partial \sigma_{xx\langle e\rangle}}{\partial \rho_{\langle e\rangle}}-\frac{\partial \sigma_{yy\langle e\rangle}}{\partial \rho_{\langle e\rangle}}-\frac{\partial \sigma_{zz\langle e\rangle}}{\partial \rho_{\langle e\rangle}}\right)D_{12}\frac{\partial \varepsilon_{yy\langle e\rangle}}{\partial v}\sigma_{VM\langle e\rangle}\right.\\
&-\left(2\sigma_{xx\langle e\rangle}-\sigma_{yy\langle e\rangle}-\sigma_{zz\langle e\rangle}\right)D_{12}\frac{\partial \varepsilon_{yy\langle e\rangle}}{\partial v}\frac{\partial \sigma_{VM\langle e\rangle}}{\partial \rho_{\langle e\rangle}}\\
&+\left(2\frac{\partial \sigma_{yy\langle e\rangle}}{\partial \rho_{\langle e\rangle}}-\frac{\partial \sigma_{xx\langle e\rangle}}{\partial \rho_{\langle e\rangle}}-\frac{\partial \sigma_{zz\langle e\rangle}}{\partial \rho_{\langle e\rangle}}\right)D_{22}\frac{\partial \varepsilon_{yy\langle e\rangle}}{\partial v}\sigma_{VM\langle e\rangle}\\
&-\left(2\sigma_{yy\langle e\rangle}-\sigma_{xx\langle e\rangle}-\sigma_{zz\langle e\rangle}\right)D_{22}\frac{\partial \varepsilon_{yy\langle e\rangle}}{\partial v}\frac{\partial \sigma_{VM\langle e\rangle}}{\partial \rho_{\langle e\rangle}}\\
&+\left(2\frac{\partial \sigma_{zz\langle e\rangle}}{\partial \rho_{\langle e\rangle}}-\frac{\partial \sigma_{xx\langle e\rangle}}{\partial \rho_{\langle e\rangle}}-\frac{\partial \sigma_{yy\langle e\rangle}}{\partial \rho_{\langle e\rangle}}\right)D_{32}\frac{\partial \varepsilon_{yy\langle e\rangle}}{\partial v}\sigma_{VM\langle e\rangle}\\
&-\left(2\sigma_{zz\langle e\rangle}-\sigma_{xx\langle e\rangle}-\sigma_{yy\langle e\rangle}\right)D_{32}\frac{\partial \varepsilon_{yy\langle e\rangle}}{\partial v}\frac{\partial \sigma_{VM\langle e\rangle}}{\partial \rho_{\langle e\rangle}}\\
&+6\frac{\partial \tau_{xy\langle e\rangle}}{\partial \rho_{\langle e\rangle}}D_{44}\frac{\partial \gamma_{xy\langle e\rangle}}{\partial v}\sigma_{VM\langle e\rangle}-6\tau_{xy\langle e\rangle}D_{44}\frac{\partial \gamma_{xy\langle e\rangle}}{\partial v}\frac{\partial \sigma_{VM\langle e\rangle}}{\partial \rho_{\langle e\rangle}}\\
&\left.+6\frac{\partial \tau_{yz\langle e\rangle}}{\partial \rho_{\langle e\rangle}}D_{55}\frac{\partial \gamma_{yz\langle e\rangle}}{\partial v}\sigma_{VM\langle e\rangle}-6\tau_{yz\langle e\rangle}D_{55}\frac{\partial \gamma_{yz\langle e\rangle}}{\partial v}\frac{\partial \sigma_{VM\langle e\rangle}}{\partial \rho_{\langle e\rangle}}\right) \quad (3.30)
\end{aligned}$$

$$\begin{aligned}
\frac{\partial}{\partial \rho_{\langle e\rangle}}\left(\frac{\partial \sigma_{VM\langle e\rangle}}{\partial w}\right) &= \frac{1}{2{\sigma_{VM\langle e\rangle}}^2}\left(\left(2\frac{\partial \sigma_{xx\langle e\rangle}}{\partial \rho_{\langle e\rangle}}-\frac{\partial \sigma_{yy\langle e\rangle}}{\partial \rho_{\langle e\rangle}}-\frac{\partial \sigma_{zz\langle e\rangle}}{\partial \rho_{\langle e\rangle}}\right)D_{13}\frac{\partial \varepsilon_{zz\langle e\rangle}}{\partial w}\sigma_{VM\langle e\rangle}\right.\\
&-\left(2\sigma_{xx\langle e\rangle}-\sigma_{yy\langle e\rangle}-\sigma_{zz\langle e\rangle}\right)D_{13}\frac{\partial \varepsilon_{zz\langle e\rangle}}{\partial w}\frac{\partial \sigma_{VM\langle e\rangle}}{\partial \rho_{\langle e\rangle}}\\
&+\left(2\frac{\partial \sigma_{yy\langle e\rangle}}{\partial \rho_{\langle e\rangle}}-\frac{\partial \sigma_{xx\langle e\rangle}}{\partial \rho_{\langle e\rangle}}-\frac{\partial \sigma_{zz\langle e\rangle}}{\partial \rho_{\langle e\rangle}}\right)D_{23}\frac{\partial \varepsilon_{zz\langle e\rangle}}{\partial w}\sigma_{VM\langle e\rangle}\\
&-\left(2\sigma_{yy\langle e\rangle}-\sigma_{xx\langle e\rangle}-\sigma_{zz\langle e\rangle}\right)D_{23}\frac{\partial \varepsilon_{zz\langle e\rangle}}{\partial w}\frac{\partial \sigma_{VM\langle e\rangle}}{\partial \rho_{\langle e\rangle}}\\
&+\left(2\frac{\partial \sigma_{zz\langle e\rangle}}{\partial \rho_{\langle e\rangle}}-\frac{\partial \sigma_{xx\langle e\rangle}}{\partial \rho_{\langle e\rangle}}-\frac{\partial \sigma_{yy\langle e\rangle}}{\partial \rho_{\langle e\rangle}}\right)D_{32}\frac{\partial \varepsilon_{zz\langle e\rangle}}{\partial v}\sigma_{VM\langle e\rangle}\\
&-\left(2\sigma_{zz\langle e\rangle}-\sigma_{xx\langle e\rangle}-\sigma_{yy\langle e\rangle}\right)D_{33}\frac{\partial \varepsilon_{zz\langle e\rangle}}{\partial w}\frac{\partial \sigma_{VM\langle e\rangle}}{\partial \rho_{\langle e\rangle}}\\
&+6\frac{\partial \tau_{yz\langle e\rangle}}{\partial \rho_{\langle e\rangle}}D_{55}\frac{\partial \gamma_{yz\langle e\rangle}}{\partial w}\sigma_{VM\langle e\rangle}-6\tau_{yz\langle e\rangle}D_{55}\frac{\partial \gamma_{yz\langle e\rangle}}{\partial w}\frac{\partial \sigma_{VM\langle e\rangle}}{\partial \rho_{\langle e\rangle}}\\
&\left.+6\frac{\partial \tau_{zx\langle e\rangle}}{\partial \rho_{\langle e\rangle}}D_{66}\frac{\partial \gamma_{zx\langle e\rangle}}{\partial w}\sigma_{VM\langle e\rangle}-6\tau_{zx\langle e\rangle}D_{66}\frac{\partial \gamma_{zx\langle e\rangle}}{\partial w}\frac{\partial \sigma_{VM\langle e\rangle}}{\partial \rho_{\langle e\rangle}}\right) \quad (3.31)
\end{aligned}$$

In two dimensions, differentiating the gradient of the von Mises stress with respect to the displacement vector by density, they are obtained as

$$\begin{aligned}
\frac{\partial}{\partial \rho_{\langle e\rangle}}\left(\frac{\partial \sigma_{VM\langle e\rangle}}{\partial u}\right) &= \frac{1}{2{\sigma_{VM\langle e\rangle}}^2}\left(\left(2\frac{\partial \sigma_{xx\langle e\rangle}}{\partial \rho_{\langle e\rangle}}-\frac{\partial \sigma_{yy\langle e\rangle}}{\partial \rho_{\langle e\rangle}}\right)D_{11}\frac{\partial \varepsilon_{xx\langle e\rangle}}{\partial u}\sigma_{VM\langle e\rangle}\right.\\
&-\left(2\sigma_{xx\langle e\rangle}-\sigma_{yy\langle e\rangle}\right)D_{11}\frac{\partial \varepsilon_{xx\langle e\rangle}}{\partial u}\frac{\partial \sigma_{VM\langle e\rangle}}{\partial \rho_{\langle e\rangle}}\\
&+\left(2\frac{\partial \sigma_{yy\langle e\rangle}}{\partial \rho_{\langle e\rangle}}-\frac{\partial \sigma_{xx\langle e\rangle}}{\partial \rho_{\langle e\rangle}}\right)D_{21}\frac{\partial \varepsilon_{xx\langle e\rangle}}{\partial u}\sigma_{VM\langle e\rangle}\\
&-\left(2\sigma_{yy\langle e\rangle}-\sigma_{xx\langle e\rangle}\right)D_{21}\frac{\partial \varepsilon_{xx\langle e\rangle}}{\partial u}\frac{\partial \sigma_{VM\langle e\rangle}}{\partial \rho_{\langle e\rangle}}\\
&\left.+6\frac{\partial \tau_{xy\langle e\rangle}}{\partial \rho_{\langle e\rangle}}D_{33}\frac{\partial \gamma_{xy\langle e\rangle}}{\partial u}\sigma_{VM\langle e\rangle}-6\tau_{xy\langle e\rangle}D_{33}\frac{\partial \gamma_{xy\langle e\rangle}}{\partial u}\frac{\partial \sigma_{VM\langle e\rangle}}{\partial \rho_{\langle e\rangle}}\right) \quad (3.32)
\end{aligned}$$

$$
\begin{aligned}
\frac{\partial}{\partial \rho_{\langle e \rangle}}\left(\frac{\partial \sigma_{VM\langle e \rangle}}{\partial v}\right) &= \frac{1}{2{\sigma_{VM\langle e \rangle}}^2}\left(\left(2\frac{\partial \sigma_{xx\langle e \rangle}}{\partial \rho_{\langle e \rangle}} - \frac{\partial \sigma_{yy\langle e \rangle}}{\partial \rho_{\langle e \rangle}}\right) D_{12}\frac{\partial \varepsilon_{yy\langle e \rangle}}{\partial v}\sigma_{VM\langle e \rangle}\right. \\
&\quad - \left(2\sigma_{xx\langle e \rangle} - \sigma_{yy\langle e \rangle}\right) D_{12}\frac{\partial \varepsilon_{yy\langle e \rangle}}{\partial v}\frac{\partial \sigma_{VM\langle e \rangle}}{\partial \rho_{\langle e \rangle}} \\
&\quad + \left(2\frac{\partial \sigma_{yy\langle e \rangle}}{\partial \rho_{\langle e \rangle}} - \frac{\partial \sigma_{xx\langle e \rangle}}{\partial \rho_{\langle e \rangle}}\right) D_{22}\frac{\partial \varepsilon_{yy\langle e \rangle}}{\partial v}\sigma_{VM\langle e \rangle} \\
&\quad - \left(2\sigma_{yy\langle e \rangle} - \sigma_{xx\langle e \rangle}\right) D_{22}\frac{\partial \varepsilon_{yy\langle e \rangle}}{\partial v}\frac{\partial \sigma_{VM\langle e \rangle}}{\partial \rho_{\langle e \rangle}} \\
&\quad \left. +6\frac{\partial \tau_{xy\langle e \rangle}}{\partial \rho_{\langle e \rangle}} D_{33}\frac{\partial \gamma_{xy\langle e \rangle}}{\partial v}\sigma_{VM\langle e \rangle} - 6\tau_{xy\langle e \rangle} D_{33}\frac{\partial \gamma_{xy\langle e \rangle}}{\partial v}\frac{\partial \sigma_{VM\langle e \rangle}}{\partial \rho_{\langle e \rangle}}\right) \quad (3.33)
\end{aligned}
$$

From the above, the modified OC method for this problem, based on the concept of the modified OC method shown in Equation (3.23), is shown in Equation (3.34). Figure 3.3 shows the derivation procedure of the Min–Max normalized (MMN) modified OC method, which is the proposed method described so far.

$$
\rho_{\langle e \rangle}^{(k+1)} = \rho_{\langle e \rangle}^{(k)}\left(\frac{\dfrac{\partial \bar{J}_{\langle e \rangle}^{*}}{\partial \rho_{\langle e \rangle}}^{(k)}}{-\Lambda_{\mathrm{mod}}^{(k)}}\right)^{\frac{1}{\iota_{\mathrm{norm}}^{(k)}}\left(-\frac{\frac{\partial \bar{J}_{\langle e \rangle}^{*}}{\partial \rho_{\langle e \rangle}}^{(k)}}{\frac{\partial^2 J_{\langle e \rangle}^{*}}{\partial {\rho_{\langle e \rangle}}^2}^{(k)}} - \iota_{\mathrm{min}}^{(k)}\right)} \quad (3.34)
$$

Here, $\frac{\partial \bar{J}_{\langle e \rangle}^{*}}{\partial \rho_{\langle e \rangle}}$ is the filtered sensitivity after offset. Moreover, ι_{min} and ι_{norm} are the shift parameter to be positive definite and parameter for normalization. The reason why using the parameter ι_{norm} is that the OC method gives a parameter in the range between zero to one. However, if the parameter ι_{norm} is not used, the modified OC method in this problem may exceed to one. Thus, it is normalized to one as an upper bound.

$$
\iota_{\mathrm{min}}^{(k)} = \min_{e \in \Omega}\left(0,\ -\frac{\dfrac{\partial \bar{J}_{\langle e \rangle}^{*}}{\partial \rho_{\langle e \rangle}}^{(k)}}{\dfrac{\partial^2 J_{\langle e \rangle}^{*}}{\partial {\rho_{\langle e \rangle}}^2}^{(k)}}\right) \quad (3.35)
$$

$$
\iota_{\mathrm{norm}}^{(k)} = \max_{e \in \Omega}\left(1,\ -\frac{\dfrac{\partial \bar{J}_{\langle e \rangle}^{*}}{\partial \rho_{\langle e \rangle}}^{(k)}}{\dfrac{\partial^2 J_{\langle e \rangle}^{*}}{\partial {\rho_{\langle e \rangle}}^2}^{(k)}} - \iota_{\mathrm{min}}^{(k)}\right) \quad (3.36)
$$

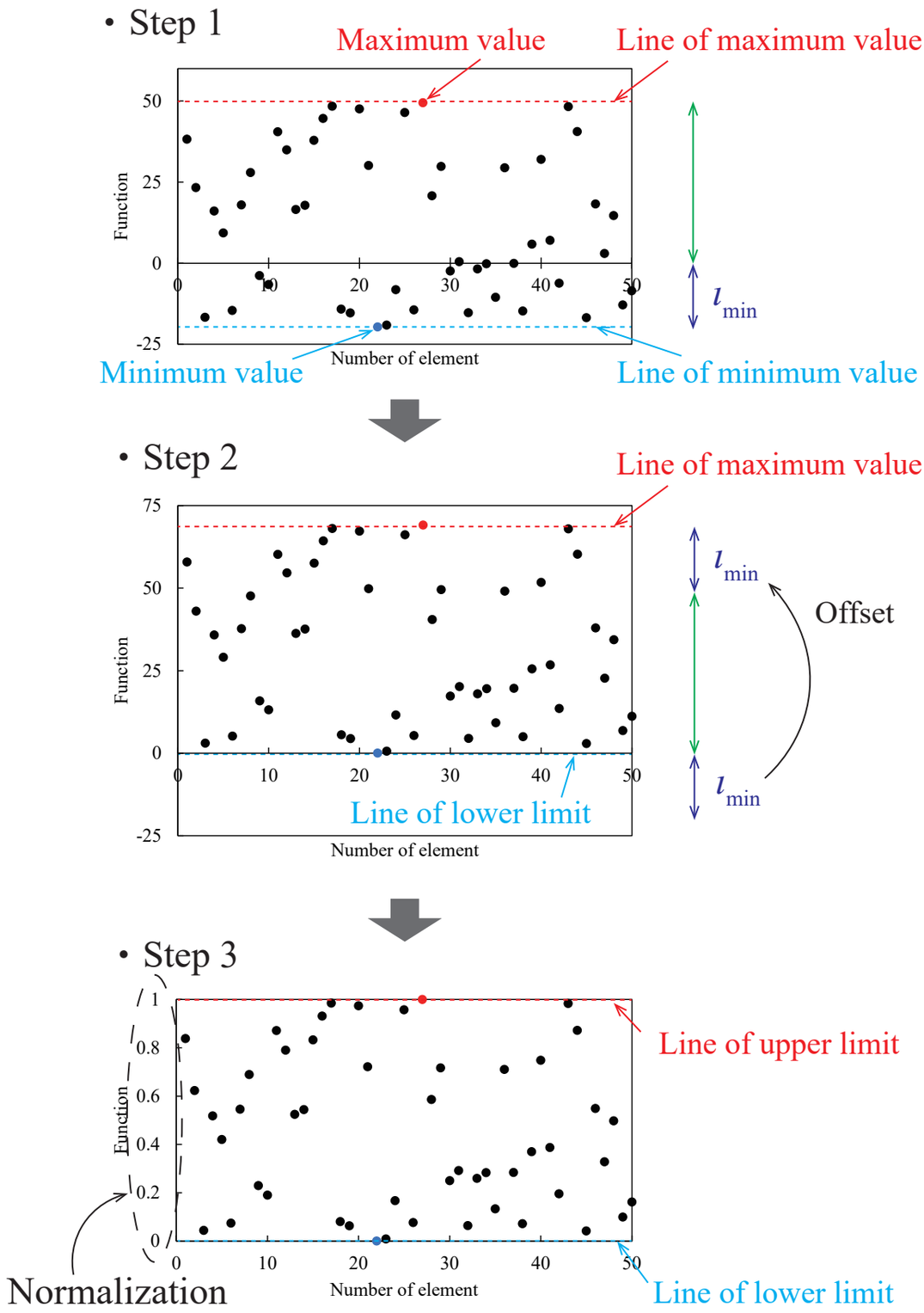

Figure 3.3: Image of the derivation process for Min–Max normalized modified OC method.

3.3 Flow of density-based topology optimization for von Mises stress minimization

This section described the flow of the density-based topology optimization for von Mises stress minimization in steady problems. The general flow of the optimization is the same as the flowchart for topology optimization to minimize strain energy, shown in Figure 2.6 in the previous chapter. The detailed procedure is as follows.

1. Input of the computation model and calculation conditions shown in next section.

2. The finite element analysis for linear elastic body is performed. The governing equation shown in Equation (3.2) is used to obtain the displacement vector $\{u\}$.

3. The von Mises stress, which is the performance function is calculated. Using the displacement vector $\{u\}$ obtained in the previous step, the performance function shown in Equation (3.1) is calculated.

4. If the judgement of convergence $k < k_{\max}$ is satisfied, the computation is finalized. Otherwise, go to the next step.

5. The sensitivity, which is the gradient of the Lagrange function $J^*_{\langle e \rangle}$ with respect to the density $\rho_{\langle e \rangle}$, is calculated. From the adjoint equation shown in Equation (3.12), the Lagrange multiplier vector $\{\lambda\}$ is obtained. After that, using the Lagrange multiplier vector $\{\lambda\}$, the sensitivity is calculated.

6. The sensitivity filter shown in Equation (2.72) is applied.

7. The density $\rho_{\langle e \rangle}$, which is the design variable, is updated. When using the OC method, Equations (2.18) and (3.22) is employed, and when using the MMN modified OC method, Equation (3.34) is employed. After updating, the number of iterations is updated to the $k+1$-th step and the process returns to step 2.

3.4 Calculation conditions in density-based topology optimization for von Mises stress minimization

This section explains about the calculation model and conditions. In this chapter, topology optimization for von Mises stress minimization in steady problems is performed. As in the previous chapter, the topology optimization is performed to verify the dependence of the move-limit ρ_{move}. The calculation models are the MBB beam model shown in Figure 3.4(a) and the hook model, used in the stress analysis example, shown in Figure 3.4(b). In the topology optimization for two dimensional problem, topology optimization is performed when the value of move-limit ρ_{move} is changed to 0.01, 0.30, or 1.00. $\rho_{\text{move}} = 0.01$ is the problem setting for finding the optimal solution, $\rho_{\text{move}} = 0.30$ is the optimization problem for a slightly larger setting, and $\rho_{\text{move}} = 1.00$ is the optimization problem with no move-limit. Based on the results of topology optimization for von Mises stress minimization in two dimensional problems, topology optimization is performed to minimize the von Mises stress in three dimensional MBB beam model and hook model shown in Figure 3.5, with thickness direction added to Figure 3.4. The influence of the update method and parameters on the three dimensional optimum results will be investigated.

First, the calculation model and conditions used in topology optimization for two dimensional problems are explained in detail. The two dimensional model shown in Figure 3.4 uses a 4-node quadrilateral element and has a structural grid divided by squares of 1 [mm] per side. The MBB beam model shown in Figure 3.4(a) is added 0.5 [N]. The hook beam model shown in Figure 2.7(b) is added 1 [N]. Other calculation conditions are shown in Table 3.1. The initial density in the design domain Ω is given uniformly by $\bar{\rho}_0$. In addition to the design domain Ω, the hook model has a non-design domain Ω_{non}. The non-design domain Ω_{non} is always updated so that the density value is zero. Next, the calculation model and conditions used in topology optimization for three dimensional problems are explained in detail. The three dimensional model shown in Figure 3.5 uses a 8-node hexahedral element and has a structural grid divided by cube of 1 [mm] per side. The MBB beam model shown in Figure

3.5(a) is added a uniformly distribution load of total load 300 [N]. The hook model shown in Figure 3.5(b) is also added a uniformly distribution load of total load 300 [N]. Figure 3.5(c) shows the hook model, shown in Figure 3.5(b), eliminated the non-design domain Ω_{non}. The other calculation conditions are shown in Table 3.2 as for the two dimensional problem.

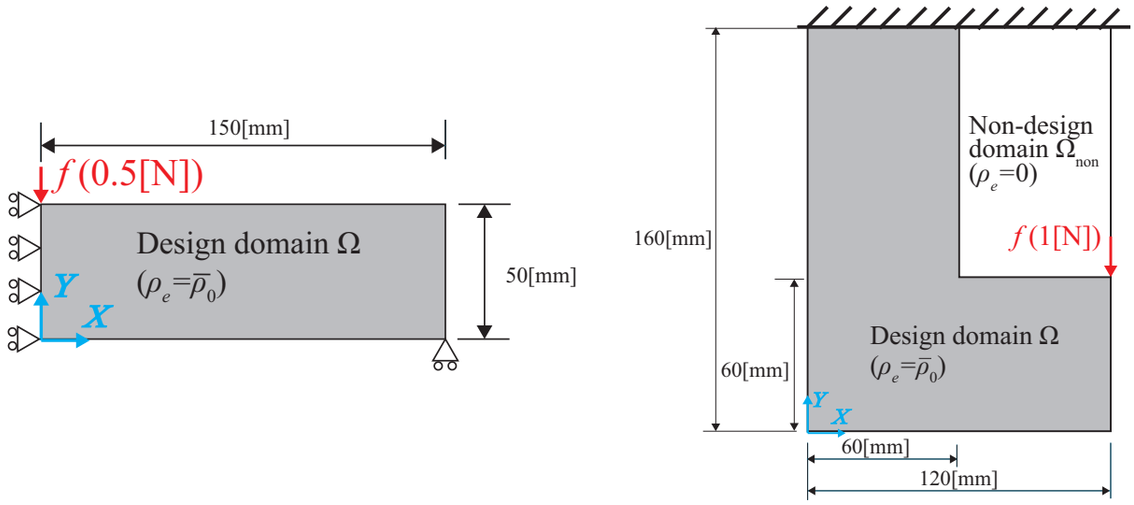

(a) MBB beam model. (b) Hook model.

Figure 3.4: Computation models on two dimension in von Mises stress energy minimization problems.

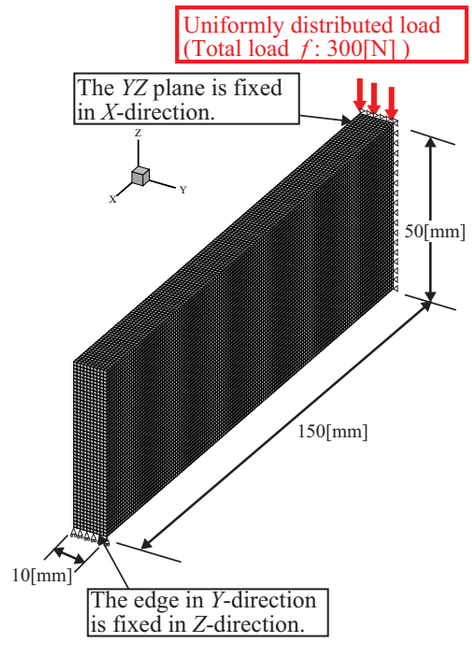

(a) MBB beam model.

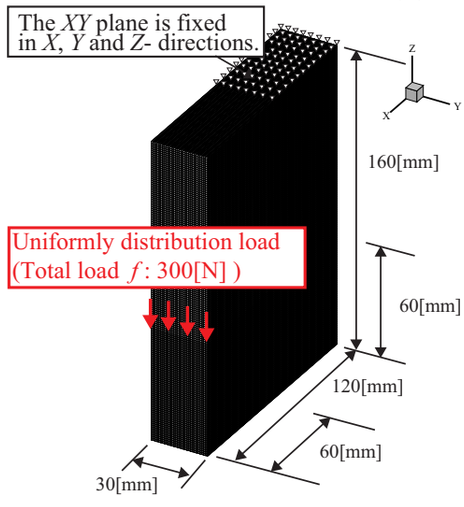

(b) Hook beam model.

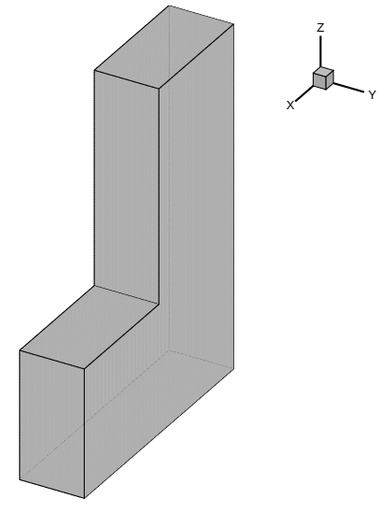

(c) Design domain in the hook model.

Figure 3.5: Computation models on three dimension in von Mises stress minimization problems.

Table 3.1: Calculation conditions of topology optimization for von Mises stress minimization in two dimensional static problems.

Model	MBB beam	Hook
Number of elements	7500	19200
Number of nodes	7701	19481
Initial density average, $\bar{\rho}_0$	0.2	0.2
Penalization parameter for the SIMP method, p_s	3.0	3.0
Penalization parameter for p–norm, p	6.0	6.0
Weighting factor, η	0.75	0.75
Filter radius, R	1.25	1.25
Maximum number of iterations, $k_{\max}$	400	500
Young's modulus, E_0 [Pa]	1.0×10^6	1.0×10^6
Poisson ratio, ν	0.3	0.3

Table 3.2: Calculation conditions of topology optimization for von Mises stress minimization in three dimensional static problems.

Model	MBB beam	Hook
Number of elements	75000	576000
Number of nodes	84711	603911
Initial density average, $\bar{\rho_0}$	0.3	0.3
Penalization parameter for the SIMP method, p_s	3.0	3.0
Penalization parameter for p–norm, p	6.0	6.0
Weighting factor, η	0.75	0.75
Filter radius, R	1.25	1.25
Maximum number of iterations, $k_{\max}$	150	150
Young's modulus, E_0 [Pa]	210×10^9	210×10^9
Poisson ratio, ν	0.3	0.3

3.5 Results and considerations of density-based topology optimization for von Mises stress minimization

3.5.1 Results of topology optimization in two dimensional steady problems

This subsection describes the results of density-based topology optimization for von Mises stress minimization in two dimensional problems. First, the results of topology optimization for MBB beam model shown in Figure 3.4(a) is discussed. Figures 3.6 to 3.8 show the density distribution obtained by topology optimization when using the OC method. Sub caption (a) in these figures shows the density distribution at $k = 20$, (b) shows the density distribution at at $k = 50$, and (c) shows the density distribution at $k = 400$. In addition, Figures 3.9 to 3.11 show the density distribution obtained by topology optimization when using the MMN modified OC method. Similarly, (a) to (c) in these figures show the density distributions at $k = 20, 50$ and 400, respectively. As shown in (a) of Figures 3.6 to 3.8, there is numerous grayscale in the density distribution because it is still in the process of being updated. As shown in (b) of Figures 3.6 to 3.8, when the number of iterations k is 50, some density distribution such as a structure is obtained, but there is grayscale in density distribution. In the topology optimization for strain energy minimization when using the modified OC method, described in the previous chapter, is obtained an optimum solution. Thus, the optimization problem, which is the von Mises stress minimization problem, that the optimum solution is difficult to find. In the density distributions at the final iteration shown in (c) of Figures 3.6 to 3.8, all of the results show a density distribution such as a structure. The density distributions obtained by topology optimization when using the OC method, shown in Figures 3.6 and 3.8, depend on the setting value of move-limit ρ_{move}. On the other hand, the density distributions obtained by topology optimization when using the MMN modified OC method, shown in Figures 3.6 and 3.11, is difficult to obtain different density distributions depending on the setting value of move-limit ρ_{move}. However, Topology

optimization when using the MMN modified OC method confirms that a small amount of grayscale remains within a density distribution. Figure 3.12 shows the von Mises stress distributions at the final iteration obtained by topology optimization using each method. The elements with a density value of 0.3 or less are eliminated. The unit of von Mises stress distributions is [MPa]. As shown in Figures 3.12(a) to 3.12(e), similar von Mises stress distributions are obtained, although the density distributions are different. However, the von Mises stress was higher only in Figure 3.12(f) due to the large amount of grayscale remaining in the density distribution. For the agreement rates, the comparison is made using the mean squared error (MSE) shown in

$$MSE = \frac{1}{mx} \sum_{e \in \Omega} \left(\rho_{\langle e \rangle} - \hat{\rho_{\langle e \rangle}} \right)^2 \tag{3.37}$$

where $\hat{\rho_{\langle e \rangle}}$ is a correct value. Topology optimization when $\rho_{\mathrm{move}} = 0.01$ is an optimization problem that steadily finds an optimum solution. Thus, the correct value $\hat{\rho_{\langle e \rangle}}$ is the density value of density distribution at the final iteration obtained by topology optimization when $\rho_{\mathrm{move}} = 0.01$. Table 3.3 shows the MSE of the density distribution obtained by topology opitmization when the move-limit ρ_{move} is set to 0.30 and 1.00. From Table 3.3, for any move-limit ρ_{move}, the MSE of topology optimization when using the MMN modified OC method is smaller than one when using the OC method. Thus, compared to the results of topology optimization when using the OC method, the results of topology optimization when using the MMN modified OC method show that the influence of the move-limit ρ_{move} on the density distribution is smaller. Figure 3.13 shows the history of performance function obtained by topology optimization when using the OC method and the MMN modified OC method. From Figure 3.13, after 100 iterations, it is found to convergence to a certain value. In addition, Table 3.4 shows that the value of normalized performance fucntion at convergence when using the MMN modified OC method was as same as the value when using the OC method. However, it is difficult to determine convergence because numerous grayscales remain in a density distribution.

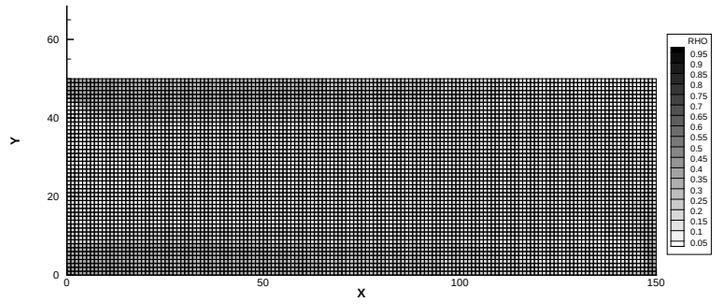

(a) 20th iteration.

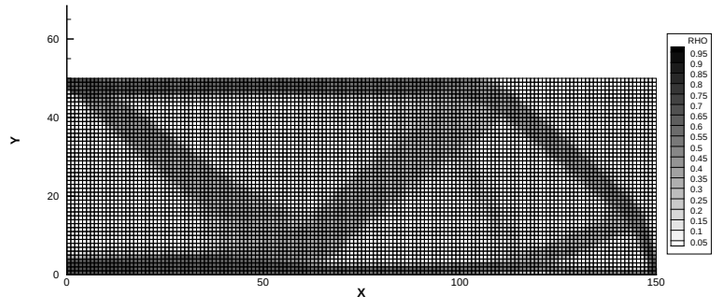

(b) 50th iteration.

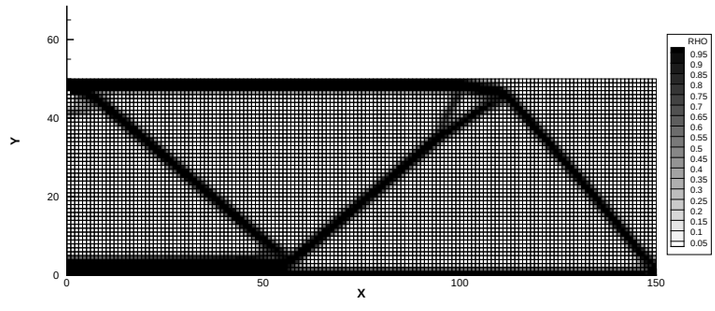

(c) Final iteration (400th iteration).

Figure 3.6: Density distributions of two dimensional MBB beam model at each iteration k when using the OC method ($\rho_{\mathrm{move}} = 0.01$).

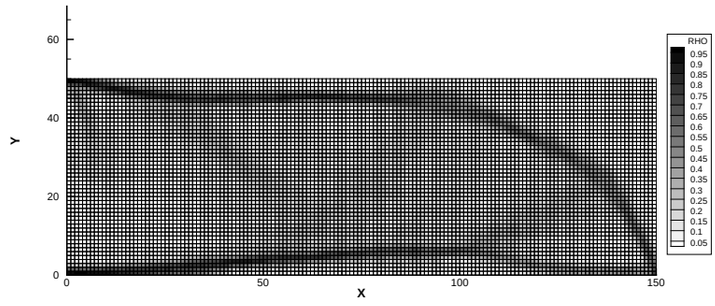

(a) 20th iteration.

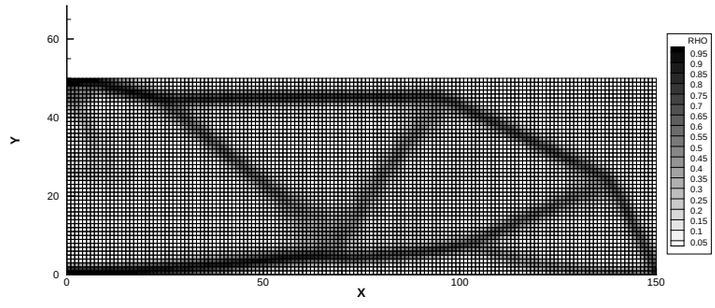

(b) 50th iteration.

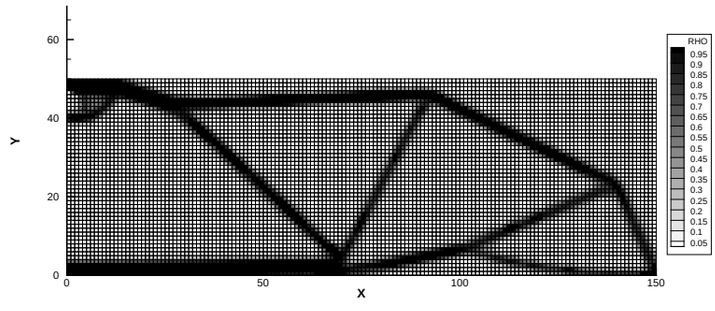

(c) Final iteration (400th iteration).

Figure 3.7: Density distributions of two dimensional MBB beam model at each iteration k when using the OC method ($\rho_{\text{move}} = 0.30$).

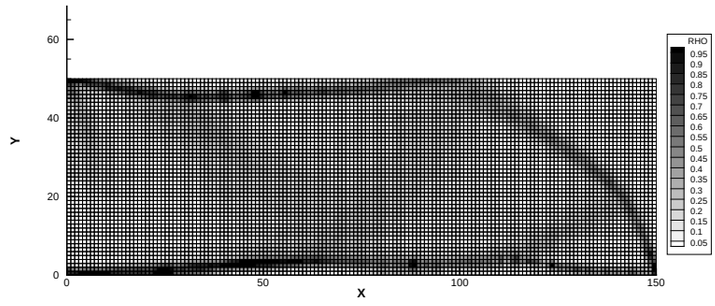

(a) 20th iteration.

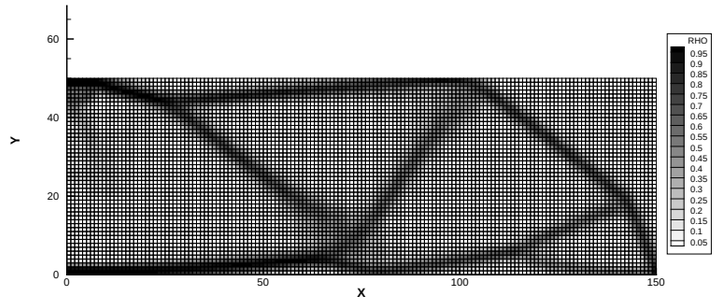

(b) 50th iteration.

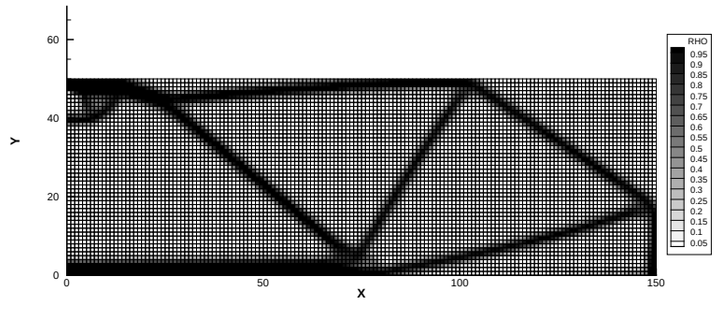

(c) Final iteration (400th iteration).

Figure 3.8: Density distributions of two dimensional MBB beam model at each iteration k when using the OC method ($\rho_{\mathrm{move}} = 1.00$).

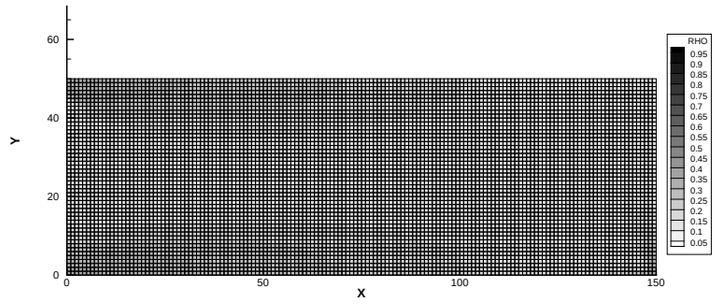

(a) 20th iteration.

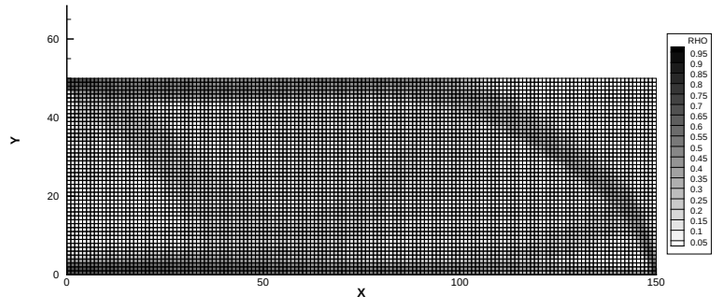

(b) 50th iteration.

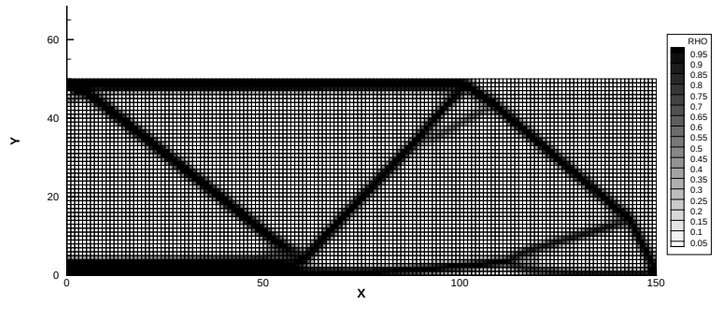

(c) Final iteration (400th iteration).

Figure 3.9: Density distributions of two dimensional MBB beam model at each iteration k when using the MMN–modified OC method ($\rho_{\mathrm{move}} = 0.01$).

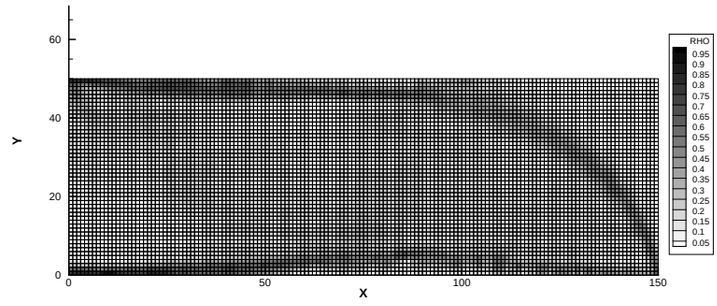

(a) 20th iteration.

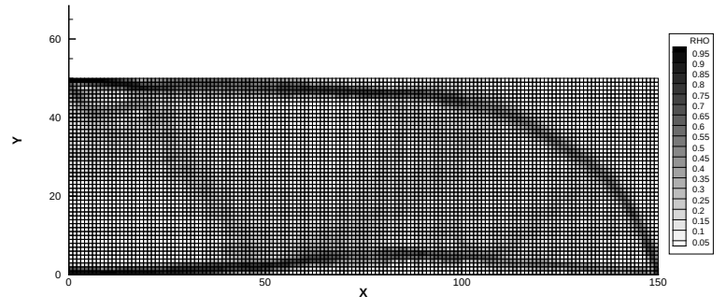

(b) 50th iteration.

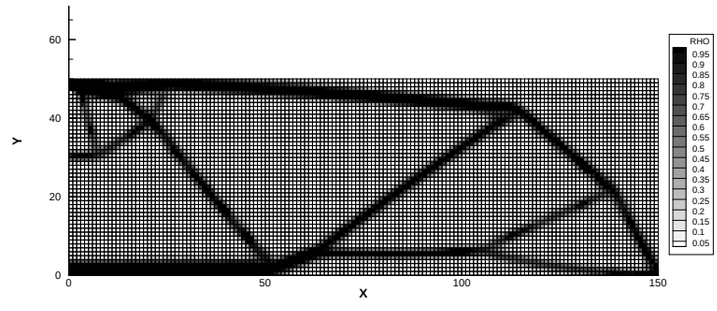

(c) Final iteration (400th iteration).

Figure 3.10: Density distributions of two dimensional MBB beam model at each iteration k when using the MMN–modified OC method ($\rho_{\text{move}} = 0.30$).

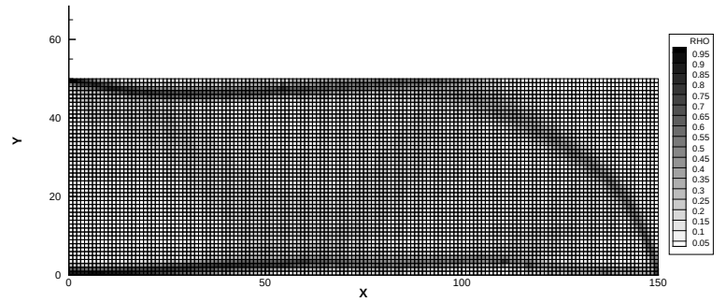

(a) 20th iteration.

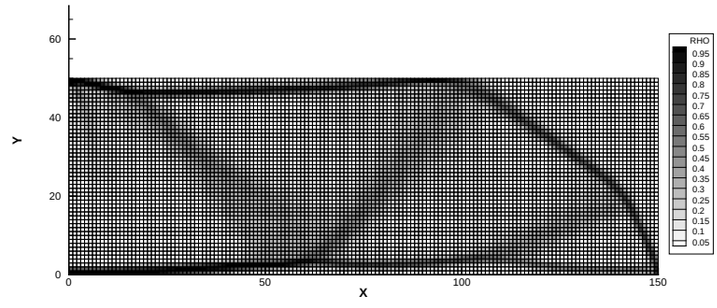

(b) 50th iteration.

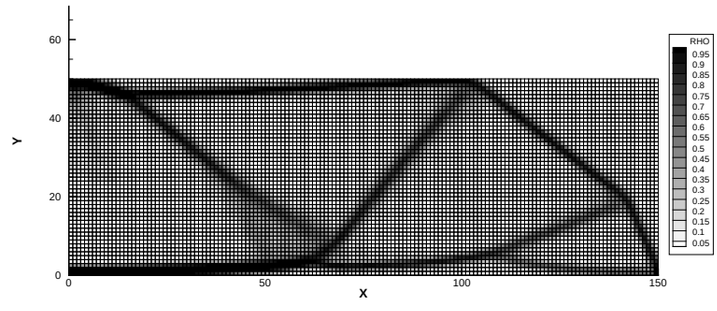

(c) Final iteration (400th iteration).

Figure 3.11: Density distributions of two dimensional MBB beam model at each iteration k when using the MMN–modified OC method ($\rho_{\text{move}} = 1.00$).

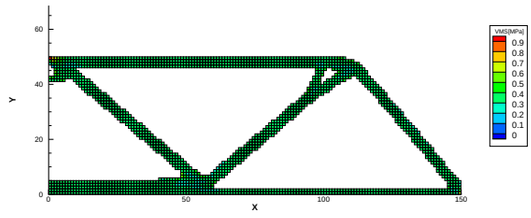

(a) When using the OC method ($\rho_{\text{move}} = 0.01$).

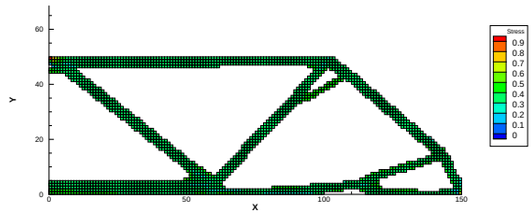

(b) When using the MMN–modified OC method ($\rho_{\text{move}} = 0.01$).

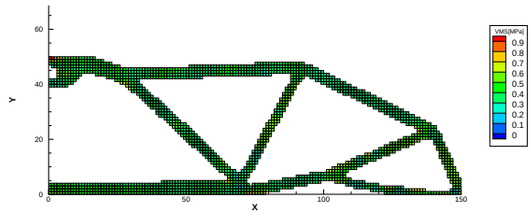

(c) When using the OC method ($\rho_{\text{move}} = 0.30$).

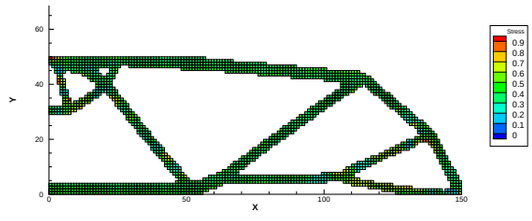

(d) When using the MMN–modified OC method ($\rho_{\text{move}} = 0.30$).

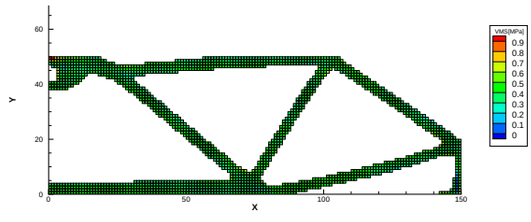

(e) When using the OC method ($\rho_{\text{move}} = 1.00$).

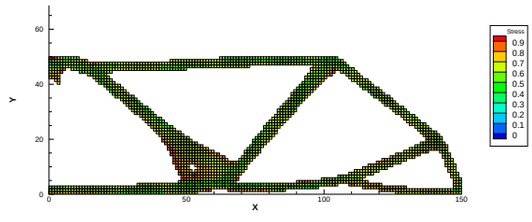

(f) When using the MMN–modified OC method ($\rho_{\text{move}} = 1.00$).

Figure 3.12: Von Mises stress distributions of two dimensional MBB beam model at final iteration.

Table 3.3: MSE for final density distribution on the MBB beam model.

Move-limit ρ_{move}	0.30	1.00
MSE when using the OC method	0.1748	0.1280
MSE when using the MMN–modified OC method	0.1290	0.0985

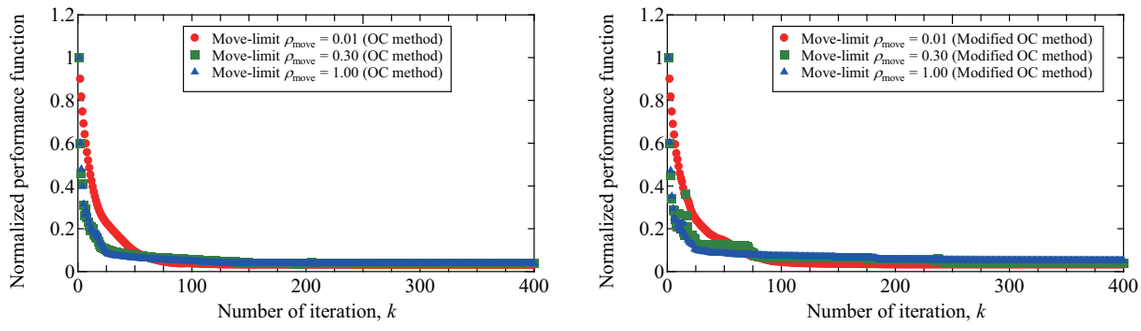

(a) When using the OC method. (b) When using the MMN–modified OC method.

Figure 3.13: The history of normalized performance functions in the two dimensional MBB beam model.

Table 3.4: Normalized performacne function at final iteration in topology optimization for von Mises stress minimization in the MBB beam model for the two dimensional static problem.

Update method	Move-limit ρ_{move}	Normalized performance function
OC	0.01	0.032
OC	0.30	0.039
OC	1.00	0.038
Modified OC	0.01	0.034
Modified OC	0.30	0.038
Modified OC	1.00	0.038

Next, the results of topology optimization for hook model shown in Figure 3.4(b) is discussed. Figures 3.14 to 3.16 show the density distribution obtained by topology optimization when using the OC method. Sub caption (a) in these figures shows the density distribution at $k = 20$ and (b) shows the density distribution at $k = 500$. In addition, Figures 3.17 to 3.19 show the density distribution obtained by topology optimization when using the MMN modified OC method. Similarly, (a) and (b) in these figures show the density distribution at $k = 20$ and 500. In the density distribution at 20th iterations as shown in (a) of Figures 3.14 to 3.19, as in the results of the MBB beam model, there is numerous grayscale in a density distribution because it is in the process of being updated. In the density distribution at the final iteration as shown in (b) of Figures 3.14 to 3.19, all of the results show a density distribution such as structure. As in the results of the MBB beam model, the density distribution obtained by topology optimization when using the OC method, shown in Figures 3.14 to 3.16, depends on the setting value of the move-limit ρ_{move}. On the other hand, the density distribution obtained by topology optimization when using the OC method, shown in Figures 3.17 to 3.19, is difficult to obtain different density distributions depending on the setting value of the move-limit ρ_{move}. However, although there is less grayscale than results

in the MBB beam model, topology optimization when using the MMN modified OC method confirms that a small amount of grayscale remains within a density distribution. Figure 3.12 shows the von Mises stress distribution at the final iteration obtained by topology optimization when using each update method, eliminating elements with density values less than 0.3. The unit of von Mises stress distributions is [MPa]. Although the obtained density distributions are different, the von Mises stress is higher at the tip of the hook where the load is added, and there is no significantly difference in the von Mises stress distribution. Using Equation (3.37), the MSE for the MBB beam model is calculated. Table 3.3 shows the MSE of the density distribution obtained by topology optimization when the move-limit ρ_{move} is set to 0.30 and 1.00. From Table 3.3, for any move-limit ρ_{move} in the hook model, the MSE of topology optimization when using the MMN modified OC method is smaller than one when using the OC method. Thus, compared to the results of topology optimization when using the OC method, the results of topology optimization when using the MMN modified OC method show that the influence of the move-limit ρ_{move} on the density distribution is smaller. Figure 3.21 shows the history of performance function obtained by topology optimization when using the OC method and the MMN modified OC method. In Figure 3.21(a), the performance functions are constant between the 100th to 200th iterations, but decreases between the 200th to 300th iterations. It then converges again to a constant value. The same trend was observed in history of performance function obtained by topology optimization when using the MMN modified OC method, shown in Figure 3.21(b). In addition, Table 3.6 shows that the value of normalized performance fucntion at convergence when using the MMN modified OC method was as same as the value when using the OC method. This is due to the complexity of the hook model compared to the MBB beam model and the normalization based on the modified Newton's method. In addition, convergence at the primary time point is not convergent because there are numerous grayscale in the density distribution.

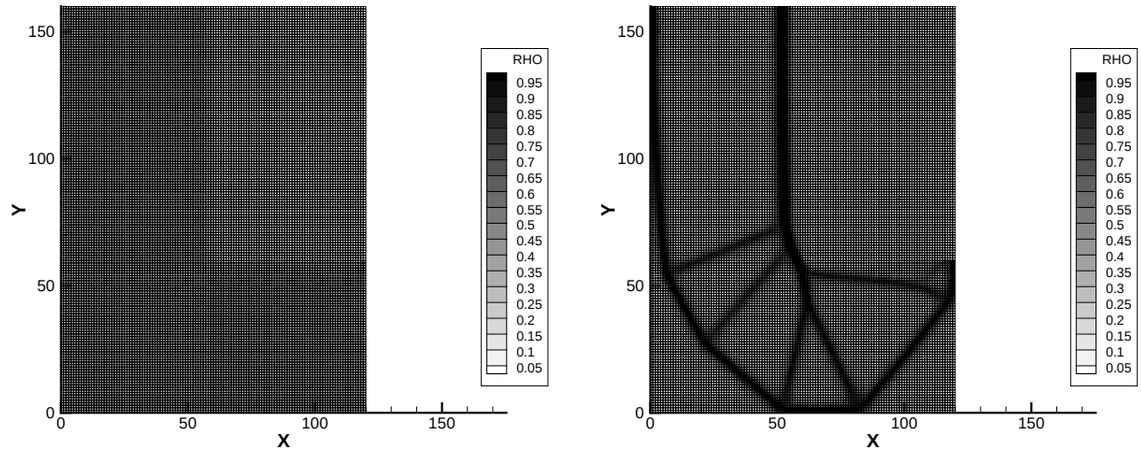

(a) 20th iteration. (b) Final iteration (500th iteration).

Figure 3.14: Density distributions of two dimensional hook model at each iteration k when using the OC method ($\rho_{\text{move}} = 0.01$).

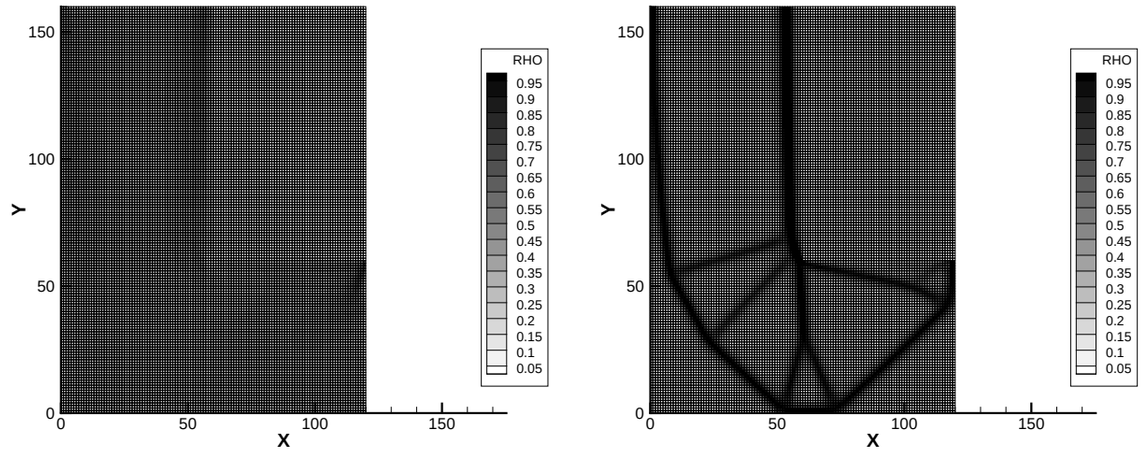

(a) 20th iteration. (b) Final iteration (500th iteration).

Figure 3.15: Density distributions of two dimensional hook model at each iteration k when using the OC method ($\rho_{\text{move}} = 0.30$).

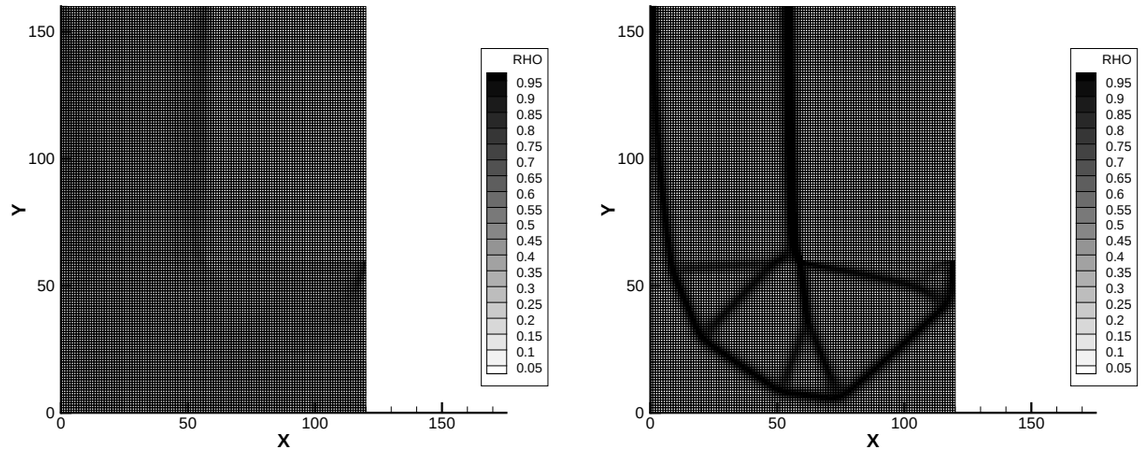

(a) 20th iteration. (b) Final iteration (500th iteration).

Figure 3.16: Density distributions of two dimensional hook model at each iteration k when using the OC method ($\rho_{\text{move}} = 1.00$).

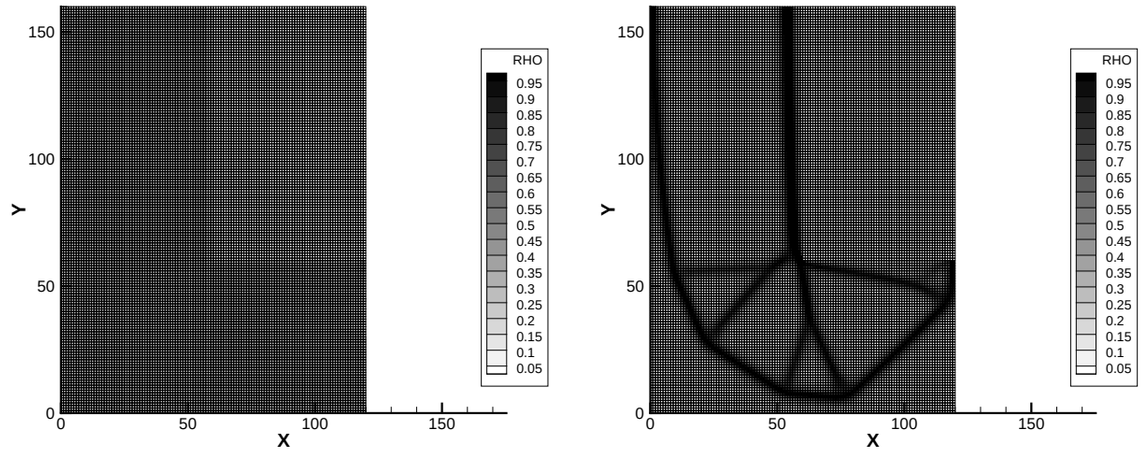

(a) 20th iteration. (b) Final iteration (500th iteration).

Figure 3.17: Density distributions of two dimensional hook model at each iteration k when using the MMN–modified OC method ($\rho_{\text{move}} = 0.01$).

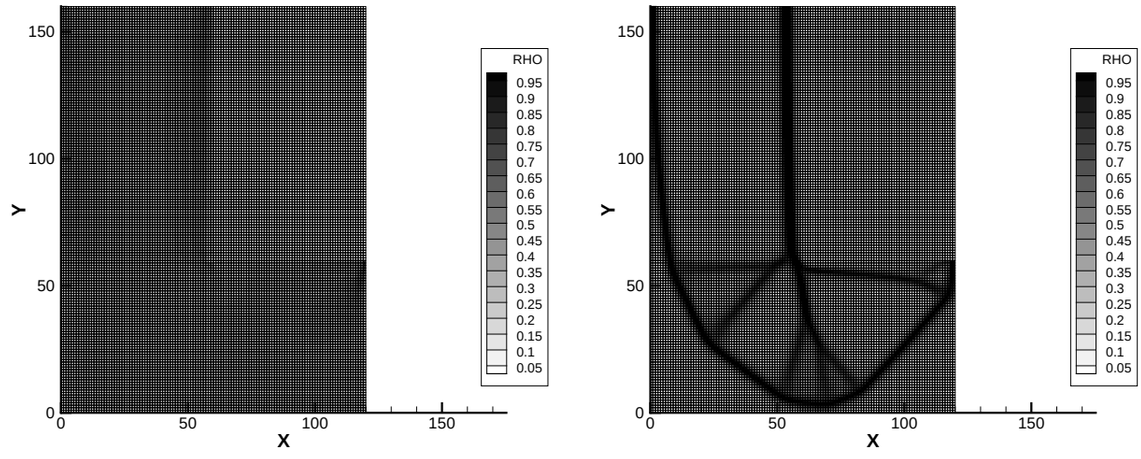

(a) 20th iteration. (b) Final iteration (500th iteration).

Figure 3.18: Density distributions of two dimensional hook model at each iteration k when using the MMN–modified OC method ($\rho_{\text{move}} = 0.30$).

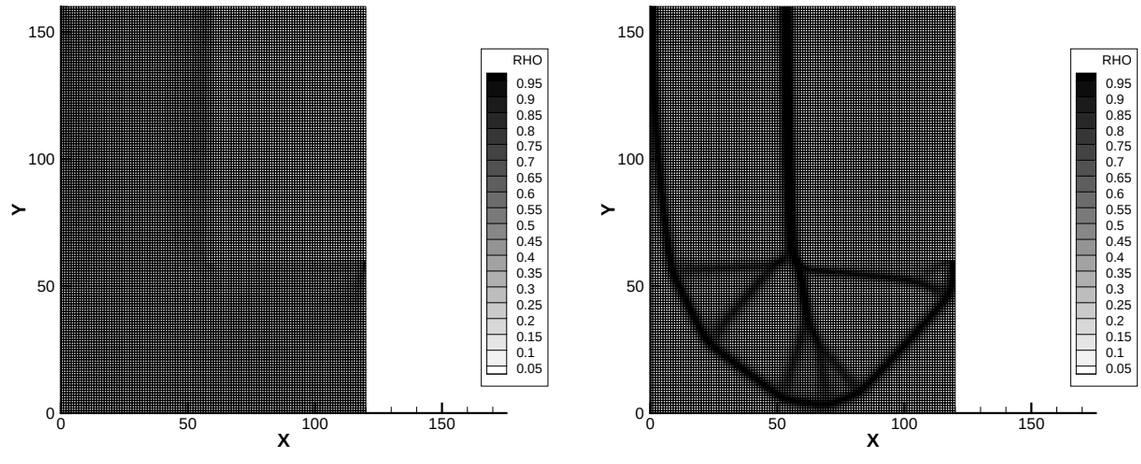

(a) 20th iteration. (b) Final iteration (500th iteration).

Figure 3.19: Density distributions of two dimensional hook model at each iteration k when using the MMN–modified OC method ($\rho_{\text{move}} = 1.00$).

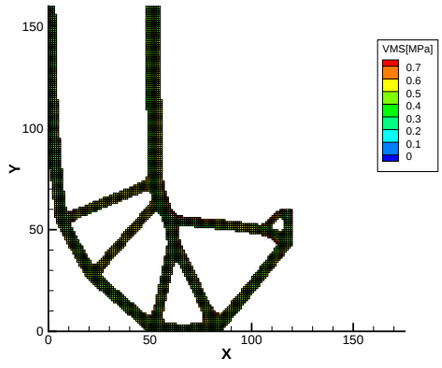

(a) When using the OC method ($\rho_{\text{move}} = 0.01$).

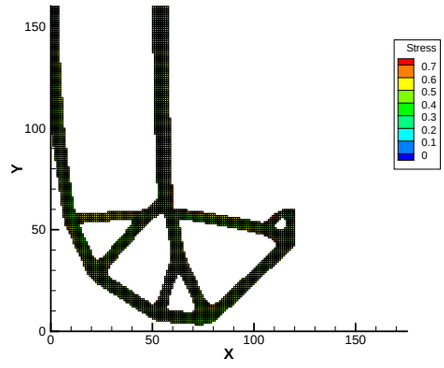

(b) When using the MMN–modified OC method ($\rho_{\text{move}} = 0.01$).

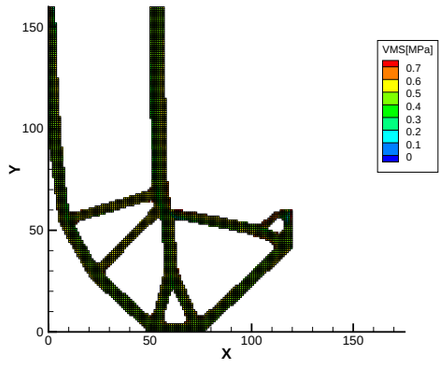

(c) When using the OC method ($\rho_{\text{move}} = 0.30$).

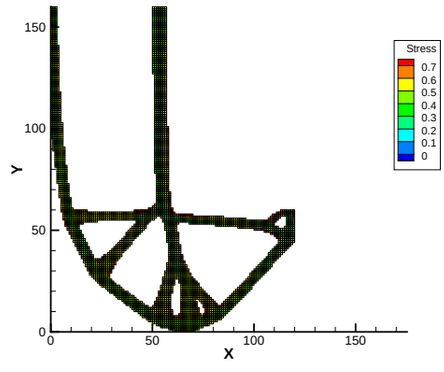

(d) When using the MMN–modified OC method ($\rho_{\text{move}} = 0.30$).

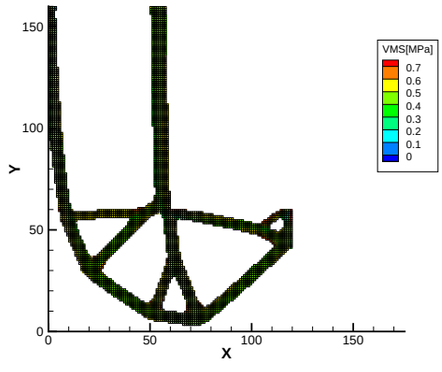

(e) When using the OC method ($\rho_{\text{move}} = 1.00$).

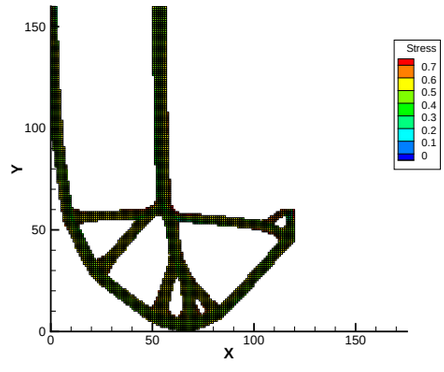

(f) When using the MMN–modified OC method ($\rho_{\text{move}} = 1.00$).

Figure 3.20: Von Mises stress distributions of two dimensional hook model at final iteration.

Table 3.5: MSE for final density distribution on the hook model.

Move-limit ρ_{move}	0.30	1.00
MSE when using the OC method	0.0335	0.0525
MSE when using the MMN–modified OC method	0.0113	0.0096

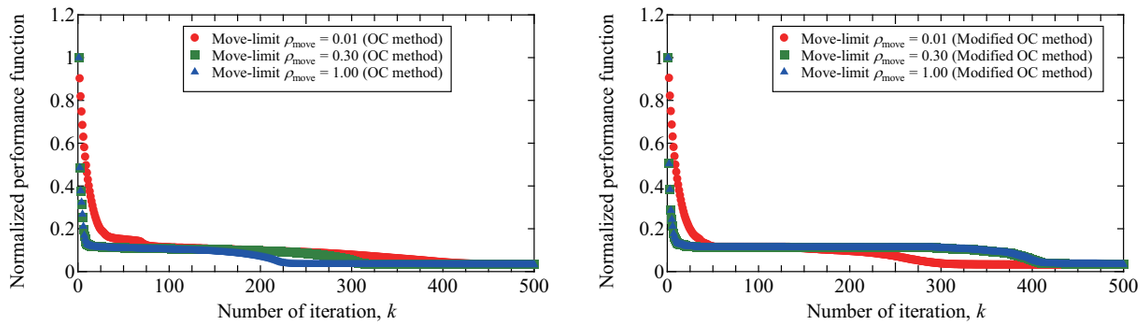

(a) When using the OC method. (b) When using the MMN–modified OC method.

Figure 3.21: The history of normalized performance functions in the two dimensional hook model.

Table 3.6: Normalized performacne function at final iteration in topology optimization for von Mises stress minimization in the hook model for the two dimensional static problem.

Update method	Move-limit ρ_{move}	Normalized performance function
OC	0.01	0.033
OC	0.30	0.033
OC	1.00	0.032
Modified OC	0.01	0.032
Modified OC	0.30	0.033
Modified OC	1.00	0.033

3.5.2 Parametric study for move-limit when using the Min–Max normalized modified optimality criteria method

This sub section describes the results when the modified OC method is employed and the value of the move-limit ρ_{move} is set more finely than in the previous sub section. The move-limit ρ_{move} is set to 0.01, which is the value shown in the previous sub section, plus increasing values in increments of 0.1. Other calculation conditions are same as in the previous sub section. Figures 3.22 and 3.23 show the density distributions obtained by topology optimization for the MBB beam model and the hook model. The density distributions of MBB beam model shown in Figure 3.22(a) and Figures 3.22(g) to (k) are relatively similar. On the other hand, in contrast to the results in the previous section, the density distributions of MBB beam model shown in Figure 3.22(b) to (f) obtained different results. The reasons for this will be discussed later. The hook model results shown in Figure 3.23 confirm that a similar structure is obtained for all move-limit setting. Thus, the von Mises stress minimization problem is difficult to obtain similar density distributions for some models. Next, the history of performance function will be confirmed. Figures 3.24 to 3.25 show the

histories of performance function obtained by topology optimization for each model. The X-axis in the history of performance function is expressed in logarithm. From the history of performance function for the hook model shown in Figure 2.21, it can be confirmed that the history of performance function when the move-limit ρ_{move} is set between 0.01 and 1.00 is generally consistent, although there are some differences. On the other hand, the history of performance function for MBB beam model shown in Figure 3.24 shows that the value of the performance function oscillate at a certain number of iterations, rather than coincide. In other words, it can be inferred that the process of updating the density distribution for each iteration in MBB beam model differs depending on the setting value of the move-limit ρ_{move}. From the history of performance function shown in Figure 3.24(a), the results at the 9th and 10th step in the topology optimization are of interest here when the move-limit $\rho_{\text{move}} = 0.20$. The reason for focusing on this number of iteration is that it is the number of iterations by which the performance function is increased. Figure 3.26 shows the density distributions at $k = 9$ and 10, and Figure 3.27 shows the distribution of von Mises stress, sensitivity distribution and exponent distribution at $k = 9$. From the density distributions shown in Figures 3.26(a) and 3.27(a), it can be confirmed that the element with higher values of density and von Mises stress have higher sensitivity as shown in Figure 3.27(b). Since the sensitivity is the gradient of the Lagrange function with respect to the density tends to increase the density, which is the design variable, in the next iteration. On the other hand, the exponent determining the update length shown in Figure 3.27(c) was significantly higher only for the upper right element and lower for the other elements. This tends to reduce the overall update length. From this, it can be inferred that the reason why similar density distribution was not obtained is that a structure with partially higher stress at certain number of iterations was obtained, which increased the sensitivity and changed the updating process. It is also believed that the restrictions on updating design variables by the move-limit ρ_{move} in the proposed method made it easier to cause this. Therefore, when the move-limit ρ_{move} is set a little higher, such as 0.1 to 0.5, the constraint caused the von Mises stress to take a partially higher form and the performance function ocsillated. On the other hand, when the

move-limit ρ_{move} is set small (0.01) and large (0.6 or more), the von Mises stress does not become partially high and an optimum solution is obtained.

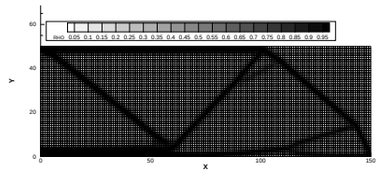

(a) When $\rho_{\text{move}} = 0.01$.

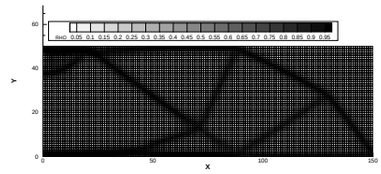

(b) When $\rho_{\text{move}} = 0.10$.

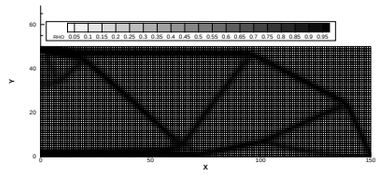

(c) When $\rho_{\text{move}} = 0.20$.

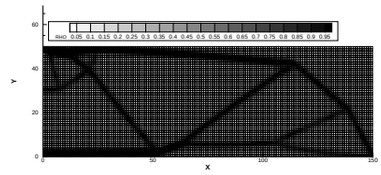

(d) When $\rho_{\text{move}} = 0.30$.

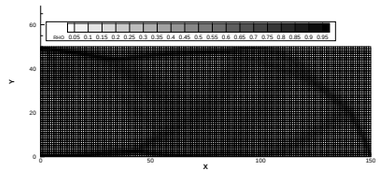

(e) When $\rho_{\text{move}} = 0.40$.

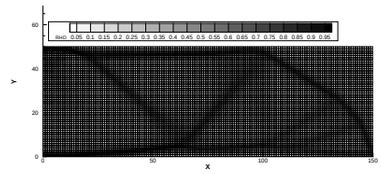

(f) When $\rho_{\text{move}} = 0.50$.

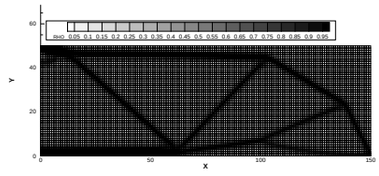

(g) When $\rho_{\text{move}} = 0.60$.

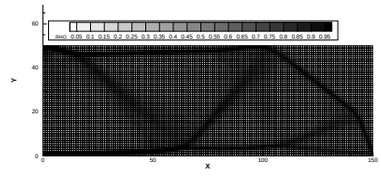

(h) When $\rho_{\text{move}} = 0.70$.

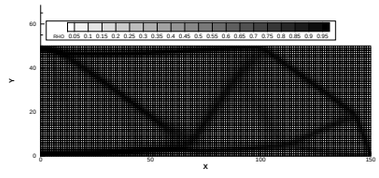

(i) When $\rho_{\text{move}} = 0.80$.

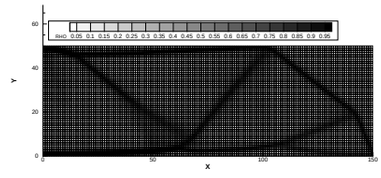

(j) When $\rho_{\text{move}} = 0.90$.

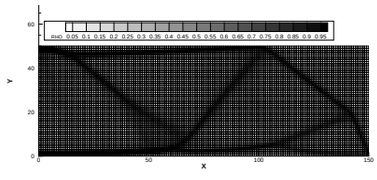

(k) When $\rho_{\text{move}} = 1.00$.

Figure 3.22: Density distributions at convergence of topology optimization for von Mises stress minimization when changing the move-limit ρ_{move} and using the MMN modified OC method in the MBB beam model.

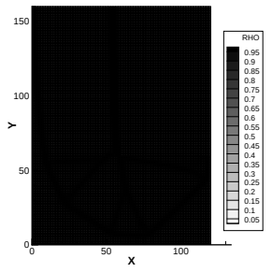

(a) When $\rho_{\text{move}} = 0.01$.

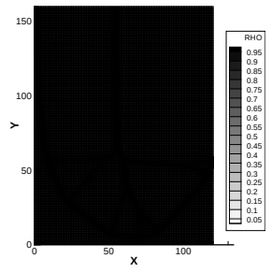

(b) When $\rho_{\text{move}} = 0.10$.

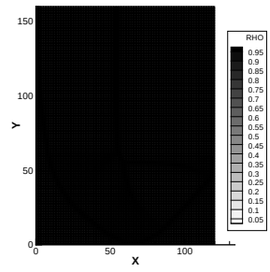

(c) When $\rho_{\text{move}} = 0.20$.

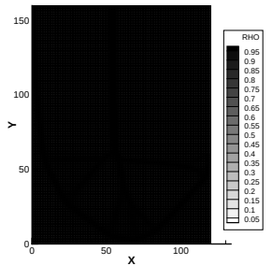

(d) When $\rho_{\text{move}} = 0.30$.

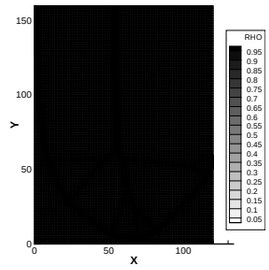

(e) When $\rho_{\text{move}} = 0.40$.

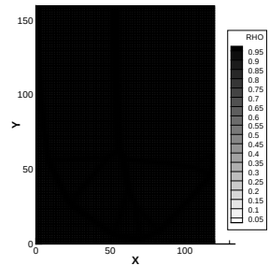

(f) When $\rho_{\text{move}} = 0.50$.

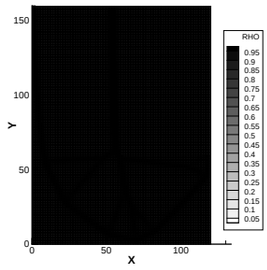

(g) When $\rho_{\text{move}} = 0.60$.

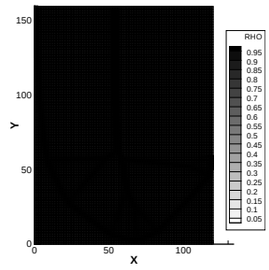

(h) When $\rho_{\text{move}} = 0.70$.

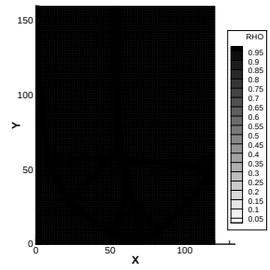

(i) When $\rho_{\text{move}} = 0.80$.

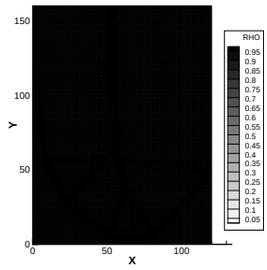

(j) When $\rho_{\text{move}} = 0.90$.

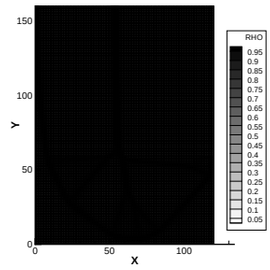

(k) When $\rho_{\text{move}} = 1.00$.

Figure 3.23: Density distributions at convergence of topology optimization for von Mises stress minimization when changing the move-limit ρ_{move} and using the MMN modified OC method in the hook model.

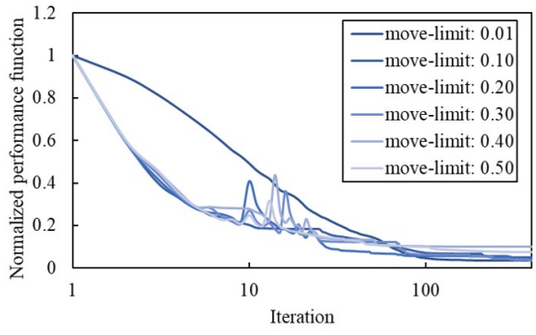

(a) When $\rho_{\text{move}} = 0.01, 0.10, 0.20,$ $0.30, 0.40$ and 0.50.

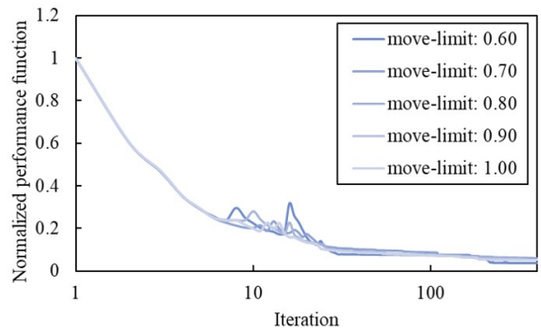

(b) When $\rho_{\text{move}} = 0.60, 0.70, 0.80,$ 0.90 and 1.00.

Figure 3.24: The history of normalized performance function when changing the move-limit ρ_{move} and using the MMN modified OC method in the MBB beam model.

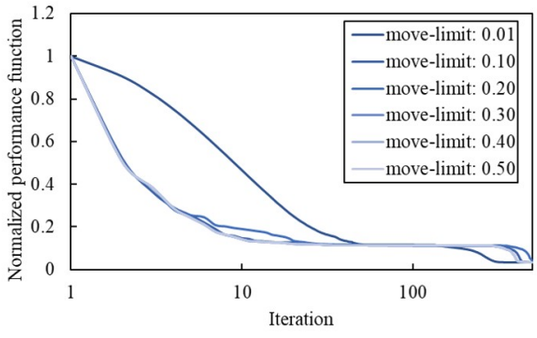

(a) When $\rho_{\text{move}} = 0.01, 0.10, 0.20,$ $0.30, 0.40$ and 0.50.

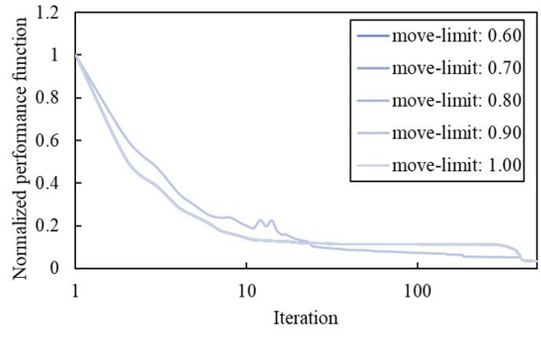

(b) When $\rho_{\text{move}} = 0.60, 0.70, 0.80,$ 0.90 and 1.00.

Figure 3.25: The history of normalized performance function when changing the move-limit ρ_{move} and using the MMN modified OC method in the hook model.

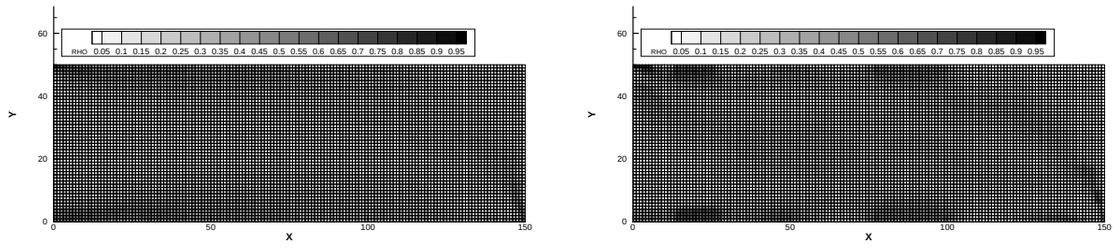

(a) When iteration $k = 9$. (b) When iteration $k = 10$.

Figure 3.26: Density distributions of topology optimization for von Mises stress minimization when using the MMN modified OC method ($\rho_{\text{move}} = 0.20$) in the MBB beam model.

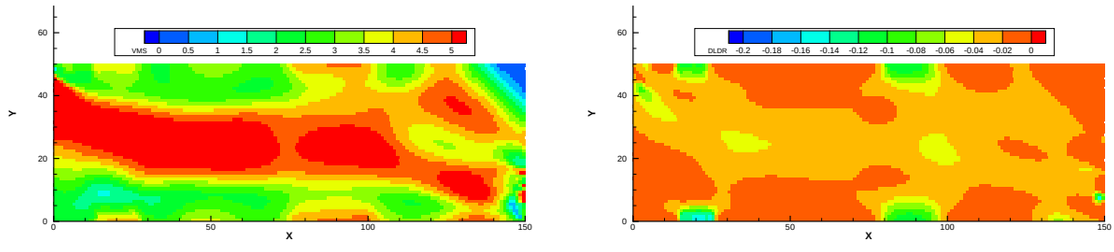

(a) Von Mises stress distribution. (b) Sensitivity distribution.

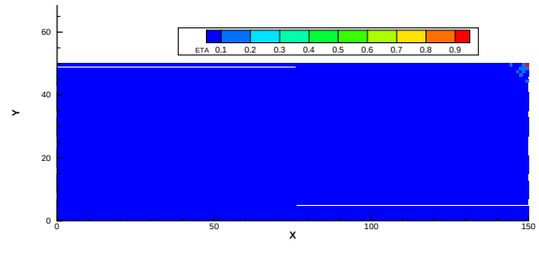

(c) Distribution of exponent.

Figure 3.27: Each distribution of topology optimization at 9th iteration for von Mises stress minimization when using the MMN modified OC method ($\rho_{\text{move}} = 0.20$) in the MBB beam model.

3.5.3 Result of topology optimization in three dimensional steady problems

This subsection describes the results of density-based topology optimization for von Mises stress minimization in three dimensional problems. Similar to the topology optimization for strain energy minimization described in the previous chapter, based on the results of topology optimization for von Mises stress minimization in two dimensional problem described in the previous subsection, the topology optimization when using the OC method and the MMN modified OC method is performed. The move-limit ρ_{move} is set to 0.01 when using the OC method and 1.00 when using the MMN modified OC method. The calculation models are the MBB beam model and hook model shown in Figure 3.5. First, the result of topology optimization in the MBB beam model is described. Figure 3.28 shows the density distribution obtained by the OC method, and Figure 3.29 shows the density distribution obtained by the MMN modified OC method. Sub caption (a) in Figures 3.28 and 3.29 shows the isometric view of density distribution at the final iteration, (b) shows the side view at the final iteration, and (c) shows the isometric view at 50th iterations. In addition, since this is a three dimensional model, elements with a density value of 0.5 or less are eliminated in (a) and (b) of these figures, and elements with a density value of 0.3 or less are eliminated in (c) to make it easier to check the depth direction. From Figures 3.28 and 3.29, it can be seen that different density distributions are obtained. As shown in Figure 3.30, the only major difference is in density distribution, and no significant difference in von Mises stress distribution. Here, too, elements with density values less than 0.5 are eliminated, and the unit of von Mises stress is [MPa]. However, the history of performance function shown in Figure 3.31 confirms that the MMN modified OC method has a faster drop in the performance function than the OC method. In addition, Table 3.7 shows that the value of normalized performance fucntion at convergence when using the modified OC method was slightly smaller than the value when using the OC method. In the results for three dimensional model, although it is difficult to distinguish between update methods,

the MMN modified OC method has a clearer density distribution at 50th iterations, and a smaller performance function.

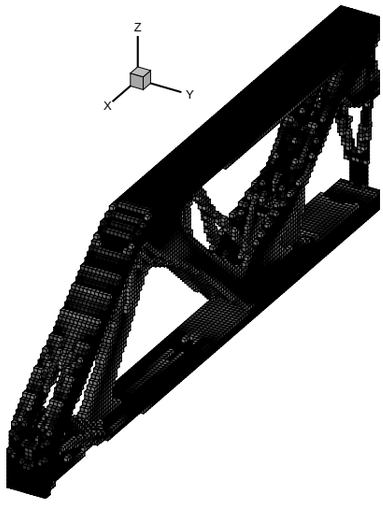

(a) Isometric view at final iteration.

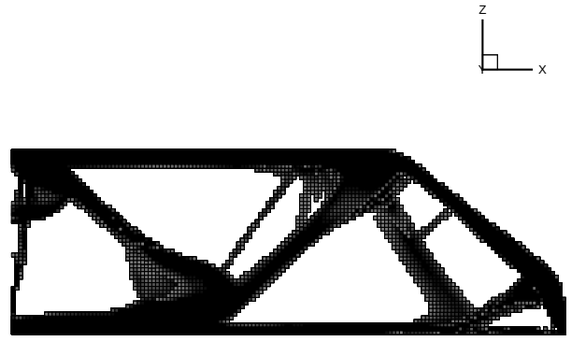

(b) Side view at final iteration.

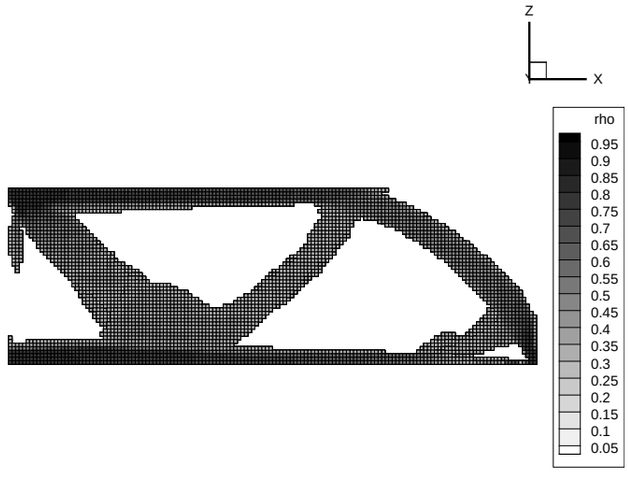

(c) Side view at 50th iteration.

Figure 3.28: Density distributions of three dimensional MBB beam model at each iteration k when using the OC method ($\rho_{\text{move}} = 0.01$).

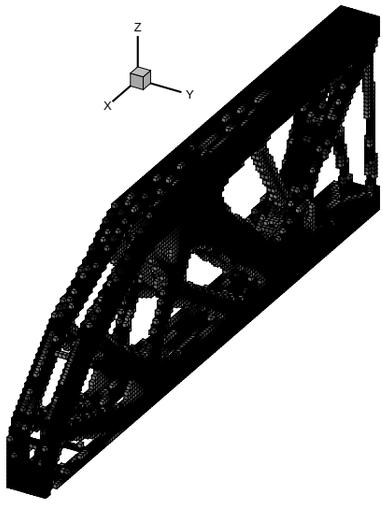

(a) Isometric view at final iteration.

(b) Side view at final iteration.

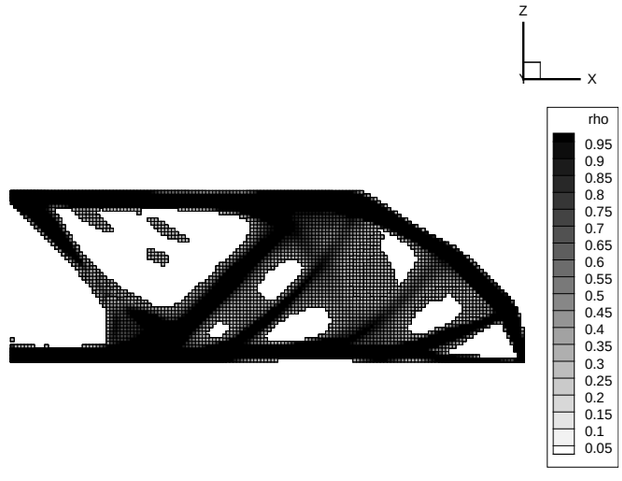

(c) Side view at 50th iteration.

Figure 3.29: Density distributions of three dimensional MBB beam model at each iteration k when using the MMN–modified OC method ($\rho_{\text{move}} = 1.00$).

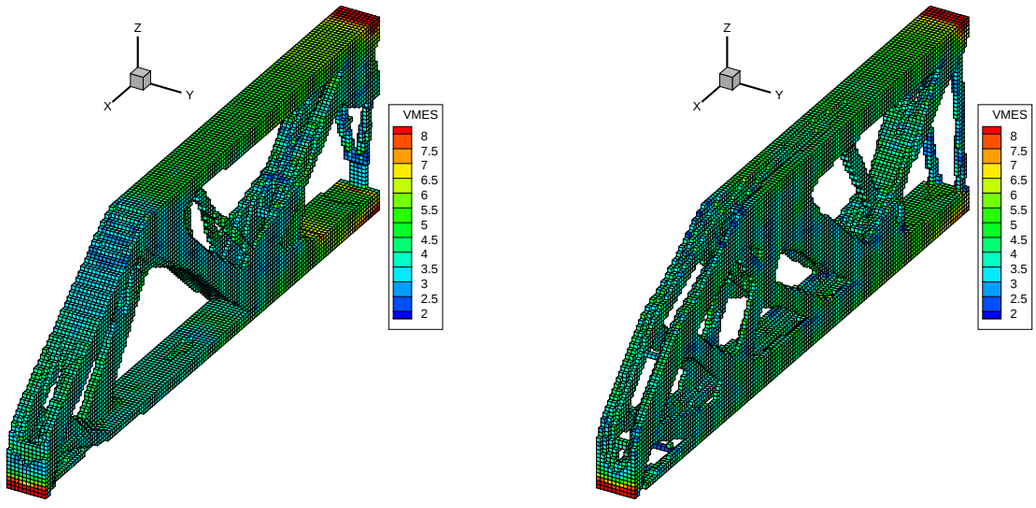

(a) When using the OC method. (b) When using the MMN–modified OC method.

Figure 3.30: Von Mises stress distributions of three dimensional MBB beam model at final iteration.

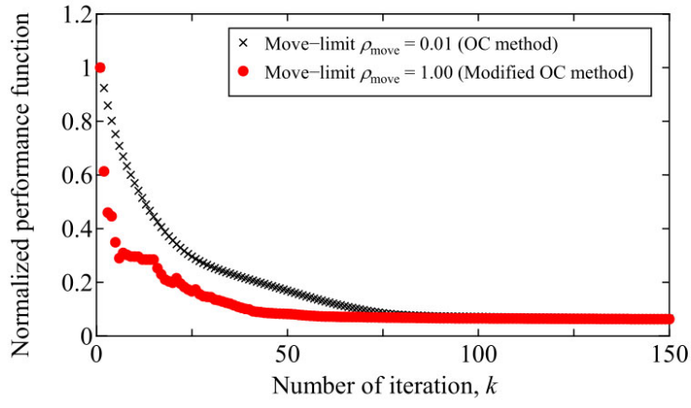

Figure 3.31: The history of normalized performance function in the topology optimization for von Mises stress minimization in the MBB beam model for the three dimensional static problem.

Table 3.7: Normalized performacne function at final iteration in topology optimization for von Mises stress minimization in the MBB beam model for the three dimensional static problem.

Update method	Move-limit ρ_{move}	Normalized performance function
OC	0.01	0.065
Modified OC	1.00	0.063

Next, the results of topology optimization in the hook model is described. As in the results for MBB beam model described above, Figure 3.32 shows the density distribution obtained by topology opitmization when using the OC method, and Figure 3.33 shows the density distribution obtained by topology opitmization when using the MMN modified OC method. Sub caption (a) in Figures 3.32 and 3.33 shows the isometric view of density distribution at the final iteration, (b) shows the side view at the final iteration, and (c) shows the isometric view at 50th iterations. In addition, since this is a three dimensional model, elements with a density value of 0.5 or less are eliminated in (a) and (b) of these figures, and elements with a density value of 0.3 or less are eliminated in (c) to make it easier to check the depth direction. From Figures 3.32 and 3.33, similar to the density distribution for strain energy minimization in three dimensional problems, the density distribution obtained by topology optimization when using the OC method yields a structure like a hollow, while the density distribution obtained by topology optimization when using the MMN modified OC method yields a structure like a solid. Figure 3.34 shows the von Mises stress distributions. Here, too, elements with density values less than 0.5 are eliminated, and the unit of von Mises stress is [MPa]. From Figure 3.34, the von Mises stress distribution obtained by topology optimization when using the MMN modified OC method tends to be slightly higher than one when using the OC method. It can be assumed that this is due to the grayscale distributed on the surface of structure, which tends to make the stresses appear slightly higher. However, the history of performance function shown in Figure 3.31 confirms that the MMN modified

OC method has a faster drop in the performance function than the OC method. In addition, Table 3.8 shows that the value of normalized performance fucntion at convergence when using the modified OC method was slightly smaller than the value when using the OC method. The MMN modified OC method has the advantages that the performance function decreased rapidly and does not require the setting of the weighting factor η and the move-limit ρ_{move}, which are arbitrary parameters. On the other hand, some grayscale may remain depending on the calculation model. In addition, based on the previous chapter, the OC method and the modified OC method are difficult to determine the convergence conditions.

(a) Isometric view at final iteration.

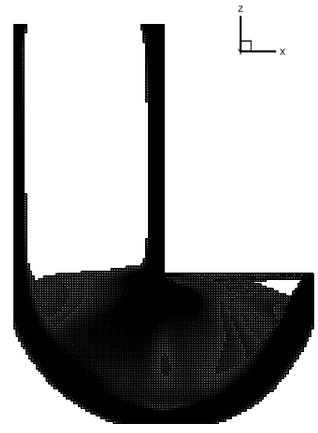

(b) Side view at final iteration.

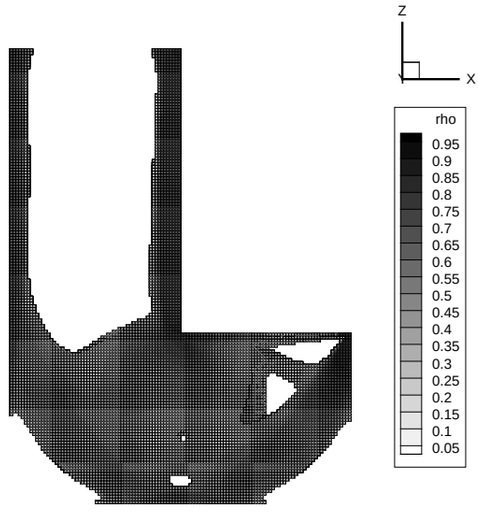

(c) Side view at 50th iteration.

Figure 3.32: Density distributions of three dimensional hook model at each iteration k when using the OC method ($\rho_{\text{move}} = 0.01$).

(a) Isometric view at final iteration.

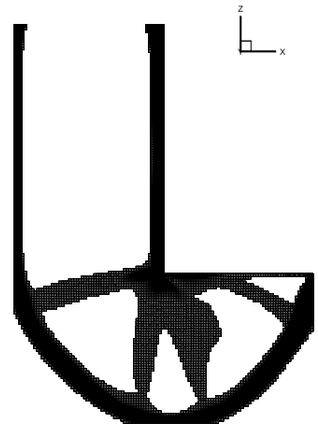

(b) Side view at final iteration.

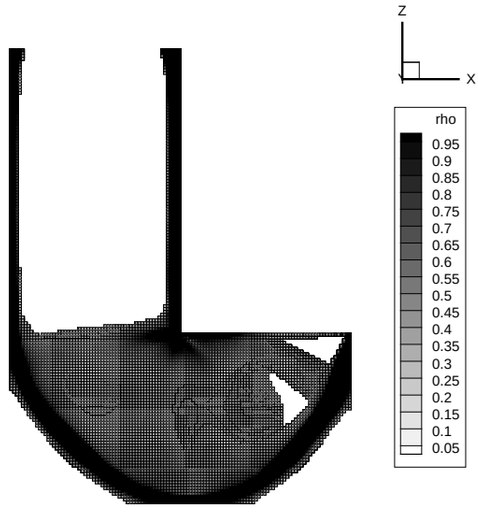

(c) Side view at 50th iteration.

Figure 3.33: Density distributions of three dimensional hook model at each iteration k when using the MMN–modified OC method ($\rho_{\text{move}} = 1.00$).

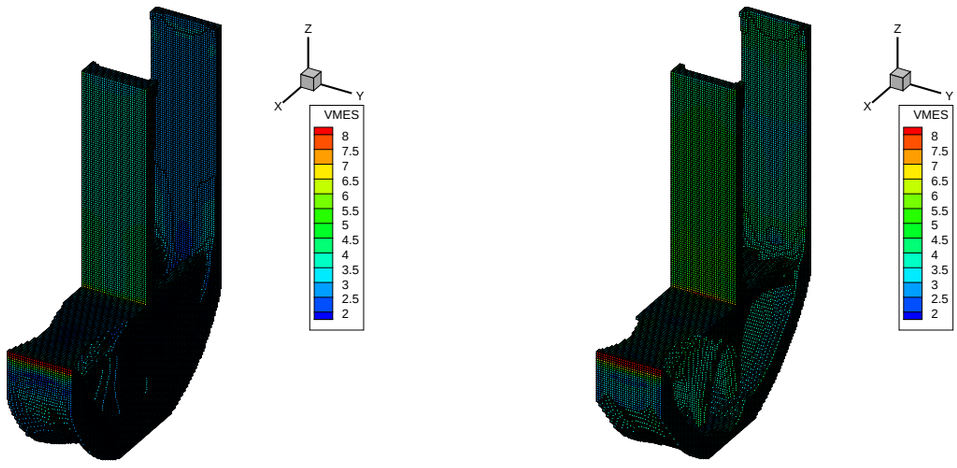

(a) When using the OC method. (b) When using the MMN–modified OC method.

Figure 3.34: Von Mises stress distributions of three dimensional hook model at final iteration.

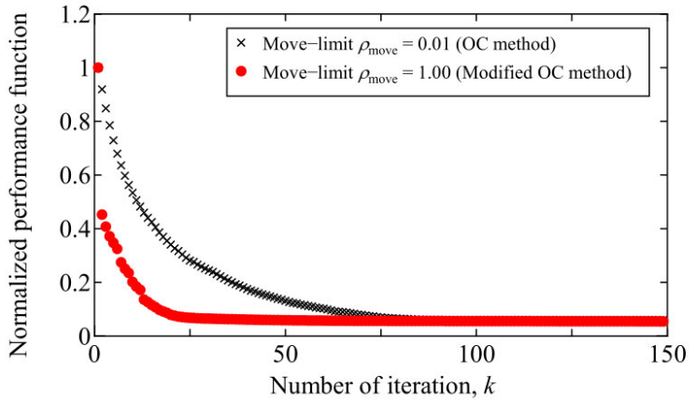

Figure 3.35: The history of normalized performance function in the topology optimization for von Mises stress minimization in the hook model for the three dimensional static problem.

Table 3.8: Normalized performacne function at final iteration in topology optimization for von Mises stress minimization in the hook model for the three dimensional static problem.

Update method	Move-limit ρ_{move}	Normalized performance function
OC	0.01	0.060
Modified OC	1.00	0.055

3.5.4 Considerations on the convergence characteristics of the modified optimality criteria method

This subsection will consider mathematical proofs of the convergence properties of the modified OC method. In providing a mathematical proof for the modified OC method, the proof of the convergence property for Newton's method was used as references[75, 76, 77]. First, the general equation of the modified OC method is shown as

$$\rho_{\langle e\rangle}^{(k+1)} = \rho_{\langle e\rangle}^{(k)} \left(A_{\langle e\rangle}^{(k)}\right)^{\left(-\frac{\partial}{\partial \rho_{\langle e\rangle}}\left(\ln A_{\langle e\rangle}^{(k)}\right)\right)^{-1}} \tag{3.38}$$

Taking the natural logarithm on both sides of Equation (3.38), it is obtained.

$$\ln \rho_{\langle e\rangle}^{(k+1)} = \ln \rho_{\langle e\rangle}^{(k)} + \left(-\frac{\partial}{\partial \rho_{\langle e\rangle}}\left(\ln A_{\langle e\rangle}^{(k)}\right)\right)^{-1} \ln A_{\langle e\rangle}^{(k)} \tag{3.39}$$

Next, the residual $\epsilon_\rho^{(k)}$ between the density at k-th iterations $\rho_{\langle e\rangle}^{(k)}$ and a certain solution $\rho_{\langle e\rangle}^{*}$ is defined as

$$\epsilon_\rho^{(k)} = \rho_{\langle e\rangle}^{(k)} - \rho_{\langle e\rangle}^{*} \tag{3.40}$$

To simply the notation, $\ln A_{\langle e\rangle}^{(k)}$ is replaced by f, and the gradient of $\ln A_{\langle e\rangle}^{(k)}$ with respect to the density $\rho_{\langle e\rangle}$ is also replaced by f'. Taylor expansion of the functions f and f', respectively, is calculated as

$$f\left(\rho_{\langle e\rangle}^{*} + \epsilon_\rho^{(k)}\right) = f\left(\rho_{\langle e\rangle}^{*}\right) + \epsilon_\rho^{(k)} f'\left(\rho_{\langle e\rangle}^{*}\right) + \frac{1}{2}{\epsilon_\rho^{(k)}}^2 f''\left(\rho_{\langle e\rangle}^{*}\right) + o\left({\epsilon_\rho^{(k)}}^3\right) \tag{3.41}$$

$$f'\left(\rho^*_{\langle e\rangle}+\epsilon^{(k)}_\rho\right)=f'\left(\rho^*_{\langle e\rangle}\right)+\epsilon^{(k)}_\rho f''\left(\rho^*_{\langle e\rangle}\right)+\frac{1}{2}{\epsilon^{(k)}_\rho}^2 f'''\left(\rho^*_{\langle e\rangle}\right)+o\left({\epsilon^{(k)}_\rho}^3\right) \tag{3.42}$$

where o is a term of higher order than the third order. Using Equations (3.41) and (3.42), the second term of Equation (3.39) is expanded as

$$\begin{aligned}\frac{\ln A^{(k)}_{\langle e\rangle}}{\frac{\partial}{\partial\rho_{\langle e\rangle}}\left(\ln A^{(k)}_{\langle e\rangle}\right)} &= \frac{f\left(\rho^*_{\langle e\rangle}+\epsilon^{(k)}_\rho\right)}{f'\left(\rho^*_{\langle e\rangle}+\epsilon^{(k)}_\rho\right)}\\ &= \frac{\frac{f\left(\rho^*_{\langle e\rangle}\right)}{f'\left(\rho^*_{\langle e\rangle}\right)}+\epsilon^{(k)}_\rho+\frac{1}{2}{\epsilon^{(k)}_\rho}^2\frac{f''\left(\rho^*_{\langle e\rangle}\right)}{f'\left(\rho^*_{\langle e\rangle}\right)}+o\left({\epsilon^{(k)}_\rho}^3\right)}{1+\epsilon^{(k)}_\rho\frac{f''\left(\rho^*_{\langle e\rangle}\right)}{f'\left(\rho^*_{\langle e\rangle}\right)}+\frac{1}{2}{\epsilon^{(k)}_\rho}^2\frac{f'''\left(\rho^*_{\langle e\rangle}\right)}{f'\left(\rho^*_{\langle e\rangle}\right)}+o\left({\epsilon^{(k)}_\rho}^3\right)}\end{aligned} \tag{3.43}$$

Using the Maclaurin expansion of $\frac{1}{1+x}$, Equation (3.43) is re-expanded as

$$\begin{aligned}&\frac{\ln A^{(k)}_{\langle e\rangle}}{\frac{\partial}{\partial\rho_{\langle e\rangle}}\left(\ln A^{(k)}_{\langle e\rangle}\right)}\\ =\;&\left(\frac{f\left(\rho^*_{\langle e\rangle}\right)}{f'\left(\rho^*_{\langle e\rangle}\right)}+\epsilon^{(k)}_\rho+{\epsilon^{(k)}_\rho}^2\frac{f''\left(\rho^*_{\langle e\rangle}\right)}{2f'\left(\rho^*_e\right)}+o\left({\epsilon^{(k)}_\rho}^3\right)\right)\\ &\times\left(1-\left(\epsilon^{(k)}_\rho\frac{f''\left(\rho^*_{\langle e\rangle}\right)}{f'\left(\rho^*_{\langle e\rangle}\right)}+{\epsilon^{(k)}_\rho}^2\frac{f'''\left(\rho^*_{\langle e\rangle}\right)}{2f'\left(\rho^*_{\langle e\rangle}\right)}\right)+\left(\epsilon^{(k)}_\rho\frac{f''\left(\rho^*_e\right)}{f'\left(\rho^*_{\langle e\rangle}\right)}\right)^2+o\left({\epsilon^{(k)}_\rho}^3\right)\right)\\ =\;&\frac{f\left(\rho^*_{\langle e\rangle}\right)}{f'\left(\rho^*_{\langle e\rangle}\right)}+\epsilon^{(k)}_\rho\left(1-\frac{f\left(\rho^*_{\langle e\rangle}\right)f''\left(\rho^*_{\langle e\rangle}\right)}{f'\left(\rho^*_{\langle e\rangle}\right)^2}\right)\\ &+{\epsilon^{(k)}_\rho}^2\left(-\frac{f''\left(\rho^*_{\langle e\rangle}\right)}{2f'\left(\rho^*_{\langle e\rangle}\right)}-\frac{f\left(\rho^*_{\langle e\rangle}\right)f'''\left(\rho^*_{\langle e\rangle}\right)}{2f'\left(\rho^*_{\langle e\rangle}\right)^2}+\frac{f\left(\rho^*_{\langle e\rangle}\right)f''\left(\rho^*_{\langle e\rangle}\right)^2}{f'\left(\rho^*_{\langle e\rangle}\right)^3}\right)\\ &+o\left({\epsilon^{(k)}_\rho}^3\right)\end{aligned} \tag{3.44}$$

When the function $A_{\langle e\rangle}$ converged to a certain solution, $A_{\langle e\rangle}$ is equal to one. Thus, when $\ln A_{\langle e\rangle}$ is equal to 0, $f\left(\rho^*_{\langle e\rangle}\right)$ in Equation (3.44) becomes 0, and can be rewritten as

$$\frac{\ln A^{(k)}_{\langle e\rangle}}{\frac{\partial}{\partial\rho_{\langle e\rangle}}\left(\ln A^{(k)}_{\langle e\rangle}\right)}=-{\epsilon^{(k)}_\rho}^2\frac{f''\left(\rho^*_{\langle e\rangle}\right)}{2f'\left(\rho^*_{\langle e\rangle}\right)}+\epsilon^{(k)}_\rho+o\left({\epsilon^{(k)}_\rho}^3\right) \tag{3.45}$$

Substituting Equation (3.45) into Equation (3.39), it is obtained

$$\ln \rho_{\langle e\rangle}^{(k+1)} = \ln \rho_{\langle e\rangle}^{(k)} + \frac{f''\left(\rho_{\langle e\rangle}^{*}\right)}{2f'\left(\rho_{\langle e\rangle}^{*}\right)}{\epsilon_{\rho}^{(k)}}^{2} - \epsilon_{\rho}^{(k)} + o\left({\epsilon_{\rho}^{(k)}}^{3}\right) \tag{3.46}$$

Transposing the first term on the right side of Equation (3.46) to the left side and back to the true numbers, it is obtained

$$\frac{\rho_{\langle e\rangle}^{(k+1)}}{\rho_{\langle e\rangle}^{(k)}} = \exp\left(\frac{f''\left(\rho_{\langle e\rangle}^{*}\right)}{2f'\left(\rho_{\langle e\rangle}^{*}\right)}{\epsilon_{\rho}^{(k)}}^{2} - \epsilon_{\rho}^{(k)} + o\left({\epsilon_{\rho}^{(k)}}^{3}\right)\right) \tag{3.47}$$

Equation (3.47) organizes the $k+1$-th variable on the left side and the k-th variable on the right side. After that, subtracting both sides by a certain solution $\rho_{\langle e\rangle}$, it can be obtained

$$\rho_{\langle e\rangle}^{(k+1)} - \rho_{\langle e\rangle}^{*} = \rho_{\langle e\rangle}^{(k)} \cdot \exp\left(\frac{f''\left(\rho_{\langle e\rangle}^{*}\right)}{2f'\left(\rho_{\langle e\rangle}^{*}\right)}{\epsilon_{\rho}^{(k)}}^{2} - \epsilon_{\rho}^{(k)} + o\left({\epsilon_{\rho}^{(k)}}^{3}\right)\right) - \rho_{\langle e\rangle}^{*} \tag{3.48}$$

Using Equation (3.40), the left side of Equation (3.46) is expressed in term of $k+1$-th residuals $\epsilon_{\rho}^{(k+1)}$, and the right side side prepared to be expressed in term of k-th residuals as well.

$$\begin{aligned}
\epsilon_{\rho}^{(k+1)} &= \rho_{\langle e\rangle}^{(k)} \cdot \exp\left(\frac{f''\left(\rho_{\langle e\rangle}^{*}\right)}{2f'\left(\rho_{\langle e\rangle}^{*}\right)}{\epsilon_{\rho}^{(k)}}^{2} - \epsilon_{\rho}^{(k)} + o\left({\epsilon_{\rho}^{(k)}}^{3}\right)\right) - \rho_{\langle e\rangle}^{*} \\
&\quad + \rho_{\langle e\rangle}^{*} \cdot \exp\left(\frac{f''\left(\rho_{\langle e\rangle}^{*}\right)}{2f'\left(\rho_{\langle e\rangle}^{*}\right)}{\epsilon_{\rho}^{(k)}}^{2} - \epsilon_{\rho}^{(k)} + o\left({\epsilon_{\rho}^{(k)}}^{3}\right)\right) \\
&\quad - \rho_{\langle e\rangle}^{*} \cdot \exp\left(\frac{f''\left(\rho_{\langle e\rangle}^{*}\right)}{2f'\left(\rho_{\langle e\rangle}^{*}\right)}{\epsilon_{\rho}^{(k)}}^{2} - \epsilon_{\rho}^{(k)} + o\left({\epsilon_{\rho}^{(k)}}^{3}\right)\right)
\end{aligned} \tag{3.49}$$

Equation (3.49) is written as

$$\begin{aligned}
\epsilon_{\rho}^{(k+1)} &= \epsilon_{\rho}^{(k)} \cdot \exp\left(\frac{f''\left(\rho_{\langle e\rangle}^{*}\right)}{2f'\left(\rho_{\langle e\rangle}^{*}\right)}{\epsilon_{\rho}^{(k)}}^{2} - \epsilon_{\rho}^{(k)} + o\left({\epsilon_{\rho}^{(k)}}^{3}\right)\right) \\
&\quad + \rho_{\langle e\rangle}^{*} \cdot \left(\exp\left(\frac{f''\left(\rho_{\langle e\rangle}^{*}\right)}{2f'\left(\rho_{\langle e\rangle}^{*}\right)}{\epsilon_{\rho}^{(k)}}^{2} - \epsilon_{\rho}^{(k)} + o\left({\epsilon_{\rho}^{(k)}}^{3}\right)\right) - 1\right)
\end{aligned} \tag{3.50}$$

From the density constraint shown in Equations (2.4), (2.25) and (3.4), $0 \leq \rho^*_{\langle e \rangle} \leq 1$ holds. That is, from inequality between the density $\rho_{\langle e \rangle}$ and a certain solution $\rho^*_{\langle e \rangle}$, the following inequality holds for the residual $\epsilon^{(k)}_\rho$.

$$-1 \leq \epsilon^{(k)}_\rho \leq 1 \tag{3.51}$$

From the above equation, o, which represents the term above the third power of $\epsilon^{(k)}_\rho$, is ignored because its influence is considered to be small. Thus, Equation (3.50) is weitten as

$$\epsilon^{(k+1)}_\rho \;=\; \epsilon^{(k)}_\rho \cdot \exp\left(F_\rho\left(\epsilon^{(k)}_\rho\right)\right) + \rho^*_{\langle e \rangle} \cdot \left(\exp\left(F_\rho\left(\epsilon^{(k)}_\rho\right)\right) - 1\right) \tag{3.52}$$

where F_ρ is as

$$F_\rho\left(\epsilon^{(k)}_\rho\right) = \frac{f''\left(\rho^*_{\langle e \rangle}\right)}{2f'\left(\rho^*_{\langle e \rangle}\right)}{\epsilon^{(k)}_\rho}^2 - \epsilon^{(k)}_\rho \tag{3.53}$$

Next, the residual $\epsilon^{(k)}_\rho$ shown in Equation (3.51) is divided into

$$\begin{cases} -1 \leq \epsilon^{(k)}_\rho < 0 & \left(\text{if } \;\rho^{(k)}_{\langle e \rangle} < \rho^*_{\langle e \rangle}\right), \\ \epsilon^{(k)}_\rho = 0 & \left(\text{if } \;\rho^{(k)}_{\langle e \rangle} = \rho^*_{\langle e \rangle}\right), \\ 0 < \epsilon^{(k)}_\rho \leq 1 & \left(\text{if } \;\rho^{(k)}_{\langle e \rangle} > \rho^*_{\langle e \rangle}\right) \end{cases} \tag{3.54}$$

- **When** $-1 \leq \epsilon^{(k)}_\rho \leq 0$

First, from the first equation in Equation (3.54), $\rho^{(k)}_{\langle e \rangle} < \rho^*_{\langle e \rangle}$, the relationships shown in Equations (3.55) to (3.57) hold.

$$F_\rho\left(\epsilon^{(k)}_\rho\right) = \frac{f''\left(\rho^*_{\langle e \rangle}\right)}{2f'\left(\rho^*_{\langle e \rangle}\right)}{\epsilon^{(k)}_\rho}^2 - \epsilon^{(k)}_\rho > 0 \quad \left(\text{if } \; \frac{f''\left(\rho^*_{\langle e \rangle}\right)}{2f'\left(\rho^*_{\langle e \rangle}\right)} \geq 0\right) \tag{3.55}$$

$$\epsilon^{(k)}_\rho \cdot \exp\left(F_\rho\left(\epsilon^{(k)}_\rho\right)\right) < 0 \quad \left(\text{if } \; -1 \leq \epsilon^{(k)}_\rho < 0\right) \tag{3.56}$$

$$\rho^*_{\langle e \rangle} \cdot \left(\exp\left(F_\rho\left(\epsilon^{(k)}_\rho\right)\right) - 1\right) > 0 \quad \left(\text{if } \; \frac{f''\left(\rho^*_{\langle e \rangle}\right)}{2f'\left(\rho^*_{\langle e \rangle}\right)} \geq 0\right) \tag{3.57}$$

From the first equation in Equation (3.54) and Equation (3.56), the left side of Equation (3.52) and the first term on the right side of Equation (3.52) are negative. However, the second term on the right side of Equation(3.52) does not have a fixed sign. If the second term is positive, the following ineqality holds.

$$\epsilon_\rho^{(k+1)} \geq \epsilon_\rho^{(k)} \cdot \exp\left(F_\rho\left(\epsilon_\rho^{(k)}\right)\right) \tag{3.58}$$

Equation (3.58) expressed in absolute value is as

$$\left|\epsilon_\rho^{(k+1)}\right| \leq \left|\epsilon_\rho^{(k)} \cdot \exp\left(F_\rho\left(\epsilon_\rho^{(k)}\right)\right)\right| \quad \left(\text{if } \ F_\rho\left(\epsilon_\rho^{(k)}\right) \geq 0, \ \ -1 \leq \epsilon_\rho^{(k)} \leq 0\right) \tag{3.59}$$

When the second term is negative, all terms on the right and left sides of Equation (3.52) are negative. Thus, since $|a+b| \leq |a| + |b|$ holds when $a \cdot b > 0$, the following inequality holds.

$$\begin{aligned}\left|\epsilon_\rho^{(k+1)}\right| \leq \left|\epsilon_\rho^{(k)} \cdot \exp\left(F_\rho\left(\epsilon_\rho^{(k)}\right)\right)\right| + \left|\rho_{\langle e\rangle}^* \cdot \left(\exp\left(F_\rho\left(\epsilon_\rho^{(k)}\right)\right) - 1\right)\right| \\ \left(\text{if } \ F_\rho\left(\epsilon_\rho^{(k)}\right) \leq 0, \ \ -1 \leq \epsilon_\rho^{(k)} \leq 0\right)\end{aligned} \tag{3.60}$$

- **When** $0 \leq \epsilon_\rho^{(k)} \leq 1$

Next, the third equation in Equation (3.54), $\rho_{\langle e\rangle}^{(k)} > \rho_{\langle e\rangle}^*$, the relationships in Equations (3.61) to (3.63) hold.

$$F_\rho\left(\epsilon_\rho^{(k)}\right) = \frac{f''\left(\rho_{\langle e\rangle}^*\right)}{2f'\left(\rho_{\langle e\rangle}^*\right)}\epsilon_\rho^{(k)2} - \epsilon_\rho^{(k)} < 0 \quad \left(\text{if } \ \frac{f''\left(\rho_{\langle e\rangle}^*\right)}{2f'\left(\rho_{\langle e\rangle}^*\right)} \leq 0\right) \tag{3.61}$$

$$\epsilon_\rho^{(k)} \cdot \exp\left(F_\rho\left(\epsilon_\rho^{(k)}\right)\right) > 0 \quad \left(\text{if } \ 0 < \epsilon_\rho^{(k)} \leq 1\right) \tag{3.62}$$

$$\rho_{\langle e\rangle}^* \cdot \left(\exp\left(F_\rho\left(\epsilon_\rho^{(k)}\right)\right) - 1\right) < 0 \quad \left(\text{if } \ \frac{f''\left(\rho_{\langle e\rangle}^*\right)}{2f'\left(\rho_{\langle e\rangle}^*\right)} \leq 0\right) \tag{3.63}$$

From the third equation in Equation (3.54) and Equation (3.62), the left side of Equation (3.52) and the first term on the right side of Equation (3.52) are positive. However, as before,

the second term on the right side of Equation (3.52) does not have a fixed sign. When the second term is positive, all terms on the right and left sides of Equation (3.52) are positive. Thus, since $|a+b| \leq |a| + |b|$ holds when $a \cdot b > 0$, the following inequality holds.

$$\left|\epsilon_\rho^{(k+1)}\right| \leq \left|\epsilon_\rho^{(k)} \cdot \exp\left(F_\rho\left(\epsilon_\rho^{(k)}\right)\right)\right| + \left|\rho^*_{\langle e\rangle} \cdot \left(\exp\left(F_\rho\left(\epsilon_\rho^{(k)}\right)\right) - 1\right)\right| \\ \left(\text{if } \; F_\rho\left(\epsilon_\rho^{(k)}\right) \geq 0, \;\; 0 \leq \epsilon_\rho^{(k)} \leq 1\right) \tag{3.64}$$

If the second term is negative, the following ineqality holds.

$$\epsilon_\rho^{(k+1)} \leq \epsilon_\rho^{(k)} \cdot \exp\left(F_\rho\left(\epsilon_\rho^{(k)}\right)\right) \tag{3.65}$$

Equation (3.65) expressed in alsolute value is as

$$\left|\epsilon_\rho^{(k+1)}\right| \leq \left|\epsilon_\rho^{(k)} \cdot \exp\left(F_\rho\left(\epsilon_\rho^{(k)}\right)\right)\right| \quad \left(\text{if } \; F_\rho\left(\epsilon_\rho^{(k)}\right) \leq 0, \;\; 0 \leq \epsilon_\rho^{(k)} \leq 1\right) \tag{3.66}$$

The function $\exp\left(F_\rho\left(\epsilon_\rho^{(k)}\right)\right)$ shown in Equations (3.59), (3.60), (3.64) and (3.66) are unknown. In addition, the functions $f'\left(\rho^*_{\langle e\rangle}\right)$ and $f''\left(\rho^*_{\langle e\rangle}\right)$ in the function F_ρ, which is shown in Equation (3.53), differ for each optimization problem. Thus, at the moment, further mathematical proof is difficult. If the relationship between the functions $f'\left(\rho^*_{\langle e\rangle}\right)$ and $f''\left(\rho^*_{\langle e\rangle}\right)$ is known, it would be possible to derive more detailed convergence characteristics under all condtions.

Chapter 4

Demonstration of numerical results by uniaxial tensile testing

4.1 Numerical analysis for tensile testing

In this chapter, the results obtained by topology optimization for strain energy minimization and von Mises stress minimization, as described in **chapter 2** and **chapter 3**, are evaluated using test to investigate actual mechanical properties. The methods for testing the properties of materials are classified into the following three categories. The first is physical testing, including acoustic test, optical test, thermal test, electromagnetic test, X-ray test, microscopic test, and pyrotechnic test. The second is mechanical testing, including static strength test, dynamic strength test, hardness test, and surface roughness test. Finally, third is scientific testing, including chemical composition, trace analysis, and so on. Thus, there are a number of testing methods[78]. Several validation experiments have been reported on the results obtained by topology optimization, including topology optimization for complex structures and topology optimization using a 3D printer[79, 80, 81]. Most of the research reports focus on topology optimization for strain energy minimization in complex models. In contrast, topology optimization for simple models and topology optimization for von Mises stress minimization have not been reported. Thus, in this study, the results of topology optimization are demonstrated using tensile testing, which is a typical test for measuring the mechanical properties of materials in the mechanical field. Tensile testing is

a static strength test in which a load is added in one direction. Thus, it is characterized by eases of reproducibility and experimentation. The optimization problems of topology optimization include the strain energy minimization and the von Mises minimization problems. Based on the results described in **chapter 2** and **chapter 3**, the update equation in topology optimization for strain energy minimization employs the modified OC method, and the update equation in topology optimization for von Mises stress minimization employs the MMN modified OC method. The strain energy minimization problem sums the entire strain energy in the design domain Ω, also known as the stiffness maximization problem. Thus, it is used to derive stiff structures. In contrast, the von Mises stress minimization problem is aggregated by applying the p-norm to the von Mises stress in the design domain Ω. Thus, elements with high value of von Mises stress are rated higher and elements with low value are rated lower. Contrary to the strain energy minimization problem, it is not uniformly evaluated. Therefore, the objective is to investigate which problem setup is more appropriate for machine design by tensile testing. The formulation and computational flow for each topology optimization can be found in **chapter 2** and **chapter 3**, respectively.

Figure 4.1 shows the ISO6892-2 Annex B2, which is a specimen for tensile testing. The hatched domain in Figure 4.1 is the domain where topology optimization is performed to reduce weight. From the symmetry of calculation model, the domain filled in black, which is the quarter model, is the design domain Ω. Figure 4.2 shows a quarter model, which is a calculation model. Table 4.1 shows the calculation conditions of topology optimization for tensile testing. The mesh size is 0.1 [mm] per side, and the material is A2017, which is an aluminum alloy, for machinability. The calculation model is the plane stress because the structure is thin in thickness relative to its width and high, as shown in Figure 4.1. Table 4.2 shows the volume rate of the design domain and minimization problem conditions for tensile testing. Case 0 is the condition for the initial model with no weight reduction, and Cases 7 to 9 are the conditions for the simply weight reduced specimen shown in Figure 4.3. The function ϕ for a simply weight reduced specimen shown in Figure 4.3 is the diameter calculated to satisfy the volume rate. In this chapter, topology optimization for strain energy

minimization and von Mises stress minimization are performed. After that, tensile testing is performed on tensile specimens based on the results of each topology optimization and specimens simply reduced in weight, and the mechanical properties will be compared.

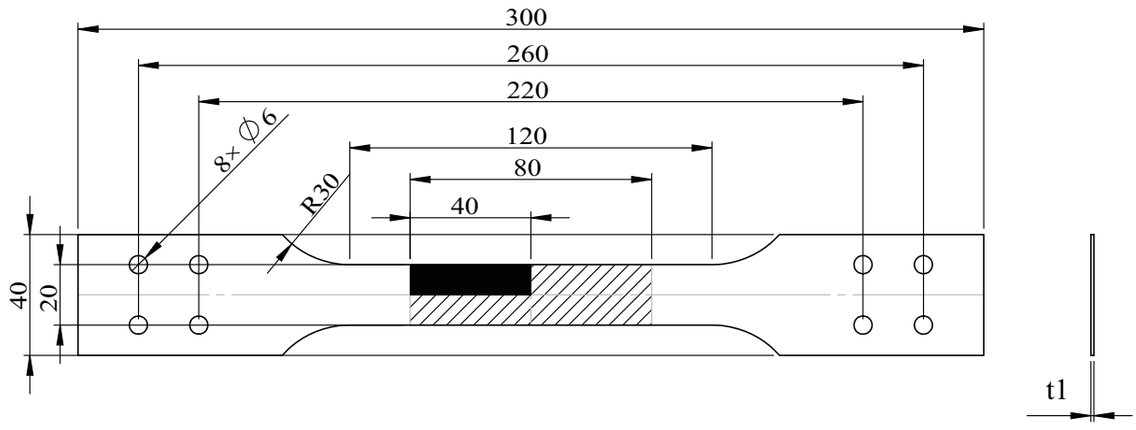

Figure 4.1: Tensile specimen model.

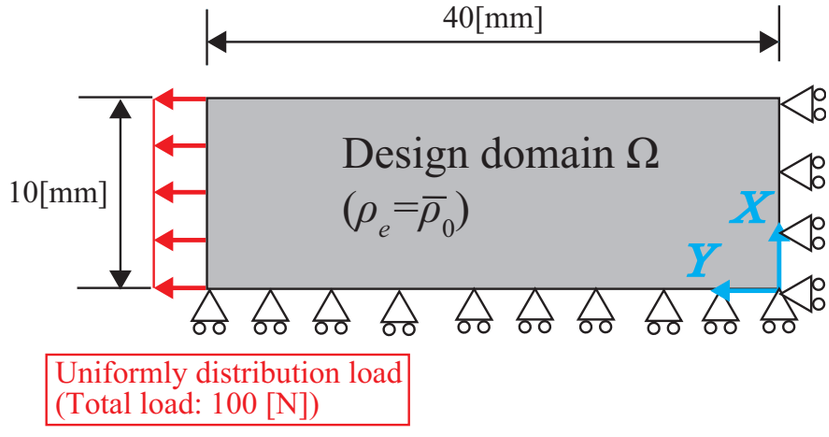

Figure 4.2: Quarter calculation model for tensile specimen.

Table 4.1: Calculation conditions of topology optimization for tensile specimen.

Number of elements	40501
Number of nodes	40000
Penalization parameter for the SIMP method, p_s	3.0
Penalization parameter for p-norm, p	6.0
Filter radius, R	0.125
Maximum number of iterations, $k_{\max}$	175
Young's modulus, E_0 [Pa]	72.6×10^9
Poisson ratio, ν	0.33

Table 4.2: Volume and minimization problem conditions for tensile specimen.

Case No.	Initial density average, $\bar{\rho}_0$	Volume in design domain, [%]	Minimization problem
0	-	100	Original model
1	0.8	80	Strain energy
2			Von Mises stress
3	0.6	60	Strain energy
4			Von Mises stress
5	0.4	40	Strain energy
6			Von Mises stress
7, 8, 9	-	80, 60, 40	Simple weight reduction

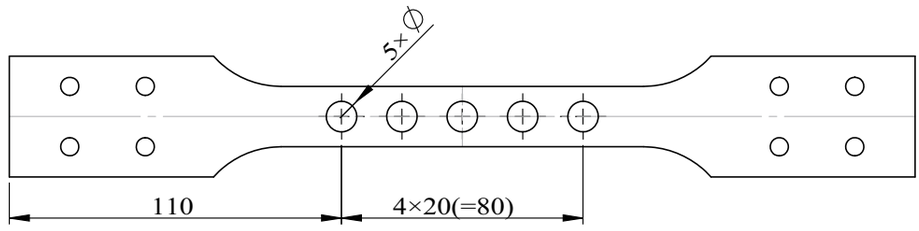

Figure 4.3: Simply lightweight tensile specimen.

4.2 Results of topology optimization for strain energy minimization and von Mises stress minimization

This section describes the results obtained by topology optimization for strain energy minimization and von Mises stress minimization, based on the calculation condition explained in the previous section. Figures 4.4 to 4.9 show the results of topology optimization in Cases 1 to 6 shown in Table 4.2. Sub caption (a) of Figures 4.4 to 4.9 shows the density distribution, (b) shows the distribution of the displacement in the same Y-direction as the load direction, (c) shows the von Mises stress distribution, respectively. In addition, (b) and (c) eliminate elements with density values less than 0.3. Even for the same volume rate, different settings of performance function in the optimization problem obtained different density distributions. In addition, for the same volume rate, no significant different was confirmed in the distribution of displacement in Y-direction shown in (b). However, the von Mises stress distributions shown in Figures 4.4(c), 4.6(c) and 4.8(c) have higher von Mises stress distribution than one for the same volume rate shown in Figures 4.5(c), 4.7(c) and 4.9(c). From the results shown in Figures 4.4 to 4.9, compared to the results of topology optimization for strain energy

minimization, the results of topology optimization for von Mises stress minimization are less deformable and stronger. In other words, the von Mises stress minimization problem can be used to optimize the design of high-stiffness and high-strength products. This trend can be seen from the history of performance functions for strain energy and von Mises stress, as shown in Figure 4.10, and their respective performance functions at final iteration, as shown in Table 4.3. The value of the performance function for strain energy minimization is W, and the value of performance function for von Mises stress minimization is J. The values of W and J for the topology optimization in the Mises stress minimization problem (Cases 2, 4, 6) are lower than the values of W and J for the topology optimization in the strain energy minimization problem (Cases 1, 3, 5) for the same volume rate. Thus, although there is a relationship between strain energy and von Mises stress, the topology optimization for von Mises stress minimization provides the optimum solution for stiffness and strength. However, the von Mises minimization problem described in **chapter 3** is a non-self-adjoint relationship problem, which requires solving the adjoint equation and has high calculation cost. It is also difficult to determine which is better, since the density distribution may have grayscale.

Table 4.3: Each performance function at final iteration for tensile testing specimen.

Case No.	Performance function for strain energy minimization, W	Performance function for von Mises stress minimization, J
1	1.44	109.61
2	1.42	66.90
3	1.97	90.71
4	1.92	85.98
5	3.32	154.38
6	3.01	124.45

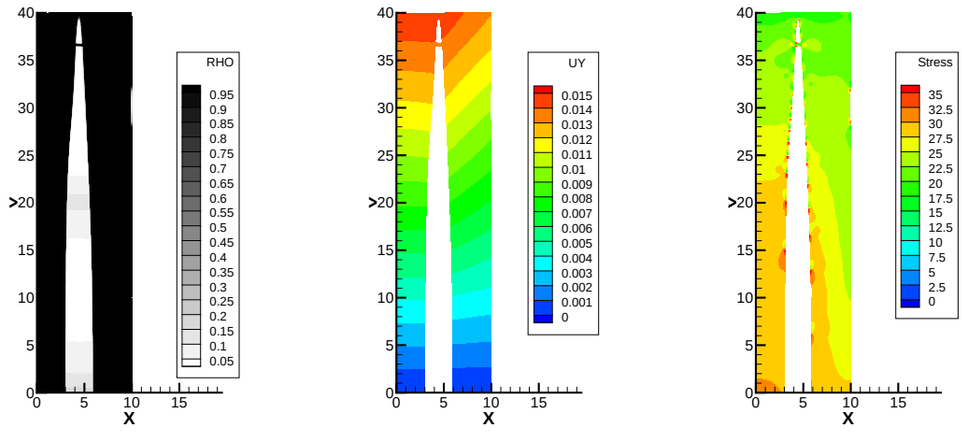

(a) Density distribution. (b) Displacement in Y-direction. (c) Von Mises stress distribution.

Figure 4.4: Result of topology optimization at final iteration for Case 1.

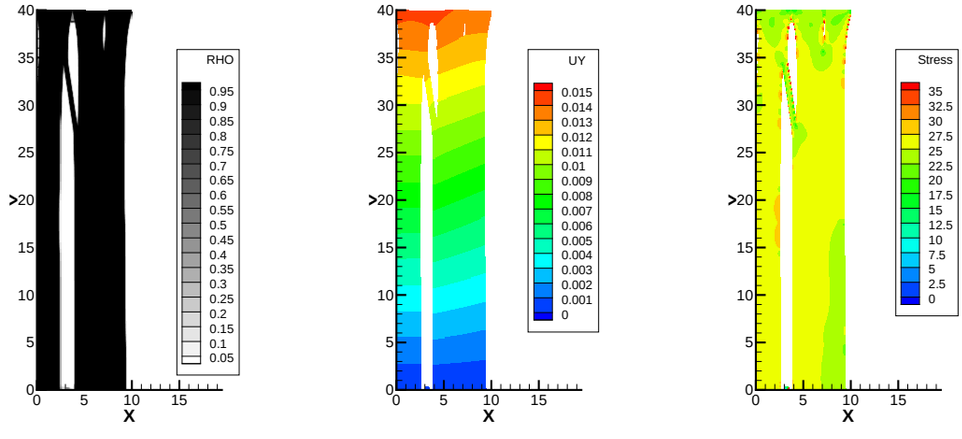

(a) Density distribution. (b) Displacement in Y-direction. (c) Von Mises stress distribution.

Figure 4.5: Result of topology optimization at final iteration for Case 2.

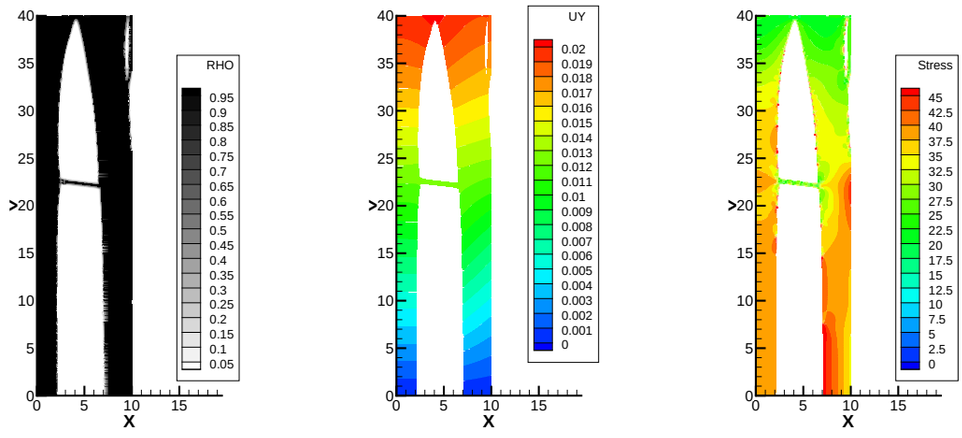

(a) Density distribution. (b) Displacement in Y-direction. (c) Von Mises stress distribution.

Figure 4.6: Result of topology optimization at final iteration for Case 3.

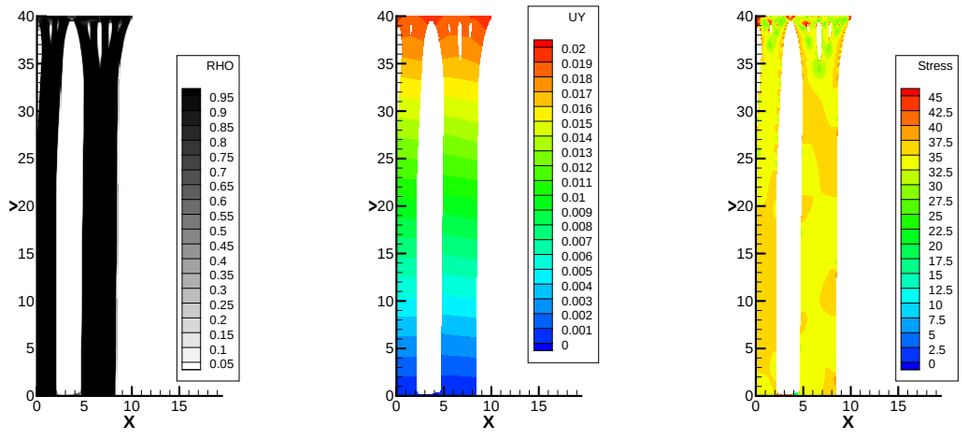

(a) Density distribution. (b) Displacement in Y-direction. (c) Von Mises stress distribution.

Figure 4.7: Result of topology optimization at final iteration for Case 4.

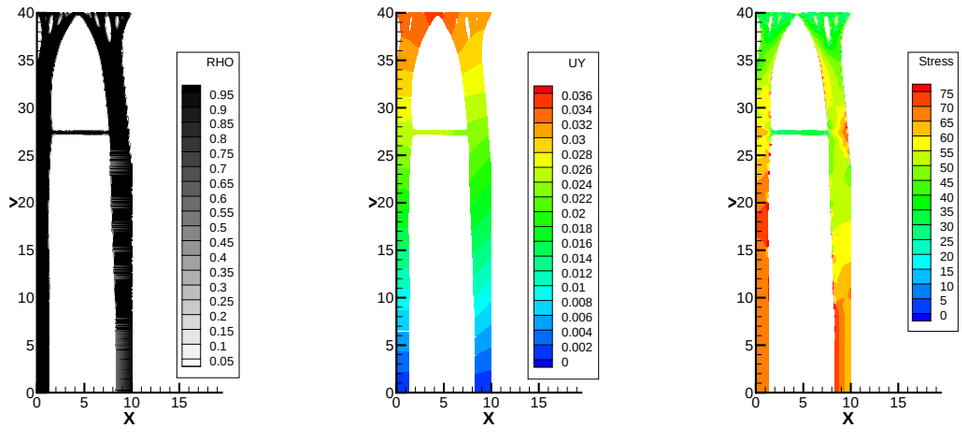

(a) Density distribution. (b) Displacement in Y-direction. (c) Von Mises stress distribution.

Figure 4.8: Result of topology optimization at final iteration for Case 5.

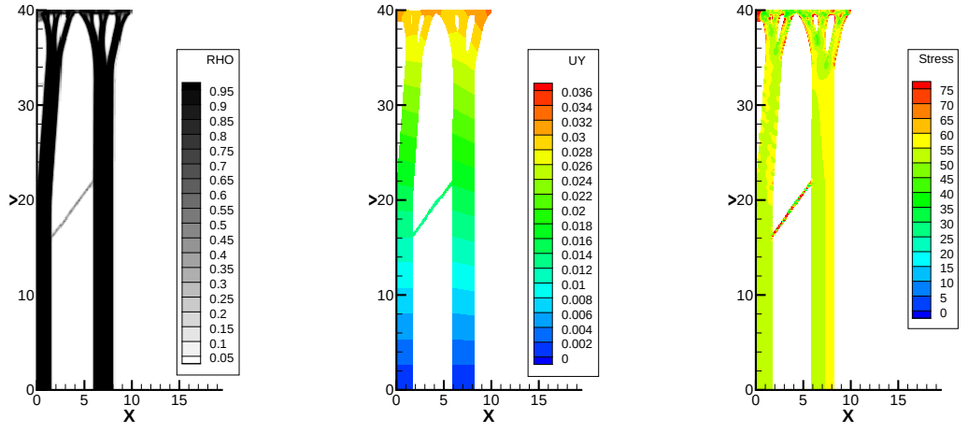

(a) Density distribution. (b) Displacement in Y-direction. (c) Von Mises stress distribution.

Figure 4.9: Result of topology optimization at final iteration for Case 6.

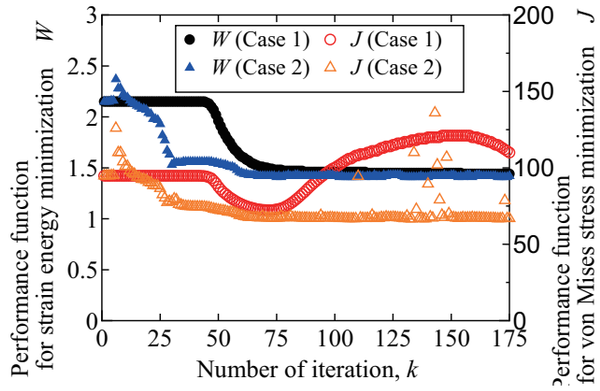

(a) When $\bar{\rho}_0 = 0.8$.

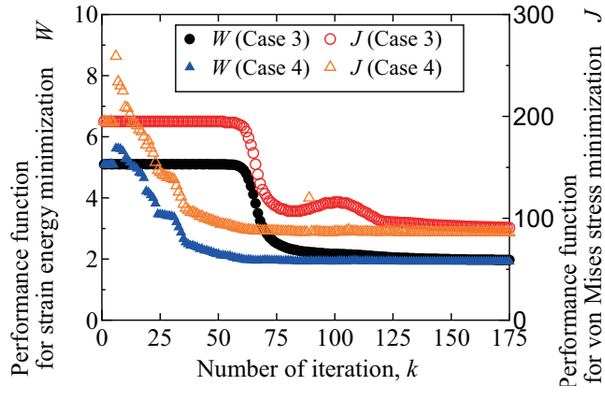

(b) When $\bar{\rho}_0 = 0.6$.

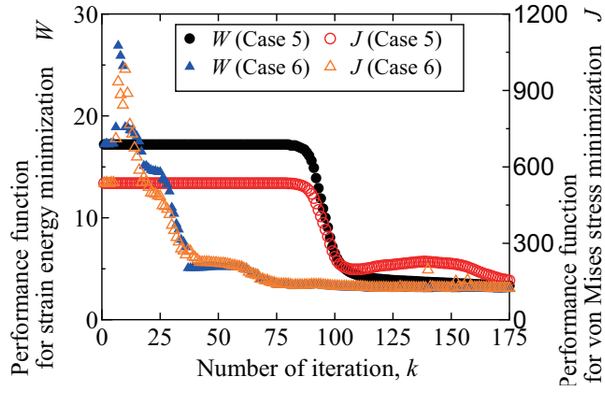

(c) When $\bar{\rho}_0 = 0.4$.

Figure 4.10: The history of each performance function for tensile specimen.

4.3 Experimental method for uniaxial tensile testing

This section explains tensile testing[82] to examine the validity of the results obtained by topology optimization. Figures 4.11 and 4.12 show the photographs of tensile testing (Shimazu Servo Pulsar EHF-EB10[83]) and jig used in the tensile testing. In the preliminary experiments, failure occurred at the fixed point when the specimen in Case 0, which is the initial model with the highest strength, was performed to a tensile testing using the pin fixation. Therefore, pin fixation was considered insufficient, and the method was changed to a gripping fixation using the M6 bolts. To add a load in Y-axis direction, a hole was drilled in the upper part of the jig to fix a pin so that tensile load would be applied on the coaxial line. See Figure 4.11 for the fixation method using the jig. Figure 4.13 shows the photograph of tensile specimens in Cases 0 to 9. The tensile specimens and jig shown in Figures 4.12 and 4.13 were machined by wire electrical discharge machining (wire EDM). However, because of the difficulty of wire EDM to faithfully reproduce the results of topology optimization described in the previous section, some holes are not processed. Table 4.4 shows the weight of each specimen and its average value. The number of tensile testing shall be three. The tensile speed is set to elongate 50 [mm] per minute. Originally, strain gauges were used in tensile testing, but since the density distribution obtained by topology optimization differ from condition to condition, making it impossible to establish representative locations. Therefore, the relationship between displacement and load and the points of failure are investigated.

Figure 4.11: Photograph of tensile testing machine.

Figure 4.12: Photograph of jig for tensile testing.

(a) Case 0

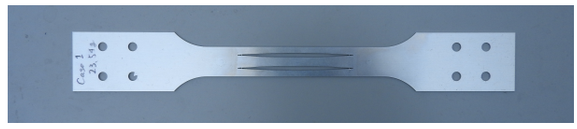

(b) Case 1

(c) Case 2

(d) Case 3

(e) Case 4

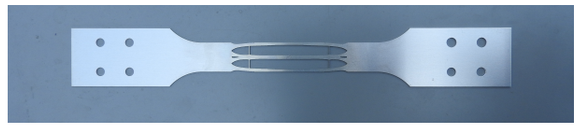

(f) Case 5

(g) Case 6

(h) Case 7

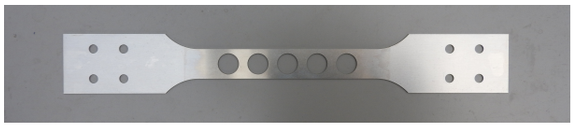

(i) Case 8

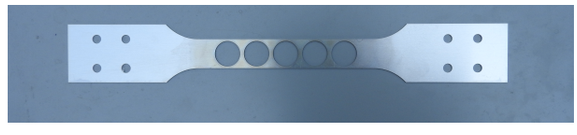

(j) Case 9

Figure 4.13: Photographs of tensile specimen.

Table 4.4: Tensile specimen masses.

Case No.	Tensile specimen mass [g]			Average mass [g]
0	24.51	24.38	24.39	24.43
1	23.37	23.34	23.54	23.42
2	23.37	23.36	23.37	23.37
3	22.59	22.48	22.52	22.53
4	22.55	22.55	22.56	22.55
5	21.42	21.47	21.50	21.46
6	21.73	21.73	21.71	21.72
7	23.27	23.28	23.17	23.28
8	22.16	22.15	22.15	22.15
9	21.02	21.03	21.02	21.02

4.4 Experimental results and discussion of uniaxial tensile testing

This section discusses the experimental results and discussion of tensile testing. Figures 4.14 to 4.17 show the load-displacement diagrams with error bars for each of the same volume rates. The horizontal axis in these figures represents the displacement in Y-direction, and the vertical axis represents the load. First, the result of tensile testing on a model with a volume rate 100% is presented. The error bars in Figure 4.14 confirms that the error is small and the experiment is reproducible. Next, the results of tensile testing on a model with a volume rate 80% are presented. The results of topology optimization for strain energy minimization (Case 1) and the results of topology optimization for strain energy minimization (Case 2) show no significant differences. However, the simple weight reduction model (Case 7) has lower allowable load and plastic deformation at earlier times than the results obtained by

topology optimization. Next, the results of tensile testing on a model with a volume rate 60% are presented. The results of topology optimization for strain energy minimization (Case 4) show a higher allowable load than the results of topology optimization for strain energy minimization (Case 3). However, similar to the result when the volume rate 80%, the simple weight reduction model (Case 8) has lower allowable load and plastic deformation at earlier times than the results obtained by topology optimization. Finally, the results of tensile testing on a model with a volume rate 40% are presented. For this volume rate, the aforementioned trend is pronounced: the results of topology optimization for strain energy minimization (Case 6) show a higher allowable load than the results of topology optimization for strain energy minimization (Case 5). In addition, the simple weight reduction model (Case 9) has lower allowable load than the results obtained by topology optimization, and it is immediately plastically deformed. From the load-displacement diagrams shown in Figures 4.14 to 4.17, the numerical data for load and displacement at break are summarized in Table 4.5. From Table 4.5, it can be seen that the specimens for simple weight reduction (Cases 7, 8, 9) have generally lower breaking loads. Moreover, the breaking loads of topology optimization for von Mises stress minimization (Cases 2, 4, 6) are larger than the breaking loads of topology optimization for strain energy minimization (Cases 1, 3, 5). In other words, topology optimization for von Mises stress minimization is suitable to create a structure with high strength. However, the setting of the von Mises stress minimization problem used in this problem is not optimum. The reason is that the failed tensile specimens shown in Figure 4.18 indicate that the failure points are concentrated at the edges of the design domain. Originally, it is appropriate for the tensile specimen to be centered as shown in Figure 4.18(a) as the breaking point of specimen. Moreover, aluminum alloy (A2017) has strong ductile properties, which causes shear fracture, which breaks at an oblique angle. Similarly, the results of topology optimization for strain energy minimization shown in Figures 4.18(b) and 4.18(d) show that the break occurs near the center. On the other hand, the results of topology optimization for von Mises stress minimization shown in Figures 4.18(c) and 4.18(e) show that the break does not occur near the center. The fracture points are the same as

the results for the specimen of simple weight reduction and occur at both ends. The cause is considered to be the interference effect of stress concentration[84]. When multiple pores exist in close proximity, mutual interference effects of stress concentration occur. Figures 4.19 and 4.20 show the interference effects of typical stress concentration[85]. Figure 4.19 shows the interference effect of increased stress concentration, and Figure 4.20 shows the interference effect of decreased stress concentration. For a single circular hole model, the stress concentration factor is known to be 3. However, when the holes are side-by-side with respect to the load as shown in Figure 4.19, the stress concentration factor exceeds 3 when the distances are close. Conversely, when the holes are aligned vertically with respect to the load as shown in Figure 4.20, the stress concentration factor for the holes located away from the load is less than 3. Since the stress concentration factor is higher for the holes near the load, failure occurs from the edge of the design domain, as shown in Figures 4.18(c), 4.18(e) and 4.18(g). From this, it can be inferred that the topology optimization for von Mises stress minimization (Cases 2, 4, 6) is causing an interference effects that increase stress concentration, while the specimens of simple weight reduction (Cases 7, 8, 9) are causing an interference effects that decrease stress concentration. Based on the above, it may be possible to create stronger structures if topology optimization considering the interference effects of stress concentration is performed.

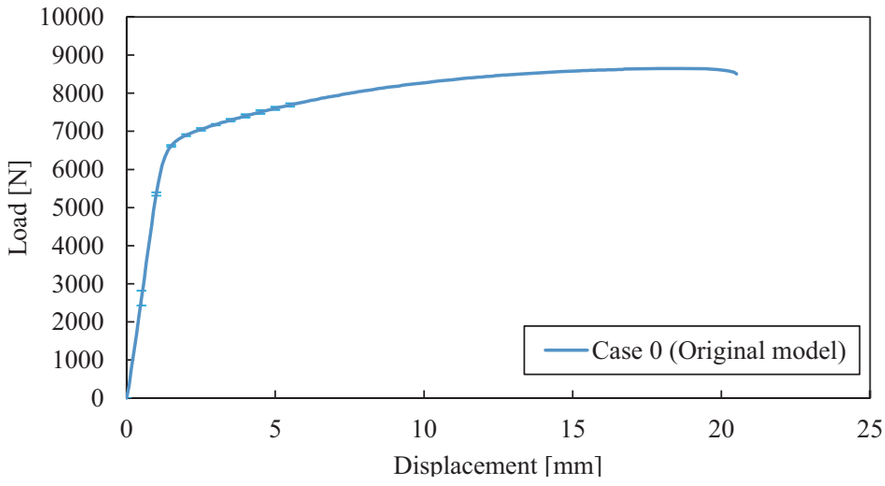

Figure 4.14: Load–displacement in Y-direction graphs with error bars in the original model.

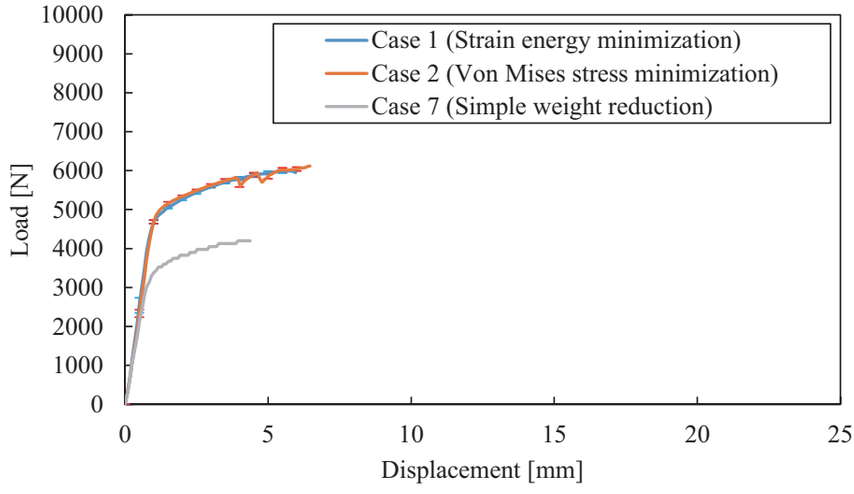

Figure 4.15: Load–displacement in Y-direction graphs with error bars in the models with 80% volume.

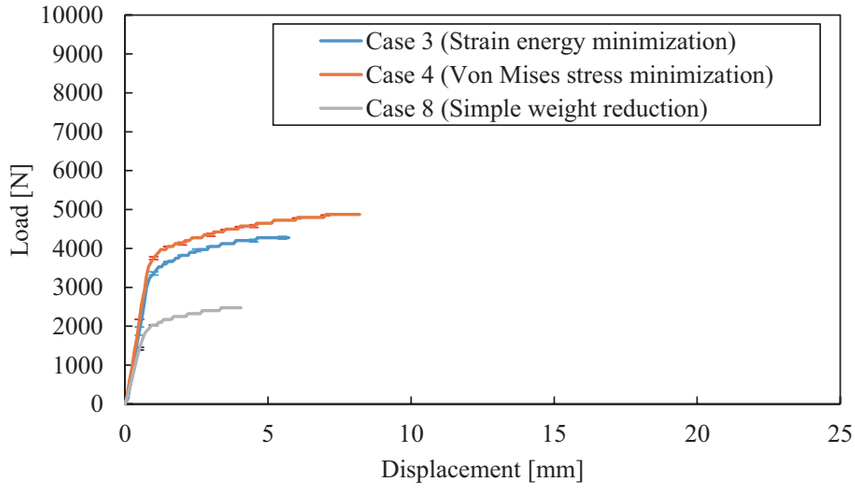

Figure 4.16: Load–displacement in Y-direction graphs with error bars in the models with 60% volume.

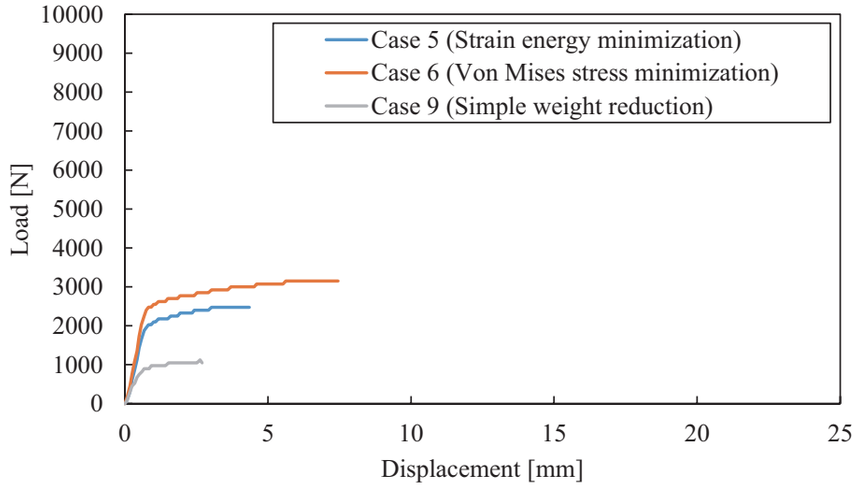

Figure 4.17: Load–displacement in Y-direction graphs with error bars in the models with 40% volume.

Table 4.5: Tensile testing results at break.

Case No.	Average of displacements at break [mm]	Average of breaking loads [N]
0	20.35	8485
1	5.99	6033
2	6.70	6190
3	5.68	4300
4	8.15	4875
5	4.30	2475
6	7.35	3150
7	4.46	4150
8	3.98	2475
9	2.65	1100

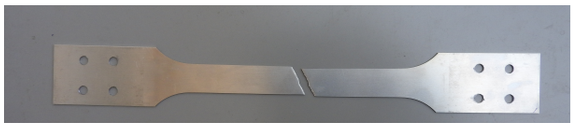

(a) Case 0

(b) Case 1

(c) Case 2

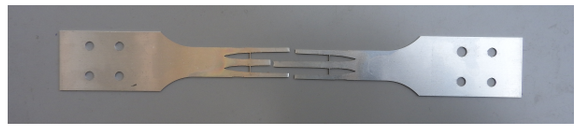

(d) Case 3

(e) Case 4

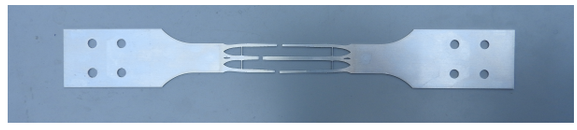

(f) Case 5

(g) Case 6

(h) Case 7

(i) Case 8

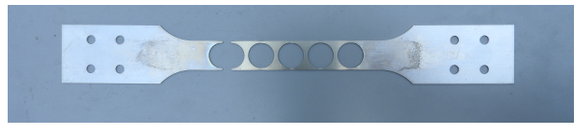

(j) Case 9

Figure 4.18: Photographs of fractured tensile specimens.

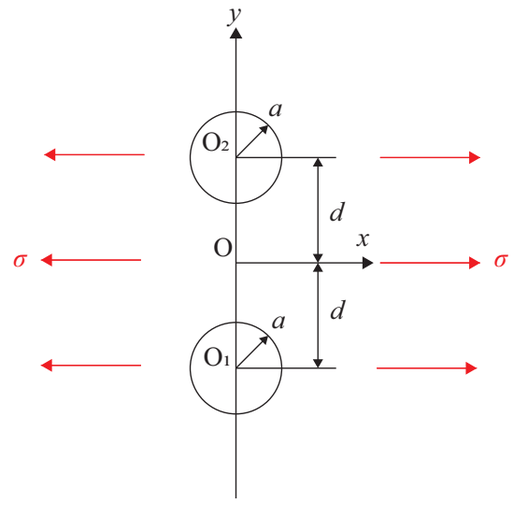

Figure 4.19: Interference effects that increase stress concentration.

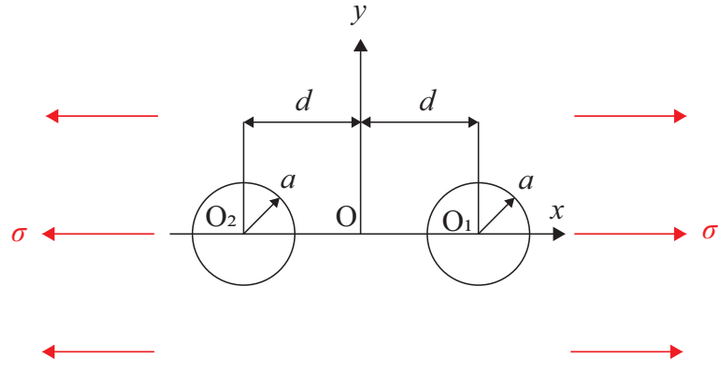

Figure 4.20: Interference effects that decrease stress concentration.

Chapter 5

Multi-objective topology optimization

5.1 Formulation of multi-objective optimization based on the weighted sum method

This chapter discusses the topology optimization for multi-objective optimization combining strain energy minimization and von Mises stress minimization problems. The previous chapters have been single-objective optimization. The aim of single-objective design is to find an optimum solution to the problem. On the other hand, multi-objective optimization is the optimization of multiple objective functions. Moreover, it is often more practical to obtain several candidate solutions, which are the pareto optimum solutions, gradually refine the design solution among them. A pareto solution is a solution that is as close as possible to an ideal solution in a multi-objective optimization problem and has a difference balance among the objective functions. Thus, one of the aims of multi-objective optimum design is to obtain a pareto optimum solution or to perform a trade-off analysis between performance functions. Methods for finding optimum solutions are classified as scalarization method, interactive method, and evolutionary computation method[87]. The scalarization method transforms the problem into a single-objective optimization problem in some way and uses various optimization methods to obtain a pareto optimum solution. The method includes the weighted sum method, weighted lp norm method, and compromise programming method. In this chapter, the weighted sum method, which is the most basic of the scalarization method,

is employed. A detailed description of the weighted sum method is given below. In the interactive method, the designer assigns a desired level, which is the required value of each performance function, to each performance function and solves the optimization problem to obtain the pareto optimum solution. If the engineer does not satisfy the pareto optimum solution, the interactive operation is repeated by changing the aspiration level and finding the pareto optimum solution again. The method includes the reference point method, STEM, and satisficing tradeoff method. While most scalarization methods find pareto optimum solutions by adjusting weights, the interactive method finds satisfactory design solutions by directly adjusting the aspiration level. Finally, evolutionary computation method is optimization algorithm that mimic the process of biological evolution, and genetic algorithms are well-known[88].

In this chapter, the topology optimization for multi-objective optimization is solved based on the weighted sum method[89, 90], in which the performance functions of strain energy minimization and von Mises stress minimization described in **chapter 2** and **chapter 3**, respectively, are multiplied by weights and summed to minimize the expended objective function. The stain energy minimization and von Mises stress minimization problems have some kind of causal relationship, which is different from the general trade-off relationship. The strain energy minimization problem shows very high convergence in numerical analysis, but the strain energy is handled in actual design. In contrast, the von Mises stress minimization problem has worse convergence in numerical analysis, but the von Mises stress is important enough to be used as safety design guide in actual design. As shown in the previous chapter, the results obtained by topology optimization for von Mises stress minimization is expected to be stronger than the results obtained by topology optimization for strain energy minimization. Thus, this chapter combines the numerical obtained by topology optimization for strain energy minimization and the reliability of the performance of the actual design obtained by topology optimization for von Mises stress minimization to obtain a better solution for an optimum design. For optimum design, the modified OC method, which is the proposed method, is employed. However, the modified OC method shown in **chapter 3** is extremely

show in updating. Therefore, a new positive definite-correspondence modified OC method based on a map function is proposed. The details of the update equation are described in the next section. This optimization problems consists of the following performance function and constraint conditions. The expanded performance function shown in Equation (5.1) is composed of the performance functions for strain energy minimization shown in Equation (5.2) and von Mises stress minimization shown in Equation (5.3). The performance functions for strain energy minimization shown in Equation (5.2) and von Mises stress minimization shown in Equation (5.3) are the same as in Equation (2.1) shown in **chapter 2** and Equation (3.1) shown in **chapter 3**. The governing equation, volume constraint, and density constraint shown in **chapter 2** and **chapter 3** are employed as constraint conditions, and shown in Equations (5.4) to (5.6).

$$\text{minimize} \quad J = \frac{w_1}{\|J_1\|} J_1 + \frac{w_2}{\|J_2\|} J_2 = W_1 J_1 + W_2 J_2 \tag{5.1}$$

$$J_1 = \frac{1}{2} \sum_{e \in \Omega} \left\{ u_{\langle e \rangle} \right\}^T \left[K_{\langle e \rangle} \right] \left\{ u_{\langle e \rangle} \right\} \tag{5.2}$$

$$J_2 = \left(\sum_{e \in \Omega} \left({\rho_{\langle e \rangle}}^{\frac{1}{2}} \sigma_{VM\langle e \rangle} \right)^p V_{\langle e \rangle} \right)^{\frac{1}{p}} \tag{5.3}$$

$$\text{subject to} \quad [K] \{u\} = \{f\} \tag{5.4}$$

$$V = \sum_{e \in \Omega} \frac{V_{\langle e \rangle} \rho_{\langle e \rangle}}{V_{\text{total}}} - \bar{\rho_0} \leq 0 \tag{5.5}$$

$$0 \leq \rho_{\langle e \rangle} \leq 1 \tag{5.6}$$

The sensitivity is obtained using a procedure similar to the formulation of topology optimization shown in **chapter 2** and **chapter 3**. Thus, duplicate content is omitted. To satisfy the governing equation shown in Equation (5.4) and to minimize the performance function shown in Equation (5.1), the Lagrange function J^* is defined as

$$\begin{aligned} J^* &= \sum_{e \in \Omega} J^*_{\langle e \rangle} \\ &= \sum_{e \in \Omega} J_{\langle e \rangle} + \left\{ \lambda_{\langle e \rangle} \right\}^T \left(\left[K_{\langle e \rangle} \right] \left\{ u_{\langle e \rangle} \right\} - \left\{ f_{\langle e \rangle} \right\} \right) \end{aligned} \tag{5.7}$$

where $\left\{\lambda_{\langle e\rangle}\right\}$ is the Lagrange multiplier vector. The variate of the Lagrange function $\delta J^*_{\langle e\rangle}$ becomes 0, as shown in

$$\delta J^*_{\langle e\rangle} = \left\{\frac{\partial J^*_{\langle e\rangle}}{\partial \lambda_{\langle e\rangle}}\right\}^T \left\{\delta\lambda_{\langle e\rangle}\right\} + \left\{\frac{\partial J^*_{\langle e\rangle}}{\partial u_{\langle e\rangle}}\right\}^T \left\{\delta u_{\langle e\rangle}\right\} + \frac{\partial J^*_{\langle e\rangle}}{\partial \rho_{\langle e\rangle}}\delta\rho_{\langle e\rangle} = 0 \tag{5.8}$$

As in the other optimizations, each term is calculated to be 0. First, the gradient of the Lagrange function with respect to the Lagrange multiplier vector shown in the first term is the same as the governing equation shown in Equation (5.4). Thus, the calculation is omitted. Next, the gradient of the Lagrange function with respect to the displacement vector shown in the second term is calculated as

$$\begin{aligned}\left\{\frac{\partial J^*_{\langle e\rangle}}{\partial u_{\langle e\rangle}}\right\}^T &= W_1\left\{u_{\langle e\rangle}\right\}^T\left[K_{\langle e\rangle}\right] + W_2 G^{\frac{1}{p}-1}{\rho_{\langle e\rangle}}^{\frac{p}{2}}{\sigma_{VM\langle e\rangle}}^{p-1}V_{\langle e\rangle}\left\{\frac{\partial\sigma_{VM\langle e\rangle}}{\partial u_{\langle e\rangle}}\right\}^T + \left\{\lambda_{\langle e\rangle}\right\}^T\left[K_{\langle e\rangle}\right] \\ &= \{0\}^T\end{aligned} \tag{5.9}$$

where G is as

$$G = \sum_{e\in\Omega}\left({\rho_{\langle e\rangle}}^{\frac{1}{2}}\sigma_{VM\langle e\rangle}\right)^p V_{\langle e\rangle} \tag{5.10}$$

Form Equation (5.9), the Lagrange multiplier vector $\left\{\lambda_{\langle e\rangle}\right\}$ is obtained as

$$\left\{\lambda_{\langle e\rangle}\right\}^T\left[K_{\langle e\rangle}\right] = -W_1\left\{u_{\langle e\rangle}\right\}^T\left[K_{\langle e\rangle}\right] - W_2 G^{\frac{1}{p}-1}{\rho_{\langle e\rangle}}^{\frac{p}{2}}{\sigma_{VM\langle e\rangle}}^{p-1}V_{\langle e\rangle}\left\{\frac{\partial\sigma_{VM\langle e\rangle}}{\partial u_{\langle e\rangle}}\right\}^T \tag{5.11}$$

The gradient of the von Mises stress with respect to the displacement vector is shown in Equations (3.13) to (3.17). Finally, the gradient of the Lagrange function with respect to the density shown in the third term is calculated as

$$\begin{aligned}\frac{\partial J^*_{\langle e\rangle}}{\partial \rho_{\langle e\rangle}} &= \frac{1}{2}W_1\left\{u_{\langle e\rangle}\right\}^T\frac{\partial\left[K_{\langle e\rangle}\right]}{\partial\rho_{\langle e\rangle}}\left\{u_{\langle e\rangle}\right\} + \frac{1}{2}W_2 G^{\frac{1}{p}-1}{\rho_{\langle e\rangle}}^{\frac{p}{2}-1}{\sigma_{VM\langle e\rangle}}^{p}V_{\langle e\rangle} \\ &\quad + \left\{\lambda_{\langle e\rangle}\right\}^T\frac{\partial\left[K_{\langle e\rangle}\right]}{\partial\rho_{\langle e\rangle}}\left\{u_{\langle e\rangle}\right\} + \Big(W_1\left\{u_{\langle e\rangle}\right\}^T\left[K_{\langle e\rangle}\right] \\ &\quad + W_2 G^{\frac{1}{p}-1}{\rho_{\langle e\rangle}}^{\frac{p}{2}}{\sigma_{VM\langle e\rangle}}^{p-1}V_{\langle e\rangle}\left\{\frac{\partial\sigma_{VM\langle e\rangle}}{\partial u_{\langle e\rangle}}\right\}^T + \{\lambda\}^T\left[K_{\langle e\rangle}\right]\Big)\left\{\frac{\partial u_{\langle e\rangle}}{\partial\rho_{\langle e\rangle}}\right\} \\ &= \frac{1}{2}W_1\left\{u_{\langle e\rangle}\right\}^T\frac{\partial\left[K_{\langle e\rangle}\right]}{\partial\rho_{\langle e\rangle}}\left\{u_{\langle e\rangle}\right\} + \frac{1}{2}W_2 G^{\frac{1}{p}-1}{\rho_{\langle e\rangle}}^{\frac{p}{2}-1}{\sigma_{VM\langle e\rangle}}^{p}V_{\langle e\rangle} \\ &\quad + \left\{\lambda_{\langle e\rangle}\right\}^T\frac{\partial\left[K_{\langle e\rangle}\right]}{\partial\rho_{\langle e\rangle}}\left\{u_{\langle e\rangle}\right\}\end{aligned} \tag{5.12}$$

Next, an extended Lagrange function L is defined by considering the volume constraint shown in Equation (5.5). Similar to the topology optimization for von Mises stress minimization, offsets are made so that the sensitivity term is always negative, and the gradient of the extended Lagrange function with respect to the density is calculated as

$$\frac{\partial J^*_{\langle e\rangle}}{\partial \rho_{\langle e\rangle}} + \Lambda \frac{V_{\langle e\rangle}}{V_{\text{total}}} + g_{\max} - g_{\max} = 0 \tag{5.13}$$

where $g_{\max}$ is the offset function and is given as

$$g_{\max} = \max_{e\in\Omega} \left(0,\ \frac{\partial J^*_{\langle e\rangle}}{\partial \rho_{\langle e\rangle}}\right) \tag{5.14}$$

Expanding Equation (5.13) into the form of a function $A_{\langle e\rangle}$ used in the OC method and the modified OC method, it is obtained as

$$\begin{aligned} A_{\langle e\rangle} &= \frac{\frac{\partial J^*_{\langle e\rangle}}{\partial \rho_{\langle e\rangle}} - g_{\max}}{-\left(\Lambda \frac{V_{\langle e\rangle}}{V_{\text{total}}} + g_{\max}\right)} \\ &= \frac{\frac{\partial J^*_{\langle e\rangle}}{\partial \rho_{\langle e\rangle}} - g_{\max}}{-\Lambda_{\text{mod}}} \end{aligned} \tag{5.15}$$

where, Λ_{mod} is the modified extended Lagrange multiplier, which is obtained by the bisection method. Due to the offset, the numerator and denominator shown in Equation (5.15) is always negative and the function $A_{\langle e\rangle}$ is always positive. Therefore, the OC method and the modified OC method can be employed.

5.2 Modified optimality criteria method based on map function

This section derives a modified OC method based on a map function. When the MMN modified OC method was applied to this problem for the exponent in the modified OC method shown in Figure 5.1(a), the update speed was slow and the performance function did not decreased. The difference between the OC method and the modified OC method is

whether the exponent is a constant or a function. Thus, in the OC method, the weighting factor is considered as a function $\Theta_{\langle e\rangle}$ given element by element.

$$\rho_{\langle e\rangle}^{(k+1)} = \rho_{\langle e\rangle}^{(k)} \left(A_{\langle e\rangle}^{(k)}\right)^{\Theta_{\langle e\rangle}^{(k)}} \tag{5.16}$$

In the MMN modified OC method, the function $\Theta_{\langle e\rangle}$ takes the range from 0 to 1, so there existed a case where no update was made for some elements in some iterations. In addition, as shown in Figure 5.1(b), although overall updates were performed, the overall function $\Theta_{\langle e\rangle}$ became smaller and updates became too gradual, resulting in a very slow update problem. Therefore, as shown in Figure 5.1(c), a map function is used to map the range from a certain value to 1 instead of from 0 to 1. Based on the above, the mapping-based modified OC method is proposed, which incorporates the general concept of the map function used in Arduino and other into the modified OC method.

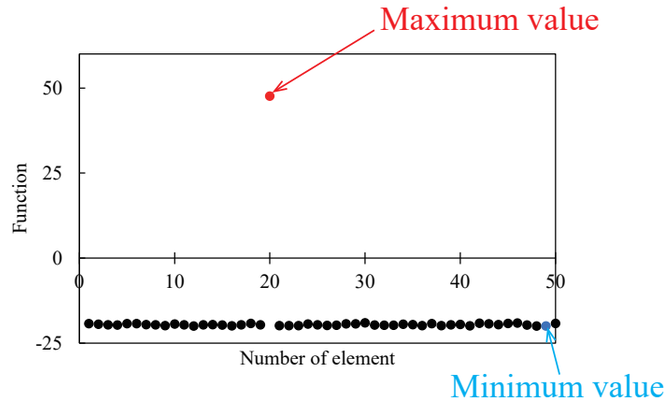

(a) Before mapping.

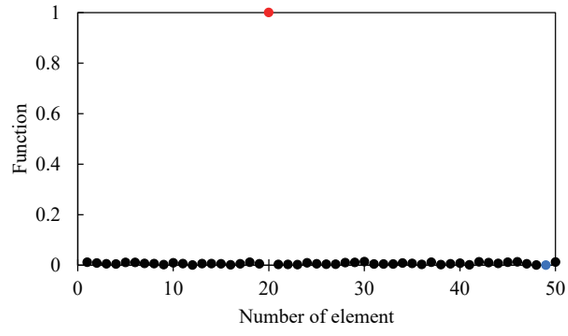

(b) When using the MMN modified OC method.

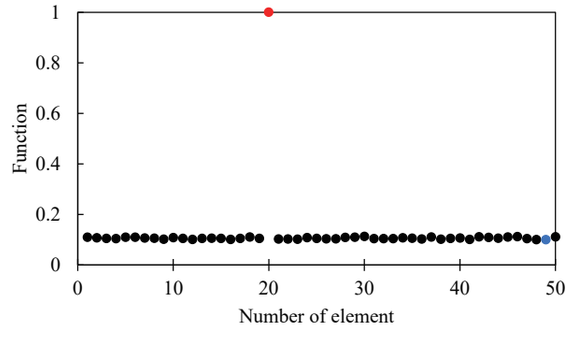

(c) When using the Mapping-based modified OC method.

Figure 5.1: Image of function Θ distribution.

The procedure is similar to the derivation of the modified OC method. First, the function located at the weighting factor is obtained. By assuming that g_{max} is 0 when differentiated by density, the function located at the weighting factor becomes

$$\left(-\frac{\partial}{\partial \rho_{\langle e\rangle}}\left(\ln A_{\langle e\rangle}^{(k)}\right)\right)^{-1} = -\left(\frac{\frac{\partial^2 J^*_{\langle e\rangle}{}^{(k)}}{\partial \rho_{\langle e\rangle}{}^2}}{\frac{\partial J^*_{\langle e\rangle}{}^{(k)}}{\partial \rho_{\langle e\rangle}} - g_{\max}}\right)^{-1} \tag{5.17}$$

The denominator in Equation (5.17) is calculated by using Equations (5.12) and (5.14). The gradient of sensitivity with respect to the density shown in the numerator of Equation (5.17) is obtained as

$$\begin{aligned}\frac{\partial^2 J^*_{\langle e\rangle}}{\partial \rho_{\langle e\rangle}{}^2} &= W_1\left\{\frac{\partial u_{\langle e\rangle}}{\partial \rho_{\langle e\rangle}}\right\}^T \frac{\partial\left[K_{\langle e\rangle}\right]}{\partial \rho_{\langle e\rangle}}\left\{u_{\langle e\rangle}\right\} + \frac{1}{2}W_1\left\{u_{\langle e\rangle}\right\}^T \frac{\partial^2\left[K_{\langle e\rangle}\right]}{\partial \rho_{\langle e\rangle}{}^2}\left\{u_{\langle e\rangle}\right\} \\ &+\frac{1}{2}W_2\left(\frac{1}{p}-1\right)G^{\frac{1}{p}-2}\frac{\partial G}{\partial \rho_e}\rho_{\langle e\rangle}{}^{\frac{p}{2}-1}\sigma_{\langle e\rangle}{}^p V_{\langle e\rangle} + \frac{1}{2}W_2\left(\frac{p}{2}-1\right)G^{\frac{1}{p}-1}\rho_{\langle e\rangle}{}^{\frac{p}{2}-2}\sigma_{VM\langle e\rangle}{}^p V_{\langle e\rangle} \\ &+\frac{1}{2}W_2 pG^{\frac{1}{p}-1}\rho_{\langle e\rangle}{}^{\frac{p}{2}-1}\sigma_{VM\langle e\rangle}{}^{p-1}\frac{\partial \sigma_{VM\langle e\rangle}}{\partial \rho_{\langle e\rangle}}V_{\langle e\rangle} + \left\{\frac{\partial \lambda_{\langle e\rangle}}{\partial \rho_{\langle e\rangle}}\right\}^T \frac{\partial\left[K_{\langle e\rangle}\right]}{\partial \rho_{\langle e\rangle}}\left\{\frac{\partial u_{\langle e\rangle}}{\partial \rho_{\langle e\rangle}}\right\} \\ &+\left\{\lambda_{\langle e\rangle}\right\}^T \frac{\partial^2\left[K_{\langle e\rangle}\right]}{\partial \rho_{\langle e\rangle}{}^2}\left\{u_{\langle e\rangle}\right\} + \left\{\lambda_{\langle e\rangle}\right\}^T \frac{\partial\left[K_{\langle e\rangle}\right]}{\partial \rho_{\langle e\rangle}}\left\{\frac{\partial u_{\langle e\rangle}}{\partial \rho_{\langle e\rangle}}\right\}\end{aligned} \tag{5.18}$$

Differentiating the governing equation shown in Equation (5.4) by the density, it is calculated as

$$\frac{\partial\left[K_{\langle e\rangle}\right]}{\partial \rho_{\langle e\rangle}}\left\{u_{\langle e\rangle}\right\} + \left[K_{\langle e\rangle}\right]\left\{\frac{\partial u_{\langle e\rangle}}{\partial \rho_{\langle e\rangle}}\right\} = \{0\} \tag{5.19}$$

The gradient of the Lagrange multiplier vector with respect to the density in Equation (5.18) is an unknown. Thus, by differentiating the adjoint equation shown in Equation (5.11) by density, the gradient of the Lagrange multiplier vector with respect to the density is obtained

as

$$\begin{aligned}\left\{\frac{\partial\lambda_{\langle e\rangle}}{\partial\rho_{\langle e\rangle}}\right\}^T\left[K_{\langle e\rangle}\right] &= -\left\{\lambda_{\langle e\rangle}\right\}^T\frac{\partial\left[K_{\langle e\rangle}\right]}{\partial\rho_{\langle e\rangle}} - W_1\left\{u_{\langle e\rangle}\right\}^T\frac{\partial\left[K_{\langle e\rangle}\right]}{\partial\rho_{\langle e\rangle}} - W_1\left\{\frac{\partial u_{\langle e\rangle}}{\partial\rho_{\langle e\rangle}}\right\}^T\left[K_{\langle e\rangle}\right] \\ &\quad -W_2\left(\frac{1}{p}-1\right)G^{\frac{1}{p}-2}\frac{\partial G}{\partial\rho_{\langle e\rangle}}{\rho_{\langle e\rangle}}^{\frac{p}{2}}{\sigma_{VM\langle e\rangle}}^{p-1}V_{\langle e\rangle}\left\{\frac{\partial\sigma_{VM\langle e\rangle}}{\partial u_{\langle e\rangle}}\right\}^T \\ &\quad -\frac{1}{2}W_2pG^{\frac{1}{p}-1}{\rho_{\langle e\rangle}}^{\frac{p}{2}-1}{\sigma_{VM\langle e\rangle}}^{p-1}V_{\langle e\rangle}\left\{\frac{\partial\sigma_{VM\langle e\rangle}}{\partial u_{\langle e\rangle}}\right\}^T \\ &\quad -W_2\left(p-1\right)G^{\frac{1}{p}-1}{\rho_{\langle e\rangle}}^{\frac{p}{2}}{\sigma_{VM\langle e\rangle}}^{p-2}V_{\langle e\rangle}\frac{\partial\sigma_{VM\langle e\rangle}}{\partial\rho_{\langle e\rangle}}\left\{\frac{\partial\sigma_{VM\langle e\rangle}}{\partial u_{\langle e\rangle}}\right\}^T \\ &\quad -W_2G^{\frac{1}{p}-1}{\rho_{\langle e\rangle}}^{\frac{p}{2}}{\sigma_{VM\langle e\rangle}}^{p-1}V_{\langle e\rangle}\frac{\partial}{\partial\rho_{\langle e\rangle}}\left(\left\{\frac{\partial\sigma_{VM\langle e\rangle}}{\partial u_{\langle e\rangle}}\right\}^T\right)\end{aligned} \tag{5.20}$$

From Equations (5.19) and (5.20), Equation (5.18) is written as

$$\begin{aligned}\frac{\partial^2 J^*_{\langle e\rangle}}{\partial{\rho_{\langle e\rangle}}^2} &= W_1\left\{\frac{\partial u_{\langle e\rangle}}{\partial\rho_{\langle e\rangle}}\right\}^T\frac{\partial\left[K_{\langle e\rangle}\right]}{\partial\rho_{\langle e\rangle}}\left\{u_{\langle e\rangle}\right\} + \frac{1}{2}W_1\left\{u_{\langle e\rangle}\right\}^T\frac{\partial^2\left[K_{\langle e\rangle}\right]}{\partial{\rho_{\langle e\rangle}}^2}\left\{u_{\langle e\rangle}\right\} \\ &\quad +\frac{1}{2}W_2\left(\frac{1}{p}-1\right)G^{\frac{1}{p}-2}\frac{\partial G}{\partial\rho_e}{\rho_{\langle e\rangle}}^{\frac{p}{2}-1}{\sigma_{VM\langle e\rangle}}^pV_{\langle e\rangle} \\ &\quad +\frac{1}{2}W_2\left(\frac{p}{2}-1\right)G^{\frac{1}{p}-1}{\rho_{\langle e\rangle}}^{\frac{p}{2}-2}{\sigma_{VM\langle e\rangle}}^pV_{\langle e\rangle} \\ &\quad +W_2\left(\frac{1}{p}-1\right)G^{\frac{1}{p}-2}\frac{\partial G}{\partial\rho_{\langle e\rangle}}{\rho_{\langle e\rangle}}^{\frac{p}{2}}{\sigma_{VM\langle e\rangle}}^{p-1}V_{\langle e\rangle}\frac{\partial\sigma_{VM\langle e\rangle}}{\partial\rho_{\langle e\rangle}} \\ &\quad +W_2\left(p-1\right)G^{\frac{1}{p}-1}{\rho_{\langle e\rangle}}^{\frac{p}{2}}{\sigma_{VM\langle e\rangle}}^{p-2}\frac{\partial\sigma_{VM\langle e\rangle}}{\partial\rho_{\langle e\rangle}}V_{\langle e\rangle}\frac{\partial\sigma_{VM\langle e\rangle}}{\partial\rho_{\langle e\rangle}} \\ &\quad +W_2G^{\frac{1}{p}-1}{\rho_{\langle e\rangle}}^{\frac{p}{2}}{\sigma_{VM\langle e\rangle}}^{p-1}V_{\langle e\rangle}\frac{\partial}{\partial\rho_{\langle e\rangle}}\left(\left\{\frac{\partial\sigma_{VM\langle e\rangle}}{\partial u_{\langle e\rangle}}\right\}^T\right)\left\{\frac{\partial u_{\langle e\rangle}}{\partial\rho_{\langle e\rangle}}\right\} \\ &\quad +2\left\{\lambda_{\langle e\rangle}\right\}^T\frac{\partial\left[K_{\langle e\rangle}\right]}{\partial\rho_{\langle e\rangle}}\left\{\frac{\partial u_{\langle e\rangle}}{\partial\rho_{\langle e\rangle}}\right\} + \left\{\lambda_{\langle e\rangle}\right\}^T\frac{\partial\left[K_{\langle e\rangle}\right]}{\partial\rho_{\langle e\rangle}}\left\{\frac{\partial u_{\langle e\rangle}}{\partial\rho_{\langle e\rangle}}\right\}\end{aligned} \tag{5.21}$$

where the function of the gradient of the von Mises stress with respect to the displacement differentiated by density is shown in Equations (3.29) to (3.33) In addition, instead of just mapping, the map function is defined as follows to maintain the size of the update length trend before mapping, as shown in Figure 5.2.

$$\Theta^{(k)}_{\langle e\rangle} = \Theta^{(k)}_{\min} + \left(\Theta^{(k)}_{\max} - \Theta^{(k)}_{\min}\right)\cdot\frac{\theta^{(k)}_{\langle e\rangle} - \theta^{(k)}_{\min}}{\theta^{(k)}_{\max} - \theta^{(k)}_{\min}} \tag{5.22}$$

Here, $\Theta_{\max}^{(k)}$, $\Theta_{\min}^{(k)}$, $\theta_{\max}^{(k)}$, and $\theta_{\min}^{(k)}$ are the upper limit after mapping, the lower limit after mapping, the maximum value before mapping, and the minimum value before mapping, respectively. In addition, $\theta_{\langle e \rangle}^{(k)}$ is a function of the exponent in the modified OC method and is shown in

$$\theta_{\langle e \rangle}^{(k)} = -\frac{\frac{\partial \bar{J^*_{\langle e \rangle}}^{(k)}}{\partial \rho_{\langle e \rangle}}}{\frac{\partial^2 J^*_{\langle e \rangle}(k)}{\partial {\rho_{\langle e \rangle}}^2}} \tag{5.23}$$

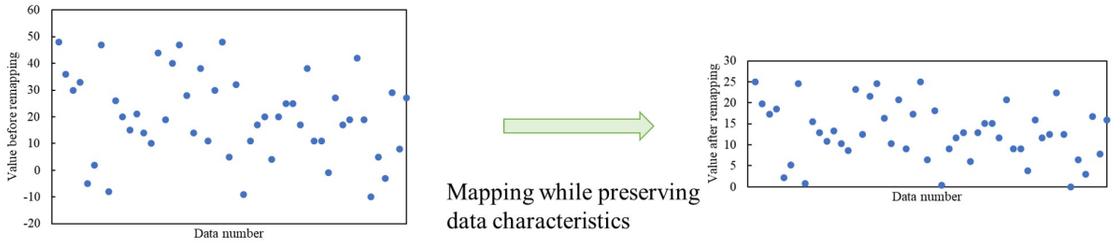

Figure 5.2: Example of mapping function.

5.3 Flow of density-based topology optimization in multi-objective optimization

This section described the flow of the density-based topology optimization in multi-objective optimization for strain energy minimization and von Mises stress minimization. The general flow of the optimization is the same as the flowchart for topology optimization to minimize strain energy, shown in Figure 2.6 in the previous chapter. The detailed procedure is as follows.

1. Input of the computation model and calculation conditions shown in next section.

2. The finite element analysis for linear elastic body is performed. The governing equation shown in Equation (5.4) is used to obtain the displacement vector $\{u\}$.

3. The extended performance function is calculated. Using the displacement vector $\{u\}$ obtained in the previous step, the performance functions shown in Equation (5.2) and (5.3) are calculated.

4. If the judgement of convergence $k < k_{\max}$ is satisfied, the computation is finalized. Otherwise, go to the next step.

5. The sensitivity, which is the gradient of the Lagrange function $J^*_{\langle e \rangle}$ with respect to the density $\rho_{\langle e \rangle}$, is calculated. From the adjoint equation shown in Equation (5.11), the Lagrange multiplier vector $\{\lambda\}$ is obtained. After that, using the Lagrange multiplier vector $\{\lambda\}$, the sensitivity is calculated.

6. The sensitivity filter shown in Equation (2.72) is applied.

7. The density $\rho_{\langle e \rangle}$, which is the design variable, is updated. When using the OC method, Equations (2.18) and (5.15) is employed, and when using the mapping-based modified OC method, Equations (5.16) to (5.23) are employed. After updating, the number of iterations is updated to the $k+1$-th step and the process returns to step 2.

5.4 Calculation conditions of density-based topology optimization in multi-objective optimization

This section described the calculation model and conditions used in this chapter. Multi-objective topology optimization is performed to minimize the strain energy and von Mises stress in steady problems. As with other topology optimizations, the MBB beam model shown in Figure 5.3 is used to verify the dependence of the move-limit ρ_{move}. Topology optimization will then be performed for the gripper of the robotic arm, which works an important role in the increasingly automated industry. The configuration of the robotic arm and the calculation model of the gripper are shown in Figure 5.4. To assume an optimum design of the gripper at the tip in Figure 5.4(a), a load is added assuming that it is completely

fixed and the workpiece is gripped on the side as shown in Figure 5.4(b). The load is uniformly distributed load of total load 100 [N]. The two dimensional models shown in Figures 5.3 and 5.4(b) use a 4-node quadrilateral element and has a structural grid divided by squares of 1 [mm] per side. Here, the topology optimization is performed when the move-limit ρ_{move} is set to 0.01, 0.10, and 1.00. The initial density in the design domain Ω is given uniformly by $\bar{\rho_0}$. Similar to the hook model, the gripper model has the design domain Ω and the non-design domain Ω_{non}. The non-design domain Ω_{non} is always updated so that the density value is zero. $\rho_{\text{move}} = 0.01$ is the problem setting for finding an optimum solution, $\rho_{\text{move}} = 0.30$ is the problem setting for a slightly larger setting, and $\rho_{\text{move}} = 1.00$ is the problem as without move-limit ρ_{move}. Since this chapter is conducted in addition to the study of changing the weight coefficient of the weighted sum method, five different ratios of w_1 to w_2 are set: 1 : 5, 1 : 3, 1 : 1, 3 : 1, and 5 : 1. Table 5.1 shows the other calculation conditions.

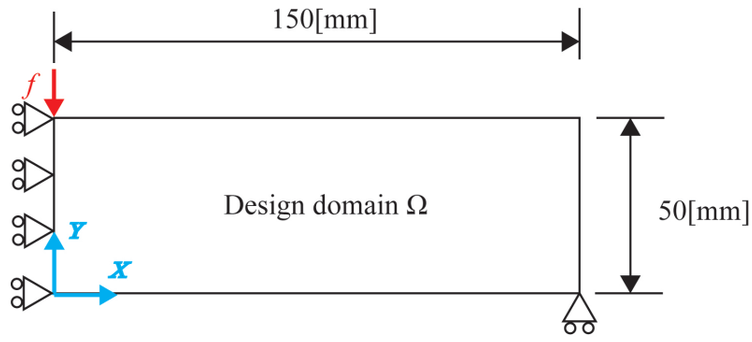

Figure 5.3: Computation model for MBB beam on two dimension in multi–objective optimization problems.

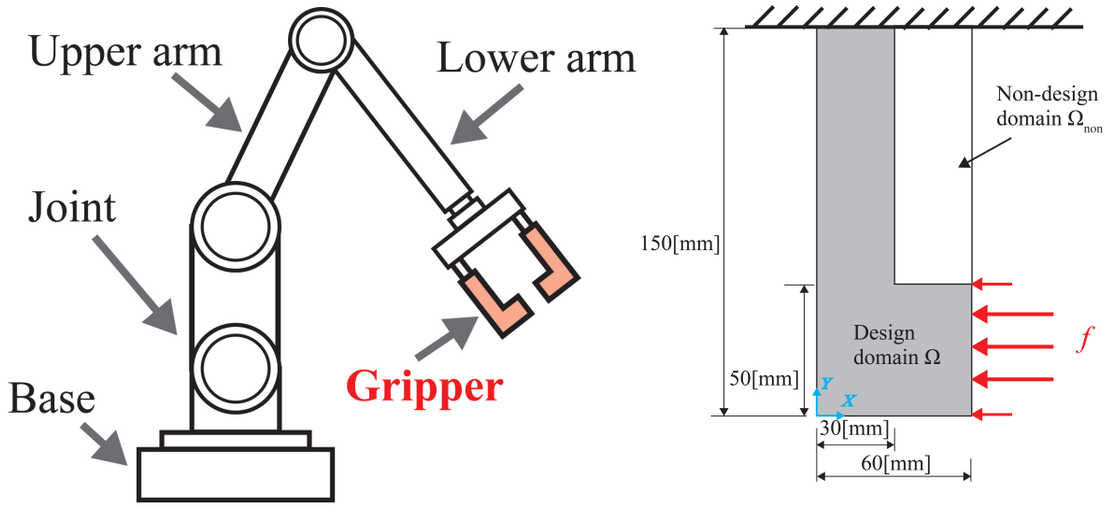

(a) Robotic arm.

(b) Gripper model (calculation model).

Figure 5.4: Computation model for the gripper of robotic arm on two dimension in multi–objective optimization problems.

Table 5.1: Calculation conditions of topology optimization for multi–objective optimization problems.

Model	MBB beam	Gripper
Number of elements	7500	9000
Number of nodes	7701	9211
Penalization parameter for p–norm, p	6.0	6.0
Penalization parameter for the SIMP method, p_s	3.0	3.0
Initial density average, $\bar{\rho}_0$	0.25	0.50
Weighting factor for the OC method, η	0.75	0.75
Filter radius, R	1.25	1.25
Upper limit of the range after remapping, $\Theta_{\max}^{(k)}$	1.0	1.0
Lower limit of the range after remapping, $\Theta_{\min}^{(k)}$	0.1	0.1
Maximum number of iterations, $k_{\max}$	400	1000
Young's modulus, E_0[Pa]	210×10^9	210×10^9
Poisson ratio, ν	0.3	0.3

5.5 Results and considerations of density-based topology optimization in multi-objective optimization

5.5.1 Effect of move-limit on the results of density-based topology optimization in multi-objective optimization

Based on the results of multi-objective topology optimization for strain energy minimization and von Mises stress minimization in two dimensional MBB beam model, this section confirms that the optimization results depend on the setting of the move-limit ρ_{move}, even when using the mapping-based modified OC method. Figures 5.5 to 5.9 show the density

distributions at the final iteration when using the OC method and the mapping-based modified OC method with a different ratio of w_1 and w_2. From Figures 5.5 to 5.9, for any ratio of weight coefficients, the density distribution obtained by topology optimization when using the OC method is different depending on the value of the move-limit ρ_{move}. On the other hand, the density distribution obtained by topology optimization when using the mapping-based modified OC method is significantly different depending on the value of the move-limit ρ_{move}. It was confirmed that the results are similar to the results of topology optimization for strain energy minimization described in **chapter 2** and the results of topology optimization for von Mises stress minimization described in **chapter 3**. Thus, the update equation based on the modified OC method does not require the weighting factor η, reducing the parameter setting burden on engineers using topology optimization. Figures 5.10 to 5.14 show the history of performance function for each weight coefficient ratio. Sub caption (a) in those figures shows the history of performance function obtained by topology optimization when using the OC method, and (b) shows the history of performance function obtained by topology optimization when using the mapping-based modified OC method. From the history of performance function obtained by topology optimization when using the OC method shown in Figures 5.10(a) to 5.14(a), it can be confirmed that it converges to a certain value in all analysis. However, when the move-limit ρ_{move} is set to large value, the performance function temporarily increases, resulting in an unstable performance function history. On the other hand, the history of performance function obtained by topology optimization when using the mapping-based modified OC method shown in Figures 5.10(b) to 5.14(b) confirms that it steadily converges to a certain solution. Next, the difference in the normalized performance function is checked using

$$Diff = \frac{\left| J^{(k)} - J^{(k-1)} \right|}{J^0} \tag{5.24}$$

As well as the history of performance function, Figures 5.15 to 5.19 show the difference in the normalized performance function obtained by topology optimization using the OC method and mapping-based modified OC method when the weight coefficients are changed.

For both methods, the difference does not become small after a certain number of iterations. The result when using the OC method shown in Figures 5.15(a) to 5.19(a) show that the difference is largest when the move-limit ρ_{move} is set to 1.00. On the other hand, the result when using the mapping-based modified OC method shown in Figures 5.15(b) to 5.19(b) show that the difference is small even when the move-limit ρ_{move} is set to 1.00. Thus, it can be inferred that the convergence criterion may be smaller than that of the OC method. However, since a uniform decreasing trend has not been obtained, it is difficult to set the convergence criterion.

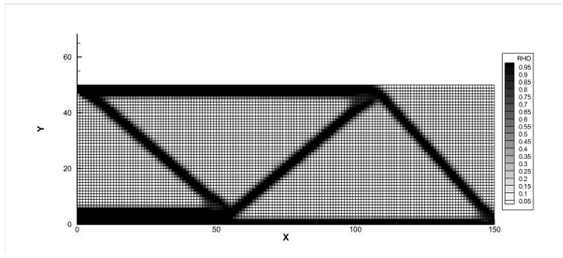

(a) When using the OC method ($\rho_{\text{move}} = 0.01$).

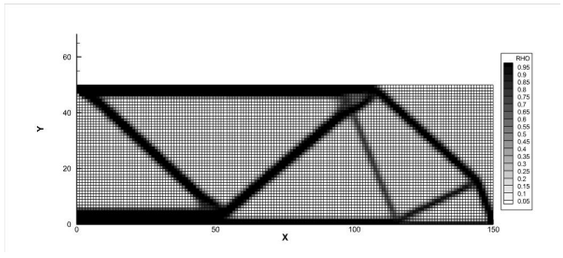

(b) When using the mapping–based modified OC method ($\rho_{\text{move}} = 0.01$).

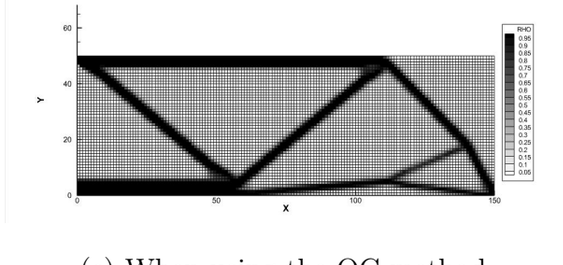

(c) When using the OC method ($\rho_{\text{move}} = 0.10$).

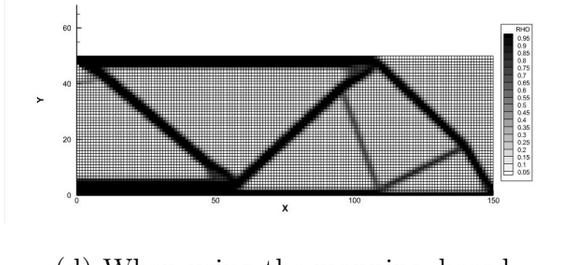

(d) When using the mapping–based modified OC method ($\rho_{\text{move}} = 0.10$).

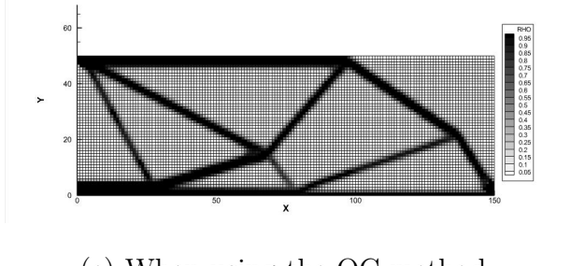

(e) When using the OC method ($\rho_{\text{move}} = 1.00$).

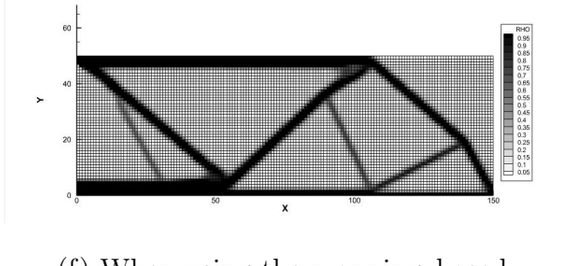

(f) When using the mapping–based modified OC method ($\rho_{\text{move}} = 1.00$).

Figure 5.5: Density distributions at final iteration of multi–objective topology optimization when $w_1 : w_2 = 1 : 5$ in the MBB beam model.

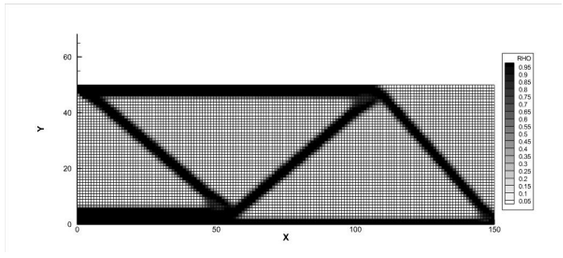

(a) When using the OC method ($\rho_{\text{move}} = 0.01$).

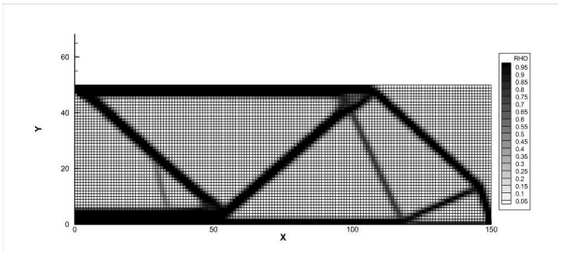

(b) When using the mapping–based modified OC method ($\rho_{\text{move}} = 0.01$).

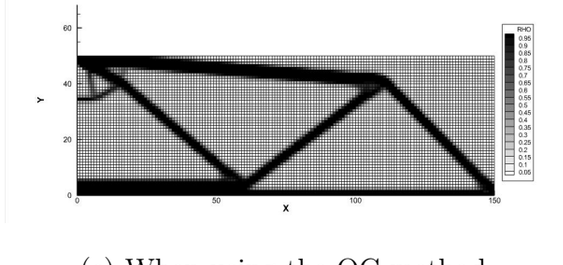

(c) When using the OC method ($\rho_{\text{move}} = 0.10$).

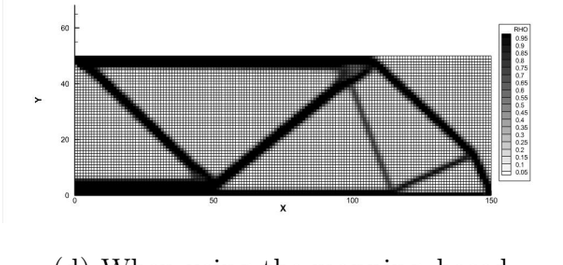

(d) When using the mapping–based modified OC method ($\rho_{\text{move}} = 0.10$).

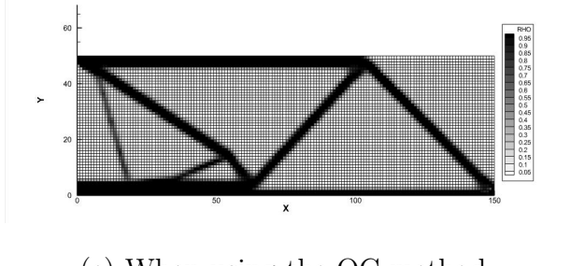

(e) When using the OC method ($\rho_{\text{move}} = 1.00$).

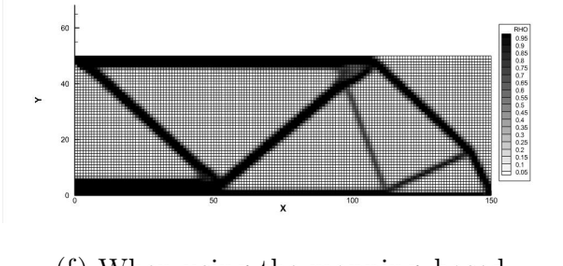

(f) When using the mapping–based modified OC method ($\rho_{\text{move}} = 1.00$).

Figure 5.6: Density distributions at final iteration of multi–objective topology optimization when $w_1 : w_2 = 1 : 3$ in the MBB beam model.

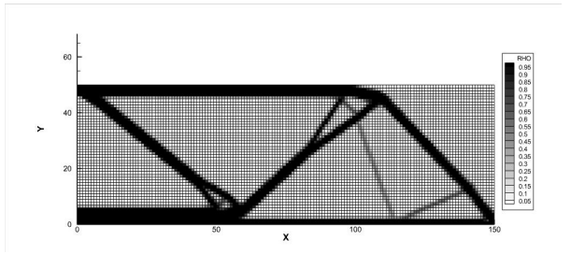

(a) When using the OC method ($\rho_{\text{move}} = 0.01$).

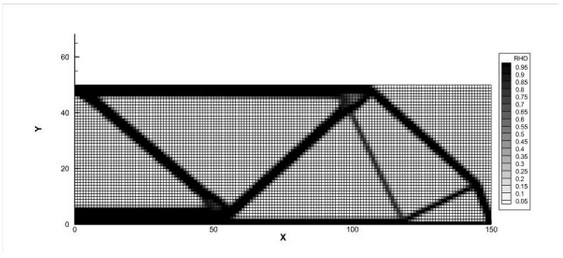

(b) When using the mapping–based modified OC method ($\rho_{\text{move}} = 0.01$).

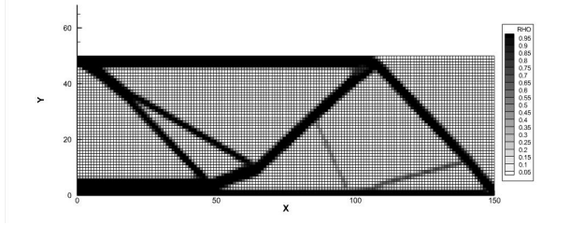

(c) When using the OC method ($\rho_{\text{move}} = 0.10$).

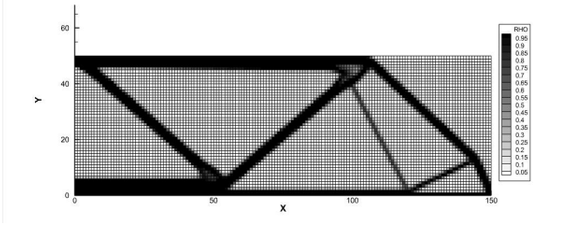

(d) When using the mapping–based modified OC method ($\rho_{\text{move}} = 0.10$).

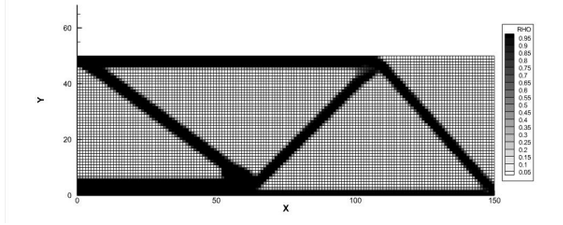

(e) When using the OC method ($\rho_{\text{move}} = 1.00$).

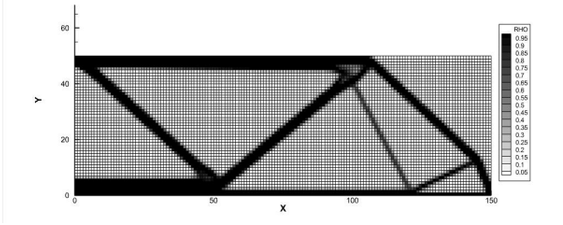

(f) When using the mapping–based modified OC method ($\rho_{\text{move}} = 1.00$).

Figure 5.7: Density distributions at final iteration of multi–objective topology optimization when $w_1 : w_2 = 1 : 1$ in the MBB beam model.

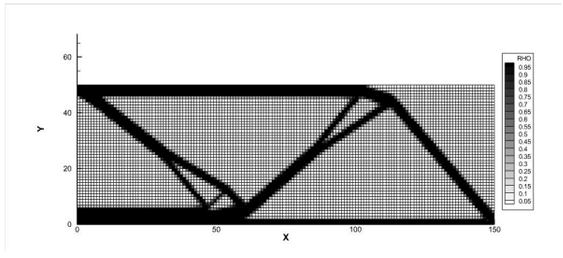

(a) When using the OC method ($\rho_{\text{move}} = 0.01$).

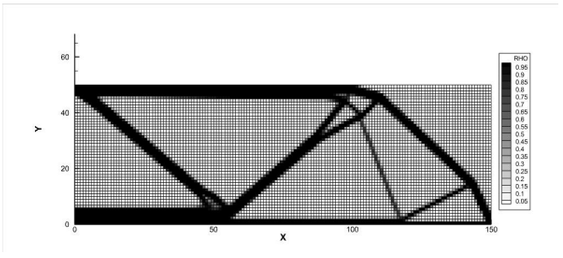

(b) When using the mapping–based modified OC method ($\rho_{\text{move}} = 0.01$).

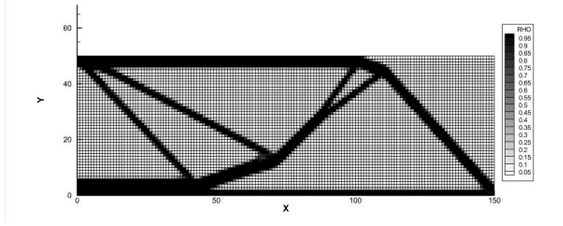

(c) When using the OC method ($\rho_{\text{move}} = 0.10$).

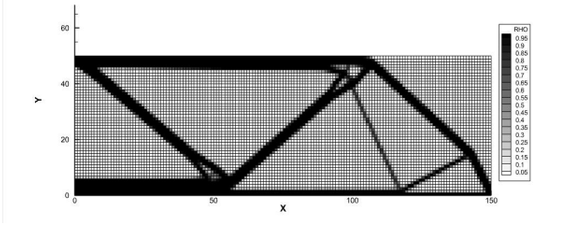

(d) When using the mapping–based modified OC method ($\rho_{\text{move}} = 0.10$).

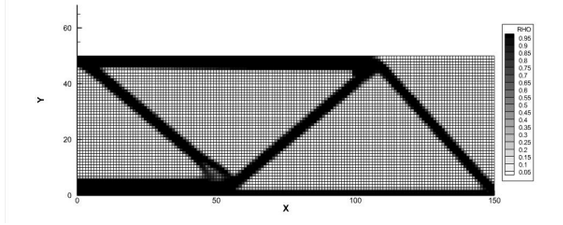

(e) When using the OC method ($\rho_{\text{move}} = 1.00$).

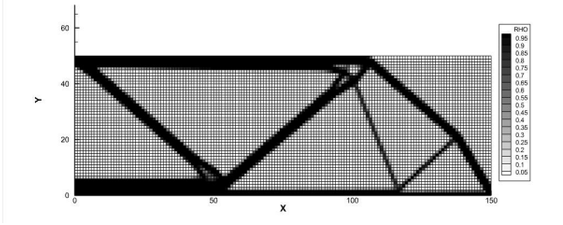

(f) When using the mapping–based modified OC method ($\rho_{\text{move}} = 1.00$).

Figure 5.8: Density distributions at final iteration of multi–objective topology optimization when $w_1 : w_2 = 3 : 1$ in the MBB beam model.

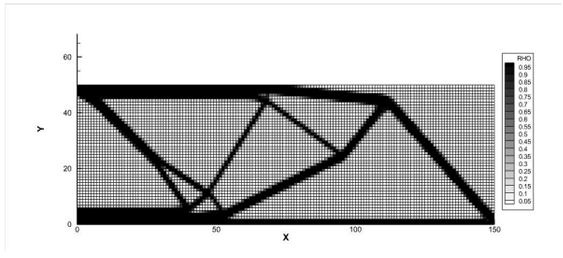

(a) When using the OC method ($\rho_{\text{move}} = 0.01$).

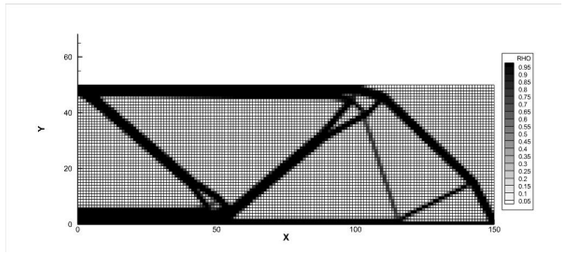

(b) When using the mapping–based modified OC method ($\rho_{\text{move}} = 0.01$).

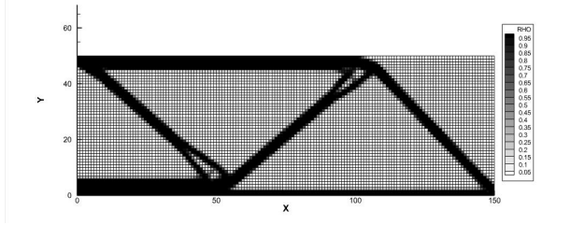

(c) When using the OC method ($\rho_{\text{move}} = 0.10$).

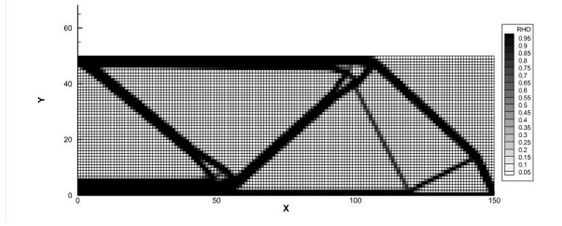

(d) When using the mapping–based modified OC method ($\rho_{\text{move}} = 0.10$).

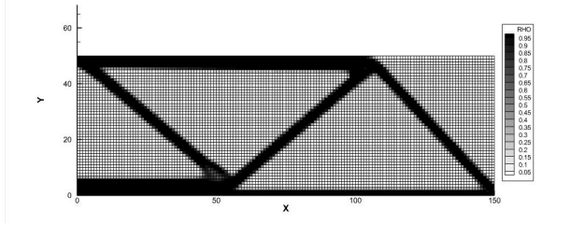

(e) When using the OC method ($\rho_{\text{move}} = 1.00$).

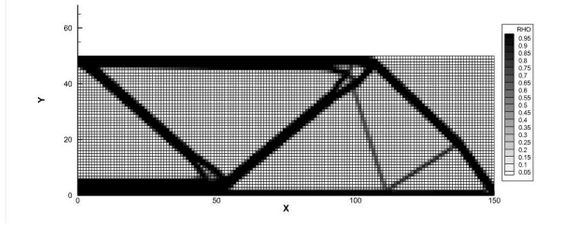

(f) When using the mapping–based modified OC method ($\rho_{\text{move}} = 1.00$).

Figure 5.9: Density distributions at final iteration of multi–objective topology optimization when $w_1 : w_2 = 5 : 1$ in the MBB beam model.

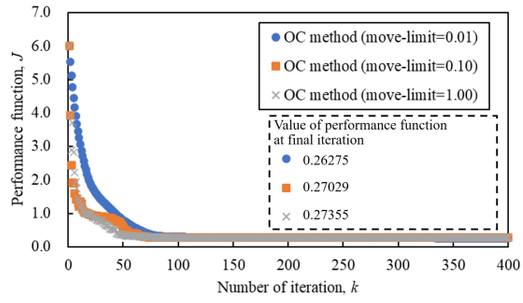

(a) When using the OC method.

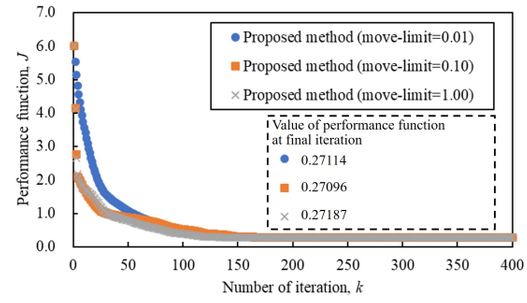

(b) When using the mapping–based modified OC method.

Figure 5.10: The history of performance functions for multi–objective topology optimization when $w_1 : w_2 = 1 : 5$ in the MBB beam model.

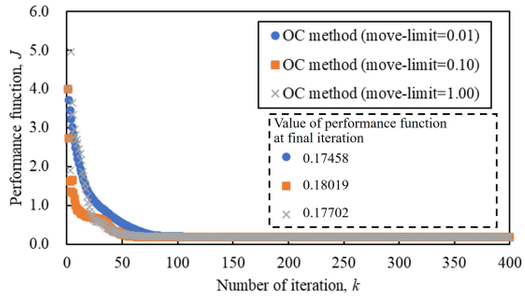

(a) When using the OC method.

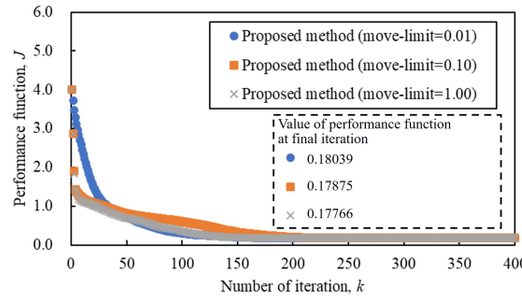

(b) When using the mapping–based modified OC method.

Figure 5.11: The history of performance functions for multi–objective topology optimization when $w_1 : w_2 = 1 : 3$ in the MBB beam model.

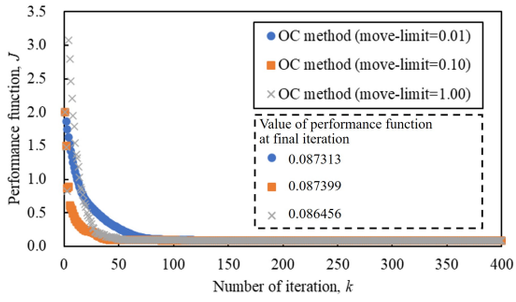

(a) When using the OC method.

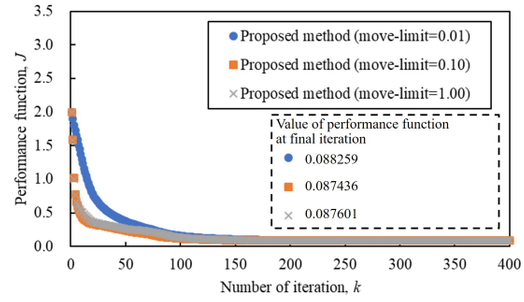

(b) When using the mapping–based modified OC method.

Figure 5.12: The history of performance functions for multi–objective topology optimization when $w_1 : w_2 = 1 : 1$ in the MBB beam model.

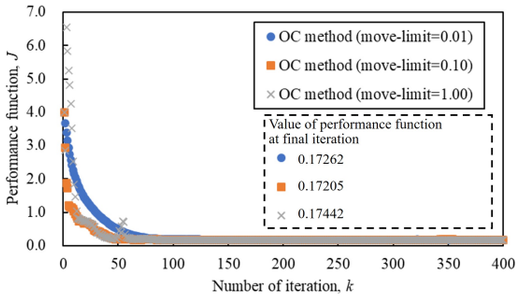

(a) When using the OC method.

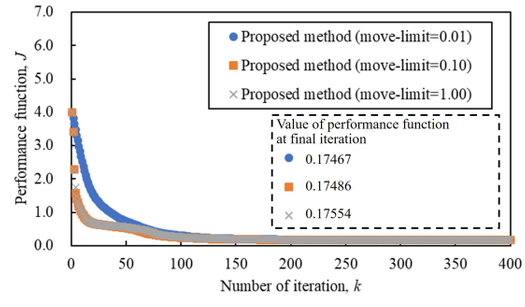

(b) When using the mapping–based modified OC method.

Figure 5.13: The history of performance functions for multi–objective topology optimization when $w_1 : w_2 = 3 : 1$ in the MBB beam model.

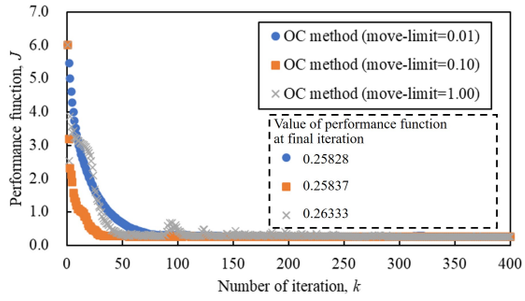

(a) When $w_1 : w_2 = 5 : 1$.

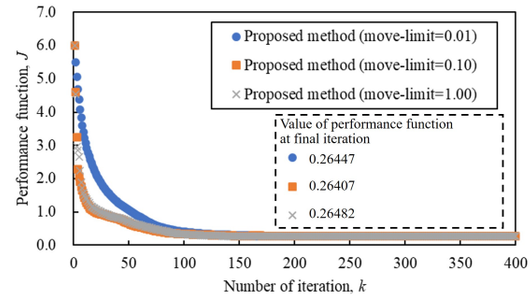

(b) When using the mapping–based modified OC method.

Figure 5.14: The history of performance functions for multi–objective topology optimization when $w_1 : w_2 = 5 : 1$ in the MBB beam model.

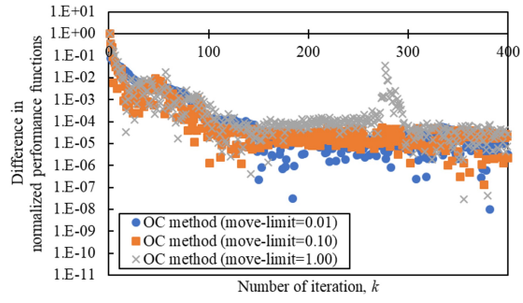

(a) When using the OC method.

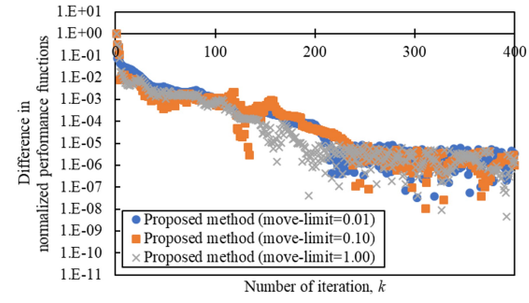

(b) When using the mapping–based modified OC method.

Figure 5.15: Difference in normalized performance functions for multi–objective topology optimization when $w_1 : w_2 = 1 : 5$ in the MBB beam model.

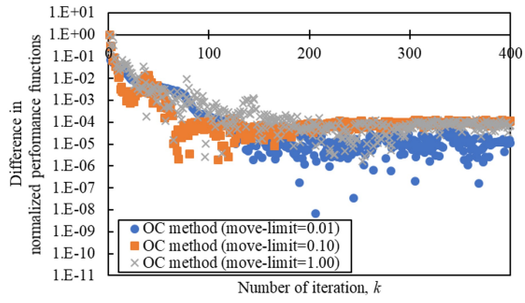

(a) When using the OC method.

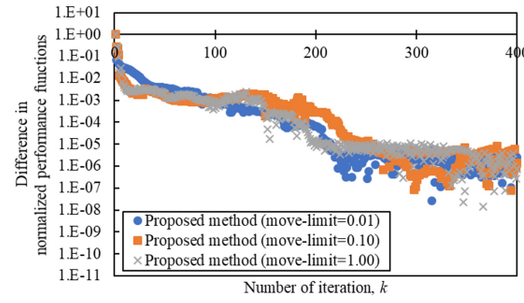

(b) When using the mapping–based modified OC method.

Figure 5.16: Difference in normalized performance functions for multi–objective topology optimization when $w_1 : w_2 = 1 : 3$ in the MBB beam model.

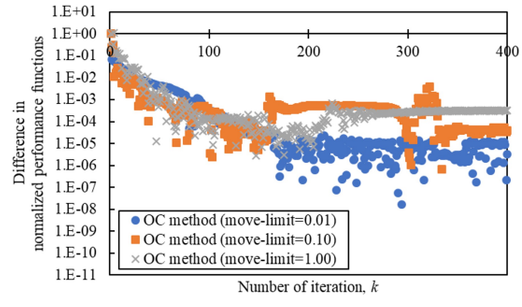

(a) When using the OC method.

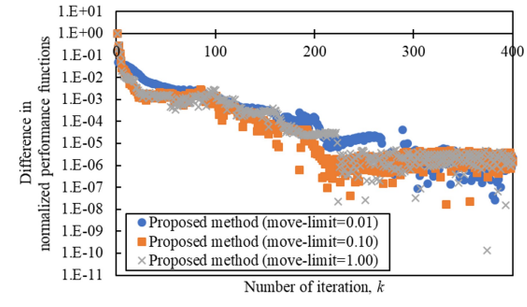

(b) When using the mapping–based modified OC method.

Figure 5.17: Difference in normalized performance functions for multi–objective topology optimization when $w_1 : w_2 = 1 : 1$ in the MBB beam model.

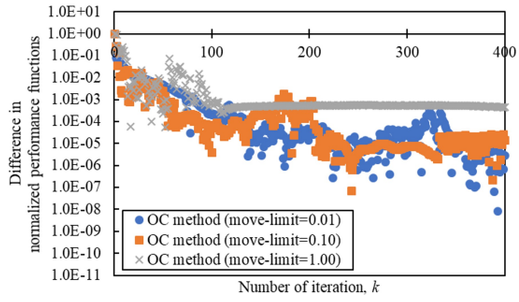

(a) When using the OC method.

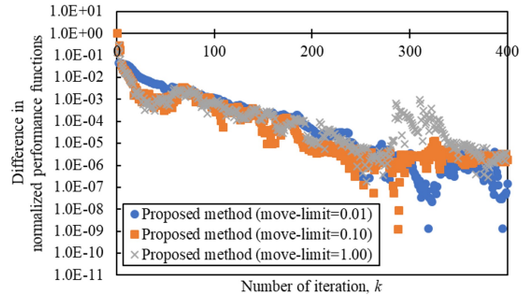

(b) When using the mapping–based modified OC method.

Figure 5.18: Difference in normalized performance functions for multi–objective topology optimization when $w_1 : w_2 = 3 : 1$ in the MBB beam model.

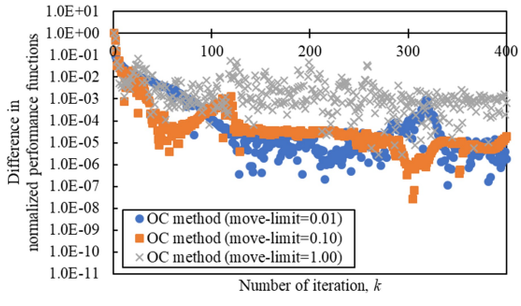

(a) When $w_1 : w_2 = 5 : 1$.

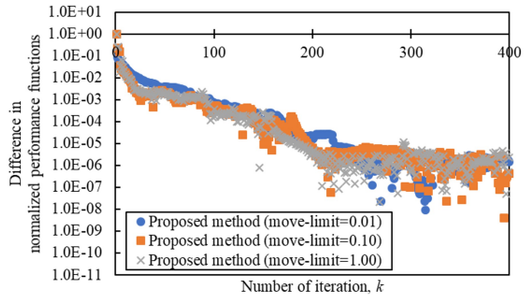

(b) When using the mapping–based modified OC method.

Figure 5.19: Difference in normalized performance functions for multi–objective topology optimization when $w_1 : w_2 = 5 : 1$ in the MBB beam model.

5.5.2 Effect of weight coefficients of weighted sum method on topology optimization results

In the previous subsection, the effect of the move-limit ρ_{move} on the results of topology optimization in multi-objective optimization was investigated, and it was confirmed that the move-limit ρ_{move} is less dependent on the topology optimization when using the mapping-based modified OC method. In this subsection, topology optimization when using the OC method and the mapping-based modified OC method is performed for the gripper of the robotic arm used in industry. Based on the results described in the previous subsection, the move-limit ρ_{move} is set to 0.01 when using the OC method, and it is set to 1.00 when using the mapping-based modified OC method. The aim of this subsection is to check how the values of performance function for strain energy minimization and von Mises stress minimization change with the ratio of the weight coefficients w_1 and w_2 in the weighted sum method. Figures 5.20 and 5.21 show the density distributions of topology optimization using the OC method and the mapping-based modified OC method when the ratio of the weight coefficients w_1 and w_2 is changed. Figures 5.20(a) and 5.21(a) show the density distribution obtained by topology optimization with $w_1 : w_2 = 1 : 5$, where the emphasis is on von Mises stress minimization, followed by an increasing weight on strain energy minimization more and more, and Figures 5.20(e) and 5.21(e) show the density distribution obtained by topology optimization with $w_1 : w_2 = 5 : 1$, where the emphasis is on strain energy minimization. Figures 5.20(c) and 5.21(c) show the density distribution obtained by topology optimization with $w_1 : w_2 = 1 : 1$. The density distributions shown in Figures 5.20 and 5.21 show that when the emphasis is on von Mises stress minimization, there is a grayscale in the density distribution, but when the emphasis is on strain energy minimization, the grayscale is suppressed. No significant differences in results were observed between the update methods. Although filter suppression has been the predominant method for suppressing grayscale, it was found that the grayscale can be suppressed by performing a multi-objective optimization problem combined with strain energy minimization. The topol-

ogy optimization for strain energy minimization can be solved stably. Also, adjusting the p in p norm for the von Mises stress minimization can also suppress grayscale. However, smaller values of p should be avoided as much as possible because the property of weighting elements with higher von Mises stress is diminished. Next, the displacement distribution is confirmed. In the gripper model, the displacement in X-direction is dominant due to the added load in X-direction. Therefore, Figures 5.22 and 5.23 show the distribution of displacement in X-direction obtained by topology optimization when using the OC method and the mapping-based modified OC method. Compared to the distribution of displacement in X-direction for the case with emphasis on von Mises stress minimization shown in Figures 5.22(a) and 5.23(a), the distribution of displacement in X-direction for the case with emphasis on strain energy minimization shown in Figures 5.22(e) and 5.23(e) has a smaller distribution of maximum displacement. The trend was that the distribution of maximum displacement decreased as the emphasis was placed on strain energy minimization. Next, the von Mises stress distribution is confirmed. Figures 5.24 and 5.25 show the von Mises stress distribution obtained by topology optimization when using the OC method and the mapping-based modified OC method. Similar to the displacement distribution shown in Figures 5.22 and 5.23, they show the von Mises stress distribution as weight coefficients are changed. Similary, the von Mises stress distribution for the case with emphasis on strain energy minimization shown in Figures 5.24(e) and 5.25(e) has fewer elements of maximum von Mises stress than one with emphasis on von Mises stress minimization shown in Figures 5.24(a) and 5.25(a). From the distributions of displacement and von Mises stress shown in Figures 5.22 and 5.25, the density distribution with numerous grayscale was found to have more displacement and higher von Mises stress. The displacement and von Mises stress were incorrectly evaluated due to grayscale, which is an intermediate material, and it can be assumed that these values became high. Next, the history of performance function is confirmed. Figure 5.26 shows the history of performance function obtained by topology optimization. The history of performance function is displayed on the logarithmic horizontal axis. From Figure 5.26, the history of performance function obtained by topology optimization when

using the mapping-based modified OC method decreased more rapidly than one when using the OC method. However, not all conditions decreased well, and in Figure 5.26(e), where too much emphasis is placed on strain energy minimization, the performance function is temporarily higher. The relationship between the performance functions of the normalized strain energy minimization and normalized von Mises stress minimization is shown in Figure 5.28. From Figure 5.28, when the emphasis is on von Mises stress minimization, both performance functions tend to be higher due to the presence of grayscale. This result can be inferred from the distributions of displacement and von Mises stress shown in Figures 5.22 to 5.25. And it can be seen that results for $w_1 : w_2 = 3 : 1$ and $w_1 : w_2 = 5 : 1$ when the emphasis is on strain energy minimization do not obtain significant differences. However, as mentioned earlier, care must be taken in setting up the problem, because in Figure 5.26(e), when too much emphasis is placed on strain energy minimization, the performance function temporarily becomes high. In addition, as in the previous sub section, Figure 5.27 shows the difference in the normalized performance function using Equation (5.24). In all conditions, when the number of iterations k approaches the maximum number of iterations $k_{\max}$, the difference in the normalized performance function using the mapping-based modified OC method is small. Finally, to investigate the cause of the remaining grayscale, the sensitivity at the final iteration and the function $\Theta_{\langle e \rangle}$ in the Mapping-based modified OC method are investigated. As a representative example, topology optimization with weight coefficient ratios $w_1 : w_2 = 1 : 3$ and $w_1 : w_2 = 3 : 1$ is discussed here. Figures 5.29 and 5.30 show the sensitivity distribution at the final iteration obtained by topology optimization when using the OC method and the mapping-based modified OC method. Although no significant differences can be observed between update methods, the sensitivity distributions, as shown in Figures 5.29(a) and 5.30(a), for the case where emphasis is placed on von Mises stress minimization show that even the grayscale elements have a sensitivity close to 0. On the other hand, the sensitivity distributions shown in Figures 5.29(b) and 5.30(b), when emphasis is placed on strain energy minimization, show greater than the sensitivity distribution shown in Figures 5.29(a) and 5.30(a). Since sensitivity is a value that indicates whether further

updates can be made, no grayscale reduction can be expected if the number of iterations is increased. This is because the sensitivity is close to 0. Figure 5.31 shows the distribution of the function $\Theta_{\langle e \rangle}$ in the mapping-based modified OC method. Figure 5.31(a) shows that the value of $\Theta_{\langle e \rangle}$ is small even for the grayscale elements, and it is close to the upper limit for the elements with low density values. In Figure 5.31(b), the function $\Theta_{\langle e \rangle}$ is higher for elements with low density values, but it is not an upper limit and the distribution is such that the boundaries of the structure can be seen. From this, it can be said that proper incorporation of the strain energy minimization problem leads to the suppression of grayscale.

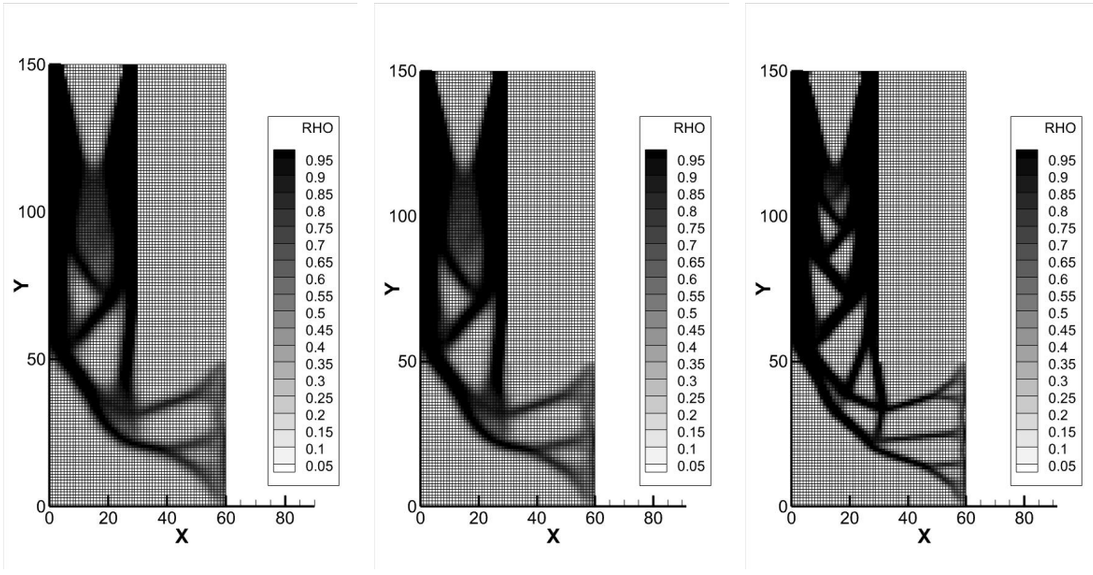

(a) When $w_1 : w_2 = 1 : 5$. (b) When $w_1 : w_2 = 1 : 3$. (c) When $w_1 : w_2 = 1 : 1$.

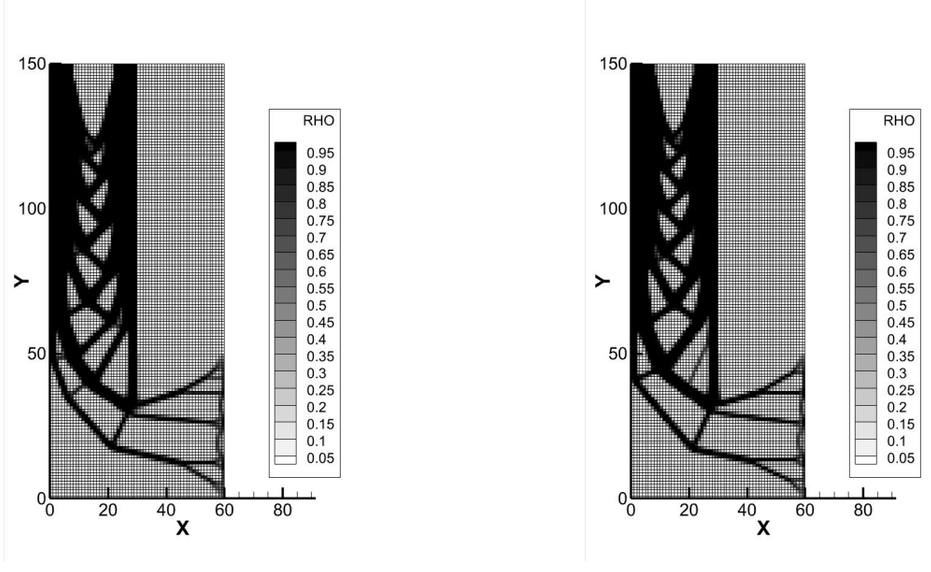

(d) When $w_1 : w_2 = 3 : 1$. (e) When $w_1 : w_2 = 5 : 1$.

Figure 5.20: Density distributions at final iteration of multi–objective topology optimization when using the OC method in the gripper model.

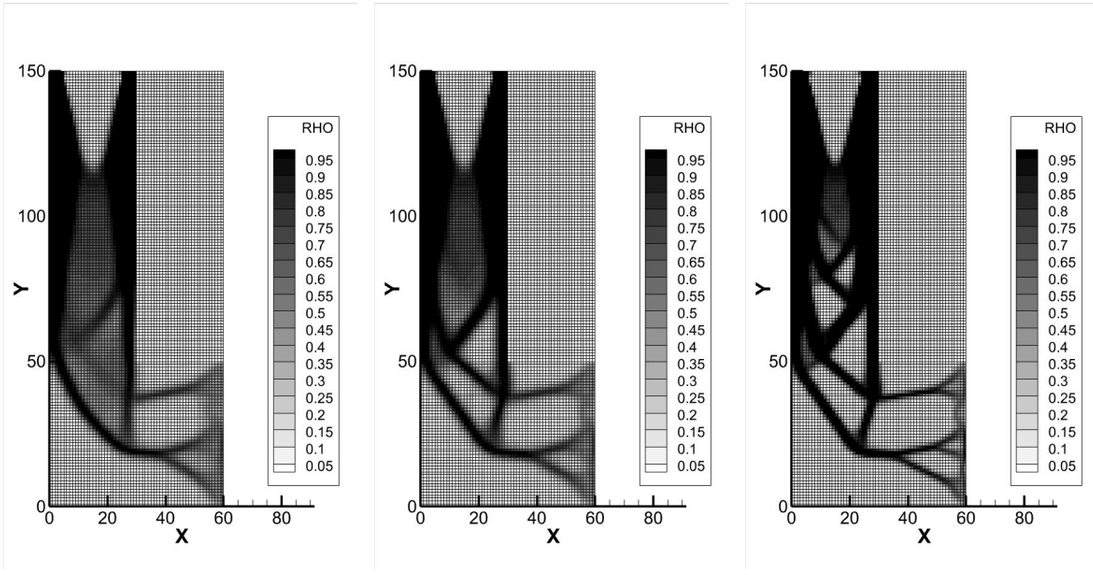

(a) When $w_1 : w_2 = 1 : 5$. (b) When $w_1 : w_2 = 1 : 3$. (c) When $w_1 : w_2 = 1 : 1$.

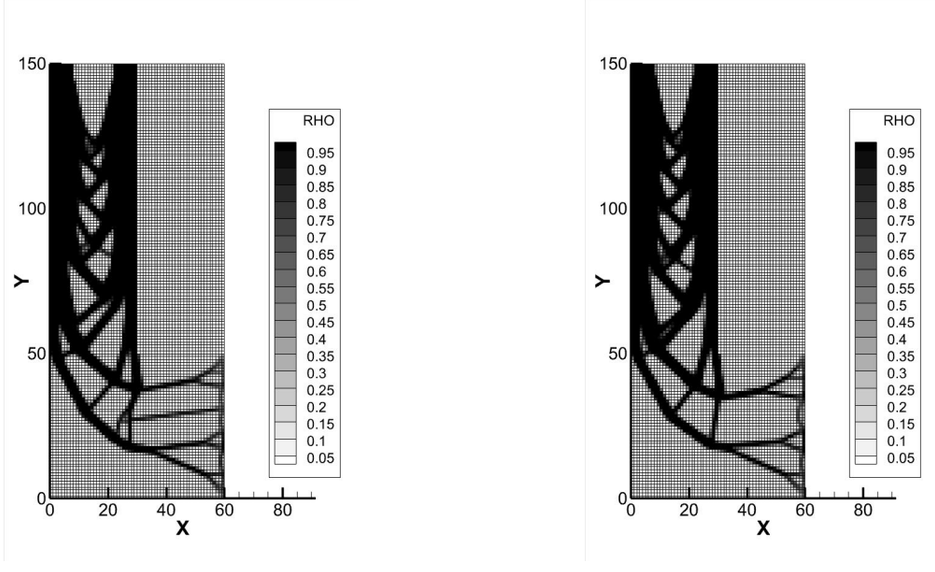

(d) When $w_1 : w_2 = 3 : 1$. (e) When $w_1 : w_2 = 5 : 1$.

Figure 5.21: Density distributions at final iteration of multi–objective topology optimization when using the mapping–based modified OC method in the gripper model.

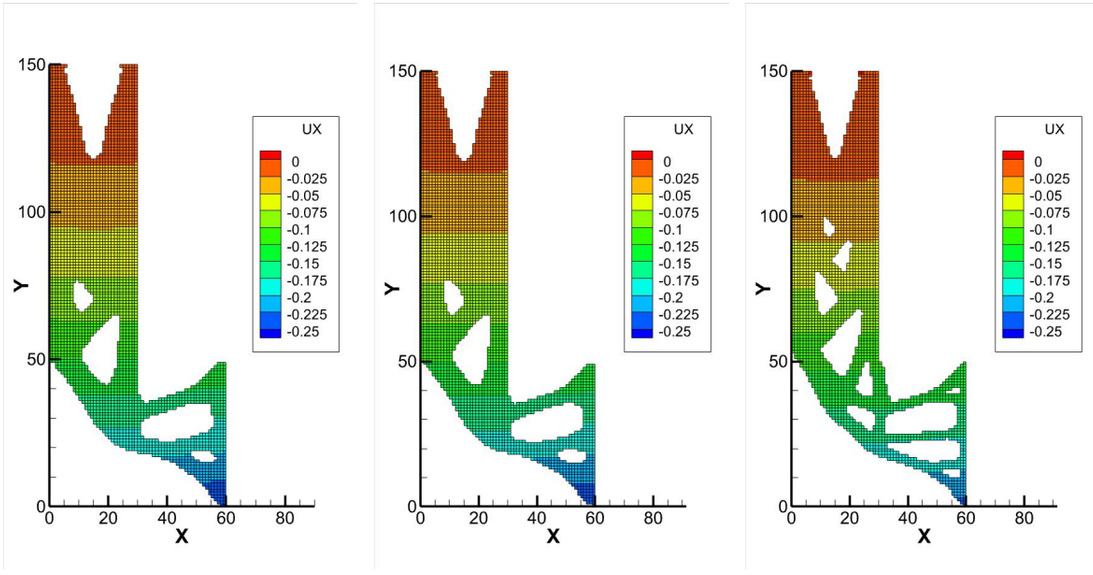

(a) When $w_1 : w_2 = 1 : 5$. (b) When $w_1 : w_2 = 1 : 3$. (c) When $w_1 : w_2 = 1 : 1$.

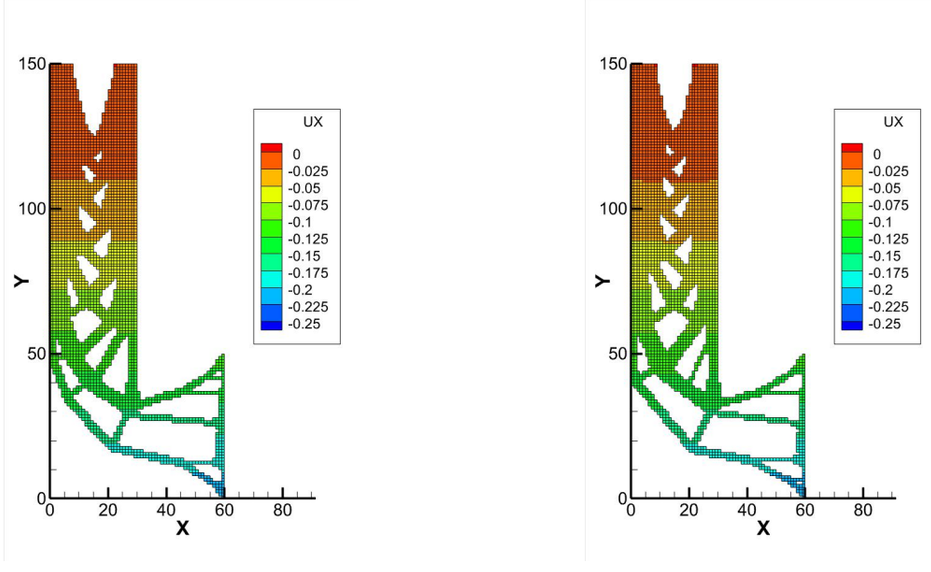

(d) When $w_1 : w_2 = 3 : 1$. (e) When $w_1 : w_2 = 5 : 1$.

Figure 5.22: Distributions of displacement in the X-direction at final iteration of multi–objective topology optimization when using the OC method in the gripper model.

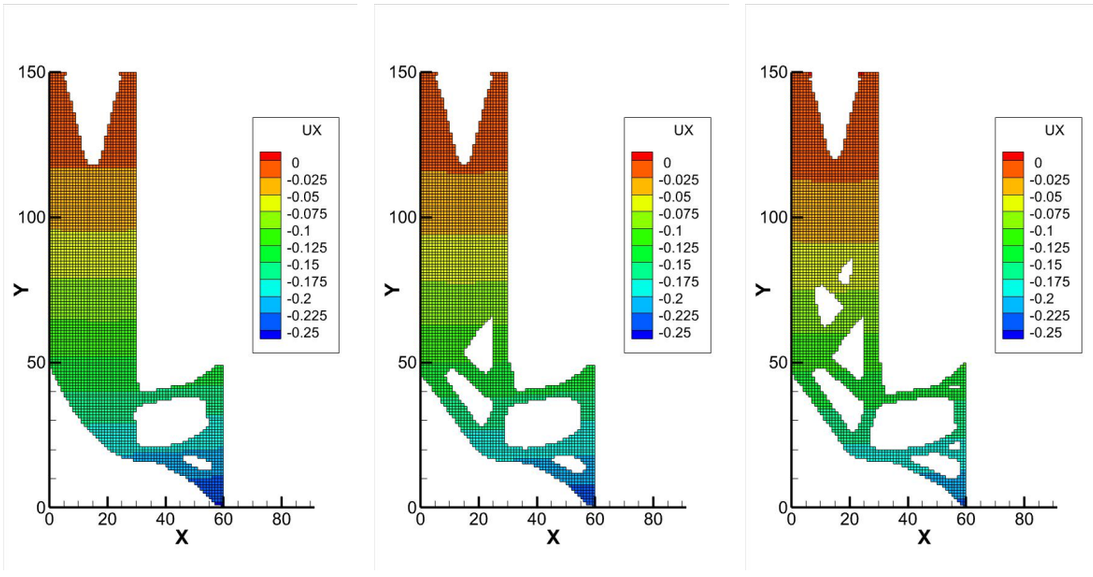

(a) When $w_1 : w_2 = 1 : 5$. (b) When $w_1 : w_2 = 1 : 3$. (c) When $w_1 : w_2 = 1 : 1$.

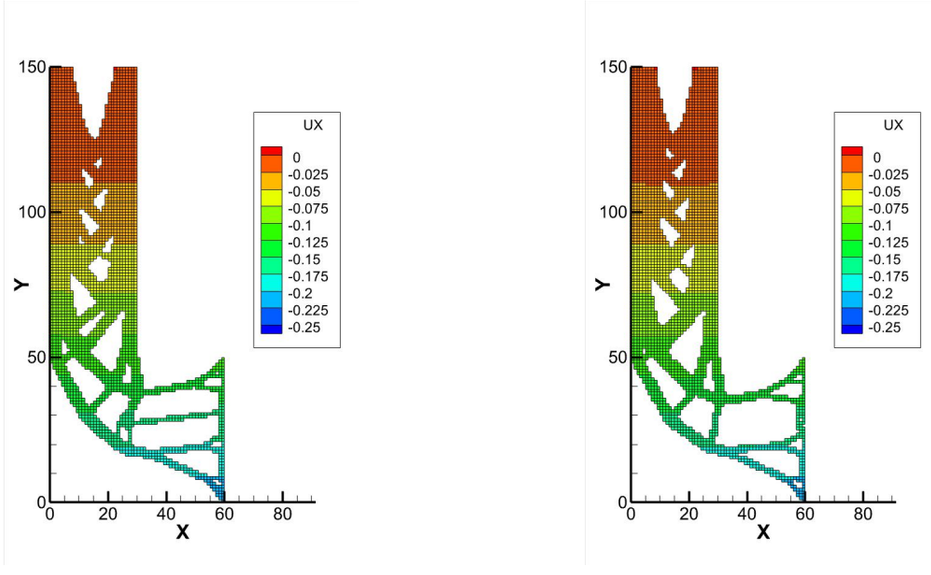

(d) When $w_1 : w_2 = 3 : 1$. (e) When $w_1 : w_2 = 5 : 1$.

Figure 5.23: Distributions of displacement in the X-direction at final iteration of multi–objective topology optimization when using the mapping–based modified OC method in the gripper model.

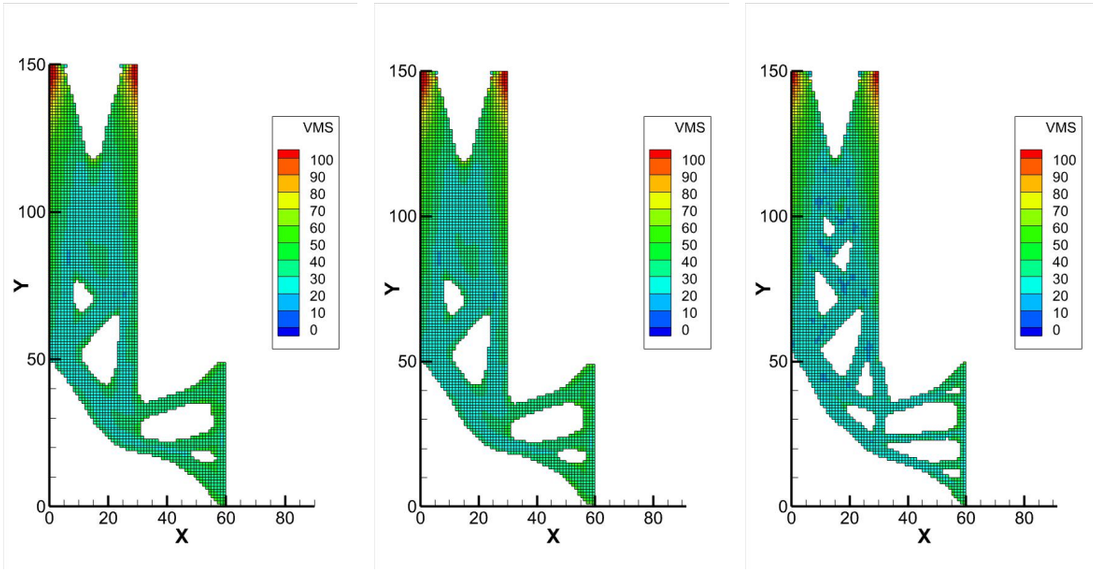

(a) When $w_1 : w_2 = 1 : 5$. (b) When $w_1 : w_2 = 1 : 3$. (c) When $w_1 : w_2 = 1 : 1$.

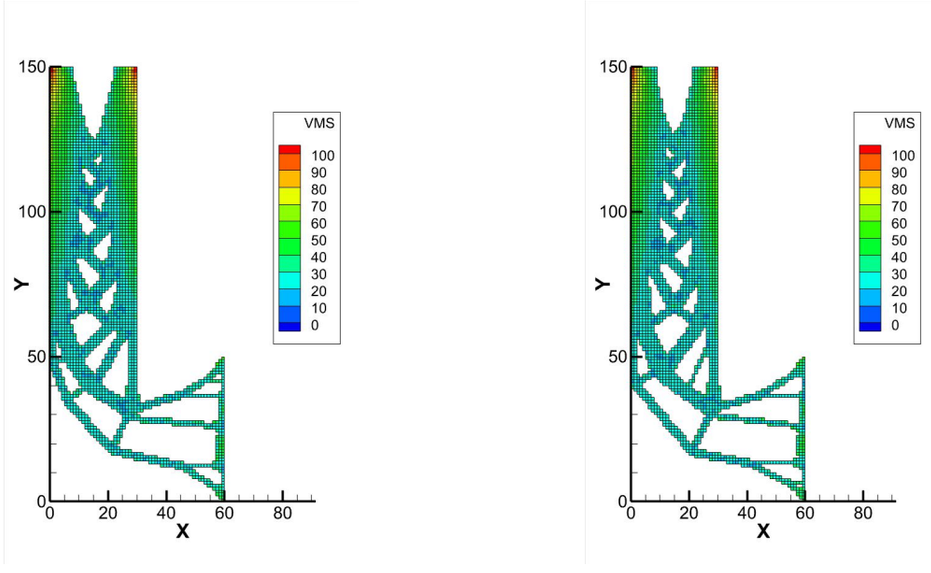

(d) When $w_1 : w_2 = 3 : 1$. (e) When $w_1 : w_2 = 5 : 1$.

Figure 5.24: Von Mises stress distributions at final iteration of multi–objective topology optimization when using the OC method in the gripper model.

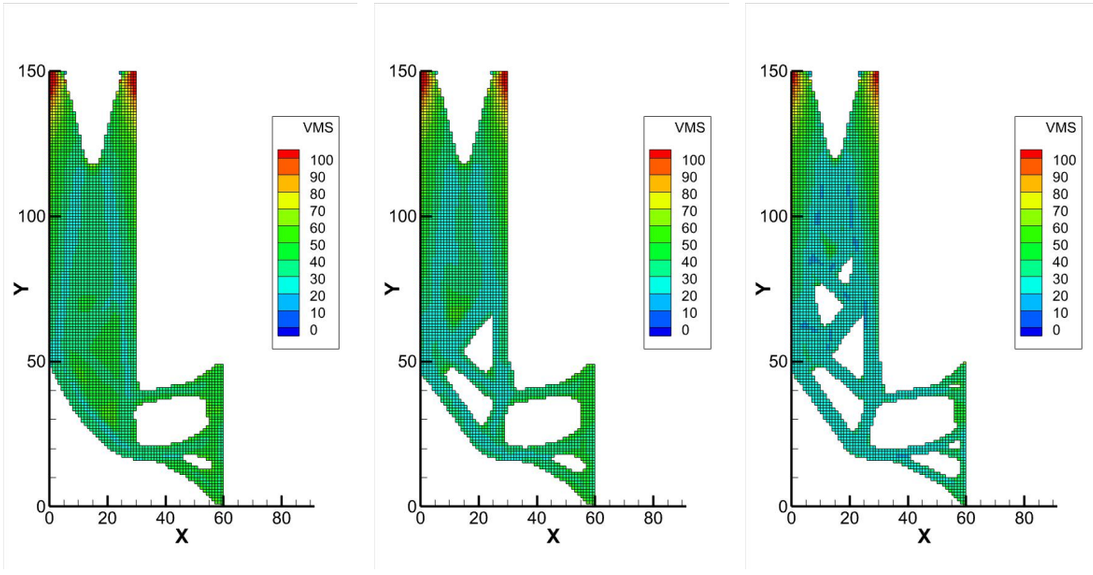

(a) When $w_1 : w_2 = 1 : 5$. (b) When $w_1 : w_2 = 1 : 3$. (c) When $w_1 : w_2 = 1 : 1$.

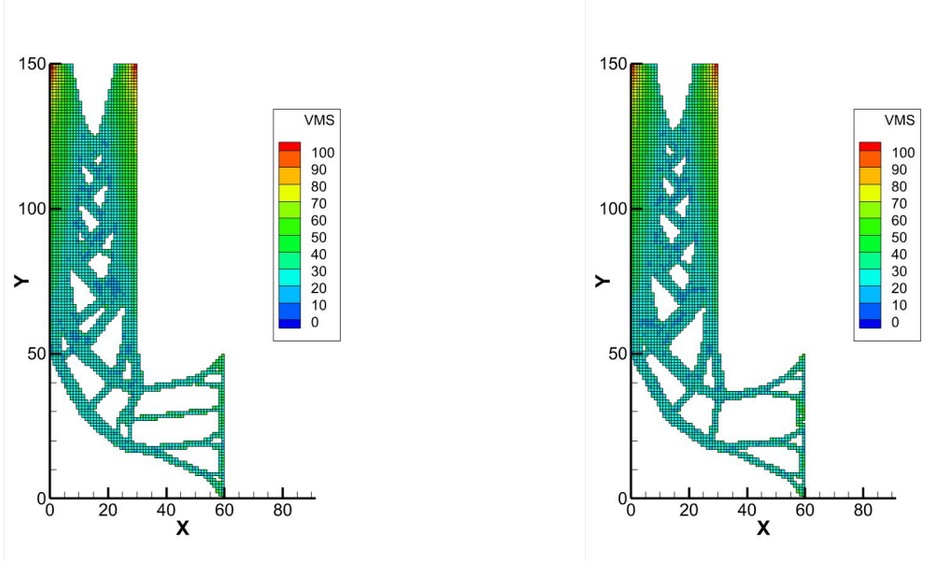

(d) When $w_1 : w_2 = 3 : 1$. (e) When $w_1 : w_2 = 5 : 1$.

Figure 5.25: Von Mises stress distributions at final iteration of multi–objective topology optimization when using the mapping–based modified OC method in the gripper model.

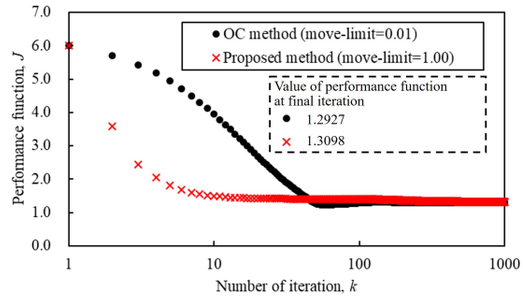

(a) When $w_1 : w_2 = 1 : 5$.

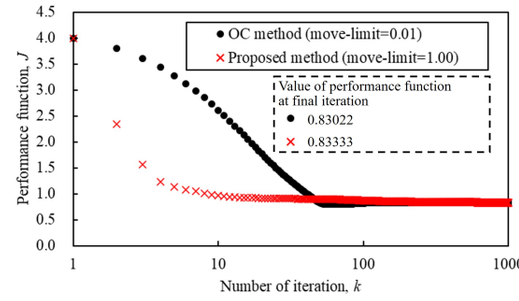

(b) When $w_1 : w_2 = 1 : 3$

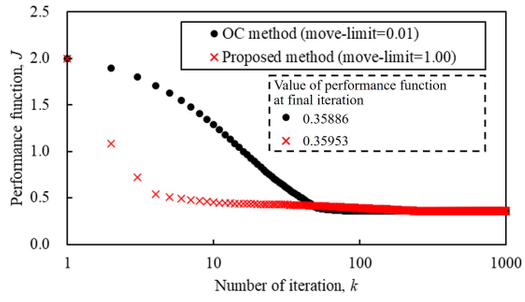

(c) When $w_1 : w_2 = 1 : 1$

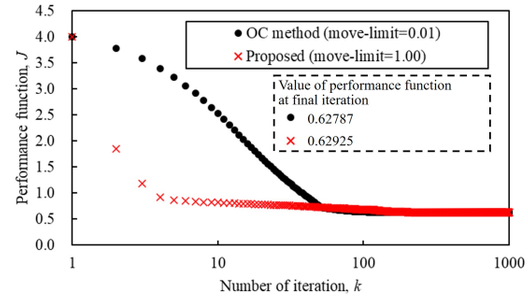

(d) When $w_1 : w_2 = 3 : 1$

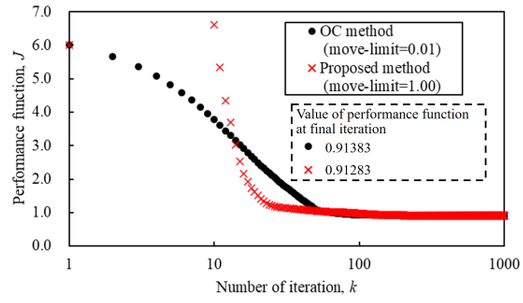

(d) When $w_1 : w_2 = 5 : 1$

Figure 5.26: The history of performance functions for multi–objective topology optimization in the gripper model.

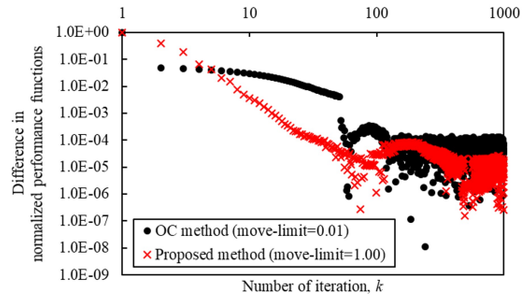

(a) When $w_1 : w_2 = 1 : 5$.

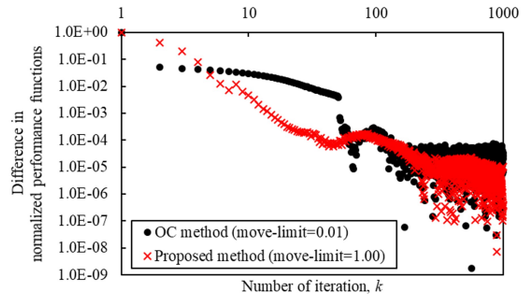

(b) When $w_1 : w_2 = 1 : 3$

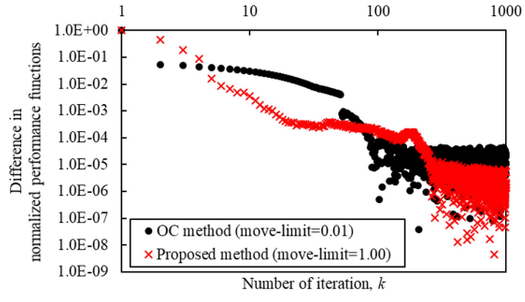

(c) When $w_1 : w_2 = 1 : 1$

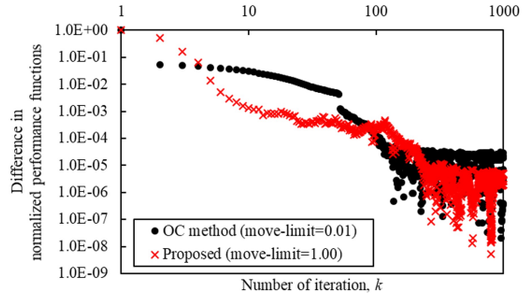

(d) When $w_1 : w_2 = 3 : 1$

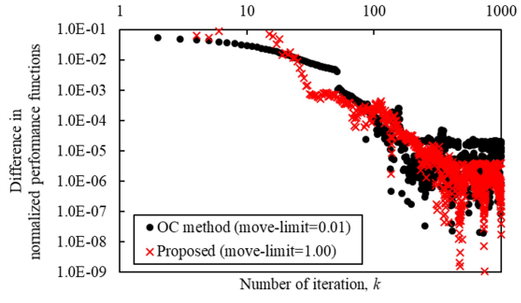

(d) When $w_1 : w_2 = 5 : 1$

Figure 5.27: Difference in normalized performance functions for multi–objective topology optimization in the gripper model.

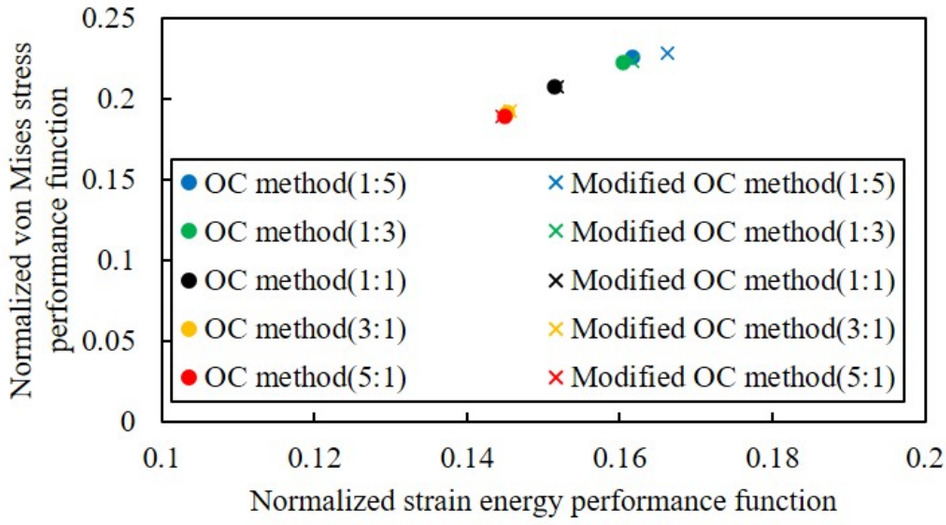

Figure 5.28: Relationship between the normalized strain energy performance function and the normalized von Mises stress performance function.

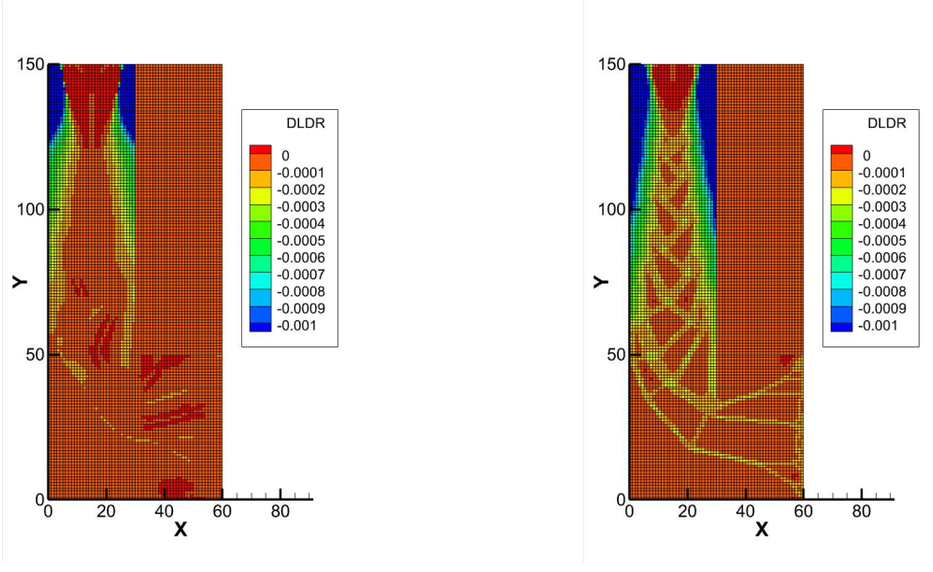

(a) When $w_1 : w_2 = 1 : 3$.

(b) When $w_1 : w_2 = 3 : 1$.

Figure 5.29: Sensitivity distributions at final iteration of multi–objective topology optimization when using the OC method in the gripper model.

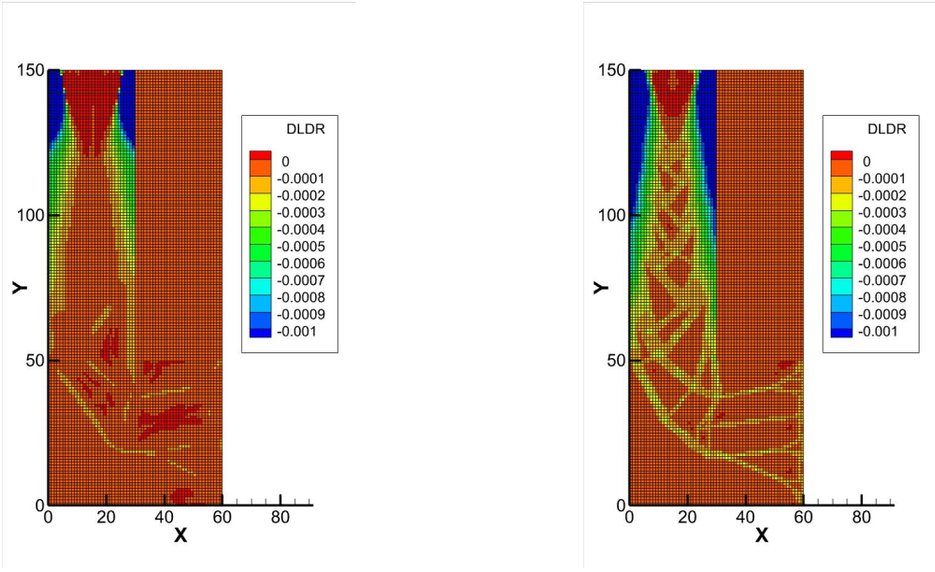

(a) When $w_1 : w_2 = 1 : 3$. (b) When $w_1 : w_2 = 3 : 1$.

Figure 5.30: Sensitivity distributions at final iteration of multi–objective topology optimization when using the mapping–based modified OC method in the gripper model.

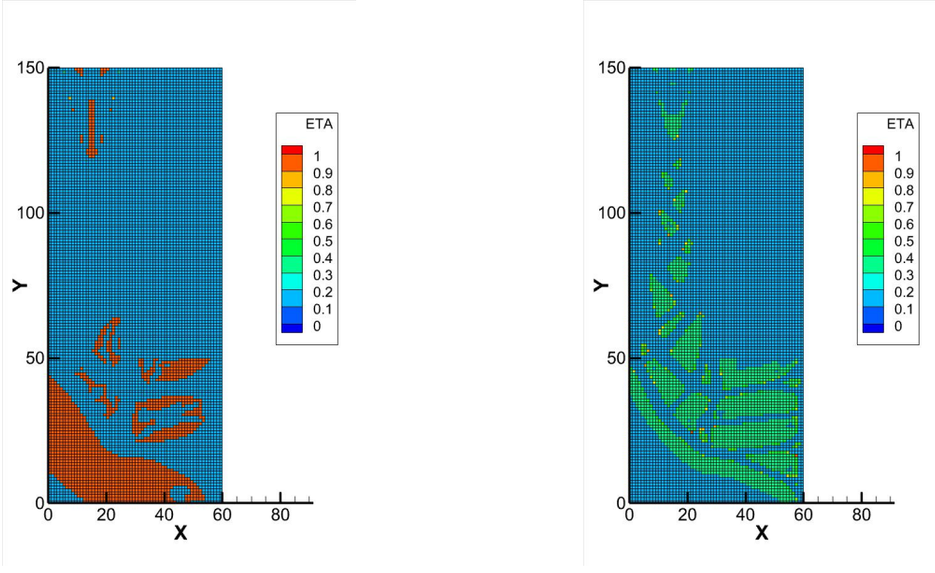

(a) When $w_1 : w_2 = 1 : 3$. (b) When $w_1 : w_2 = 3 : 1$.

Figure 5.31: Distributions of function $\Theta_{\langle e \rangle}$ at final iteration of multi–objective topology optimization when using the mapping–based modified OC method in the gripper model.

Chapter 6

Conclusions

This study proposes and verifies a new update method that incorporates the OC method, which is closely related to fully stressed method, and the Newton's method, which is a fast algorithm for nonlinear equation. The proposed modified OC method was employed for topology optimization based on the density method. The FEM was used to discretize the spatial direction. For numerical verification problems, topology optimization was performed for three optimization problems: the self-adjoint relationship problem, non-self-adjoint relationship problem, and multi-objective optimization problem combining self-adjoint relationship and non-self-adjoint relationship problems. In this thesis, the self-adjoint relationship problem shown in **chapter 2** is the strain energy minimization problem. And, the non-self-adjoint relationship problem shown in **chapter 3** is the von Mises stress minimization problem. Additionally, based on the results obtained by topology optimization for the self-adjoint relationship and the non-self-adjoint relationship problems, tensile testing was performed as a demonstration of optimization problem setup.

In **chapter 2**, a modified OC method that incorporates the concept of the Newton's method, which is known as a fast computation method for nonlinear equation, into the OC method, which is often used in conventional density-based topology optimization was proposed. As the verification problem in **chapter 2**, a topology optimization was performed to minimize strain energy, which is a self-adjoint relationship problems. In topology optimization for strain energy minimization in two dimensional steady problems, the differences in the results obtained using the conventional OC method, the gradient method with first-order

and second-order derivatives, and the proposed modified OC method are described. Topology optimization when using the OC method and the gradient method with first-order and second-order derivatives did not obtain an optimum density distribution as the setting value of move-limit ρ_{move} increased. On the other hand, topology optimization when using the modified OC method obtained an optimum density distribution independent of the move-limit ρ_{move}. The move-limit ρ_{move} when setting more than 1 is given to be the same when the move-limit ρ_{move} is not set. In addition, a tendency for the performance function to decrease rapidly with in the initial number of iterations was obtained, and an optimum density distribution was obtained with a small number of iterations. Next, topology optimization for strain energy minimization in three dimensional steady problems was performed based on the results of topology optimization for strain energy minimization in two dimensional steady problems. When the move-limit ρ_{move} was set to a small value, a hollow-like structure was obtained, and when it was set to a large value, a solid-like structure was obtained. Similarly, a tendency for the performance function to decrease rapidly with in the initial number of iterations was obtained, and an optimum density distribution was obtained with a small number of iterations. In actual manufacturing, the structure obtained when the move-limit ρ_{move} is set to a large value is easier to manufacture. For topology optimization for strain energy minimization in steady problems described in **chapter 2**, the modified OC method is simple to represent and easy to implement. Additionally, topology optimization for strain energy minimization in three dimensional dynamic oscillation problems was performed. Strain energy was replaced with work and divided into two cases, positive work and negative work, as a positive work minimization problem and a negative work minimization problem. Similar to the results for steady problems, a tendency for the performance function to decrease rapidly with in the initial number of iterations was obtained, and an optimum density distribution was obtained with a small number of iterations. The displacement waveforms of the structure obtained by topology optimization when using the modified OC method have a shorter period than that obtained by topology optimization when using the OC method. From the above, it can be said that the modified OC method is independent of the move-limit ρ_{move}

and the characteristic of obtaining a significant reduction in the performance function in the initial number of iterations. Moreover, since the weighting factor η in the OC method is given as a function, the modified OC method does not require the setting of the weighting factor and the move-limit ρ_{move} as described above. Therefore, the modified OC method is an engineer-friendly method.

In **chapter 3**, a topology optimization was performed to minimize von Mises stress, which is a non-self-adjoint relationship problems. The verification problems are two dimensional and three diemensional steady problems. In the von Mises stress minimization problems, in addition to the need to solve the adjoint equation, the exponent is negative value in the modified OC method. Thus, it is difficult to find an optimum solution. As a countermeasure, the MMN modified OC method was proposed, which incorporates the concept of a modified Newton's method that can handle negative value instead of Newton's method. Similar to **chapter 2**, the MMN modified OC method obtained a tendency for the performance function to decrease rapidly in the initial number of iterations, independent of the move-limit ρ_{move}. However, in this problem, it was difficult to reduce the number of iterations. The reason for this is that even if the performance function converges to a certain value, there are grayscale elements in a density distribution. Thus, it is difficult to set an appropriate convergence judgment. To clarify the convergence characteristics of the modified OC method, which is the proposed method, it refferd to the proof of the convergence property for the Newton's method. An attempt was made to clarify the convergence characteristics for each conditions, assuming the conditions that can occur in the calculation. However, as with typical convergence characteristics, they could not be clarified. At the moment, formula expansion involves functions that depend on each optimization problem. Without their clarification, mathematical proofs and expansions are difficult.

In **chapter 4**, tensile testing was performed to demonstrate the results obtained by topology optimization. Based on the results obtained by topology optimization described in **chapter 2** and **chapter 3**, topology optimization for strain energy minimization and von Mises stress minimization was performed for tensile specimens. Topology optimization for

strain energy minimization employs the modified OC method, and topology optimization for von Mises stress minimization employs the MMN modified OC method. The results obtained by topology optimization for von Mises stress minimization have smaller performance functions for strain energy minimization than that obtained by topology optimization for strain energy minimization. Based on the density distribution obtained by topology optimization, tensile specimens were machined by the wire electrical discharge machining. The results obtained from the tensile experiments show that the tensile specimens based on the topology optimization for von Mises stress minimization have higher strength than those based on the topology optimization for strain energy minimization. However, the tensile specimens based on topology optimization for von Mises stress minimization were broken from the edges of the design domain, rather than near the center, where the failure point was. This may be related to the interference effect of the stress concentration factor. Therefore, higher strength structures may be obtained if topology optimization considering the interference effects of stress concentrations can be performed.

In **chapter 5**, a multi-objective topology optimization was performed to minimize strain energy and von Mises stress. In **chapter 3**, the MMN modified OC method was performed. However, in **chapter 5**, the update speed of topology optimization when using the MMN modified OC method is very slow, making updates impractical. Therefore, a new mapping-based modified OC method was proposed. Similar to **chapter 2** and **chapter 3**, the mapping-based modified OC method obtained a tendency for the performance function to decrease rapidly in the initial iterations, independent of the move-limit ρ_{move}. Additionally, the multi-objective topology optimization combining the strain energy minimization problem and the von Mises stress minimization problem had the effect of suppressing grayscale within the density distribution. Grayscale suppression is generally addressed by improving the filter method. However, some filters may lead to an increase in the value of performance function and the number of iterations. Therefore, it can be said that multi-objective topology optimization combining the strain energy minimization problem and the von Mises stress minimization problem does not increase the value of the performance function while

suppressing grayscale.

These research results show that the modified OC method developed in this study can be applied to several optimization problems. For each optimization problem, it is not necessary to set the weighting factor and the move-limit, which are arbitrary parameters that must be set by the engineers. It also proved that the performance function decreases rapidly in the initial number of iterations. Topology optimization using the proposed method was demonstrated in tensile testing. Guidelines for setting up an optimization problem and advantages of both optimization problems were clarified. In summary, the proposed method is a useful alternative that reduces the number of arbitrary parameters to be set and significantly reduce the number of iterations. In addition, the proposed method can be employed for several optimization problems, including topology optimization by other methods because it is an update equation.

References

[1] M. Ishihama, Automobile vibration and noise control methods learned from 70 cases, The Nikkan Kogyo Shimbun, 2018 (in Japanese).

[2] W. Prager, A note on discretized Michell structures, Computer Methods in Applied Mechanics and Engineering, Vol. 3, p.349, 1974.

[3] K. Svanberg, Optimization of geometry in truss design, Computer Methods in Applied Mechanics and Engineering, Vol. 28, pp.63-80, 1981.

[4] O. C. Zienkiewicz, Shape optimization and sequential linear programming, in optimum structural design, Optimum Structural Design, pp.109-126, 1973.

[5] O. Pironneau, Optimal Shape Design for Elliptic Systems, Springer, 1984.

[6] H. Azegami, Shape optimization problems, Morikita Publishing Co., Ltd., 2016 (in Japanese).

[7] H. Azegami, Shape Optimization Problems, Springer, 2020.

[8] M. P. Bendsøe and N. Kikuchi, Generating optimal topologies in structural design using a homogenization method, Computer Methods in Applied Mechanics and Engineering, vol.71, pp.891-909, 1988.

[9] M. P. Bendsøe and O. Sigmund, Topology Optimization: "Theory, Methods and Applications", Springer, 2013.

[10] G. Allaire, Shape Optimization by the Homogenization Method, Springer, 2002.

[11] S. Nishiwaki, K. Izui and N. Kikuchi, Topology optimization – Computational mechanics lecture course –, Maruzen Publishing Co.,Ltd., 2013 (In Japanese).

[12] SolidWorks Corporation, 2023, SOLIDWORKS Simulation, https://www.solidworks.com/ja/product/solidworks-simulation. (Retrieved September 28th, 2023)

[13] ANSYS, Inc., 2023, Ansys, https://www.ansys.com/ja-jp. (Retrieved September 28th, 2023)

[14] Autodesk Inc., 2023, Autodesk Fusion 360, https://www.autodesk.co.jp/products/fusion-360. (Retrieved September 28th, 2023)

[15] N. Takeuchi, K. Kashiyama and K. Terada, Computational Mechanics, Morikita Publishing Co., Ltd., 2003 (in Japanese).

[16] K. Washizu, H. Miyamoto, Y. Yamada, Y. Yamamoto and T. Kawai, Handbook of Finite Element Method –Fandamentals–, Baifukan Co., Ltd., 1982 (in Japanese).

[17] K. Washizu, H. Miyamoto, Y. Yamada, Y. Yamamoto and T. Kawai, Handbook of Finite Element Method –Applications–, Baifukan Co., Ltd., 1983 (in Japanese).

[18] H. Kardestuncer and D. H. Norrie, Finite Element Handbook, McGraw-Hill, 1987.

[19] G. Yagawa and S. Yoshimura, Finite Element Method –Computational mechanics and CAE– Baifukan Co., Ltd., 1991 (in Japanese).

[20] L. P. Chew, Constrained delaunay triangulations, Algorithmica, vol.4, pp.97-108, 1989.

[21] Z. Hashin and S. Shtrikman, A variational approach to the theory of the elastic behaviour of multiphase materials, Journal of the Mechanics and Physics of Solids, vol.11, pp.127-140, 1963.

[22] K. Terada and N. Kikuchi, Introduction to Homogenization Method, Maruzen Publishing Co.,Ltd., 2003 (In Japanese).

[23] C. Jog, R. Haber and M. P. Bendsøe, Topology design with optimized, self-adaptive materials, International Journal for Numerical Methods in Engineering, vol.37(8), pp.1323-1350, 1994.

[24] M. P. Bendsøe, Optimal shape design as a material distribution problem, Structural and Multidisciplinary Optimization, vol.1(4), pp.193-202, 1989.

[25] N. Olhoff, On optimum design of structures and materials, Meccanica, vol.31(2), pp.143-161, 1996.

[26] K. Suzuki and N. Kikuchi, A homogenization method for shape and topology optimization, Computer Methods in Applied Mechanics and Engineering, vol.93(3), pp.291-318, 1991.

[27] K. Matsui and K. Terada, Continuous approximation of material distribution for topology optimization, International Journal for Numerical Methods in Engineering, vol.59(14), pp.1925-1944, 2004.

[28] R. Yang and C. Chuang, Optimal topology design using linear programming, Computers & Structures, vol.52(2), pp.265-275, 1994.

[29] H. Mlejnek and R. Schirrmacher, An engineer's approach to optimal material distribution and shape finding, Computer Methods in Applied Mechanics and Engineering, vol.106(1), pp.1-26, 1993.

[30] M. Y. Wang, X. Wang and D. Guo, A level set method for structural topology optimization, Computer Methods in Applied Mechanics and Engineering, vol.192(1), pp.227-246, 2003.

[31] G. Allaire, F. Jouve and A. Toader, Structural optimization using sensitivity analysis and a level-set method, Journal of Computational Physics, vol.194(1), pp.363-393, 2004.

[32] A. A. Novotny, R. A. Feijóo, E. Taroco and C. Padra, Topological sensitivity analysis, Computer Methods in Applied Mechanics and Engineering, vol.192, pp.803-829, 2003.

[33] Y. Nishio, Y. Liu, N. Ono and M. Shimoda, Optimum design of shear panel damper under cyclic load, Transactions of the Japan Society of Mechanical Engineers, vol.86(891), p.20-00046, 2020 (In Japanese).

[34] Y. Y. Liu, C. Yang, P. Wei, P. Zhou and J. Du, An ODE-driven level-set density method for topology optimization, Computer Methods in Applied Mechanics and Engineering, vol.387, 114159, 2021.

[35] Y. Kozuka, K. Furuta, K. Izui and S. Nishiwaki, Level set-based topology optimization considering aesthetic preferences based on texture energy, Transactions of the Japan Society of Mechanical Engineers, vol.89(924), p.22-00296, 2023 (In Japanese).

[36] United Nations, 2023, THE 17 GOALS — Sustainable Development, https://sdgs.un.org/goals. (Retrieved September 1st, 2023)

[37] Cabinet Office, 2023, Society 5.0 –Science and Technology Policy–, https://www8.cao.go.jp/cstp/society5_0/ (In Japanese). (Retrieved September 1st, 2023)

[38] United Nations, 2015, United Nations Millennium Development Goals, https://www.un.org/millenniumgoals/. (Retrieved September 1st, 2023)

[39] METI Ministry of Economy, Trade and Industry, Ministry of Health, Labour and Welfare and Ministry of Education, Culture, Sports, Science and Technology, 2020, Manufacturing White Paper 2020, https://www.meti.go.jp/report/whitepaper/mono/2020/honbun_pdf/pdf/all.pdf (In Japanese). (Retrieved September 1st, 2023)

[40] METI Ministry of Economy, Trade and Industry, Ministry of Health, Labour and Welfare and Ministry of Education, Culture, Sports, Science and Technology, 2020, Manufacturing White Paper 2023 –Annual report based on Artical 8 of the Basic Act on the Promotion of Core Manufacturing Technol-

ogy, https://www.meti.go.jp/report/whitepaper/mono/2023/pdf/all.pdf (In Japanese). (Retrieved September 1st, 2023)

[41] Japan Automobile Manufacturers Association, Inc., 2022, Japan's Automobile Industry in 2020, https://www.jama.or.jp/library/publish/mioj/ebook/2022/MIoJ2022_j.pdf (In Japanese). (Retrieved September 1st, 2023)

[42] T. Nomura, A. Kawamoto, T. Kondoh, E. M. Dede, J. Lee, Y. Song and N. Kikuchi, Inverse design of structure and fiber orientation by means of topology optimization with tensor field variables, Composites Part B: Engineering, vol.176, 2017.

[43] G. I. N. Rozvany, Structural Design via Optimality Criteria: The Prager Approach to Structural Optimization, Springer, 1989.

[44] E. Katamine, T. Tsubato and H. Azegami, Solution to Shape Optimization Problem of Viscous Flow Fields Considering Convection Term, Inverse Problems in Engineering Mechanics 4, pp.401-408, 2003.

[45] T. Kurahashi, T. Koike, M. Kishida, Y. Murakami and F. Ikeda, Application of level-set type topology optimization for defect topology identification analysis using hammering response data, Materials Today: Proceedings, 2023.

[46] N. Aage, E. Andreassen, B. S. Lazarov and O. Sigmund, Giga-voxel computational morphogenesis for structural design, Nature, vol.550(7674), pp.84-86, 2017.

[47] N. Aulig, W. Nutwell, S. Menzel and D. Detwiler, Preference-based topology optimization for vehicle concept design with concurrent static and crash load cases, Structural and Multidisciplinary Optimization, vol.57, pp.251-266, 2018.

[48] W. M. Vicente, R. Picelli, R. Pavanell and Y. M. Xie, Topology optimization of frequency responses of fluid–structure interaction systems, Finite Elements in Analysis and Design, vol.98, pp.1-13, 2015.

[49] S. Schwarz and E. Ramm, Sensitivity analysis and optimization for non-linear structural response, Engineering Computations, vol.18, pp.310-641, 2001.

[50] J. Kato, H. Hoshiba, S. Takase, K. Terada and T. Kyoya, Accuracy validation of analytical sensitivity in topology optimization for elastoplastic, Transactions of the Japan Society for Computational Engineering and Science, p20140012, 2014 (In Japanese).

[51] J. Baiges, J, Martínez-Fritos, D. Herrero-Pérez, F. Otero and A. Ferrer, Large-scale stochastic topology optimization using adaptive mesh refinement and coarsening through a two-level parallelization scheme, Computer Methods in Applied Mechanics and Engineering, vol.343, pp.186-206, 2019.

[52] S. Sasaoka and T. Kurahashi, Proposal of texture shape optimization algorithm under constant load condition and considerations on new shape update equation (Texture shape optimization for minimization of friction coefficient), Journal of Fluid Science and Technology, vol.15, JFST0022, 2019.

[53] H. Arata, M. Kishida and T. Kurahashi, Texture shape optimization analysis using a new acceleration gradient method based on the Taylor expansion and conjugate direction, Journal of Fluid Science and Technology, vol.17, JFST0011, 2022.

[54] A. Nishioka and Y. Kanno, Accelerated projected gradient method with adaptive step size for compliance minimization problem, Japan Society for Industrial and Applied Mathematics Letters, vol.13, pp.33-36, 2021.

[55] A. Nishioka and Y. Kanno, Inertial projected gradient method for large-scale topology optimization, Japan Journal of Industrial and Applied Mathematics, vol.40, pp.877-905, 2023.

[56] N. Strömberg, Topology optimization structures with manufacturing and unilateral contact constrains by minimizing an adjustable compliance-volume project, Structural and Multidisciplinary Optimization, vol.42, pp.341-350, 2010.

[57] L. Yin and W. Yang, Optimality criteria method for topology optimization under multiple constraints, Computers and Structures, vol.79, pp.1839-1850, 2001.

[58] W. H. Zhang and P. Duysinx, Dual approach using a variant perimeter constraint and effect sub-iteration scheme for topology optimization, Computers and Structures, vol.81, pp.2173-2181, 2003.

[59] C. Y. Sheu and W. Prager, Minimum-Weight Design with Piecewise Constrant Specific Stiffness, Journal of optimization theory applications, vol.2, pp.179-186, 1968.

[60] O. Sigmund and K. Maute, Topology optimization approaches, Structural and Multidisciplinary Optimization, vol.48, pp.1031-1055, 2013.

[61] M. P. Bendsøe and O. Sigmund, Material interpolation schemes in topology optimization, Archive of Applied Mechanics, vol.69(9), pp.635-654, 1999.

[62] M. Stolpe and K. Svanberg, An alternative interpolation scheme for minimum compliance topology optimization, Structural and Multidisciplinary Optimization, vol.22(2), pp.116-124, 2001.

[63] T. Borrvall, Topology optimization of elastic continua using restriction, Archive of Computational Methods in Engineering, vol.8(4), pp.351-385, 2001.

[64] T. Bruns and D. Tortorelli, Topology optimization of non-linear elastic structures and compliant mechanics, Computer Methods in Applied Mechanics and Engineering, vol.190(26), pp.3443-3459, 2001.

[65] B. Bourdin, Filters in topology optimization, International Journal for Numerical Methods in Engineering, vol.50(9), pp.2143-2158, 2001.

[66] O. Sigmund, Morphology-based black and white filters for topology optimization, Structural and Multidisciplinary Optimization, vol.33, pp.401-424, 2007.

[67] D. Fujii, K. Suzuki and H Ohtsubo, Topology optimization of frame structures using CONLIN optimizer, Journal of Structural and Construction Engineering, vol.548, pp.59-66, 2001.

[68] U. Kirsch, On singular topologies in optiimum structural design, Structural Optimization, vol.2(3), pp.133-142, 1990.

[69] G. Cheng and X. Guo, ε–relaxed approach in structural topology optimization, Structural Optimization, vol.13(4), pp.258-266, 1997.

[70] G. Rozvany and J. Sobieszczanski-Sobieski, New optimality criteria methods: forcing uniqueness of the adjoint strains by corner-rounding at constraint intersections, Structural Optimization, vol.4(3-4), pp.244-246, 1992.

[71] M. Bruggi, On an alternative approach to stress constraints relaxation in topology optimization, Structural Multidisciplinary Optimization, vol.36(2), pp.125-141, 2008.

[72] C. Le, J. Norato, T. Bruns, C. Ha and D. Tortorelli, Stress-based topology optimization for continua, Structural Multidisciplinary Optimization, vol.41(4), pp.605-620, 2010.

[73] X. Zhang and B. Zhu, Topology optimization of compliant mechanisms, Springer, 2018.

[74] Gill, P. E., W. Murray and M. H. Wright, Practical Optimization, Academic Press, 1981.

[75] K. Kanatani, Optimization Mathmatics –From basic principles to computational methods–, Kyoritsu Shuppan Co.,Ltd., 2005 (In Japanese).

[76] Y. Kanno and F. Komaki, Introduction to Optimization Method, Kodansha Ltd., 2019 (In Japanese).

[77] S. Umetani, Mathematical Optimization –From models to algorithms–, Kodansha Ltd., 2020 (In Japanese).

[78] Y. Kawada, Y. Matsura, M. Mizuno and M. Miyagawa, Material Tests, Kyoritsu Shuppan Co.,Ltd., 1974 (In Japanese).

[79] K. Yoshihara, T. Kurahashi and M. Kobayashi, Numerical and practical experiments for maximally stiff structure based on the topology optimization theory and the FEM, Japan Society for Industrial and Applied Mathematics, vol.10, pp.73-76, 2018.

[80] G. Vantyghem, W. D. Corte, E. Shakour and O. Amir, 3D printing of a post-tensioned concrete girder designed by topology optimization, Automation in Construction, vol.112, 103084, 2020.

[81] Z. Yang, K. Fu, Z. Zhang, J. Zhang and Y. Li, Topology optimization of 3D-printed continuous fiber-reinforced composites considering manufacturability, Composites Science and Technology, vol.230(1), 109727, 2022.

[82] The Society of Materials Science, Japan, Handbook of Metal Material Strength Test, Yokendo Co.,Ltd., 1977 (In Japanese).

[83] Shimadzu, 2023, EHF-E Series, https://www.an.shimadzu.co.jp/products/materials-testing/fatigue-testingimpact-testing/ehf-e-series/index.html (in Japanese). (Retrieved October 11th, 2023)

[84] M. Nishida, Stress Concentration, Morikita Publishing Co., Ltd., 1973 (in Japanese).

[85] Y. Murakami, Concept of Stress Concentration, Yokendo Co.,Ltd., 2005 (In Japanese).

[86] S. Kitayama, Design Optimization for Engineering –Theory and Practice using Computational Intelligence– Kyoritsu Shuppan Co.,Ltd., 2021 (In Japanese).

[87] J. Branke, K. Deb, K. Miettinen and R. Slowinski, Multiobjective Optimization: Interactive and Evolutionary Approaches, Springer, 2008.

[88] K. Deb, Multi–objective Optimization using Evolutionary Algorithms, Wiley, 2001.

[89] E. Katamine and Y. Arai, Multi-objective shape optimization for maximizing stiffness in thermo-elastic fields, Transactions of the Japan Society of Mechanical Engineers, vol.83(845), p.16-00490, 2017 (In Japanese).

[90] M. Mohamad, V. Asha, A. K. Kamran, I. H. A. Mohamed and K. A. A. Rashid, Multi-objective topology optimization of passive heat sinks including self-weight based on triply periodic minimal surface lattices, Case Studies in Thermal Engineering, vol.42, 102684, 2023.

[91] Research Institute for Information Technology, Kyushu University, 2021, Introduction of ITO, https://www.cc.kyushu-u.ac.jp/scp/eng/system/ITO/01_intro.html. (Retrieved December 11th, 2023)

Acknowledgments

I would like to express my sincere gratitude to my advisor, Professor Takahiko Kurahashi of Nagaoka University of Technology. He was also very enthusiastic in giving me guidance on how to research and how to teach students. I have been studying with him since I was student at fifth year at National Institute of Technology (KOSEN), Gifu College, and have had various experiences such as joint research and overseas research internship since I was assigned to his laboratory. These experiences have helped me grow significantly as an engineer, researcher, and educator. I would also like to thank you for taking care not to interfere with my research even after I started working at KOSEN, Gifu College in fourth year of the 5-year Integrated Doctoral Program.

I would like to express my sincere gratitude to Professor Noboru Yamada, Associate Professor Wataru Yamazaki, and Associate Professor Yuki Hidaka of Nagaoka University of Technology, and Professor Yoshihiro Kanno of University of Tokyo for their valuable guidance in the review and preparation of this paper. Professor Yamada and Asocciate Professer Yamazaki taught me thermohydrodynamics and compressible fluids in Applied Fluid Mechanics during my third year of undergraduate studies. After that, they have been very helpful in the activities of Science of Technology Innovation. Associate Professor Hidaka gave me severe opinions about the optimum results during the preliminary examination, and I had an opportunity to reaffirm the importance of my research. Professor Kanno checked every detail of the draft of my doctoral thesis and gave me many comments. He also gave me various opinions from a mathematical point view, and gave me an opportunity to review the derivation and proof.

Mr. Masanari Kobayashi and other members of Oiles corporation gave me experiments

using vibration tests on automobile parts and discussions on topology optimization for industry. They also taught me ideas that I could not learned at only university. I would like to express my deepest gratitude to them.

I am grateful to Associate Professor Joan Baiges of Polytechnic University of Catalonia, Spain, for kindly accepting my oversea research internship and for teaching me about the weighted sensitivity in topology optimization using topological derivatives.

I would thank mathematical design laboratory's members, Mr. Towa Koike, Mr. Masaya Kobayashi, and Mr. Kazuki Yamamoto, second-year master's students, Mr. Mizuki Ikarashi, Mr. Hideto Oda, Mr. Kosuke Shimizu, Mr. Yudai Sugiyama, and Mr. Soma Hiroka, first-year master's students, Mr. Nguyen Van Quang, Mr. Akihiro Takemori, Mr. Koya Hatashita, and Mr. Syo Fukushige, fourth-year Bachelor's students, Mr. Kazuma Kimura, Mr. Keito Hiyamizu, Mr. Daimu Ikarashi, and Mr. Mizuki Yamada, third-year Bachelor's students. I would also like to thank my classmates, Mr. Takashi Aoki, Mr. Sota Inoue, and Mr. Syuta Sasaoka, as well as the graduates and alumni of Kurahashi's laboratory.

In addition, I would like to express my gratitude to Adjunct Professor Hisakazu Oguri of the Department of Mechanical Engineering, KOSEN, Gifu College, who taught me the tensile testing, and Mr. Masahiko Sato of Techno Center, KOSEN, Gifu College, who produced the specimens for tensile testing.

Finally, I would like to express my gratitude to my family, the faculty and staff, and my friends who have supported me and made my school life possible. I am particularly grateful to all those who have helped me.

February, 2024

Science of Technology Innovation, 5-year Integrated Doctoral Program

Graduate School of Engineering, Nagaoka University of Technology

Masayuki Kishida

Chapter A

Optimum design problem for stepped one dimensional linear elastic body

In this appendix, a material property identification problem is performed for a stepped bar, a one dimensional linear elastic body, that reaches a target deformation. The proposed modified OC method is employed as the update equation. The aim of this problem is to verify whether the same optimum solution can be searched for a simplified model when the move-limit ρ_{move} is changed. Thus, the values of this parameter used in the analysis have no engineering significance. Figure A.1 shows a one dimensional linear elastic body, which is a stepped bar composed of two members. This optimization problem is to identify the Young's modulus E_1 and E_2 for the overall deformation U to be the same as the target deformation $\hat{U}$. Young's modulus E_1 and E_2 are calculated by the SIMP method. Figure A.1 is represented by a spring system as shown in Figure A.2. Thereafter, the optimum design is performed for this model.

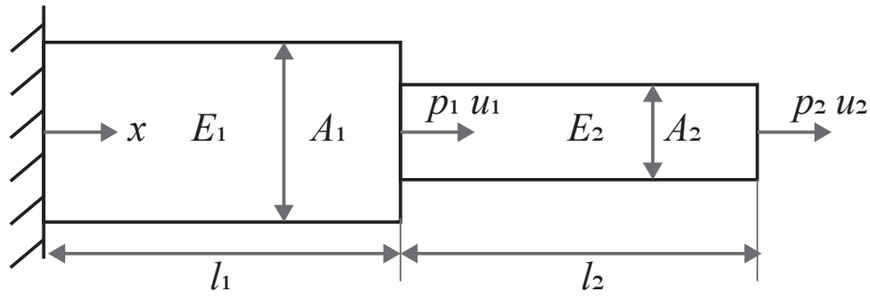

Figure A.1: One dimensional linear elastic body.

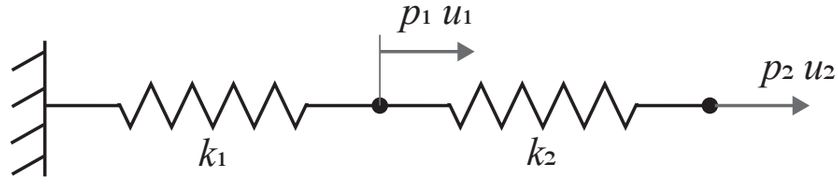

Figure A.2: Two–degree–of–freedom spring system.

Equation (A.1) is the square of the residual between the overall deformation U and the target deformation $\hat{U}$ as the performance function, and Equation (A.2) is the force balance equation obtained by Figure A.2. In addition, Equations (A.3) and (A.4) are volume constraint and density constraint similar to other optimization problems.

$$\text{minimize} \qquad J = \left(U - \hat{U}\right)^2 = \left((u_1 + u_2) - \hat{U}\right)^2 \tag{A.1}$$

$$\text{subject to} \qquad [K]\{u\} = \{f\} \tag{A.2}$$

$$V = \frac{1}{V_{\text{total}}}\left(A_1 l_1 \rho_1 + A_2 l_2 \rho_2\right) - \bar{\rho_0} \leq 0 \tag{A.3}$$

$$0 \leq \rho_i \leq 1 \quad (i = 1, 2) \tag{A.4}$$

Here, the stiffness matrix $[K]$ of a stepped one dimensional elastic body is expressed as

$$[K] = \begin{Bmatrix} k_1 + k_2 & -k_2 \\ -k_2 & k_2 \end{Bmatrix} = \begin{Bmatrix} \frac{E_1 A_1}{l_1} + \frac{E_2 A_2}{l_2} & -\frac{E_2 A_2}{l_2} \\ -\frac{E_2 A_2}{l_2} & \frac{E_2 A_2}{l_2} \end{Bmatrix} \tag{A.5}$$

This optimization is also solved in the same way, using the adjoint variable method to find an optimum solution. The gradient of the Lagrange function J^* with respect to the displacement is shown in

$$\left\{\frac{\partial J^*}{\partial u}\right\} = 2\left(U - \hat{U}\right)\left\{\frac{\partial U}{\partial u}\right\} + [K]\{\lambda\} \tag{A.6}$$

From Equation (A.6), the Lagrange multiplier vector $\{\lambda\}$ is calculated as shown in

$$\{\lambda\} = 2\left(U - \hat{U}\right)[K]^{-1}\left\{\frac{\partial U}{\partial u}\right\} \tag{A.7}$$

Using the Langrange multiplier vector $\{\lambda\}$, the gradients of the Lagrange function J^* with respect to the densities ρ_1 and ρ_2 are obtained as

$$\frac{\partial J^*}{\partial \rho_1} = \lambda_1 \frac{\partial k_1}{\partial \rho_1} u_1 \tag{A.8}$$

$$\frac{\partial J^*}{\partial \rho_2} = \lambda_1 \left(\frac{\partial k_2}{\partial \rho_2} u_1 - \frac{\partial k_2}{\partial \rho_2} u_2\right) + \lambda_2 \left(-\frac{\partial k_2}{\partial \rho_2} u_1 + \frac{\partial k_2}{\partial \rho_2} u_2\right) \tag{A.9}$$

To employ the modified OC method as shown in Equation (2.83), it is necessary to find the second derivative, which is the gradient of the sensitivity with respect to the density. The gradient of the sensitivity with respect to the density is calculated as shown in

$$\frac{\partial^2 J^*}{\partial {\rho_i}^2} = \left\{\frac{\partial \lambda}{\partial \rho_i}\right\} \frac{\partial [K]}{\partial \rho_i}\{u\} + \{\lambda\} \frac{\partial^2 [K]}{\partial {\rho_i}^2}\{u\} + \{\lambda\} \frac{\partial [K]}{\partial \rho_i}\left\{\frac{\partial u}{\partial \rho_i}\right\} \tag{A.10}$$

The gradients of the Langrange multiplier vector $\{\lambda\}$ with respect to the densities ρ_1 and ρ_2 in the above equation is obtained as

$$\left\{\frac{\partial \lambda}{\partial \rho_1}\right\} = \begin{pmatrix} \frac{-4\frac{\partial U}{\partial \rho_1}k_1 + 4\left(U-\hat{U}\right)\frac{\partial k_1}{\partial \rho_1}}{{k_1}^2} \\ \frac{-2\frac{\partial U}{\partial \rho_1}(k_1+2k_2)k_1k_2 - 2\left(U-\hat{U}\right)k_1k_2 + 2\left(U-\hat{U}\right)(k_1+2k_2)k_2}{(k_1k_2)^2} \end{pmatrix} \tag{A.11}$$

$$\left\{\frac{\partial \lambda}{\partial \rho_2}\right\} = \begin{pmatrix} \frac{-4\frac{\partial U}{\partial \rho_2}}{k_1} \\ \frac{-2\frac{\partial U}{\partial \rho_2}(k_1+2k_2)k_1k_2 - 4\left(U-\hat{U}\right)k_1k_2 + 2\left(U-\hat{U}\right)(k_1+2k_2)k_1}{(k_1k_2)^2} \end{pmatrix} \tag{A.12}$$

Table A.1 shows the calculation conditions for this optimization problem. The move-limit

ρ_{move} is set to 1.0, 10^{-1}, 10^{-2}, 10^{-3} and 10^{-4}, since there are only two members in the model. Here, when the move-limit ρ_{move} is set to 1.0, it is the same as if the move-limit ρ_{move} is not employed. The analysis is performed under two conditions. Case 1 is the analysis when the parameters are set appropriately, and Case 2 is the analysis in which the target deformation is the deformation when Young's modulus are $E_1 = 6.2$, $E_2 = 7.4$ are used as the target deformation values.

Table A.1: Calculation conditions for material property identification problem.

	Case 1	Case 2
Cross–sectional area of member 1 / 2 , A_1 / A_2	4.0 / 1.0	4.0 / 1.0
Length of member 1 / 2 , l_1 / l_2	6.0 / 6.0	6.0 / 6.0
Load of member 1 / 2 , p_1 / p_2	0.0 / 3.0	0.0 / 3.0
Young's modulus , E_0	100.0	100.0
Initial density average, $\bar{\rho_0}$	0.5	0.4
Penalization parameter for the SIMP method, p_s	3.0	3.0
Convergence criterion, $\varepsilon_{\mathrm{conv}}$	1.0×10^{-3}	1.0×10^{-3}
Target deformation, $\hat{U}$	1.0	3.1

The results in this optimization problem are described. Figures A.3 and A.4 show the histories of performance function for the material property identification problems that are Cases 1 and 2, Table A.2 shows the Young's modulus E_1 and E_2 obtained by the material property identification problems. The X-axis in the history of performance function is displayed in logarithmic scale. The results of Case 1 will be reviewed. From Figure A.3, it can be confirmed that the number of iterations decreases as the setting value of move-limit ρ_{move} is increased. The history of performance function when the move-limit ρ_{move} is set to 1.0 was generally consistent with the history of performance function when the move-limit ρ_{move} is set to 0.1. Moreover, it can also be seen that the value of performance function is convergence after decreasing. This result also tends to the Young's modulus at convergence

shown in Table A.2. Table A.2 shows that, although there are some errors, they converge to some extent at the same Young's modulus. Next, the results of Case 2 will be reviewed. As well as in Figure A.3, from Figure A.4, it can be confirmed that the number of iterations decreases as the setting value of move-limit ρ_{move} is increased. In addition, Case 2 aims to find the optimum solution with $E_1 = 6.2$ and $E_2 = 7.4$ as the correct solution, and it can be seend from Table A.2 that the optimum solution to be reached has been obtained. In fact, Figure A.5 shows what the relationship between the density ratio and the performance function looks like in the graph. From the volume constraint shown in Equation (A.3), the total density is the same and can be expressed as a density ratio since they are two members. The density ratio that is assumed to be the correct solution is marked in red in Figure A.5. Since the initial density is given uniformly, the initial density ratio is 1. In optimization with gradients, the step length must be small and the update must be gradual in order to obtain an optimum solution consistently. If the step length is increased, there is a possiblity of large deviations from an optimum solution or oscillation in a solution. However, the same results are obtained in the proposed method even when the move-limit ρ_{move}, which limits the size of the step length, is increased, as shown in Table A.2 and Figure A.5. THe reason for this is thought to be that the wighting factor η, which is the step length, is a function of the number of iterations, allowing for appropriate updates at each iteration. Additionally, as shown in Figures A.3 and A.4, it does not show large oscillation behavior even before the convergence. Therefore, the proposed modified OC method is capable of obtaining the same optimum solution with a significantly reduced number of iterations to reach an optimum solution. In addition, it reduces the number of trials for numerical experiments, since fewer parameters are needed for updating. The proposed method can be used in short-term product development situations.

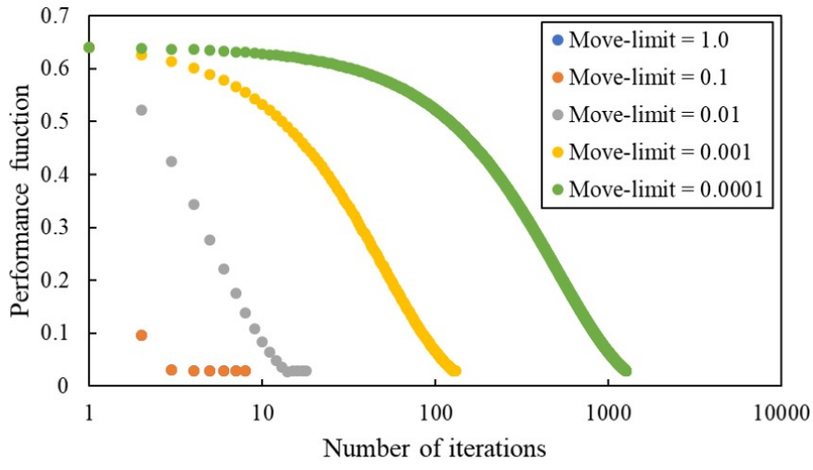

Figure A.3: The history of performance function for material property identification problem (Case 1).

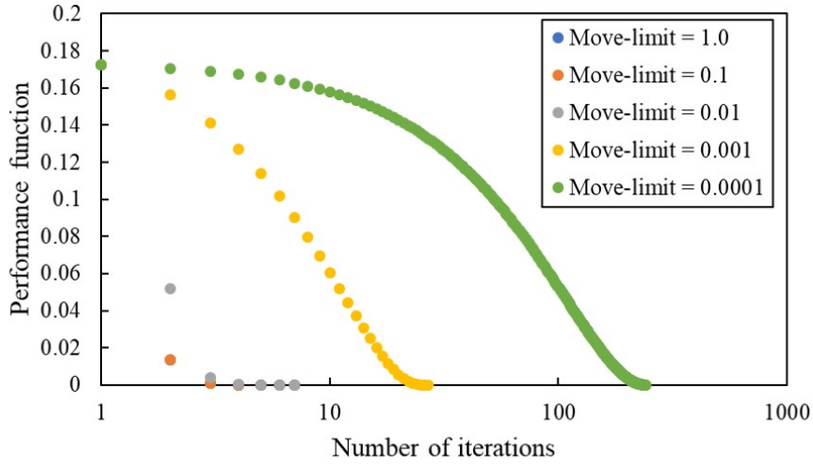

Figure A.4: The history of performance function for material property identification problem (Case 2).

Table A.2: Results in material property identification problem.

	Case 1		Case 2	
Move-limit ρ_{move}	E_1	E_2	E_1	E_2
1.0	10.2721	24.6173	6.1198	7.6114
10^{-1}	10.2721	24.6173	6.1198	7.6114
10^{-2}	10.2722	24.6174	6.1199	7.6108
10^{-3}	10.2722	24.6175	6.1199	7.6112
10^{-4}	10.2722	24.6174	6.1198	7.6117

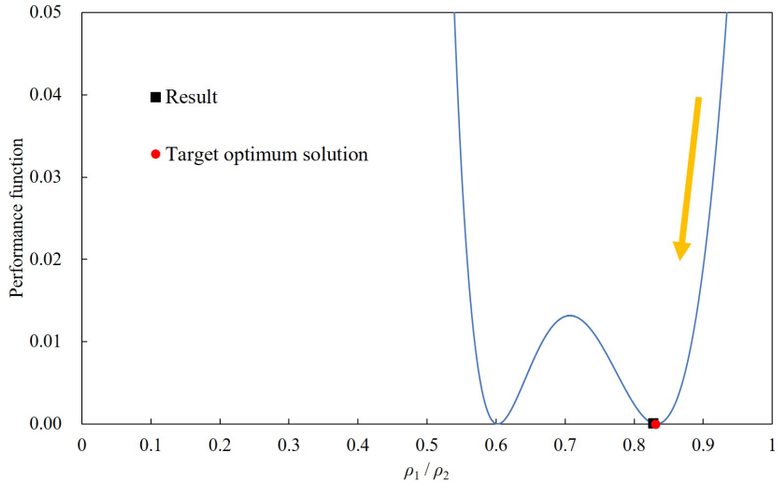

Figure A.5: Graph of relationship between density ratio and performance function in Case 2.

Chapter B

Topology optimization when using the steepest descent method

This appendix describes the result of topology optimization when using the steepest descent method. The steepest descent method for this problem is shown in

$$\rho_{\langle e\rangle}^{(k+1)} = \rho_{\langle e\rangle}^{(k)} - \alpha_s \left(\frac{\partial \bar{J}_{\langle e\rangle}^{*}}{\partial \rho_{\langle e\rangle}}^{(k)} + \Lambda \frac{\partial V}{\partial \rho_{\langle e\rangle}}^{(k)} \right) \tag{B.1}$$

where α_s is the step length. As an example, topology optimization is performed for a two dimensional cantilever beam model in the stran energy minimization problem described in **chapter 2**. The computation model is the cantilever beam model shown in Figure 2.7(a), and the calculation conditions are shown in Table 2.1. However, the convergence criterion $\varepsilon_{\mathrm{conv}}$ should be set as small as 1.0×10^{-7}. Additionally, to check the trend by the steepest descent method, the maximum number of iterations $k_{\max}$ is set to 10000.

Figures B.1 and B.2 show the history of performance function and density distributions obtained by topology optimization when using the steepest descent method. Figure B.2(a) shows the density distribution when the move-limit ρ_{move} is set to 0.01 and the step length α_s is set to 10^{-6}. Figures B.2(b) to B.2(f) show the density distributions when the move-limit ρ_{move} is set to 1.00 and the step length α_s is between 10^{-6} to 10^{-10}. From Figure B.2(a), a density distribution similar to that described in **chapter 2** was obtained at 1298th iteration. From Figure B.1, it can be confirmed that the performance function also continues to decrease. However, the density distributions when the step length α_s is set from 10^{-6} to

10^{-8} ash shown in Figures B.2(b) to B.2(d) is different from an optimum result. This can also be seen from Figure B.1, where the value of the performance function is oscillating and the analysis is not stable. The elements with a low density value will essentially be updated as having no material. However, those elements have a higher sensitivity values at a certain number of iterations, making the update unstable. If the step length is reduced in order to supress this, the results are as shown in Figures B.2(e) and B.2(f), and it can be inferred that a large number of iterations are required to find an optimum result. When using the steepest descent method in topology optimization, it is necessary to adjust the step length when the sensitivity value becomes high for elements with low values of the density mentioned above. Additionally, it can also be seen that giving the step length as a constant is not useful in this analysis.

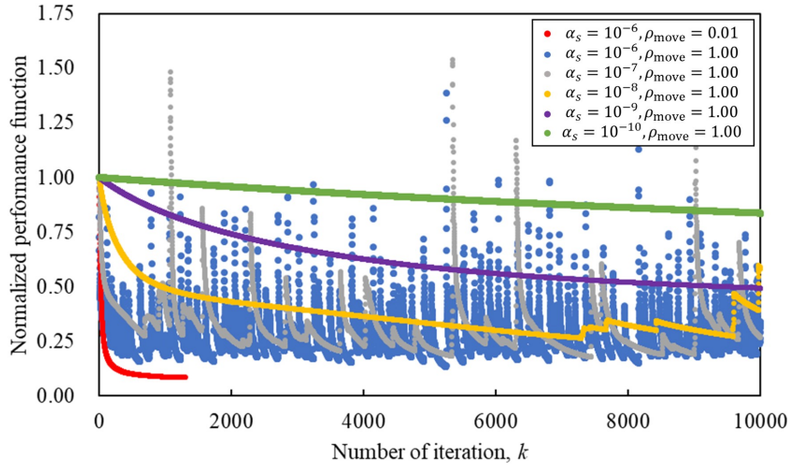

Figure B.1: History of normalized performance function in the topology optimization for strain energy minimization in the cantilever beam model when using the steepest descent method.

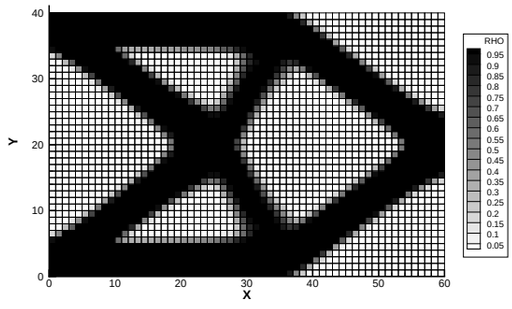

(a) When $\alpha_s = 10^{-6}$ and $\rho_{\text{move}} = 0.01$.

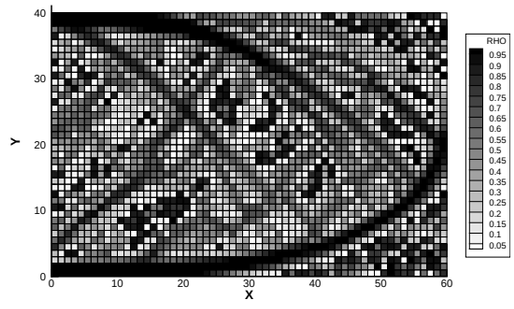

(b) When $\alpha_s = 10^{-6}$ and $\rho_{\text{move}} = 1.00$.

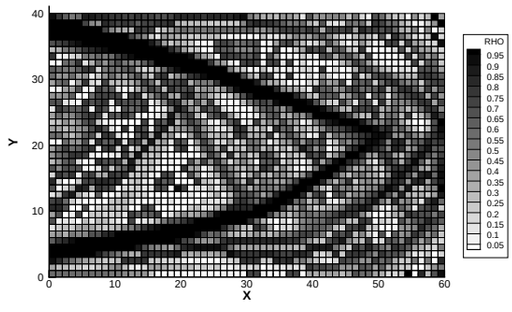

(c) When $\alpha_s = 10^{-7}$ and $\rho_{\text{move}} = 1.00$.

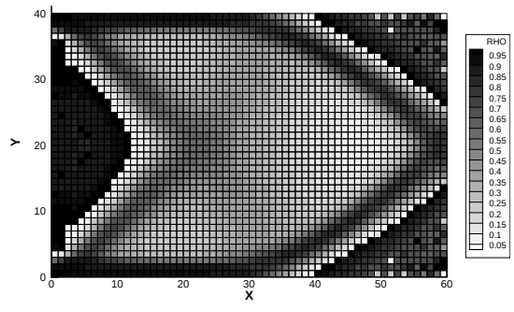

(d) When $\alpha_s = 10^{-8}$ and $\rho_{\text{move}} = 1.00$.

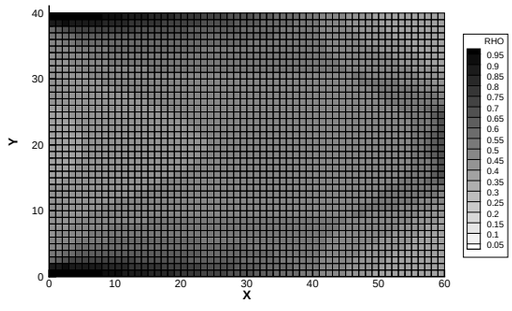

(e) When $\alpha_s = 10^{-9}$ and $\rho_{\text{move}} = 1.00$.

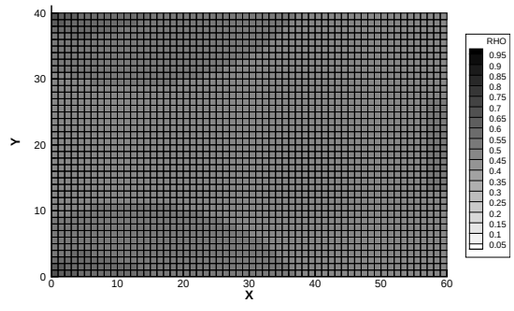

(f) When $\alpha_s = 10^{-10}$ and $\rho_{\text{move}} = 1.00$.

Figure B.2: Density distributions at final iteration when using the steepest descent method.

Chapter C

Calculation time for topology optimization

This appendix describes the calculation time of topology optimization performed in this study for strain energy minimization and von Mises stress minimization. Subsystem A of the supercomputer system ITO at Research Institute for Information Technology, Kyushu University, was used for the analysis[91]. Table C.1 shows the specifications of subsystem A. Tables C.2 to C.9 show the calculation time and number of iterations for each optimization problem, respectively. In topology optimization for strain energy minimization shown in Tables C.2 to C.7, no significant difference in calculation time per iteration was identified. However, in topology optimization for von Mises stress minimization shown in Tables C.8 to C.11, the calculation time increased for the same number of iterations due to the increased computation required to find the exponents in the proposed method. It can be seen that the proposed method takes longer calculation time per iteration than the OC method. In contrast, the proposed method does not require the setting of parameters such as the move-limit and weighting factor. In other words, the number of parametric study trials is reduced, which in turn reduces the process time required for analysis for product development.

Table C.1: Specifications of subsystem A of super computer system ITO at Research Institute for Information Technology, Kyushu University.

CPU	Intel Xeon Gold 6154 (Skylake-SP) (3.0 GHz (Turbo 3.7 GHz), 18 core) × 2 / node
Theoretical peak performance	3,456 GFLOPS / node (Double Precision)
Amount of memory	DDR4 192 GB / node
Amount of bandwidth	255.9 GB/sec / node

Table C.2: Calculation times of topology optimization for strain energy minimization in the cantilever beam model for the two dimensional static problem.

Figure No.	Update method	Total time [sec]	Iteration	Time per iteration
2.10(a)	OC	15.76	61	0.26
2.10(b)	OC	56.43	200	0.28
2.11(a)	Gradient	14.97	60	0.25
2.11(b)	Gradient	2.58	10	0.26
2.12(a)	Modified OC	19.23	69	0.28
2.12(b)	Modified OC	12.83	44	0.29

*Gradient: Gradient method with first-order and second-order derivatives.

Table C.3: Calculation time of topology optimization for strain energy minimization in the MBB beam model for the two dimensional static problem.

Figure No.	Update method	Total time [sec]	Iteration	Time per iteration
2.14(a)	OC	37.15	74	0.50
2.14(b)	OC	116.11	200	0.58
2.15(a)	Gradient	36.68	74	0.50
2.15(b)	Gradient	8.79	15	0.59
2.16(a)	Modified OC	44.00	85	0.52
2.16(b)	Modified OC	25.58	46	0.56

*Gradient: Gradient method with first-order and second-order derivatives.

Table C.4: Calculation time of topology optimization for strain energy minimization in the cantilever beam model for the three dimensional static problem.

Figure No.	Update method	Total time [sec]	Iteration	Time per iteration
2.22	OC	73.69	57	1.29
2.23	Modified OC	58.87	43	1.37

Table C.5: Calculation time of topology optimization for strain energy minimization in the MBB beam model for the three dimensional static problem.

Figure No.	Update method	Total time [sec]	Iteration	Time per iteration
2.27	OC	387.37	104	3.72
2.28	Modified OC	348.10	84	4.14

Table C.6: Calculation time of topology optimization for strain energy minimization in the cantilever beam model for the three dimensional dynamic problem.

Figure No.	Update method	Total time [min]	Iteration	Time per iteration
2.30	OC	3810	54	71
2.31	Modified OC	4753	30	158

Table C.7: Calculation time of topology optimization for strain energy minimization in the MBB beam model for the three dimensional dynamic problem.

Figure No.	Update method	Total time [min]	Iteration	Time per iteration
2.35	OC	8246	90	92
2.36	Modified OC	5720	31	185

Table C.8: Calculation time of topology optimization for von Mises stress minimization in the MBB beam model for the two dimensional static problem.

Figure No.	Update method	Total time [sec]	Iteration	Time per iteration
3.6	OC	259.42	400	0.65
3.7	OC	243.93	400	0.61
3.8	OC	254.29	400	0.64
3.9	Modified OC	445.72	400	1.11
3.10	Modified OC	417.08	400	1.04
3.11	Modified OC	413.06	400	1.03

Table C.9: Calculation time of topology optimization for von Mises stress minimization in the hook model for the two dimensional static problem.

Figure No.	Update method	Total time [sec]	Iteration	Time per iteration
3.14	OC	607.99	500	1.22
3.15	OC	746.14	500	1.49
3.16	OC	709.49	500	1.42
3.17	Modified OC	830.49	500	1.66
3.18	Modified OC	707.89	500	1.42
3.19	Modified OC	708.44	500	1.42

Table C.10: Calculation time of topology optimization for von Mises stress minimization in the MBB beam model for the three dimensional static problem.

Figure No.	Update method	Total time [min]	Iteration	Time per iteration
3.28	OC	63	150	0.42
3.29	Modified OC	187	150	1.25

Table C.11: Calculation time of topology optimization for von Mises stress minimization in the hook model for the three dimensional static problem.

Figure No.	Update method	Total time [min]	Iteration	Time per iteration
3.28	OC	641	150	4.27
3.29	Modified OC	1624	150	10.83

Research Achievements

- Published Paper

  1. **Masayuki Kishida** and Takahiko Kurahashi, Proposal of a modified optimality criteria method for topology optimization analysis in 3-dimensional dynamic oscillation problems, *International Journal for Numerical Methods in Engineering*, vol. 123(3), pp.866–896, 2022.

  2. **Masayuki Kishida** and Takahiko Kurahashi, Development of a novel non-positive definite correspondence modified optimality criteria method for multi-objective density-based topology optimization, *Mechanical Engineering Journal*, vol. 10(6), No.23–00353, 2023.

  3. **Masayuki Kishida**, Takahiko Kurahashi and Hisakazu Oguri, Density-based topology optimization for minimizing von Mises stress using the modified optimality criteria method and demonstration by tensile testing, *Engineering optimization*, 2023. (Accepted)

- Associated Paper

  1. Hiroaki Arata, **Masayuki Kishida** and Takahiko Kurahashi, Texture shape optimization analysis using a new acceleration gradient method based on the Taylor expansion and conjugate direction, *Journal of Fluid Science and Technology*, vol. 17(4), JFST0011, 2022.

  2. Takahiko Kurahashi, Kengo Takeuchi, Towa Koike, **Masayuki Kishida**, Yuki Murakami and Fujio Ikeda, Numerical studies for defect topology identification

based on the adjoint variable and the finite element methods, *Mechanical Engineering Journal*, vol. 10(3), 2023.

- Paper with conference presentation

1. **Masayuki Kishida** and Takahiko Kurahashi, Application of Sigmoid Function for Definition Equation of Young's Modulus in Topology Optimization Based on the Density Method, *Transactions of the Japan Society for Computational Methods in Engineering*, vol. 20, pp.23–30, 2020 (in Japanese).
2. **Masayuki Kishida** and Takahiko Kurahashi, Considerations on relationship between each sensitivity term and results of topology optimization in unsteady oscillation problem for 3d cantilever beam, *World Congress in Computational Mechanics and ECCOMAS Congress*, vol. 1300, pp.1–10, 2021.
3. **Masayuki Kishida** and Takahiko Kurahashi, 3D Topology Optimization Analysis for Minimization of Strain Energy in Oscillation Problems –Application of Topology Optimized Density Distribution in Steady Problems to Initial Density Distribution in Unsteady Problems–, *Transaction on GIGAKU*, vol. 8(1) pp.1–8, 2021.
4. **Masayuki Kishida**, Takahiko Kurahashi and Joan Baiges, Application of a weighted sensitivity approach for topology optimization analysis of time dependent problems based on the density method, *JSIAM Letters*, vol. 13, pp.68–71, 2021.
5. **Masayuki Kishida** and Takahiko Kurahashi, Consideration on Numerical Parameters in Density Update Equation Used in the Density-based Topology Optimization, *Transactions of the Japan Society for Computational Methods in Engineering*, vol. 21, pp.17–26, 2021 (in Japanese).
6. **Masayuki Kishida** and Takahiko Kurahashi, Considerations on the Updating Process in Density-based Topology Optimization Using the Modified Optimality

Criteria Method, *WCCM-APCOM 2022*, 2022.

7. **Masayuki Kishida** and Takahiko Kurahashi, Density-Based Topology Optimization Analysis Using the Modified Optimality Criteria Method in 3D Dynamic Oscillation Problem, *Transaction on GIGAKU*, vol. 9(2) pp.1–8, 2021.
8. **Masayuki Kishida**, Takahiko Kurahashi, Taichi Yoshiara, Ryohei Kaneko, Yuta Ishii, Wataru Nishioka, Tomohiro Yamada, and Masanari Kobayashi, Topology optimization analysis for minimization of strain energy using the modified optimality criteria method, *JSIAM Letters*, vol. 14, pp.96–99, 2022.
9. Hiroaki Arata, **Masayuki Kishida** and Takahiko Kurahashi, Proposal of a Modified Acceleration Gradient Method for Shape Optimization Problem of Texture on Bearing Surface (Considerations for Minimization Problem of Friction Coefficient Considering Oil Clearance), *Transactions of the Japan Society for Computational Methods in Engineering*, vol. 22, pp.87–96, 2022 (in Japanese).
10. Takahiko Kurahashi, Towa Koike, **Masayuki Kishida**, Yuki Murakami and Fujio Ikeda, Application of level-set type topology optimization for defect topology identification analysis using hammering response data, *Materials Today: Proceedings*, 2023.
11. **Masayuki Kishida**, Takahiko Kurahashi, Kazuhiko Akeda, Kenichi Okumura, Noboru Nakagawa, Syuichi Yamaguchi and Hidetoshi Kaida, Topology optimization based on the modified optimality criteria method for application to products, *JSIAM Letters*, vol. 15, pp.65–68, 2023.
12. Kosuke Shimizu, **Masayuki Kishida** and Takahiko Kurahashi, Level–set based topology optimization for bi–linear type elasto–plastic problems, *JSIAM Letters*. (Accepted)

- Bulletin paper

1. **Masayuki Kishida**, Takahiko Kurahashi, Tetsuro Iyama, Masanari Kobayashi

and Ryo Kato, Fabrication of topology optimization structure for the automobile's chassis parts based on 3D printing technology and experimental evaluation by vibration tests, *Research Bulletin of National Institute of Technology, Nagaoka Collage*, vol. 55, pp.21–28, 2020 (in Japanese).

2. Ryota Sakai, Kenta Yoshihara, **Masayuki Kishida**, Takahiko Kurahashi and Tetsuro Iyama, Formulation on Topology Optimization Using the Level Set Method Based on Discrete System and Numerical Experiments, *Research Bulletin of National Institute of Technology, Nagaoka Collage*, vol. 56, pp.11–16, 2021 (in Japanese).
3. Natsuki Moriyama, **Masayuki Kishida**, Takahiko Kurahashi, Fujio Ikeda and Tetsuro Iyama, Development and experiment of a defect detection machine for non-destructive inspection using a non-contact laser displacement meter, *Research Bulletin of National Institute of Technology, Nagaoka Collage*, vol. 57, pp.8–14, 2022 (in Japanese).
4. Hiroaki Arata, **Masayuki Kishida**, Takahiko Kurahashi and Tetsuro Iyama, Shape optimization of herringbone textures for minimization of the friction coefficient –Numerical experiments by changing magnitude of sliding velocity–, *Research Bulletin of National Institute of Technology, Nagaoka Collage*, vol. 58, pp.1–6, 2023 (in Japanese).
5. Tomoyuki Imakita, **Masayuki Kishida**, Takahiko Kurahashi and Tetsuro Iyama, Topology optimization using sensitivity filtering based on equivalent stress, *Research Bulletin of National Institute of Technology, Nagaoka Collage*, vol. 58, pp.13–20, 2023 (in Japanese).

- Award

1. 6th STI-Gigaku, Sumitomo Riko Award.

- International conference

1. **M. Kishida**, M. Yamamoto, M. Nanko, T. Katumi, M. Miya, M. Kondo Kawaii Rika Project: Challenge against decline in student's positive attitude toward science, *4th STI-Gigaku 2019*, 2019.
2. **M. Kishida** and T. Kurahashi, 3D topology optimization analysis for minimization of strain energy in oscillation problems –Application of topology optimized density distribution in steady problems to initial density distribution in unsteady problems–, *5th STI-Gigaku 2020*, 2020.
3. **M. Kishida** and T. Kurahashi, Considerations on Relationship between Each Sensitivity Term and Results of Topology Optimization in Unsteady Oscillation Problem for 3D Cantilever Beam, *14th World Congress on Computational Mechanics & ECCOMAS Congress 2020*, 2021.
4. **M. Kishida** and T. Kurahashi, Proposal of Optimality Criteria Method Considering the Newton's Method in Topology Optimization Problems Based on the Density Method, *Computational Science and AI in Industry 2021*, 2021.
5. **M. Kishida** and T. Kurahashi, Topology Optimization Analysis Based on the Density Method Using the Modified Optimality Criteria Method in 3D Dynamic Oscillation Problem, *6th STI-Gigaku 2021*, 2021.
6. T. Kurahashi, K. Takeuchi, M. Shimada and **M. Kishida**, Defect topology identification analysis using hammering response data based on level-set type topology optimization, *Asian Society for Structural and Multidisciplinary Optimization 2022*, 2022.
7. **M. Kishida** and T. Kurahashi, Considerations on the updating process in density-based topology optimization using the modified optimality criteria method, *15th World Congress on Computational Mechanics & 8th Asian Pacific Congress on Computational Mechanics*, 2022.
8. Takahiko Kurahashi, Towa Koike, **Masayuki Kishida**, Yuki Murakami and Fujio Ikeda, Application of level-set type topology optimization for defect topology

identification analysis using hammering response data, *3rd Indo Japan Bilateral Symposium on Futuristic Materials and Manufacturing for Sustainable Development Goals*, 2022.

9. Towa Koike, Takahiko Kurahashi, **Masayuki Kishida**, Yuki Murakami and Fujio Ikeda, Identification analysis of defect topologies using level-set-based topology optimization with weighted sensitivity, *ICIAM2023*, 2023.
10. Mizuki Ikarashi, **Masayuki Kishida** and Takahiko Kurahashi, Application of density-based topology optimization for maximally stiff structure problem using two-phase materials, *ICIAM2023*, 2023.
11. Kosuke Shimizu, **Masayuki Kishida** and Takahiko Kurahashi, Level-set-based topology optimization for bi-linear type elasto-plastic problems, *ICIAM2023*, 2023.
12. **Masayuki Kishida** and Takahiko Kurahashi, Density-based topology optimization using a modified optimality criteria method, *ICIAM2023*, 2023.
13. Seiya Matsunaga, Mizuki Ikarashi, Towa Koike, Takahiko Kurahashi and **Masayuki Kishida**, Multi-material topology optimization for stiffness maximization and tensile testing, *8th STI-Gigaku 2023*, 2023.

- Domestic conference

1. **Masayuki Kishida**, Masaya Shimada, Haruya Takahashi, Kenta Yoshihara, Takahiko Kurahashi, Ryo Kato and Masanari Kobayashi, Topology optimization analysis for strain energy minimization problem in automotive chassis components, *Annual Meeting of the Japanese Society for Industrial and Applied Mathematics 2019*, 2019.
2. **Masayuki Kishida** and Takahiko Kurahashi, Topology optimization analysis for strain energy minimization in three dimensional oscillation problems, *CMD2020*, 2020.

3. **Masayuki Kishida** and Takahiko Kurahashi, Application of Sigmoid Function for Definition Equation of Young's Modulus in Topology Optimization Based on the Density Method, *Symposium of the Japan Society for Computational Methods in Engineering 2020*, 2020.
4. **Masayuki Kishida**, Takahiko Kurahashi and Joan Baiges, Application of a weighted sensitivity approach for topology optimization analysis of time dependent problems based on the density method, *17th JSIAM Research Symposium*, 2021.
5. Tomoyuki Imakita, **Masayuki Kishida** and Takahiko Kurahashi, Influence of filtering processes in topology optimization for stress distribution of optimized structure, *CMD2021*, 2021.
6. **Masayuki Kishida** and Takahiko Kurahashi, Consideration on Numerical Parameters in Density Update Equation Used in the Density-based Topology Optimization, *Symposium of the Japan Society for Computational Methods in Engineering 2021*, 2021.
7. **Masayuki Kishida**, Topology optimization for industrial applications –Example of numerical analysis of topology optimization–, *Nagaoka University of Technology Industry-Academia Collaboration Forum*, 2021.
8. **Masayuki Kishida**, Takahiko Kurahashi, Taichi Yoshiara, Ryohei Kaneko, Yuta Ishii, Wataru Nishioka, Tomohiro Yamada, and Masanari Kobayashi, Topology optimization analysis for minimization of strain energy using the modified optimality criteria method, *18th JSIAM Research Symposium*, 2022.
9. **Masayuki Kishida** and Takahiko Kurahashi, Application of the Modified Optimality Criteria Method to Density-Based Topology Optimization for Minimizing Equivalent Stress, *CMD2022*, 2022.
10. Hiroaki Arata, **Masayuki Kishida** and Takahiko Kurahashi, Texture Shape Optimization Analysis for Minimization of Friction Coefficient using Modified Ac-

celerated Gradient Method, *CMD2022*, 2022.

11. Hiroaki Arata, **Masayuki Kishida** and Takahiko Kurahashi, Proposal of a Modified Acceleration Gradient Method for Shape Optimization Problem of Texture on Bearing Surface (Considerations for Minimization Problem of Friction Coefficient Considering Oil Clearance), *Symposium of the Japan Society for Computational Methods in Engineering 2022*, 2022.
12. **Masayuki Kishida**, Optimization to aid design and development, *Techno Symposium 2023 in KOSEN, Gifu Collage*, 2023.
13. Towa Koike, Takahiko Kurahashi, **Masayuki Kishida**, Yuki Murakami and Fujio Ikeda, Defect topology identification analysis based on level set type topology optimization using weighted sensitivity, *The Japan Society of Mechanical Engineers, Hokuriku-Shinetsu Branch 2023 Joint Meeting*, 2023.
14. **Masayuki Kishida**, Takahiko Kurahashi, Kazuhiko Akeda, Kenichi Okumura, Noboru Nakagawa, Syuichi Yamaguchi and Hidetoshi Kaida, Topology optimization based on the modified optimality criteria method for application to products, *19th JSIAM Research Symposium*, 2023.
15. **Masayuki Kishida**, Towa Koike, Mizuki Ikarashi and Takahiko Kurahashi, Optimization problems by density-based topology optimization using the modified optimality criteria method, *2023 M&M/CMD Symposium for Young Researchers*, 2023.
16. Takahiko Kurahashi, Kousuke Mizuki and **Masayuki Kishida**, Level-set based topology optimization analysis for bi-linear elasto-plastic structure model, *33rd Annual Conference of the Design and Systems Division, The Japan Society of Mechanical Engineers*, 2023.
17. **Masayuki Kishida** and Takahiko Kurahashi, Topology Optimization Using the Modified Optimality Criteria method for Von Mises Stress Minimization Structures, *CMD2023*, 2023.

- Other

    1. Offered a position as Japan Society for the Promotion of Science Research Fellow (DC2); declined due to employment at KOSEN, Gifu College.